

THE UNIVERSITY OF MANITOBA

HOLOGRAPHIC IMAGING OF TRANSILLUMINATED
PARTICLE FIELDS, USING A LOCAL OPTICALLY
PROCESSED REFERENCE WAVE

by

MAX L. A. GASSEND

A THESIS

SUBMITTED TO THE FACULTY OF GRADUATE STUDIES
IN PARTIAL FULFILLMENT OF THE REQUIREMENTS FOR THE DEGREE
OF DOCTOR OF PHILOSOPHY

DEPARTMENT OF ELECTRICAL ENGINEERING

WINNIPEG, MANITOBA R3T 2N2

August 1976

"HOLOGRAPHIC IMAGING OF TRANSILLUMINATED
PARTICLE FIELDS, USING A LOCAL OPTICALLY
PROCESSED REFERENCE WAVE"

by

MAX L. A. GASSEND

A dissertation submitted to the Faculty of Graduate Studies of
the University of Manitoba in partial fulfillment of the requirements
of the degree of

DOCTOR OF PHILOSOPHY

© 1976

Permission has been granted to the LIBRARY OF THE UNIVER-
SITY OF MANITOBA to lend or sell copies of this dissertation, to
the NATIONAL LIBRARY OF CANADA to microfilm this
dissertation and to lend or sell copies of the film, and UNIVERSITY
MICROFILMS to publish an abstract of this dissertation.

The author reserves other publication rights, and neither the
dissertation nor extensive extracts from it may be printed or other-
wise reproduced without the author's written permission.

A MON PERE ET MA MERE

Pour leur affection et leurs encouragements

A MON FILS PASCAL

Pour l'espoir qu'il m'a apporté

RÉSUMÉ

Cette thèse présente l'étude théorique et expérimentale de nouvelles méthodes et de nouveaux principes, dans le domaine de l'holographie de scènes illuminées en transparence. Seules les méthodes holographiques, qui utilisent une onde locale de référence sont considérées. Malgré les difficultés d'alignement du filtre des fréquences spatiales avec le faisceau d'illumination, il est démontré que ces méthodes sont en fait très bien adaptées à la formation d'images de champs de particules. Les sujets développés dans les trois parties de la thèse sont distincts, bien que très étroitement apparentés.

Dans la première partie, on étudie une nouvelle méthode holographique, qui utilise une onde de référence obtenue en séparant les composantes du spectre des fréquences spatiales; il est ainsi possible de filtrer simultanément: premièrement l'image agrandie avant l'enregistrement holographique et deuxièmement l'onde de référence. En particulier, un filtrage strioscopique de l'image est recommandé lorsque l'on désire observer des champs de particules. Une étude détaillée des propriétés des images strioscopiques est présentée, et une analyse mathématique fournit les lois de variation de l'amplitude et de l'intensité du champ électrique des images Gaussiennes de réseaux et de disques opaques. Les travaux expérimentaux qui sont présentés à la fin de la première partie, confirment la validité des discussions théoriques; d'autre part, une étude comparative des propriétés des images normales et des images strioscopiques démontre que le filtrage strioscopique facilite considérablement l'obtention des paramètres physiques des particules.

Dans la deuxième partie, on se propose d'introduire des principes originaux qui ont pour but d'améliorer les conditions d'utilisation des appareils holographiques qui engendrent une onde locale obtenue soit par les méthodes de division (division de l'amplitude ou de la surface d'onde), ou par la méthode introduite dans la première partie. Des trièdres réfléchissants procurent un alignement très précis de l'appareil holographique avec le faisceau d'illumination. Plusieurs montages holographiques sont proposés. Parmi ces montages, il faut mentionner celui qui permet la formation d'images à trois dimensions de champs de particules se déplaçant à très grandes vitesses. Les études expérimentales fournissent des résultats obtenus par simulations conduites en laboratoire.

Enfin, dans la troisième partie, on examine l'utilisation éventuelle d'éléments d'optique, formés à partir de deux hologrammes, dans un appareil holographique. Il est suggéré de construire ces éléments selon une méthode de compensation qui permet d'enregistrer les hologrammes sur des substrats très économiques ou sur des surfaces curvilignes. De plus, l'effet de la dimension finie des sources de construction sur la résolution d'éléments d'optique formés à partir d'un grand nombre d'hologrammes est étudié. Afin de montrer les avantages de l'appareil holographique ayant des hologrammes pour éléments d'optique, un hologramme d'une mire est enregistré.

ABSTRACT

This thesis encompasses theoretical and experimental studies of new methods and principles in the area of holographic imaging of transilluminated scenes. Only holographic methods using local optically processed reference waves are considered. It is shown in the course of the dissertation that these methods are well suited to imaging of particle fields, in spite of the fact that the spatial filters, which process the reference waves, must be accurately aligned with the illuminating beams. Distinct but related topics are studied in the three parts of the thesis.

In the first part, a holographic method, using a local reference wave obtained by spatial frequency component separation, is disclosed. This method permits simultaneous filtering of a magnified aerial image before recording, and generation of a local reference beam. Dark-field filtering of the aerial image is particularly appropriate for particle measurements. A detailed study of the properties of dark-field images is presented, and a mathematical analysis gives the expressions of the electric field amplitude and intensity distributions of the filtered Gaussian images of one-dimensional gratings and opaque disks. The experimental investigations substantiate the theoretical discussions, and a comparative study of the properties of bright-field and dark-field images indicates that dark-field filtering considerably facilitates the recovery of the pertinent particle parameters.

The second part proposes original principles aimed at improving the practicality of holocameras using local optically processed reference

waves obtained either by amplitude/wavefront division methods, or by means of the method presented in the first part. Trihedral corner reflectors are used to provide accurate alignment of the holocameras with the illuminating beams. Different holographic configurations are proposed. Of utmost interest is the configuration intended for imaging of hypervelocity particle fields. The experimental studies of the different configurations present the results of simulations which confirm the feasibility of such holocameras.

In the third part, the use of holographic optical elements in a holocamera is discussed, and a compensation method, which permits construction of a two-hologram optical element of high quality on very economical substrates or on curvilinear surfaces, is suggested. In addition, the effect of the finite extent of the construction sources on the resolution of multiple-hologram optical elements is considered. In order to show the potential advantages of the holocamera, holographic recording of a test target is performed.

ZUSAMMENFASSUNG

Diese Dissertation enthält theoretische und experimentelle Untersuchungen neuer Methoden und Prinzipien auf dem Gebiete der holographischen Abbildung durchleuchteter Gebilde. Nur solche holographische Methoden wurden betrachtet, die ein örtlich generiertes Referenzwellenfeld benutzen. Es wird in dieser Arbeit gezeigt, daß diese Methoden sich gut dazu eignen Teilchenfelder abzubilden trotz des Umstandes, daß die räumlichen Frequenzfilter, die das Referenzwellenfeld generieren genau mit dem einfallenden Strahl ausgerichtet sein müssen. In sich abgeschlossene, jedoch mit einander verwandte Themen werden in den drei Teilen der Arbeit behandelt.

Im Ersten Teil wird eine holographische Methode, die ein örtliches Referenzwellenfeld, das durch Aufteilung der räumlichen Frequenzkomponenten erhalten wurde, eingeführt. Diese Methode erlaubt gleichzeitig das Filtern eines vergrößerten räumlichen Bildes vor der Aufnahme und die Aufarbeitung eines örtlichen Referenzwellenfeldes. Dunkelfeldfilterung des räumlichen Bildes erweist sich als besonders geeignet für Teilchenmessungen. Eine detaillierte Studie der Eigenschaften von Dunkelfeldbildern wurde durchgeführt, und eine mathematische Analyse gibt die Ausdrücke der elektrischen Feldamplitude und Intensitätsverteilung der gefilterten Gauss'schen Abbildung von eindimensionalen Streugittern und undurchlässigen Scheiben wieder. Die experimentellen Untersuchungen unterstützen die theoretischen Abhandlungen, und eine vergleichende Studie der Eigenschaften von Hellfeld- und Dunkelfeld-Abbildungen zeigt, daß die Dunkelfeldfilterung die Wiedergewinnung der bedeutenden Teilchenparameter stark fördert.

Der Zweite Teil behandelt originelle Prinzipien, die sich mit der Verbesserung der praktischen Ausnutzung von Holokameras befaßen, die örtlich generierte optische Referenzwellenfelder benutzen welche entweder durch die Amplituden/Wellenfront-Teilungsmethode oder durch jene im Ersten Teile beschriebene Methode erhalten wurden. Dreieckige Eckenreflektoren wurden benutzt um genaue Ausrichtung der Holokameras mit dem Einfallsstrahl zu erhalten. Verschiedene Zusammenstellungen wurden vorgeschlagen. Von ganz besonderer Interesse ist die Zusammenstellung die für die Abbildung von hyperschnellen Teilchenfeldern ausgearbeitet wurde. Die experimentellen Untersuchungen der verschiedenen Zusammenstellungen erhalten die Ergebnisse von Simulationen, die die praktische Anwendbarkeit solcher Holokameras zeigen.

Im Dritten Teil wird die Anwendung von optischen Elementen in einer Holokamera untersucht und eine Kompensationsmethode wird vorgeschlagen, die die Konstruktion eines Zwei-Hologramm-Optoelements hoher Güte auf recht billigem Material (oder auf einer krummen Fläche) erlaubt. Weiterhin wird die Auswirkung der endlichen Größe der Strahlungsfläche auf die Auflösbarkeit von Vielfach-Hologramm-Elementen untersucht. Um die potentiellen Vorteile der Holokameras zu zeigen, wurden holographische Aufnahme von Musterzielen durchgeführt.

ACKNOWLEDGEMENTS

I would like to thank the members of my advisory committee for their guidance during the course of my studies. A special note of thanks is due to Dr. W. M. Boerner who accepted my candidature at the Faculty of Graduate Studies, and whose help and encouragement have led me to the successful completion of my studies.

My sincere gratitude is expressed to Dr. W.M. Boerner and Mr. D.K. Morland who laid the foundations of the Laser Optical Research Laboratory (LORL). Without their pioneer efforts the laboratory would never have existed. It is a pleasure to acknowledge the constant cooperation of Dr. T.R. Hsu, with whom some laboratory facilities are shared. I also wish to acknowledge the helpful attitude of Dr. K.C. Kao who let me use some of his equipment, and the useful advice of Dr. G. C. Tabisz and Dr. S. K. Sen.

My appreciation is expressed to Dr. A. Boivin, Dr. S.C. Som, Dr. R.A. Lessard, Dr. H.H. Arsenault, Dr. H.J. Caulfield, Dr. J.D. Trolinger and Dr. K.G. Birch, with whom I have had most stimulating discussions. In particular, I express my sincere gratitude to Dr. S.C. Som who accepted to referee this thesis.

Finally, I sincerely acknowledge my debt to my friends Maggie Cohoe and William Holm for the care they conferred in the proof-reading. The friendship of Mr. Kim I. Davis, who worked in the LORL for one year, and of other members of the Department of Electrical Engineering, has not been forgotten.

Special thanks are due to Mrs. Shirley Clubine for her understanding, and for her expert typing of the final version of the manuscript.

The computation work was performed with the facilities of the University of Manitoba Computer Center.

The financial assistance was provided by the Canadian Department of External Affairs and the government of the Province of Manitoba (Award No. 759 193 administered by the Canada Council).

Max L. A. Gassend

TABLE OF CONTENTS

	<u>PAGE</u>
RÉSUMÉ	i
ABSTRACT	iii
ZUSAMMENFASSUNG	v
ACKNOWLEDGEMENTS	vii
TABLE OF CONTENTS	ix
LIST OF FIGURES	xv
LIST OF TABLES	xxii
LIST OF SYMBOLS	xxiii
<i>Chapter One</i> GENERAL INTRODUCTION	1
1.1 SYNOPSIS	2
1.2 HOLOGRAPHIC IMAGING OF PARTICLE FIELDS	3
1.3 RELEVANCE OF PARTICLE MEASUREMENTS	4
1.3.1 In Pollution Monitoring	4
1.3.2 In Cloud Microphysics	5
1.3.3 In Limnology and Oceanography	6
1.3.4 In Electromagnetic Wave Propagation	6
1.3.5 In Other Fields of Science	6
<i>Chapter Two</i> SURVEY OF LITERATURE REVIEW	8
2.1 INTRODUCTION	8
2.2 MEASUREMENT OF PARTICLE PARAMETERS BY MODERN METHODS	9
2.2.1 Microholography	9
2.2.2 Laser-Doppler Velocimeters	9
2.2.3 Diffraction Methods	10
2.2.4 Holographic Methods	11

2.3	HOLOGRAPHIC PROCESS	12
2.3.1	Gabor Holography (In-Line Holography)	12
2.3.2	Fraunhofer Holography (Far Field In-line Holography)	13
2.3.3	Leith-Upatnieks Holography (Off-Axis Holography)	14
2.3.4	Phase Holograms	15
2.4	LOCAL GENERATION OF THE REFERENCE BEAM	19
2.4.1	Objectives	19
2.4.2	Implementation	20
<u>PART A</u>		
	LOCAL REFERENCE WAVE GENERATION BY SPATIAL FREQUENCY COMPONENT SEPARATION	26
<i>Chapter Three</i>	THEORETICAL STUDIES OF THE METHOD	27
3.1	INTRODUCTION	27
3.2	THE METHOD	28
3.3	IMPLEMENTATION	31
3.3.1	Single-Lens Optical Processor	31
3.3.2	Two-Lens Optical Processor	33
3.3.3	Telescope Optical Processor	33
3.3.4	Spatial Filter	36
3.3.5	Holocameras	38
3.4	ANALYSIS OF THE BASIC HOLOGRAPHIC SYSTEMS	42
3.4.1	Two-Lens Holographic System	42
3.4.2	Single-Lens Holographic System	45
3.4.3	Telescope Holographic System	46
3.4.4	Comments	48
3.4.5	Image Filtering	49
3.4.6	Reference Wave	50

3.5	RECONSTRUCTED IMAGES	52
3.5.1	Position of the Reconstructed Filtered Images	52
3.5.2	Post-Recording Addition of the Central Ordinate	53
3.6	SUMMARY	53
<i>Chapter Four</i>	MATHEMATICAL ANALYSIS OF THE RECONSTRUCTED FILTERED IMAGES	57
4.1	INTRODUCTION	57
4.2	RECONSTRUCTED IMAGE OF A ONE-DIMENSIONAL OBJECT	57
4.2.1	Dark-Field Filter	58
4.2.2	Focussing Properties of Dark-Field Images	59
4.2.3	Phase Contrast Filter	61
4.3	RECONSTRUCTED DARK-FIELD IMAGE OF AN OPAQUE DISK	61
4.3.1	Formulation	63
4.3.2	Evaluations of the Integral	64
4.3.3	Exact Value of the Field on the Profile of the Gaussian Image	78
4.4	IMPULSE RESPONSE	80
4.5	SUMMARY	80
<i>Chapter Five</i>	EXPERIMENTAL STUDIES OF THE METHOD	82
5.1	INTRODUCTION	82
5.2	QUALITATIVE STUDY OF DARK-FIELD IMAGES OF CIRCULAR APERTURES	83
5.2.1	Introduction	83
5.2.2	Experiment A1	86
5.2.3	Experiment A2	88
5.2.4	Experiment A3	88
5.2.5	Experiment A4	97
5.2.6	Experiment A5	97
5.3	VERIFICATION OF THE GENERAL PROPERTIES	101

5.3.1	Experiment A6	102
5.3.2	Experiment A7	102
5.3.3	Experiment A8	105
5.3.4	Experiment A9	105
5.4	COMPARATIVE STUDY: BRIGHT-FIELD/DARK-FIELD IMAGES	110
5.4.1	Experiment A10	110
5.4.2	Experiment A11	115
5.5	REDUCTION OF THE DISTANCE z_h	118
5.5.1	Experiment A12	118
5.6	USE OF PARTIALLY FILTERED REFERENCE BEAMS	120
5.6.1	Experiment A13	121
5.6.2	Experiment A14	121
5.7	USE OF DIFFUSED REFERENCE BEAMS	123
5.7.1	Experiment A15	126
5.7.2	Experiment A16	126
5.8	SUMMARY AND COMMENTS	129
 <u>PART B</u>		
	ORIGINAL PRINCIPLES IN HOLOGRAPHIC INSTRUMENT DESIGN	131
<i>Chapter Six</i>	THEORETICAL STUDIES	132
6.1	INTRODUCTION	132
6.2	ELECTROOPTICAL TRACKING SYSTEM	135
6.3	USE OF RETROREFLECTORS IN HOLOGRAPHY	139
6.4	PRINCIPLE OF THE BEAM-FOLDED CONFIGURATION	146
6.4.1	Analysis of the Configuration	146
6.4.2	Effect of the Scene Motion on the Fringe Visibility	148
6.4.3	Effect of Linear Motion on the Image Sharpness	155
6.4.4	Effect of Linear Recording Medium Motion	159

6.4.5	Effect of the Retroreflector Motion	161
6.5	PRINCIPLE OF THE TWO-RETROREFLECTOR CONFIGURATION	162
6.5.1	Analysis of the Configuration	163
6.5.2	Total Compensation of the Object Motion	165
6.5.3	Comments	167
6.6	PRINCIPLE OF THE CONFIGURATION ALLOWING IMAGING OF HYPERVELOCITY TRANSILLUMINATED SCENES	171
6.6.1	Analysis of the Configuration	172
6.6.2	Effect of the Rotation of the Illuminating Beam	174
6.6.3	Partial Compensation for the Object Motion	175
6.6.4	Effect of Partial Compensation on the Sharpness of the Reconstructed Image	180
6.6.5	Comments	181
6.7	HOLOGRAPHIC TOMOGRAPHY	183
6.7.1	Principle of the Configuration Allowing Holographic Tomography of Motionless Scenes	184
6.8	SUMMARY	189
<i>Chapter Seven</i>	EXPERIMENTAL INVESTIGATIONS	190
7.1	INTRODUCTION	190
7.2	BEAM-FOLDED CONFIGURATION	191
7.2.1	Experiment B1	191
7.3	MEASUREMENT OF TIME VARYING FIELDS OF PARTICLES WITH THE BEAM-FOLDED CONFIGURATION	199
7.3.1	Experiment B2	201
7.3.2	Experiment B3	205
7.4	TWO-RETROREFLECTOR CONFIGURATION	211
7.4.1	Experiment B4	214
7.4.2	Experiment B5	214
7.4.3	Experiment B6	217

7.5	SIMULATION WORK RELATIVE TO THE CONFIGURATION ALLOWING IMAGING OF HYPERVELOCITY TRANSILLUMINATED SCENES	217
7.5.1	Experiment B7	220
7.5.2	Experiment B8	229
7.6	SUMMARY	233
<u>PART C</u>		
	USE OF HOLOGRAPHIC OPTICAL ELEMENTS IN A HOLOCAMERA USING A LOCALLY PROCESSED REFERENCE BEAM	235
<i>Chapter Eight</i>	GENERATION OF HOLOGRAPHIC OPTICAL ELEMENTS	236
8.1	INTRODUCTION	236
8.2	PRINCIPLE OF THE HOLOCAMERA	237
8.3	RECORDING OF THE HOLOGRAM OPTICAL ELEMENTS	240
8.4	COMMENTS	247
8.5	SUMMARY	249
<i>Chapter Nine</i>	RESOLUTION OBTAINABLE WITH MULTIPLE-HOLOGRAM OPTICAL ELEMENTS	250
9.1	INTRODUCTION	250
9.2	THEORETICAL ANALYSIS	251
9.2.1	H_0 and H_1 are Sequentially Recorded	252
9.2.2	H_0 and H_1 are Independently Recorded	258
9.2.3	Generalization to a (n)-Hologram Optical Element	259
9.3	APPLICATIONS	260
9.4	SUMMARY	261
<i>Chapter Ten</i>	CONCLUSIONS	264
10.1	RÉSUMÉ OF THE ACHIEVEMENTS	264
10.2	SUGGESTIONS FOR APPLICATIONS AND FURTHER RESEARCH	268
	APPENDIX	272
	REFERENCES	275
	CURRICULUM VITAE	281

LIST OF FIGURES

		<u>PAGE</u>
Fig. 2.1	Typical recording and readout holographic configurations	16
Fig. 2.2	Generation of a local reference beam by amplitude division methods	21
Fig. 2.3	Generation of a local reference beam by wavefront division methods	23
Fig. 2.4	Configuration in which the cross-polarized terms of the diffracted illuminating wave are holographically recorded without being attenuated when the diffracted rays are incident under Brewster angle on the prism	24
Fig. 3.1	Generation of a local reference beam by the new holographic method	30
Fig. 3.2	Single lens optical processor allowing holographic recording of the filtered aerial image formed by the lens	32
Fig. 3.3	Two-lens optical processor allowing holographic recording of the filtered aerial image formed by the two lenses	34
Fig. 3.4	Telescope optical processor allowing holographic recording of the filtered aerial image	35
Fig. 3.5	Different devices that can be used as spatial filters	37
Fig. 3.6	Single-lens holocamera	40
Fig. 3.7	Telescope holocamera using two holographic gratings to provide ideal optical path matching between the two interfering waves	41
Fig. 3.8	Post recording addition of the central ordinate in the case of holograms recorded with the single-lens holocamera of Fig. 3.6	54
Fig. 3.9	Post-recording addition of the central ordinate in the case of holograms recorded with the telescope holocamera of Fig. 3.7	55
Fig. 4.1	Effect of dark-field filtering on a grating having an amplitude transmittance represented by a square wave	60

List of Figures cont.

	<u>Page</u>
Fig. 4.2 Amplitude distribution of the image field $\epsilon = 0.5\text{mm}$	74
Fig. 4.3 Intensity distribution of the image field $\epsilon = 0.5\text{mm}$	75
Fig. 4.4 Amplitude distribution of the image field $\epsilon = 1.25\text{mm}$	76
Fig. 4.5 Intensity distribution of the image field. $\epsilon = 1.25\text{mm}$	77
Fig. 5.1 Optical processor allowing photographic recording of a filtered image	85
Fig. 5.2 Dark-field images of complementary disks. $a = 3\text{mm}$, $\epsilon = 0.1\text{mm}$, $\tau = 15\text{mm}$ and $M'' = -10$	87
Fig. 5.3 Bright-field images recorded in three different planes. $a = 0.5\text{mm}$, $\epsilon = 15\text{mm}$ and $d = 0.4074\text{m}$	89
Fig. 5.4 Dark-field images recorded in three different observation planes. $a = 0.5\text{mm}$, $\epsilon = 0.1\text{mm}$ and $d_1 = 0.4074\text{m}$	90
Fig. 5.5 Dark-field images recorded in the conjugate plane. $a = 0.5\text{mm}$, $\epsilon = 0.1\text{mm}$ and $M'' = -55$	92
Fig. 5.6 Dark-field images recorded in the conjugate plane. $a = 0.5\text{mm}$, $\epsilon = 0.5\text{mm}$ and $M'' = -55$	93
Fig. 5.7 Dark-field images recorded in the conjugate plane. $a = 0.5\text{mm}$, $\epsilon = 1.25\text{mm}$ and $M'' = -55$	94
Fig. 5.8 Dark-field images recorded in the conjugate plane. $a = 0.05\text{mm}$, $\epsilon = 1.25\text{mm}$ and $M'' = -55$	95
Fig. 5.9 Dark-field images recorded in the conjugate plane. $a = 0.05\text{mm}$, $\epsilon = 2.5\text{mm}$ and $M'' = -55$	96
Fig. 5.10 (a) and (c) are dark-field images recorded in front of and behind the conjugate plane res- pectively. (b) is the dark-field image recorded in the conjugate plane. $a = 0.05\text{mm}$ and $\epsilon = 2.5\text{mm}$	96
Fig. 5.11 (a) is the dark-field image in the conjugate plane and (b) is the dark-field image in a plane slightly away from the conjugate plane. $a = 0.005\text{mm}$, $\epsilon = 10\text{mm}$ and $\tau = 50\text{mm}$	98

List of Figures cont.

	<u>Page</u>	
Fig. 5.12	Bright-field images recorded in three different planes. $a = 0.5\text{mm}$ and $\tau = 15\text{mm}$	98
Fig. 5.13	Spatial frequency spectra (Airy patterns) for circular apertures of different radii placed in the object plane	100
Fig. 5.14	Imaging of a continuous tone transparency	103
Fig. 5.15	Imaging of amplitude and phase objects	104
Fig. 5.16	Imaging of opaque objects	106
Fig. 5.17	Reconstructed images recorded in two different conjugate planes	107
Fig. 5.18	Reconstructed bright-field images recorded in two different planes	108
Fig. 5.19	Reconstructed dark-field images in two different planes	109
Fig. 5.20	(a) and (b) are two different views of the arrangement embodying the single-lens holocamera	111
Fig. 5.21	(a) and (b) show the sprayed flat glass; (c) and (d) show the directly recorded bright-field images	112
Fig. 5.22	(a) and (b) show the directly recorded dark-field images. (c) and (d) show the holographically reconstructed dark-field images. $z_h = .75\text{m}$	114
Fig. 5.23	(a), (c), (b) and (d) show the directly recorded bright-field and dark-field images. $z_h = 4.75\text{m}$. (e) shows a contact print of the sprayed flat glass	116
Fig. 5.24	Reconstructed bright-field and dark-field images in the two conjugate planes. $z_h = 4.75\text{m}$	117
Fig. 5.25	Reconstructed dark-field images in the two conjugate planes. $z_h = 0.5\text{m}$	119
Fig. 5.26	(a) is a contact print of the hologram. The reference beam is partially filtered and not collimated. (b) and (c) are the reconstructed dark-field images in the conjugate planes	122
Fig. 5.27	(a) is a contact print of the hologram. The reference beam is partially filtered and collimated. (b) and (c) are the reconstructed dark-field images in the conjugate planes	124

<u>List of Figures</u> cont.		<u>Page</u>
Fig. 5.28	(a) is a contact print of the recorded hologram. The diffused reference source of a 6mm diameter is located at 0.75m from the hologram plane. (b) and (c) are the contact prints of the holograms recorded in Experiment All	127
Fig. 5.29	(a) and (b) are the contact prints of the holograms of bright-field and dark-field images. The diffused reference source of a .2mm diameter is located at .75m from the hologram plane. (c) and (d) are the bright-field and dark-field reconstructed images	128
Fig. 6.1	Applications of holocameras with local optically processed reference beams to remote sensing	133
Fig. 6.2	Possible arrangements of the holocamera with respect to the laser source	134
Fig. 6.3	Block diagram	136
Fig. 6.4	Implementable systems for remote sensing applications	137
Fig. 6.5	Types of retroreflectors	141
Fig. 6.6	Defining the coordinate systems	144
Fig. 6.7	Setup illustrating the basic beam-folded configuration	147
Fig. 6.8	Recording geometry	151
Fig. 6.9	Effective numerical aperture of the hologram as a function of the number of wavelengths of scene motion	156
Fig. 6.10	Reconstructed image of an object point having a linear motion	158 158
Fig. 6.11	Modified beam-folded configuration	164
Fig. 6.12	Compensation for transverse scene displacements	169
Fig. 6.13	Holographic configuration	173
Fig. 6.14	Two-dimensional representation	176
Fig. 6.15	Image motion with respect to the holocamera	177

List of Figures cont.

	<u>Page</u>
Fig. 6.16 Holographic tomography	185
Fig. 6.17 Holographic tomography	188
Fig. 7.1 Close up of one of the tetrahedral prism reflectors used in the experiments	192
Fig. 7.2 Photograph of the setup	192
Fig. 7.3 General view of the beam-folded configuration	194
Fig. 7.4 Overall view of the setup	195
Fig. 7.5 (a) and (b), effect of the object motion on the reconstructed images. (c), (d) and (e), effect of the retroreflector motion on the reconstructed images	196
Fig. 7.6 Compensation for a reduction in illuminating beam cross section	198
Fig. 7.7 Arrangements used for dark-field holographic recording of particle fields	200
Fig. 7.8 Reconstructed images of glass beads falling freely in the water-filled liquid gate	203
Fig. 7.9 Reconstructed dark-field images of relatively dense spatial distributions of glass beads	204
Fig. 7.10 Two dark-field images reconstructed from the same hologram	206
Fig. 7.11 Holographic imaging of diatoms	{ 208 209 210
Fig. 7.12 General views of the experimental setup	212
Fig. 7.13 Experimental setups of the bright-field holocamera and of the dark-field holocamera	213
Fig. 7.14 Photographs directly recorded in the conjugate plane of the object	215
Fig. 7.15 Photographs of the holographically reconstructed images	216
Fig. 7.16 Holographically recorded images of the three-dimensional moving scenes when the scene motion is compensated for	218

List of Figures cont.

	<u>Page</u>	
Fig. 7.17	Holocameras used in the experimental simulation of the configuration allowing imaging of hyper-velocity transilluminated scenes	219
Fig. 7.18	General view of the simulation setup enabling synchronization between the angular motion of the rotating mirror and the transverse scene motion	221
Fig. 7.19	General perspective of the simulation setup	222
Fig. 7.20	Bright-field photographs recorded in the conjugate planes of the three objects. Exposure time: 10 sec, transverse displacement: 0	223
Fig. 7.21	Bright-field photographs recorded in the conjugate planes of the three objects. Exposure time: 10 sec, transverse displacement: $\sim 7\text{mm}$, the mirror rotation is not linked with the transverse scene motion	224
Fig. 7.22	Bright-field photographs recorded in the conjugate planes of the three objects. Exposure time: 10 sec, transverse displacement: $\sim 7\text{mm}$, the mirror rotation is linked with the transverse scene motion	225
Fig. 7.23	Dark-field photographs recorded in the conjugate planes of the three objects. Exposure time: 10 sec, transverse displacement: 0	226
Fig. 7.24	Dark-field photographs recorded in the conjugate planes of the three objects. Exposure time: 10 sec, transverse displacement: $\sim 7\text{mm}$, the mirror rotation is not linked with the transverse scene motion	227
Fig. 7.25	Dark-field photographs recorded in the conjugate planes of the three objects. Exposure time: 10 sec, transverse displacement: $\sim 7\text{mm}$, the mirror rotation is linked with the transverse scene motion	228
Fig. 7.26	Bright-field image reconstructed from a hologram. Exposure time: 10 sec, transverse displacement: $\sim 7\text{mm}$, the mirror rotation is not linked with the transverse scene motion	230

List of Figures cont.

		<u>Page</u>
Fig. 7.27	Bright-field images reconstructed from the same hologram. Exposure time of the hologram: 10 sec, transverse displacement: ~ 7 mm, the mirror rotation is linked with the transverse scene motion	231
Fig. 7.28	Dark-field images reconstructed from the same hologram. Exposure time of the hologram: 10 sec, transverse displacement: ~ 7 mm, the mirror rotation is linked with the transverse scene motion	232
Fig. 8.1	Holocamera using three holographic optical elements	238
Fig. 8.2	Imaging system composed of a two-hologram optical element	241
Fig. 8.3	Recording of the auxiliary hologram H'	243
Fig. 8.4	Recording of the hologram H_0	243
Fig. 8.5	Recording of the auxiliary hologram H''	245
Fig. 8.6	Recording of the hologram H_1	246
Fig. 9.1	Holographic imaging of a resolution test target by means of the holocamera embodying three-hologram optical elements	262
Fig. 10.1	Imaging of particle fields in cloud microphysics	269
Fig. 10.2	Imaging of particle fields in pollution control	270
Fig. A.1	Rayleigh-Sommerfeld diffraction model	273

LIST OF SYMBOLS

Mathematical Operators

Latin Alphabet:

$Ci(\rho_j)$	Cosine integral, defined in (4.21)
$E_n(A,B;x_j,y_j)$	$= \exp\{i\alpha_n [A(x_j,y_j) ^2 + B(x_j,y_j) ^2]\}$
$\mathcal{F}_{1/\lambda_s} [\]$	Fourier transform operator, evaluation at spatial frequencies $x_j/(\lambda_s)$ and $y_j/(\lambda_s)$
$H_s(x_j,y_j)$	Gaussian function with complex variance $= \exp[(i\pi/\lambda_s)(x_j^2+y_j^2)]$
$\mathcal{H}_{1/\lambda_s} [\]$	Hankel transform operator, evaluation at spatial frequency $\rho_j/(\lambda_s)$
$J_n(\rho_j)$	Bessel function of the first kind and nth order
P_j^-	Plane located just in front of the plane $\{x_j,y_j\}$, case of the telescope holographic system
P_j^+	Plane located just behind the plane $\{x_j,y_j\}$, case of the telescope holographic systems
$Si(\rho_j)$	Sine integral, defined in (4.19)
$\{X,Y,Z\}$	Cartesian coordinates
arg	Argument of
$f(\rho_j)$	Auxiliary function, defined in (4.25)
$g(\rho_j)$	Auxiliary function, defined in (4.26)
i	Complex operator $= \sqrt{-1}$
rect (t)	$= \begin{cases} 1 & t \leq 1/2 \\ 0 & \text{otherwise} \end{cases}$
$si(\rho_j)$	Sine integral, defined in (4.20)
sinc(t)	$= (\text{sint})/t$
$\{x,y,z\}$	Cartesian coordinates
$\{x_j,y_j,z_j\}$	Cartesian coordinates

Greek Alphabet:

π_j^-	Plane located just in front of the plane $\{x_j, y_j\}$, case of the two-lens and of the single-lens holographic system
π_j^+	Plane located just behind the plane $\{x_j, y_j\}$, case of the two-lens and of the single-lens holographic system
$\sum_{n=..}^{\dots}$	Sum of
$\delta(x_j, y_j)$	Dirac delta function
$[]^*$	Conjugate of
$[] * []$	Convolution operator
$[]!$	Factorial operator
$ [] $	Magnitude of

Symbols for Variable Physical Quantities

Latin Alphabet:

$A(x_j, y_j)$	Amplitude distribution of the electric field of the object bearing wave, in the plane $\{x_j, y_j\}$
$A(x_j, y_j, t)$	Time-varying phasor of the object wave
$A_0(x_j, y_j)$	Magnitude of the phasor $A(x_j, y_j, t)$
$B(x_j, y_j)$	Amplitude distribution of the electric field of the reference wave, in the plane $\{x_j, y_j\}$
$B(x_j, y_j, t)$	Time-varying phasor of the reference wave
$B_0(x_j, y_j)$	Magnitude of the phasor $B(x_j, y_j, t)$
$D_0(x_2, y_2)$	Amplitude transmittance of the substrate of the hologram H_0
$D_1(x_2, y_2)$	Amplitude transmittance of the substrate of the hologram H_1
$E(x_j, y_j)$	Film exposure
$F_r(x_2, y_2)$	Amplitude reflectance of the spatial filter

$F_t(x_2, y_2)$	Amplitude transmittance of the spatial filter
$G(x_j, y_j)$	Electric field of the reconstructed image, in the plane $\{x_j, y_j\}$
$H(\omega')$	Transfer function, defined in (6.20)
$I(x_j, y_j)$	Intensity distribution in the plane $\{x_j, y_j\}$
$I(x_j, y_j, t)$	Time-varying irradiance distribution in the plane $\{x_j, y_j\}$
L	Half the spatial period of the amplitude transmittance of a grating
M	Represents one of the transverse magnification factors (M'_n, M''_n or M'''_n)
M''	Transverse magnification factor (case of the single-lens holographic system)
M'_n	Transverse magnification factor in the image plane of the (n)th planar distribution (case of the two-lens holographic system.) Defined in (3.14)
M''_n	Transverse magnification factor in the image plane of the (n)th planar distribution (case of the single-lens holographic system). Defined in (3.17)
M'''_n	Transverse magnification factor in the image plane of the (n)th planar distribution (case of the telescope optical system). Defined in (3.31)
\mathcal{M}'''_n	Longitudinal magnification factor defined in (3.32), case of a telescope holographic system
$[M]$	Matrix, refer to (6.4)
$[M']$	Matrix, refer to (6.4)
N	Number of planar distributions
$O(x_5, y_5, z)$	Three-dimensional amplitude distribution of the electric field in the image space (case of the telescope holographic system)

$O_j(x_j, y_j)$	In Part C only, collimated wave defined in (8.1), this wave is reconstructed by the hologram H' and bears the substrate irregularities of the hologram H_0
$O_j(x_j, y_j)$	In Part A only, amplitude distribution of the electric field in the plane $\{x_j, y_j\}$
$O_0(x_0, y_0, d)$	Three-dimensional amplitude distribution of the electric field radiated by the scene
$[O_j(x_j, y_j)]^-$	Amplitude distribution of the electric field in a plane located just in front of the plane $\{x_j, y_j\}$
$[O_j(x_j, y_j)]^+$	Amplitude distribution of the electric field in a plane located just behind the plane $\{x_j, y_j\}$
$O_j^{(n)}(x_j, y_j)$	Amplitude distribution of the electric field engendered by the (n)th planar distribution, in the plane $\{x_j, y_j\}$
$O_0^{(n)}(x_0, y_0, d_n)$	Amplitude distribution of the electric field radiated by the (n)th planar distribution
$[O_j^{(n)}(x_j, y_j)]^-$	Amplitude distribution of the electric field engendered by the (n)th planar distribution, in a plane located just in front of the plane $\{x_j, y_j\}$
$[O_j^{(n)}(x_j, y_j)]^+$	Amplitude distribution of the electric field engendered by the (n)th planar distribution, in a plane located behind the plane $\{x_j, y_j\}$
P	Real integer, $P \leq N$
P_j^-	Plane located just in front of the plane $\{x_j, y_j\}$
P_j^+	Plane located just behind the plane $\{x_j, y_j\}$
$P_j(x_j, y_j)$	Unaberrated diverging wave, the expression of which is given by (9.15)
$Q_2(x_2, y_2)$	In Part C only, readout wave generated by the ideal point source (Dirac delta function), is defined in (9.6)

$Q_5(x_5, y_5, z)$	Three-dimensional amplitude distribution of the electric field in the image space (case of the single-lens holographic system)
$R_j(x_j, y_j)$	Unaberrated collimated wave, the expression of which is given by (9.17)
$S_j(x_j, y_j)$	Wave reconstructed upon illumination of H_0 with the readout wave $P_1(x_1, y_1)$, defined in (9.2)
T	Exposure time
T_1	Period of vibration
$T_j(x_j, y_j)$	Unaberrated converging wave, the expression of which is given by (9.16)
$[T_1]$	Matrix, refer to (6.5)
$U_5(x_5, y_5)$	In Part A only, electric field in the conjugate plane $\{x_5, y_5\}$ when no screen is present in the object plane. Defined in (5.1)
$U_j(x_j, y_j)$	In Part C only, converging wave defined in 8.3, this wave is reconstructed by the hologram H'' and bears the substrate irregularities of the hologram H_1
$U'_5(x_5, y_5)$	Electric field in the conjugate plane $\{x_5, y_5\}$ when the object is a disk. Introduced in (5.1)
$U''_5(x_5, y_5)$	Electric field in the conjugate plane $\{x_5, y_5\}$ when the object is the complementary aperture of the disk. Introduced in (5.1)
$X_c, X_m, X'_m, X''_m, X_n$ $Y_c, Y_m, Y'_m, Y''_m, Y_n$ $Z_c, Z_m, Z'_m, Z''_m, Z_n$	Coordinates of the points C, M, M', M'' and N
$X_{c0}, X_{m0}, X'_{m0}, X''_{m0}, X_{n0}$ $Y_{c0}, Y_{m0}, Y'_{m0}, Y''_{m0}, Y_{n0}$ $Z_{c0}, Z_{m0}, Z'_{m0}, Z''_{m0}, Y_{n0}$	Coordinates of the points C, M, M', M'' and N at $t = 0$

$$\begin{matrix} \dot{X}_c, \dot{X}_m, \dot{X}'_m, \dot{X}''_m, \dot{X}_n \\ \dot{Y}_c, \dot{Y}_m, \dot{Y}'_m, \dot{Y}''_m, \dot{Y}_n \\ \dot{Z}_c, \dot{Z}_m, \dot{Z}'_m, \dot{Z}''_m, \dot{Z}_n \end{matrix}$$

Time derivatives of the coordinates of the points C, M, M', M'' and N respectively

- a In Part A only, radius of the particle, disk or aperture
- a In Part B only, constant
- a_j Parameter
 $a_j = (r_j/\rho_j)^2 / [(\lambda\rho_j f_j)^2 + r_j^4 (f_j + \rho_j)^2]$
- a_n Real coefficient, introduced in (4.4) and (4.5)
- $a(x_j, y_j, t)$ Time-varying complex function, defined in 6.13
- b In Part B only, parameter defined in (6.29)
- b In Part C only
 $= 1/\lambda f_j$
- b_n Real coefficient, introduced in (4.4) and (4.5)
- $b(x_j, y_j)$ Complex function, defined in (6.14)
- c In Part B only, constant
- c In Part C only,
 $= [r_j^4 \rho_j (f_j + \rho_j)] / [\lambda f_j [(\lambda\rho_j f_j)^2 + r_j^4 (f_j + \rho_j)^2]$
- $c_1, c_2, \dots, c_7, c_8$ Coefficients found in (6.25) and (6.26)
- c_k Complex coefficient of the Fourier series (4.1)
- d In Part A only, distance between the plane $\{x_0, y_0\}$ and the lens L_1
- d In Part B only, constant
- d In Part C only, distance between the origin of the coordinate system $\{x_3, y_3\}$ and the origine of the coordinate system $\{X_3, Y_3\}$
- d_n Distance between the (n)th planar distribution and the lens L_1

e	$= (a^2 + b^2 + c^2)^{1/2}$
e_n	Parameter defined in (3.12)
f_1, f_2, f_3	Focal lengths of the lenses L_1, L_2 and L_3 respectively
g	Function related to the numerical aperture of the hologram $= [(x_4 - x_4')^2 + (y_4 - y_4')^2]^{1/2} / h$
g_a	Function related to the numerical aperture of the hologram, case of axial scene displacement. Defined in (6.35)
g_n	Introduced in (3.25) $= f \ell_n / (f + \ell_n)$
g_t	Function related to the numerical aperture of the hologram, case of transverse displacement. Defined in (6.36)
h	In Part A only, thickness of transparent varnish
h	In Part B only, distance between the object point M and the recording plane, see Fig. 6.8
k	Integer, $k = 0, \pm 1, \pm 2 \dots$
ℓ	Length of the line source $= vT$
ℓ_n	Introduced in (3.25) $= f_1^2 / (f_1 - d_n)$
m_0	Largest integer satisfying the inequality $m_0 < 2\epsilon L / \lambda f_1$
m_1	Largest integer satisfying the inequality $m_1 < 2\tau L / \lambda f_1$
m_x	Parameter $= (id - iz \sin \gamma) (3a_0 + 2a_2 \cos^2 \gamma + ic_0)$
m_y	Parameter $= [m_x]_{\gamma=0}$
\bar{n}	Unit vector normal to the aperture, see Fig. A.1
n_b	Absolute refractive index of balsam

n_v	Absolute refractive index of varnish
P_0	Distance between the middle of the line source and the point $P\{x_4, y_4\}$, see Fig. 6.10
P_x	Parameter $= (3a_0 + a_1 + 2a_2 \cos^2 \gamma - ic_0 + ic_1)$
P_y	Parameter $= [P_x]_{\gamma=0}$
P_x^r	Parameter $= P_x - 2a_0$
P_y^r	Parameter $= [P_x^r]_{\gamma=0}$
q_x	Parameter $= (3a_0 + a_1 + 2a_2 \cos^2 \gamma)$
q_y	Parameter $= [q_x]_{\gamma=0}$
q_x^r	Parameter $= q_x - 2a_0$
q_y^r	Parameter $= [q_x^r]_{\gamma=0}$
r_{21}	Magnitude of the vector \bar{r}_{21}
r_a	Radius of the lens aperture
r_0, r_1, r_2	Radius of the pinholes which are used for the spatial filtering of the construction sources
r_{12}	Distance between two points, see Fig. A.1
r_p	Radius of the pinhole placed behind the spatial filter
\bar{r}_{21}	Vector defined in Fig. A.1
s	Distance between two planes, see Fig. A.1
t	Time
t_0	High average level of amplitude transmittance
$t(x_j, y_j)$	Amplitude transmittance

- u Introduced in (3.35)
 $= (z_h + z_n)$ in the case of a two-lens or a single-lens holographic system
 $= f_2$ in the case of a telescope holographic system
- v In Part A only, introduced in (3.34)
 $= e_n$ (case of the two-lens holographic system)
 $= [e_n]_{f_2 \rightarrow \infty}$ (case of the single-lens holographic system)
 $= z_h + z - f_2^2 / g_n$ (case of the telescope holographic system)
- v In Part B only, velocity of the scene or of the recording medium
- w, w_0, w_1, w_2 Beam half-width of beams having Gaussian profiles
- x_4^t
 y_4^t Coordinates of the point 0, see Fig. 6.8
- $x_c, x_m, x_m^t, x_m^{tt}, x_n$
 $y_c, y_m, y_m^t, y_m^{tt}, y_n$
 $z_c, z_m, z_m^t, z_m^{tt}, z_n$ Coordinates of the points C, M, M', M'' and N respectively
- z In Part A only, distance from the object to the recording plane (or hologram plane)
- z In Part B only, abscissa, see Fig. 6.10
- z In Part C only, distance between two holographic elements, see Fig. 8.2
- z_a Axial displacement, see Fig. 6.12
- z_h Distance between the recording plane and the lens L_2 . Defined in (3.13) and (3.29) in the case of the two-lens and telescope holographic systems respectively. Also, distance between the recording plane and the spatial filter in the case of a single-lens holographic system. Defined in (3.16)
- z_n Distance between the recording plane (or the hologram plane) and the image of the (n)th planar distribution. Defined in (3.13), (3.16) and (3.29) in the cases of two-lens, single-lens and telescope holographic systems respectively

z_t	Transverse displacement, see Fig. 6.12
Greek Alphabet:	
$\Gamma_t(x_2, y_2)$	Composite amplitude transmittance of the filter as defined in (3.4)
$\Delta t(x_j, y_j)$	Variation about the average value of the amplitude transmittance of an object
ΔT	Short exposure such that $\Delta T \ll T_1$
$\Delta[P\{x_4, y_4\}]$	Phase difference between the unscattered and scattered rays at point $P\{x_4, y_4\}$
\int	Area of the aperture, see Fig. A.1
Ω	Angle of rotation of the rotating mirror
$\dot{\Omega}$	Time derivative of Ω
$\Omega_j(x_j, y_j)$	Point spread function of the two-hologram optical element $H_0 - H_1$, its expression is given in (9.9)
α	In Part A only, deflection angle, see Fig. 3.7
α	In Part B only, angle defined in Fig. 6.8
α_0	Real coefficient such that $0 \leq \alpha_0 < 1$
α_n	Proportionality constant, introduced in (2.9)
$\alpha(\rho_2)$	Amplitude transmittance defined in (3.36)
β	Angle, see Fig. 6.8
$\beta(\rho_2)$	Amplitude transmittance defined in (3.36)
γ	In Part B only, angle defined in Fig. 6.8
γ	In Part C only, angle defined in Fig. 8.2
$\gamma(\rho_2)$	Amplitude transmittance defined in (3.36)
δ	Angle, see Fig. 6.8
δ_v	Phase retardation or advancement introduced by the central spot of varnish. Defined in (3.1)

ϵ	Parameter of the spatial filter (small radius)
θ	Angle of rotation, see Fig. 6.12
θ_a	Value of θ when $t = 0$
θ_n	$= \arg A(x_j, y_j) - \arg B(x_j, y_j)$
$\theta_j(x_j, y_j)$	Amplitude distribution of the electric field in the plane $\{x_j, y_j\}$
$\theta_s(x_s, y_s, z)$	Three-dimensional amplitude distribution of the electric field in the image space (case of the two-lens holographic system)
$\theta_j^{(n)}(x_j, y_j)$	Amplitude distribution of the electric field engendered by the (n)th planar distribution, in the plane $\{x_j, y_j\}$
$[\theta_j(x_j, y_j)]^-$	Amplitude distribution of the electric field in a plane located just in front of the plane $\{x_j, y_j\}$
$[\theta_j(x_j, y_j)]^+$	Amplitude distribution of the electric field in a plane located just behind the plane $\{x_j, y_j\}$
$[\theta_j^{(n)}(x_j, y_j)]^-$	Amplitude distribution of the electric field engendered by the (n)th planar distribution, in a plane located just in front of the plane $\{x_j, y_j\}$
$[\theta_j^{(n)}(x_j, y_j)]^+$	Amplitude distribution of the electric field engendered by the (n)th planar distribution, in a plane located just behind the plane $\{x_j, y_j\}$
λ	Wavelength of the electromagnetic source of radiation
μ_k	$= k\pi/L$
ν	Optical frequency
ρ_0, ρ_1, ρ_2	Focal length of the microscope objectives used for focussing the collimated beams onto the pinholes
ρ_c	Distance from the corner point to the axis of rotation θ , see Fig. 6.12
ρ_j	Defined by $\rho_j = (x_j^2 + y_j^2)^{1/2}$

σ	Infinitely small area of the aperture
τ	Parameter of the spatial filter (large radius)
$\tau_n(x_j, y_j)$	Amplitude transmittance of the hologram H_n
$\phi_0(x_j, y_j)$	Phase of $A(x_j, y_j)$
$\phi_r(x_j, y_j)$	Phase of $B(x_j, y_j)$
$\phi_0(x_j, y_j, t)$	Phase of $A(x_j, y_j, t)$
$\phi_r(x_j, y_j, t)$	Phase of $B(x_j, y_j, t)$
$\psi(x_4, y_4)$	Electric field distribution engendered by the line source in the plane $\{x_4, y_4\}$
$\psi_j(x_j, y_j)$	Wave reconstructed upon illumination of the hologram H_0 with the readout wave $Q_2(x_2, y_2)$, its expression is given by (9.7)
ω	Angular frequency = $2\pi\nu$
ω'	Difference between the angular frequencies of the reference and object waves, which is caused by Doppler frequency shift
ω_n	Beam half-width of an (n)-hologram optical element, the hologram being sequentially recorded
ω_n^r	Beam half-width of an (n)-hologram optical element, the holograms being independently recorded
ω_x	Beam half-width of the point spread function (in the direction of the x axis)
ω_y	Beam half-width of the point spread function (in the direction of the y axis)

Notations Used in the Figures

The figure captions clearly define the notations used.

*Chapter One*GENERAL INTRODUCTION

More than a quarter of a century has elapsed since D. Gabor (1971 Nobel laureate) invented holography (Greek ὅλος: whole) [1-3]. During the years following Gabor's invention of holography, many scientists throughout the world explored this new method of image formation. However, original applications faced technical difficulties and it was not until the coming of continuous wave and pulsed laser sources, in the early 1960's, that holography gained full recognition from the scientific community at large. In the meantime another factor contributing to the sudden revival of holography was the introduction of new concepts by E. Leith and J. Upatnieks at the October 1961 meeting of the Optical Society of America [4].

Very rapidly, measurement of particle fields by holographic methods became one of the major domains of application of holography. The Fraunhofer holographic method, directly derived from Gabor's original method, led to very promising results for general applications in particle measurements. The Leith-Upatnieks' method alleviated difficulties in recording particles of large dimension or very dense particle fields [5]. Applications of holography to particle studies are numerous because holography permits high resolution viewing of dynamic particle fields throughout a deep sample volume. Hence, the applications of holography to the measurement of particle fields have been put to use in almost every field of science. However, in spite of more than fifteen years of intensive research and development, which has resulted in a multitude of scientific articles,

little new basic knowledge, as pointed out by Trolinger [6], has been introduced in this area in nearly ten years, and the breakthroughs have essentially been of a technological nature.

1.1 SYNOPSIS

This thesis encompasses theoretical and experimental studies of new methods and principles which should, in the near future, completely change the concepts of holographic recording of three-dimensional transilluminated scenes¹ and, more specifically, of particle fields.

The thesis has been divided into three major parts in order to clearly present its content. In each of these parts the experimental investigations have been separated from the theoretical analyses. The reasons for this separation are: (i) purely mathematical derivations are not encumbered with experimental results which do not directly contribute to the logical development of the derivations, (ii) the same experimental arguments may sometimes be used to substantiate several properties already analytically proved, and (iii) the reader who is not directly interested in following all the theoretical discussions may easily appreciate the relevance of the methods or the principles introduced from the experimental results.

Part A discloses a new holographic method that permits simultaneous image filtering and optical processing of a local reference wave by means of spatial frequency component separation.

¹
The words scene and object are used interchangeably throughout the thesis.

Part B is concerned with the introduction of original principles in holographic instrument design, using holocameras² with local optically processed reference waves, obtained either by amplitude/wavefront division or by the new method disclosed in Part A.

Part C proposes the use of multiple hologram optical elements in holocameras, or other imaging systems which operate over a narrow frequency spectrum, and gives a theoretical analysis of the resolution obtainable with these elements.

1.2 HOLOGRAPHIC IMAGING OF PARTICLE FIELDS

The major property inherent in holography is that the reconstructed wave can be identical to the recorded wave; thus, all the original information on the scene is preserved. In holographic measurement of particles, a pulsed laser freezes a three-dimensional event without interfering with it; later, a three-dimensional image is reconstructed and it is required to focus either the eyes or the camera to properly view the event of different depths. The image obtained has a considerable depth of field and brightness when compared to normal image formation (photography). It must be pointed out that holography and photography are the only known techniques which permit (i) recovery of individual particle parameters such as particle size, shape, canting angle and velocity, and (ii) study of coalescence and disintegration of particles (the measurements are made

² Holocamera: an enclosed unit (containing the optical components and the radiation sensitive recording material) which permits holographic recording of the radiation wavefront impinging upon it.

without any physical contact with the particles). Furthermore, retrieving of group parameters (spatial, size, velocity and density distributions) is rendered possible by scanning the three-dimensional image of the particle field.

1.3 RELEVANCE OF PARTICLE MEASUREMENT

1.3.1 In Pollution Monitoring

Environmental pollution due to airborne particulate matter created by human activities has reached an alarming level in many highly industrialized areas. The steady inflow of airborne dirt affects the breathing of living organisms. Many allergies are directly connected to airborne particulates. Inhalation of airborne particulate matter may permit a more rapid and concentrated penetration of dangerous gases than would normally occur. Knowledge of particle size and shape is important because the human lung inhales and exhales particles smaller than $1 \mu\text{m}$ in size with little or no trapping by normal filtration, whereas particles larger than $5 \mu\text{m}$ tend to be filtered out by the cilia before reaching the lungs. In addition, particle size permits, to a certain extent, the determination of the origin and composition of the particulate matter.

Pollution by airborne particles also has an influence on the climate. It affects in two ways: (i) each particle acts as a condensation nucleus, inducing fog and cloud formation and (ii) particles create layers of haze which reflect light. (Many scientists attribute a mean global temperature decrease to the steadily increasing global concentration of airborne

particles in the atmosphere .) Airborne particles represent the most obvious and also the most complex type of air pollutant. Air may contain organic solids such as soil particles, soot, pollen grains and rubber, and may also contain inorganic solids such as salt, metal fragments, cement, fly ash, asbestos fiber, etc.

1.3.2 In Cloud Microphysics

Clouds and fog can be described as colloidal suspensions of liquid water droplets, or ice crystals, in air, and are often referred to as an atmospheric aerosol. The formation of this aerosol is dependent upon the conversion of some of the water vapor in the atmosphere to either the liquid or the solid state, or a combination of both. The changes of state of water vapor in the atmosphere that result in the formation of clouds depend upon (i) the number and types of condensation and sublimation nuclei present, and (ii) the state of saturation of the surrounding air. For the nucleation process to proceed, it is necessary for the air to be maintained in a saturated or nearly saturated state. This, in essence, requires some means of continuously supplying the water vapor. In general, a cloud is formed when air containing water vapor rises to the higher altitudes where a continuous decrease in atmospheric pressure results in expansion and subsequent cooling of the moist air until some of the water vapor condenses or sublimates on the available nuclei.

It is seen that the study of cloud microphysics requires the knowledge of many parameters such as temperature, pressure and turbidity. However, the parameters relevant to the physical aspects of the particles, or nuclei,

must also be known for a better understanding of drop and crystal formation.

1.3.3 In Limnology and Oceanography

Pollution of lakes and seas is responsible for a change in biological equilibrium. The number of diatoms counted as a function of species, diversity over a period of time, and found in different depths and locations, can give significant information on the pollution present in water. Besides pollution control, in situ imaging of diatoms is most useful to the biologist who wants to identify and determine the life cycle of diatoms, or other algae, in a given location.

1.3.4 In Electromagnetic Wave Propagation

The knowledge of the effects of atmospheric precipitations in electromagnetic wave propagation is of fair importance to the establishment of reliable communications links. The feasibility of frequency sharing between earth-space and terrestrial line-of-sight communication systems depends on the ability to predict the interference between these systems over given paths. During propagation, the signal is attenuated, scattered and even depolarized. Hence, accurate predetermination of the effects of atmospheric precipitations on a propagating signal requires accurate data about individual and group particle parameters.

1.3.5 In Other Fields of Science

The list of other fields of science which demand accurate determination

of particle parameters is quite extensive, and new imaging problems are encountered every day. Of importance are, for example, imaging of energetic and dynamic aerosols, and bubble chamber photography.

*Chapter Two*SURVEY OF LITERATURE REVIEW2.1 INTRODUCTION

Reliable, accurate and convenient methods which allow monitoring of size, distribution and terminal velocities of raindrops, and which permit study of the shape and disintegration of large raindrops, have been the object of intensive research in the twentieth century. These methods are either based on laboratory simulations of physical parameters or on direct measurements performed from ground level. Significant accomplishments have been made in the laboratory simulations; however, simulation of physical parameters becomes more and more laborious as the state of knowledge advances and man's search for the absolute becomes more profound. On the other hand, ground level measurements provide data which are unfortunately affected by environmental conditions. Thus, the results achieved in the laboratory and those which are observed in nature often are uncorrelatable.

The analysis of physical interaction between natural phenomena (such as atmospheric precipitations or underwater biological systems) and an artifact (like pollution) necessitates very specialized and sophisticated instrumentation that allows in situ monitoring. The ever growing need for probing more specific parameters is aroused by the development of science.

In the present literature review a brief description of modern methods

used for in situ and/or remote monitoring of particle parameters which are directly connected to holography, is followed by a detailed introduction to the holographic process and to holography with a locally processed reference beam. (An outline of the classical methods can be found in the book by Mason [7]). A good understanding of Sections 2.3 and 2.4 is required since they lead to a logical introduction to the new concepts which will be developed in the following chapters.

2.2 MEASUREMENT OF PARTICLE PARAMETERS BY MODERN METHODS

2.2.1 Microphotography

Photographic recording of individual particle parameters is possible [8,9]. However, high resolution photography of particles ranging in size from 3 μm to 1 mm produces pictures with an extremely limited depth of field. Consequently photographic imaging is not satisfactory.

2.2.2 Laser-Doppler Velocimeters

Laser-Doppler velocimeters (LDV's) have been used for a number of years to assist in the analysis of flow measurement problems such as those encountered in wind tunnels, clear-air turbulence, wake vortices, atmospheric wind studies, and determination of particle velocities at large [10]. LDV's are based on measurement of the Doppler frequency shift created by moving particles; in principle, it is admitted that the phase shift is due solely to the Doppler effect if the light is assumed to be quasi-elastically scattered by moving particles. A detector measures

the light-beating frequency which in turn gives the velocity of displacement of the particle fields. Two points have to be noted: firstly, LDV's do not measure the velocity of each particle, but measure the mean velocity of a group of particles, and secondly, velocity measurements are usually given with directional ambiguity, and the velocity is recovered in one direction only. In comparison, double exposure holographic methods give information on the three-dimensional velocity vector for each particle, and the directional ambiguity can easily be removed by giving two different exposure times for each recording. The advantage of LD methods are in remote applications which are easy to implement, and give real time results. However, the holographic remote sensing methods presented in this thesis can certainly compete with LDV methods.

At least two methods for determining the sizes of small particles from scattered light observed with LDV's have been reported [11,12]. In the first one, it was shown that if a number of assumptions were made regarding the spatial kinetic properties of very small particles, spectral analysis of the heterodyne or homodyne signal used in conjunction with the Rayleigh scattering theory, would permit recovery of particle size [11]. In the second method, an attempt was made to determine the particle size by measuring the absolute value of the scattered intensity and correlating this value with that predicted from a Mie cross-section calculation [12]. It is readily seen that these two methods deviate from the basic LD methods and are more related to diffraction methods.

2.2.3 Diffraction Methods

As mentioned earlier, microphotographic techniques used to be the only

measurement techniques which could give information concerning the physical parameters of each particle. The problems encountered in microphotography were: firstly, depth of field was insufficient for measuring microparticles, and secondly, recording was limited to two dimensions in the plane of focus of the camera. Leading to holographic techniques, a number of approaches using light diffraction methods appeared in the 1960's. However, diffraction methods are only suitable if the particle size range is very narrow and if the mean diameter of spherically shaped particles can be determined. Particle shapes which are not spherical are very difficult to handle, in particular if the particles are randomly orientated. It can be known whether a composite diffraction pattern (made up of the sum of a variety of individual patterns) can be used to determine the particle size distribution only if some information is available beside the composite diffraction pattern [13-15].

2.2.4 Holographic Methods

The first attempts to use holographic methods for particle measurements were made by B.J. Thompson and co-workers [16-18]. From some previous work on diffraction measurement methods [19-21], Thompson was led to realize that holographic recording of the diffracted field could be used to generate three-dimensional images of the sample volume containing particles of any shape. Since the images are fixed in time, the sample volume can be explored at will and the size and shape of each particle, as well as its position relative to other particles, can be recovered. Gabor's basic holographic configuration was used for recording the far field diffraction pattern of the particles (see Section

2.3.2). The hologram was reproduced by recording the Fraunhofer diffraction pattern with the coherent background (undiffracted light). Firstly, a pulsed laser source "froze" the motion of the particles in the sample volume in the formation of the hologram; secondly, the illumination of the hologram with a coherent quasi-monochromatic beam of radiation produced images of the three-dimensional sampled volume with a depth of field of several centimeters.

Since Thompson's first investigations, Leith-Upatnieks holographic configurations (refer to Section 2.3.3) have also been successfully used in the field of particle measurements. A review article by Thompson [5] gives an excellent account of the progress made in recent years.

2.3 HOLOGRAPHIC PROCESS

2.3.1 Gabor Holography (in-line holography)

Square-law detectors such as the human eye or photographic films are energy sensitive. Thus, if an object wave, defined by the phasor of its electric field $A(x_1, y_1) = |A(x_1, y_1)| \exp\{i\phi(x_1, y_1)\}$, impinges onto a square-law detector, only the intensity

$$I(x_1, y_1) = A(x_1, y_1)A(x_1, y_1)^* = |A(x_1, y_1)|^2 \quad (2.1)$$

is detected and the phase information $\phi(x_1, y_1)$ is lost.

Gabor [1-3] showed that by adding a coherent background $B(x_1, y_1)$ to a coherent object wave $A(x_1, y_1)$ it is possible to record both the amplitude and the phase information. By assuming that a highly transmissive

object with amplitude transmittance

$$t(x_0, y_0) = t_0 + \Delta t(x_0, y_0) \quad (2.2)$$

(t_0 is a high average level of transmittance, and Δt represents the variation about this average, with $\Delta t \ll |t_0|$) is back illuminated by a plane wave, a coherent background $B(x_1, y_1) = \text{constant} = B$ can then be conceptually separated from the varying part of the object wave $A(x, y)$.

Hence, the intensity recorded by a photographic film is now given by

$$I(x_1, y_1) = |A(x_1, y_1) + B|^2 = |A(x_1, y_1)|^2 + B^2 + BA(x_1, y_1) + BA^*(x_1, y_1). \quad (2.3)$$

It appears that the third and the fourth terms in the RHS of (2.3) are proportional to the original object wave and to its conjugate respectively; $|A(x_1, y_1)|^2$ is the intermodulation term and B^2 is a constant bias illumination. Illumination of the processed photographic film by a plane wave, duplicating the coherent background, leads to the reconstruction of a virtual image $A(x_1, y_1)$ and of a real image $A^*(x_1, y_1)$ (also called the twin image). The intermodulation term $|A(x_1, y_1)|^2$ does not affect the reconstructed image if the class of objects recorded is such that $|\Delta t| \ll |t_0|$. However, the presence of the twin image considerably reduces the visibility of the reconstructed virtual image.

2.3.2 Fraunhofer Holography (Far Field In-line Holography)

The terms Fresnel and Fraunhofer diffraction are used to describe different regions of a diffracted field. Fresnel and Fraunhofer regions correspond respectively to the intermediate and far fields [21,22].

One of the great drawbacks of the original Gabor configuration is the troublesome twin image effect. If the virtual image is of interest,

an out-of-focus real image appears in the plane of the virtual image. However, with the Fraunhofer holograms formed in the same way, the real image (although still present) contributes to only a very small error term because it exists essentially at infinity, since the far field condition

$$z \gg (2a)^2/\lambda \quad (2.4)$$

is an approximation to infinity. (z is the distance from the object to the hologram plane, λ is the wavelength of the electromagnetic field illuminating the object, and $2a$ is the dimension of the object.)

2.3.3 Leith-Upatnieks Holography (Off-Axis Holography)

Spatial separation of the real and virtual images, and of the intermodulation term, can easily be provided if object and reference waves impinge onto the recording material from different directions [23]. Thus, the limitation on the class of objects which can be recorded is no longer restricted by the assumption that the object is highly transmissive (i.e. $|\Delta t| \ll t_0$), and the presence of the twin image does not impair the reconstructed image.

The coherent background is now represented by $B(x,y)$, and thus the intensity in the recording plane yields the value

$$I(x_1, y_1) = |A(x_1, y_1)|^2 + |B(x_1, y_1)|^2 + B^*(x_1, y_1)A(x_1, y_1) + B(x_1, y_1)A^*(x_1, y_1) \quad (2.5)$$

The exposure on the film is defined by:

$$E(x_1, y_1) = \int_{-T/2}^{T/2} I(x_1, y_1) dt \quad (2.6)$$

$E(x_1, y_1) \propto I(x_1, y_1)$ if $I(x_1, y_1)$ is assumed to be time invariant. The relationship between the exposure and the transmittance $\tau_n(x_1, y_1)$ of recording materials is not completely linear. However, in the following it is assumed that the exposure is within the linear range of the curve τ_n -E and it follows that

$$\tau_n(x_1, y_1) \propto E(x_1, y_1) \propto I(x_1, y_1) \quad (2.7)$$

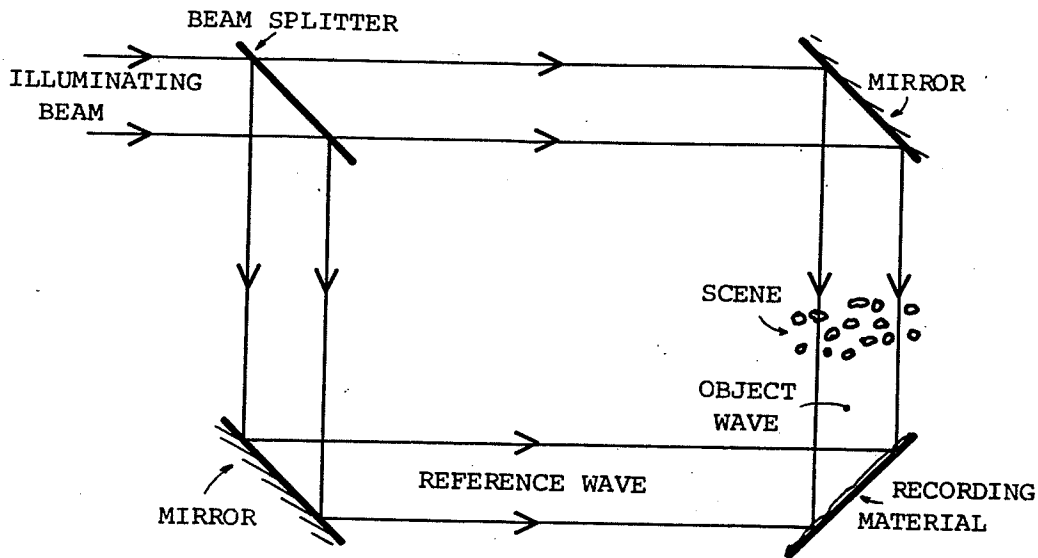
At the reconstruction stage, the hologram is illuminated by a duplicate of the reference wave $B(x_1, y_1)$. As a result, the amplitude distribution behind the hologram is proportional to

$$G(x_1, y_1) = B(x_1, y_1)\tau_n(x_1, y_1) = B(x_1, y_1)|A(x_1, y_1)|^2 + B(x_1, y_1)|B(x_1, y_1)|^2 + |B(x_1, y_1)|^2 A(x_1, y_1) + (B(x_1, y_1))^2 A^*(x_1, y_1) \quad (2.8)$$

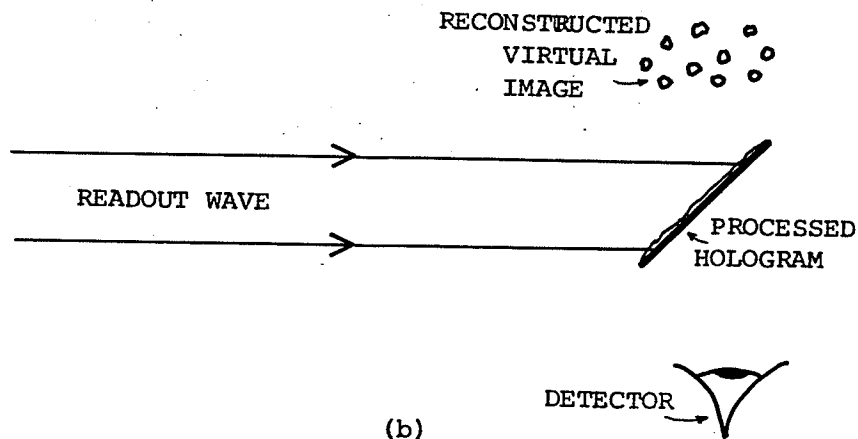
Assuming that $|B(x_1, y_1)|$ is constant over the entire aperture of the hologram, it is clear that the third term of the RHS of (2.8) generates a perfect duplicate of the object wave. Spatial separation of the reconstructed image from the twin image, and from other deleterious reconstructed terms, is assured by proper choice of $B(x_1, y_1)$. Thus any class of objects can be holographically reconstructed. In order to obtain reconstructed images with little aberration, plane or spherical waves are usually chosen for the reference beam, as they can be easily duplicated. Typical recording and readout holographic configurations are shown in Fig. 2.1.

2.3.4 Phase Holograms

Images of good quality are reconstructed from Leith-Upatnieks holograms, yet they are often very dim in intensity when they are reconstructed from amplitude holograms. Phase volume holograms must be used in order to



(a)



(b)

Fig. 2.1 Typical recording and readout holographic configurations. (a) A modified Mach-Zehnder interferometer is used for recording the hologram. (b) A duplicate of the reference wave illuminates the processed hologram; a detector (eyes or camera) can be used to visualize or record the virtual image of the three-dimensional scene. A real image is reconstructed if the readout wave is the conjugate of the reference wave.

obtain a good diffraction efficiency [24,25]; hence, these holograms will be considered in the thesis, and in addition, the recording configurations will be such that the Bragg angle effect enhances the diffraction efficiency. Limiting the analysis to a two-dimensional recording medium, it can be rapidly shown that, for instance, by bleaching an amplitude hologram recorded on a photographic film, an unaberrated image can be reconstructed.

Assuming that after being bleached the hologram has a pure imaginary transmission function, which is proportional to the irradiance distribution over the hologram, by using (2.5), the transmission function of the hologram is readily obtained

$$\tau_n(x_1, y_1) = E_n(A, B; x_1, y_1) \exp[2i\alpha_n |A(x_1, y_1)| |B(x_1, y_1)| \cos\theta_n] \quad (2.9)$$

where $E_n(A, B; x_1, y_1) = \exp\{i\alpha_n [|A(x_1, y_1)|^2 + |B(x_1, y_1)|^2]\}$, α_n is a proportionality constant and $\theta_n = \arg A(x_1, y_1) - \arg B(x_1, y_1)$. Expanding the right hand side of (2.9) in a Fourier-Bessel series, it follows that

$$\tau_n(x_1, y_1) = E_n(A, B; x_1, y_1) \sum_{k=-\infty}^{\infty} i^k J_k [2\alpha_n |A(x_1, y_1)| |B(x_1, y_1)|] \exp(ik\theta_n) \quad (2.10)$$

If a duplicate of the reference wave illuminates the hologram, the amplitude distribution just behind it is $G(x_1, y_1) = B(x_1, y_1) \tau_n(x_1, y_1)$. It appears that an infinite number of diffracted orders are generated, yet only two diffracted orders, namely the ± 1 st orders, lead to the desired reconstruction. In addition, since the physical thickness of the recording medium is finite, one can obtain an enhanced image produced by a single first diffracted order. Since Bragg's condition is satisfied for all the configurations described in the course of the thesis, the

expression for $\tau_n(x_1, y_1)$ reduces to

$$\tau_n(x_1, y_1) \sim iE_n(A, B; x_1, y_1) J_1 [2\alpha_n |A(x_1, y_1)| |B(x_1, y_1)|] \exp(i\theta_n) . \quad (2.11)$$

For small values of the argument of the Bessel function, $J_1(z)$ can be expanded in an ascending series. Thus, the transmission function of the hologram yields

$$\tau_n(x_1, y_1) \sim iE_n(A, B; x_1, y_1) B(x_1, y_1)^* A(x_1, y_1) , \quad (2.12)$$

and the expression of the reconstructed wave becomes

$$G(x_1, y_1) = iE_n(A, B; x_1, y_1) |B(x_1, y_1)|^2 A(x_1, y_1) . \quad (2.13)$$

For

$$E_n(A, B; x_1, y_1) \sim 1 , \quad (2.14)$$

$G(x_1, y_1)$ is identical to the third term of the RHS of (2.8), and therefore $G(x_1, y_1)$ generates an unaberrated image.

Eqn. (3.13) is quite satisfactory when (i) the size of the hologram is such that the diffraction phenomenon induced by the finite size of the hologram does not affect noticeably the image resolution and (ii) when the substrate does not introduce any phase errors. There are, of course, numerous other factors that prevent the reconstructed wave from being a perfect duplicate of the object wave; yet the study of their influence on the image quality is not within the scope of this thesis.

For a comprehensive study of these deleterious factors, the reader should, for example, refer to the book by Smith [26].

2.4 LOCAL GENERATION OF THE REFERENCE BEAM

2.4.1 Objectives

It may be surprising to introduce the notion of local reference beam generation after having shown that the in-line holographic configuration conceptually separates the constant coherent background from the varying parts of the signal. In essence, the in-line configuration has a reference beam which is locally processed. However, the limitations on the class of objects to be imaged, the twin image problem, and the need to illuminate the object with an illuminating wave that is easy to duplicate, drastically limit the range of application of such a configuration.

The off-axis configuration allows imaging of any objects. In addition, the beam that illuminates the object may have a very complex wavefront since it does not provide the coherent background which will be duplicated at the reconstruction stage. Due to the coherence requirements on the reference and object waves, both reference and object waves are provided by the same source. Usually, the reference wave merely bypasses the object and impinges directly onto the recording medium, while the object wave is scattered by the object and bears the object information when it hits the recording medium. Optical path matching between the two interfering waves must be kept within the coherence length of the source if fringes with good visibility are to be recorded. Poor fringe visibility results in reduced diffraction efficiency of the holographic structure, causing a decrease in image intensity. Thus, the off-axis configuration is applicable to any class of object; yet the reference wave which bypasses the object must be unaberrated when it reaches the recording plane, and optical paths must be matched.

Intuitive reasoning leads one to think that excellent imaging of any object could be performed if a method combining advantages of both configurations were thought up. It appears that optical path matching is not critical when the reference wave is derived from the wave illuminating the object (as in the case of in-line holography). In addition, if optical filtering of the reference wave derived from the illuminating beam is done before the reference wave reaches the recording plane but after the illuminating beam has been scattered by the object, duplication of the reference wave at the construction stage can be easily performed. Therefore, off-axis configurations using local optically processed reference beams will be quite satisfactory since most of the drawbacks inherent in the two basic methods can be overcome.

2.4.2 Implementation

Following the above reasoning, a reference wave can be derived from the object-scattered wave by simply placing the latter in the illuminating wave as illustrated in Fig. 2.2(a). Both the object and the reference waves bear the object information, and duplication of the reference wave is impossible. However, by introducing an optical spatial filter which allows separation of the coherent background from the object information, perfect duplication of the reference wave is now possible (see Fig. 2.2(b)). The optical spatial filter is composed of: (i) a Fourier transform lens, (ii) a pinhole spatial filter which lets the zero spatial frequency component propagate without any attenuation, and which blocks the other spatial frequency components, and (iii) a collimating lens. Note that the collimating lens may be omitted as shown in Fig. 2.2(c).

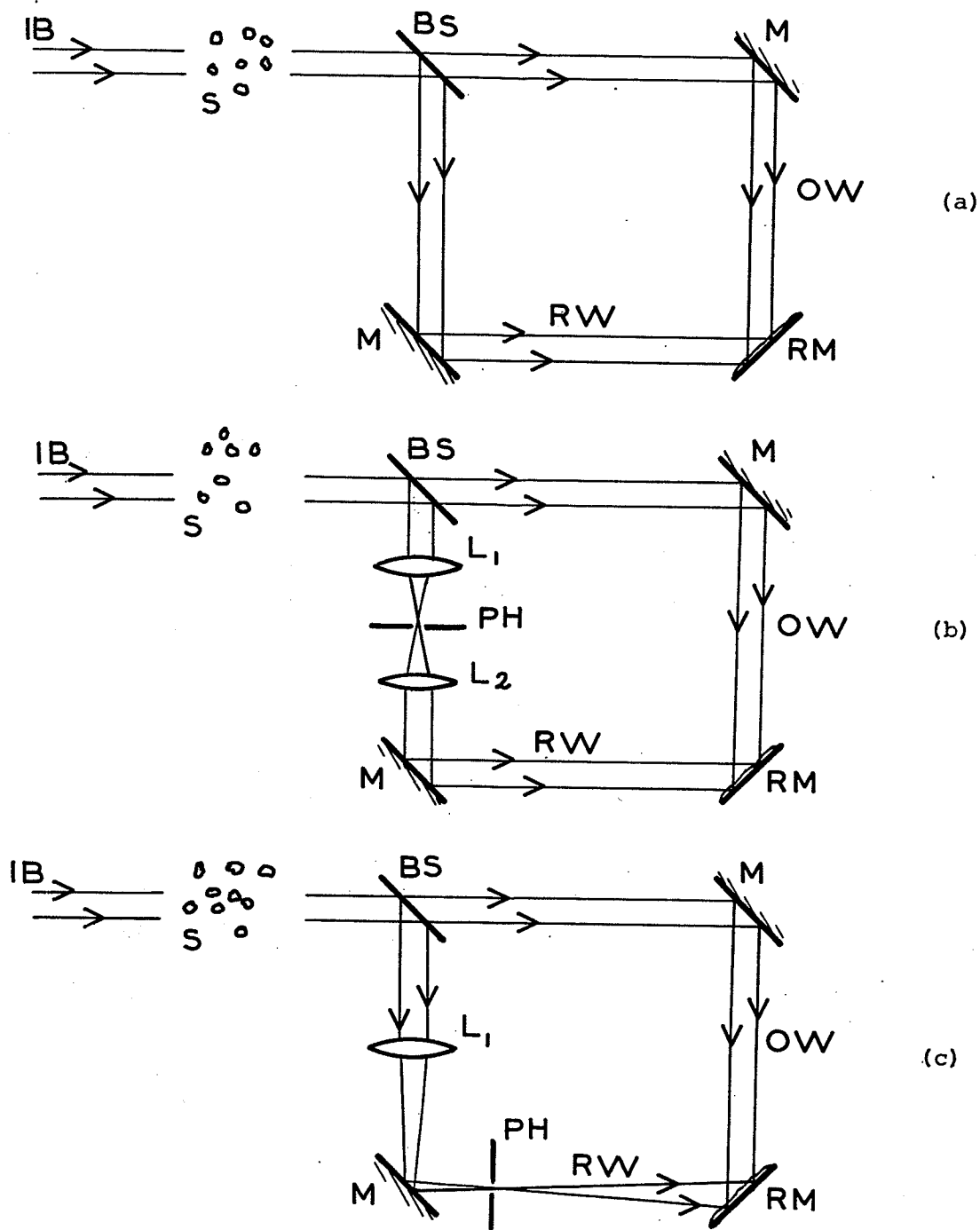


Fig. 2.2 Generation of a local reference beam by amplitude division methods. (a) The reference wave is not filtered; (b) and (c) a pinhole placed in the back focal plane of L_1 filters the reference wave. Notations are as follows: "IB" illuminating beam, "S" scene, "BS" beam splitter, "M" mirror, "RM" recording material, " L_1 " and " L_2 " lenses and "PH" pinhole spatial filter.

Two configurations similar to that of Figs. 2.2(b) and (c) have been published in the literature [27-29]. They provide local reference waves by dividing the amplitude of the diffracted illuminating beam. Providing that the object diffracts only part of the illuminating beam wavefront, generation of the reference beam may be done without any spatial filtering, by dividing the wavefront of the diffracted illuminating wave (see Fig. 2.3(a)). Of course, it may be argued that the latter configuration does not locally generate a reference wave since the part of the illuminating beam wavefront which serves to generate the reference wave bypasses the object. Spatial filtering of the reference wave is required when the object also diffracts the part of the illuminating beam wavefront which generates the reference wave (see Fig. 2.3(b) and (c)).

Another configuration which has not yet been described in the literature would consist of separating the cross-polarized terms of the diffracted illuminating wave in order to obtain the object wave without attenuating it. It is known that an object of irregular shape will generate a cross-polarized component when illuminated by a linearly polarized wave [30]. Thus parallel and perpendicular components are present in the diffracted wave. Fig. 2.4 shows a configuration which allows recording of an unattenuated cross-polarized wavefront. (Under Brewster incidence [31], the cross-polarized component of the electric vector propagates through the prism without any attenuation.) An analyser and a half wave plate are used to allow interference of the object and reference waves in the recording plane. Methods based on this configuration could find extremely useful applications in the study of object discontinuities. However, objects having smooth contours cannot be recorded in this way

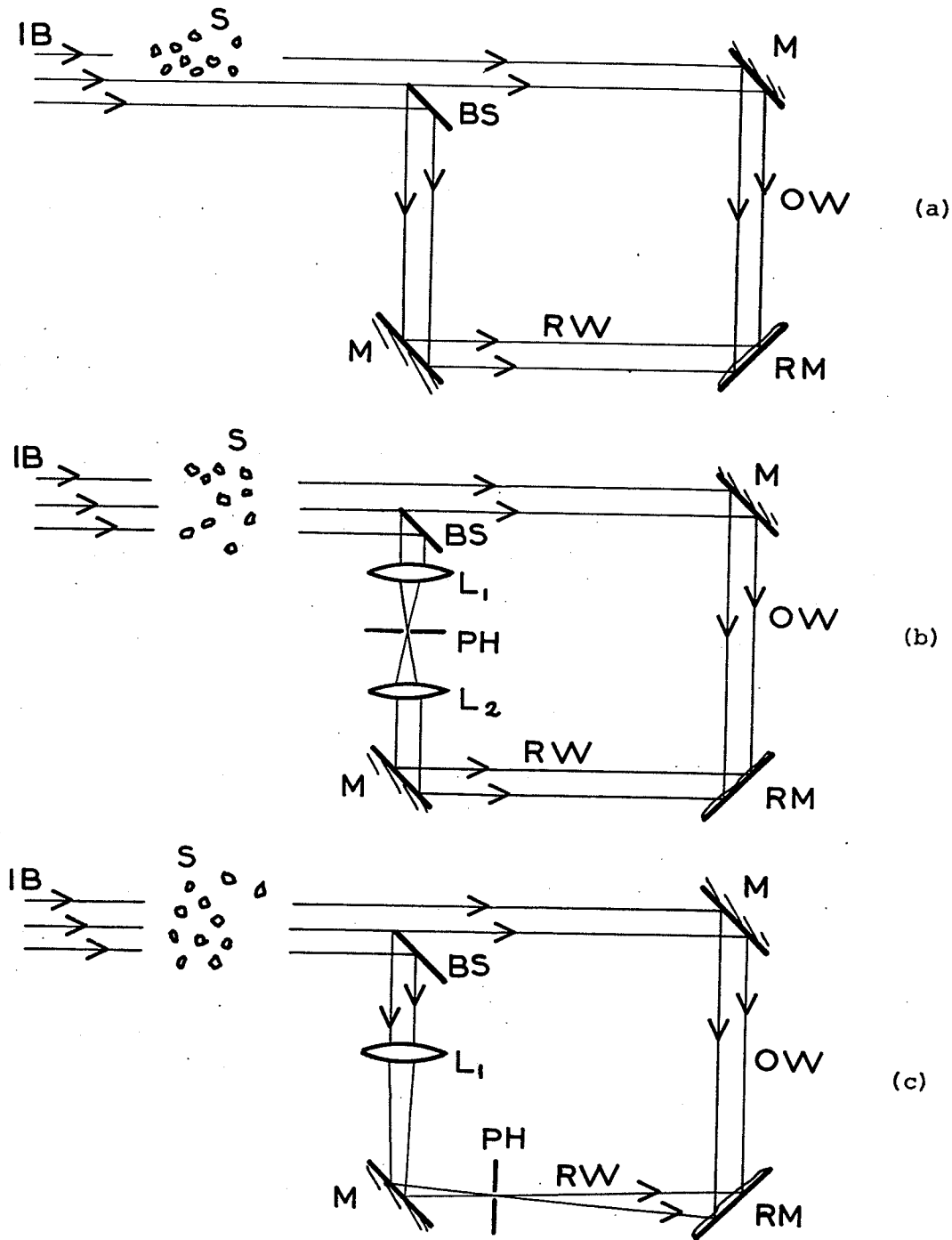


Fig. 2.3 Generation of a local reference beam by wavefront division methods. (a) The reference wave is not filtered; (b) and (c) a pinhole placed in the back focal plane of the lens filters the reference wave. Notations are as follows: "IB" illuminating beam, "S" scene, "BS" beam splitter, "M" mirror, "RM" recording material, "L₁" and "L₂" lenses and "PH" pinhole spatial filter.

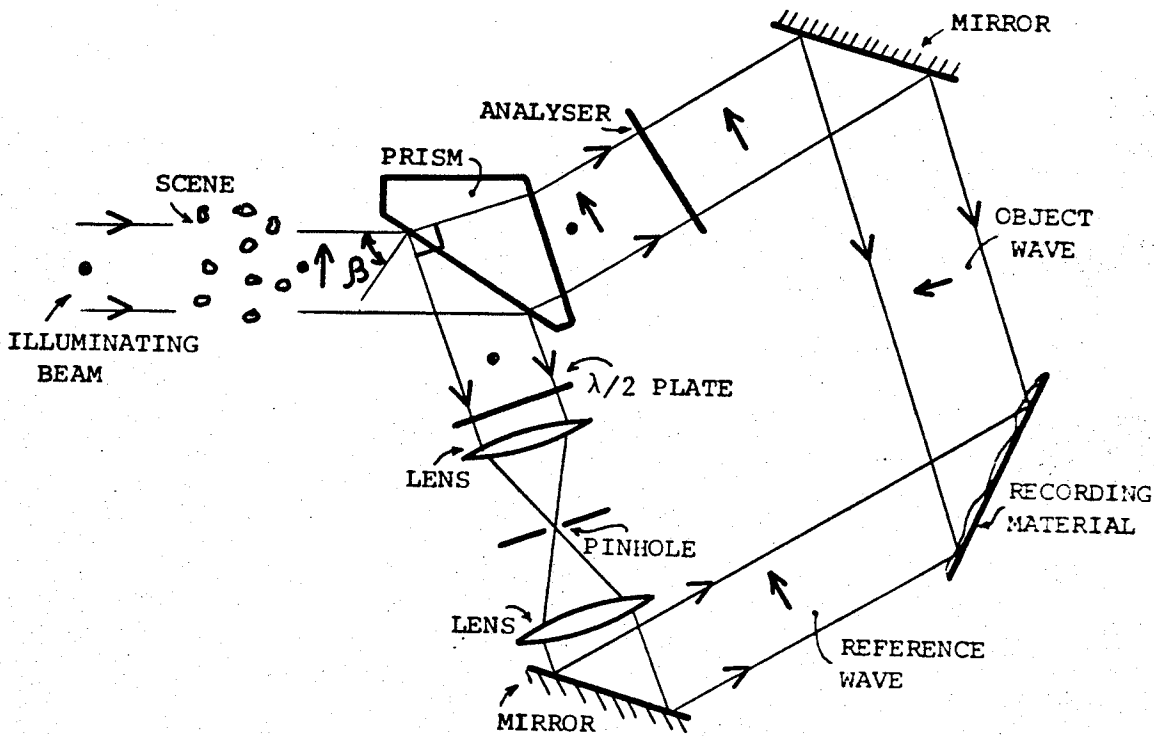


Fig. 2.4 Configuration in which the cross-polarized terms of the diffracted illuminating wave are holographically recorded without being attenuated when the diffracted rays are incident under Brewster angle on the prism. Note that it is possible to obtain a desirable reference-to-object intensity ratio by changing the state of polarization of the illuminating beam.

because the cross-polarized terms are too weak. It must be noted that conventional holographic methods have already been used for recording a particular linearly polarized component of the object wave (see, for instance, [91]).

Finally, a new configuration enabling holographic recording of an unattenuated object bearing wave will be studied in detail in Section A of this thesis.

It must be mentioned in passing that local generation of the reference beam has been performed by attaching a mirror to the object [32] or by using speckle reference beam techniques [33]. However, these two techniques do not permit recording of transilluminated objects. One more method worth mentioning here consists of recording volume holograms which can be viewed in reflection [34]. In this method the reference wave itself illuminates the object after propagating through the recording material. The light scattered by the object interferes with the reference wave. White light illumination may be used to reconstruct the image. The major drawback of reflection type holograms lies in the fact that an extremely feeble motion of the object during the exposure may reduce the fringe visibility to zero; moreover the fringe spacing within the recording material requires the use of very high resolution recording media. Neumann and Penn have overcome the object motion problem by attaching the recording plate directly onto the object [35].

PART A

LOCAL REFERENCE WAVE GENERATION BY
SPATIAL FREQUENCY COMPONENT SEPARATION

*Chapter Three*THEORETICAL STUDIES OF THE METHOD3.1 INTRODUCTION

At a time when the off-axis configuration is almost exclusively used in all holographic applications, it is surprising to realize that this configuration has not been extensively used by researchers engaged in imaging particle fields. The lack of further development of the off-axis method in the domain of particle imaging is due to four primary reasons: (i) a reference wave having an optical path different from the object wave is required, and therefore coherence requirements from the source are greatly dependent upon the optical path matching between the reference and the object waves, (ii) the embodiment of the apparatus is bulky, (iii) holographic recording is usually done without any premagnification of the recorded scene, and thus the image resolution obtainable from off-axis holographic recording is inferior to that obtained with an in-line arrangement, (iv) the fringe visibility is highly compromised by any object motion during the exposure of the hologram.

Comparatively, the formerly developed in-line Fraunhofer arrangement is indeed best suited to particle imaging, since: (i) the coherence requirements are reduced to a minimum, (ii) the far field condition is easily implementable, (iii) high image resolution is obtained by recording a magnified aerial image of the scene and (iv) object motion has almost no effect on the fringe visibility in the region of the hologram where fringes are caused by interference of low order diffracted rays. Object motion

simply reduces the image resolution by causing a blurring similar to that encountered in photographic imaging of moving scenes, and by limiting the effective aperture of the hologram, since the high order diffracted rays will not coherently contribute to any interference fringe recording.

In spite of these advantages, the class of objects to be imaged by means of the Fraunhofer method is restricted to objects having a high average level of transmittance, with a small signal transmittance variation about this average (refer to (2.2)). Therefore, applications are strictly limited to imaging of light density particle fields. The image quality decreases as the density of the field density increases. In addition, the far field condition cannot be met when imaging large objects.

It seems that the holographic methods using local optically processed reference waves overcome most of the restrictions inherent in the in-line and off-axis configurations. In those configurations, however, the amount of energy being allocated to the object wave represents only a small fraction of the energy available from the illuminating beam. Wavefront or amplitude division methods allot most of the energy to local reference wave generation.

3.2 THE METHOD

In an effort to devise a new method that would encompass the advantages inherent in Gabor's holography, Leith and Upatnieks' holography, and already proposed holographic techniques using local reference wave generation [27-29], a novel holographic method using a local reference wave

was thought up [36-38].

High resolution imaging can be obtained from the off-axis method by recording a magnified aerial image. This can be implemented by introducing an imaging lens between the scene and the beam splitter, and by removing the Fourier transform lens from the arrangement shown in Fig. 2.2(c). The new arrangement is shown in Fig. 3.1(a). Depending upon the numerical aperture of the imaging lens, an extremely high image resolution may be obtained. Besides, the hologram is now close to the aerial image that is recorded; thus, the effective hologram aperture is increased and the image resolution is further improved.

Retrieval of the scene physical characteristics may be eased by performing spatial filtering of the object wave in the back focal plane of the imaging lens. Fig. 3.1(b) shows the configuration. Note that spatial filtering of the reconstructed image can also be implemented [92].

It is seen that both generation of the reference wave and image spatial filtering are performed in the back focal plane of the same lens in two different spatial locations. By moving the objective lens a little farther from the beam splitter, the focal point may be brought onto the surface of the beam splitter. (It is assumed here that the beam splitter thickness is reduced to an infinitely small value). If the two spatial filters are compatible, they may be positioned in such a way that they have a common center of symmetry located right at the focal point of the lens. Since the beam splitter previously used has been removed, the reference beam spatial filter must therefore be reflective. An extremely small reflective disk will perform the required filtering, since the

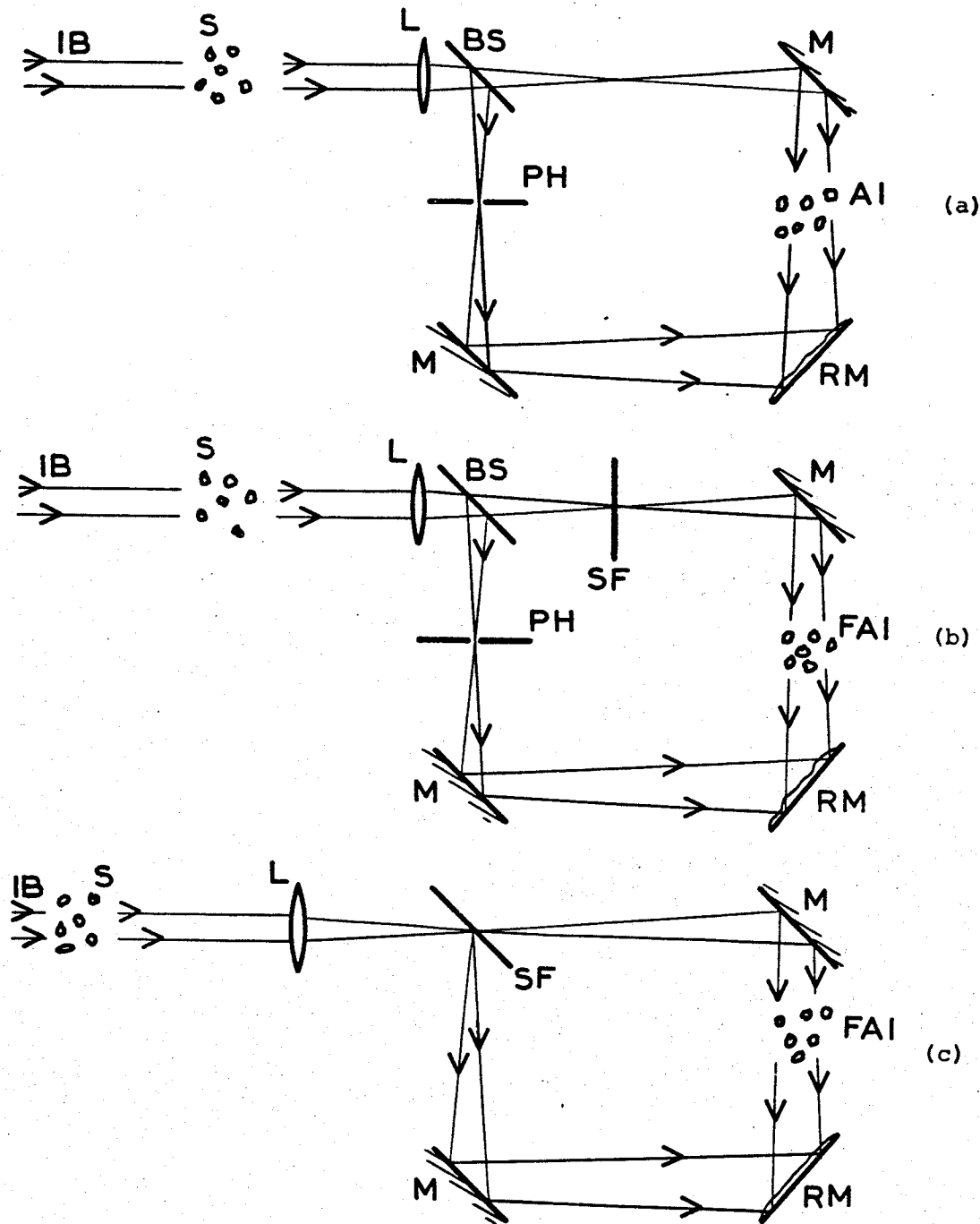


Fig. 3.1 Generation of a local reference beam by the new holographic method. (a) and (b) lead to the configuration (c). (c) illustrates the method allowing generation of a local optically processed reference beam by means of spatial frequency component separation in the back focal plane of the imaging lens. Notations are as follows: "IB" illuminating beam, "S" scene, "L" imaging lens, "PH" pinhole, "SF" spatial filter, "M" mirror, "AI" aerial image, "FAI" filtered aerial image and "RM" recording material.

central ordinate (zero-order wave) only will be reflected by this tiny reflective spot. The high spatial frequency components, and a fraction of the central ordinate, propagate through the transmittance image spatial filter. The configuration of the new method is schematically represented in Fig. 3.1(c).

3.3 IMPLEMENTATION

Although the configuration shown in Fig. 3.1(c) is quite adequate for a physical description of the new method, there are in fact many arrangements which lead to essentially similar imaging of the scene, and to the generation of a local reference wave, by separating the spatial frequency components in the back focal plane of the objective lens. In fact, three different imaging techniques and two basic types of spatial filters will be discussed in what is to follow. In all the configurations presented, any position of the filtered aerial image FAI with respect to the recording plane can be obtained.

3.3.1 Single-Lens Optical Processor

A very slight modification of Fig. 3.1(c) leads to the configuration of the single-lens optical processor shown in Fig. 3.2. The rays of light that are undiffracted by the scene S are focussed by the imaging lens L_1 onto a small reflective disk placed on the spatial filter SF . The disk deflects part of these rays onto the steering mirror M_3 while the other part is allowed to propagate through SF in the direction of the steering mirror M_2 . The rays diffracted by S are not brought to focus on the central reflective disk, and thus they are merely attenuated as they

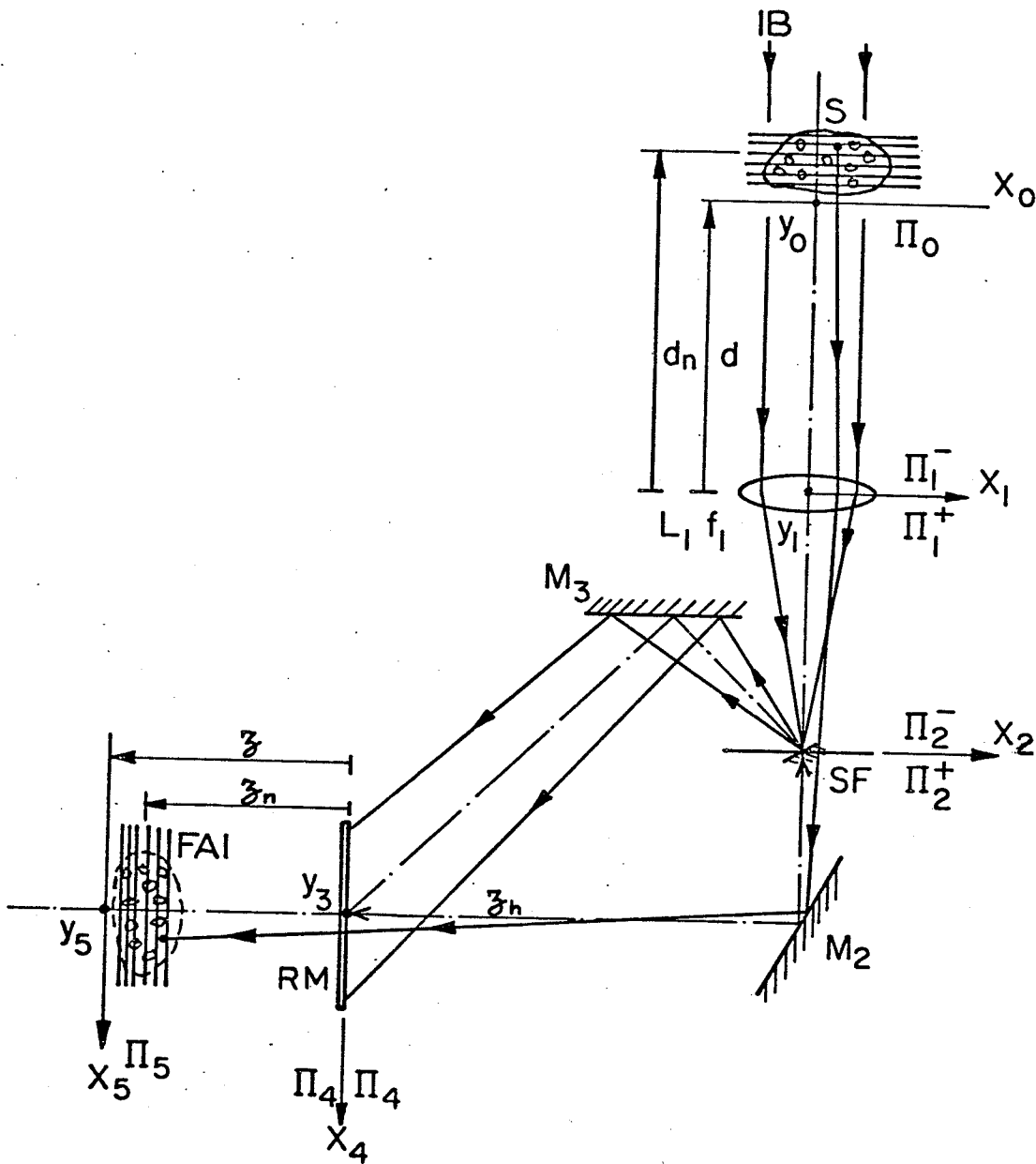


Fig. 3.2 Single-lens optical processor allowing holographic recording of the filtered aerial image formed by the lens. The notations are as follows: "IB" illuminating beam, "S" scene, "L₁" imaging lens, "SF" spatial filter, "M₁" and "M₂" mirrors, "RM" recording material and "FAI" filtered aerial image.

propagate in the direction of M_2 . The mirrors M_2 and M_3 steer the filtered object and the locally processed reference waves onto the recording plane in which they interfere. The reference wave is a spherical one.

3.3.2 Two-Lens Optical Processor

This scheme is of interest since it permits correction of the aberrations introduced by the lens L_1 by substituting a lens L_2 to the spatial filter. The small reflective disk centered on the axis of the optical processor contributes to the processing of the reference wave and to the filtering of the object wave. Fig. 3.3 illustrates the arrangement. The reference wave is again spherical. The lens L_1 may be designed to provide best focussing of the collimated bundle of rays, while the lens L_2 may correct the geometrical aberrations of L_1 .

3.3.3 Telescope Optical Processor

This configuration corresponds to the well known arrangement used, for example, in astronomical telescopes or in beam expanders. The processor is illustrated in Fig. 3.4. It is seen that two lenses L_2 and L_3 are added to the one-lens optical processor. In order to keep a certain symmetry in the two arms of the system, the focal lengths f_2 and f_3 are equal. However, the lenses L_2 and L_3 must be devised according to the specific different roles they perform. From the well known properties of telescope systems, it is readily seen that the reference wave is collimated by the lens L_3 and that the aerial image formed by the lens L_2

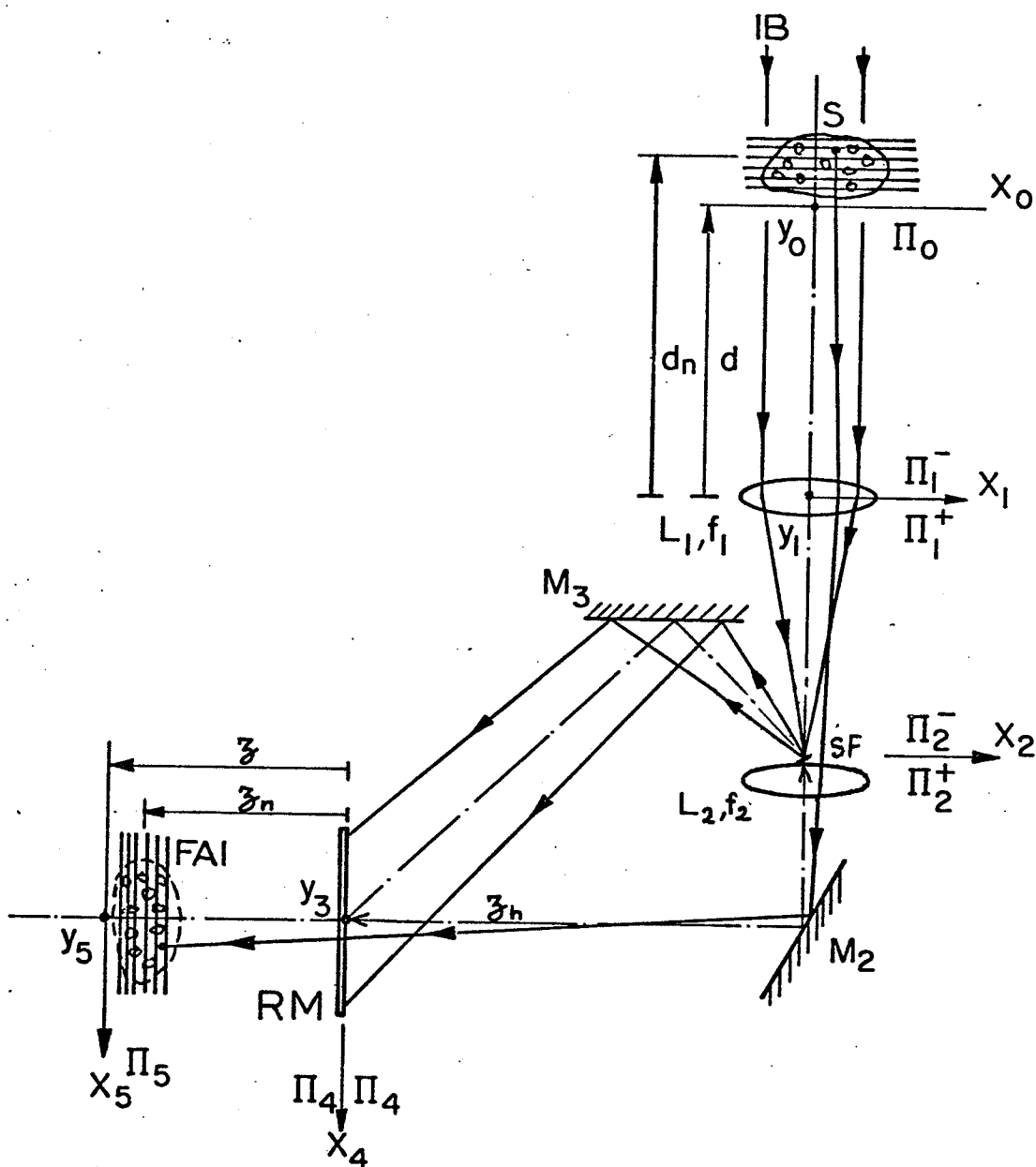


Fig. 3.3 Two-lens optical processor allowing holographic recording of the filtered aerial image formed by the two lenses. The notations are as follows: "IB" illuminating beam, "S" scene, " L_1 " and " L_2 " lenses, "SF" spatial filter, " M_2 " and " M_3 " mirrors, "RM" recording material and "FAI" filtered aerial image.

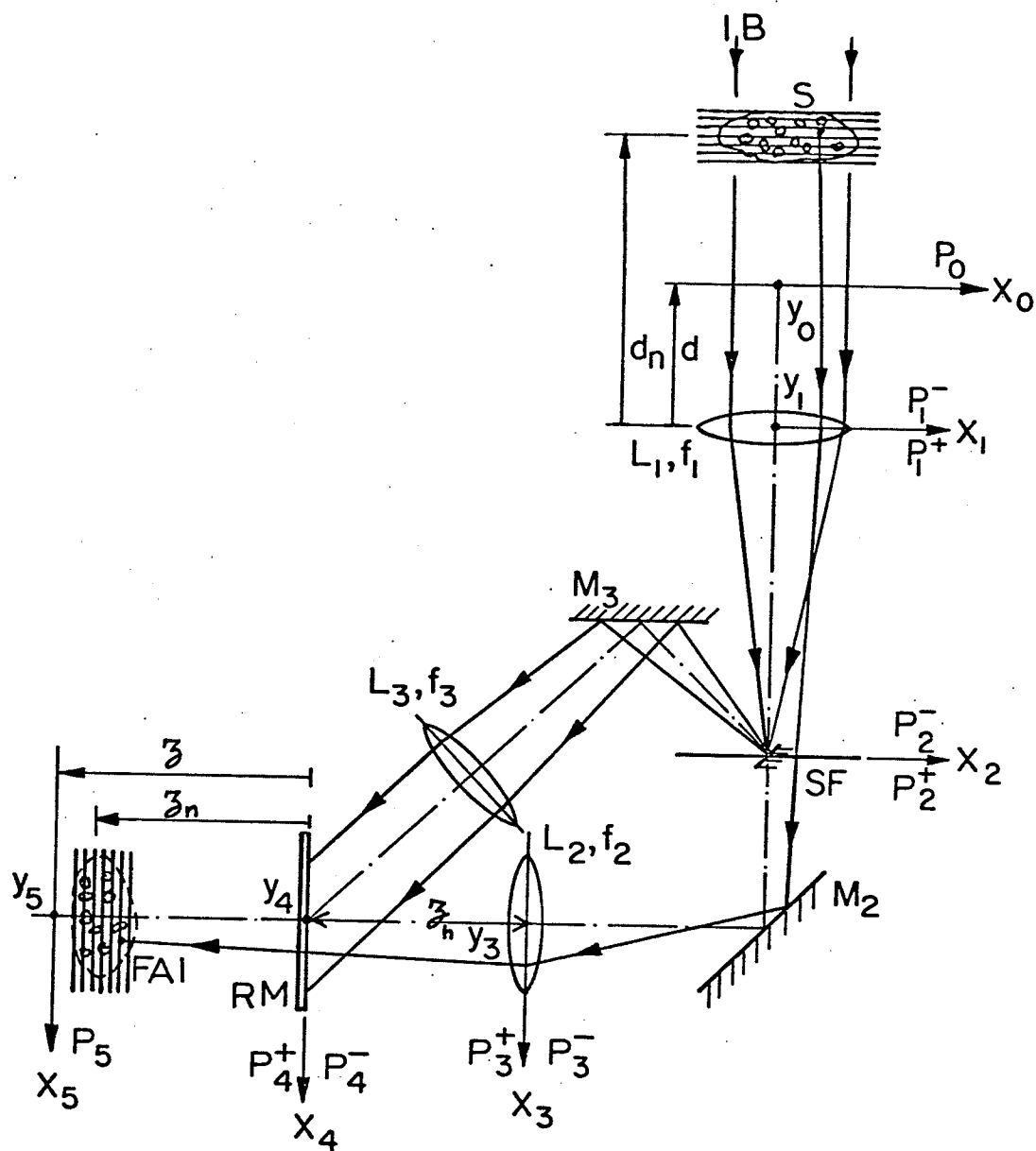


Fig. 3.4 Telescope optical processor allowing holographic recording of the filtered aerial image. The notations are as follows: "IB" illuminating beam, "S" scene, " L_1 ", " L_2 " and " L_3 " are lenses, "SF" spatial filter, " M_2 " and " M_3 " mirrors, "RM" recording material and "FAI" filtered aerial image.

has a magnification factor which is independent of the scene position.

3.3.4 Spatial Filter

The spatial filter SF is composed of reflective and transmissive regions with amplitude reflectance $F_r(x_2, y_2)$ and amplitude transmittance $F_t(x_2, y_2)$. The type of spatial filter used so far was partly reflective and partly transmissive in the small central dot, and only transmissive elsewhere. Such a filter may be designed in many ways; Fig. 3.5(a) shows a possible design. The prism A is silvered on the surface of separation with the prism B. The reflectivity is a function of the amount of silver deposit. A simple filter giving a dark field image would have a 100% reflectivity on a central disk and a 100% transmittivity elsewhere (the central disk may be apodized). An index matching balsam is used between the prisms A and B. A filter allowing imaging of a phase contrast image with contrast improvement consists of a partially reflective central disk backed with a well defined deposit of transparent varnish having an optical density different from that of the balsam. The phase retardation or advancement introduced between the central ordinate and the high order components, being a function of the thickness h of the transparent varnish and of the difference in optical density between the varnish and the balsam, is given by

$$\delta_v = 2\pi/\lambda (n_b - n_v) h \quad (3.1)$$

where n_b and n_v are the absolute refractive indices of balsam and varnish.

Other combinations of reflective and transmissive regions are implementable. Of interest is the one depicted in Fig. 3.5(b). Fabrication of

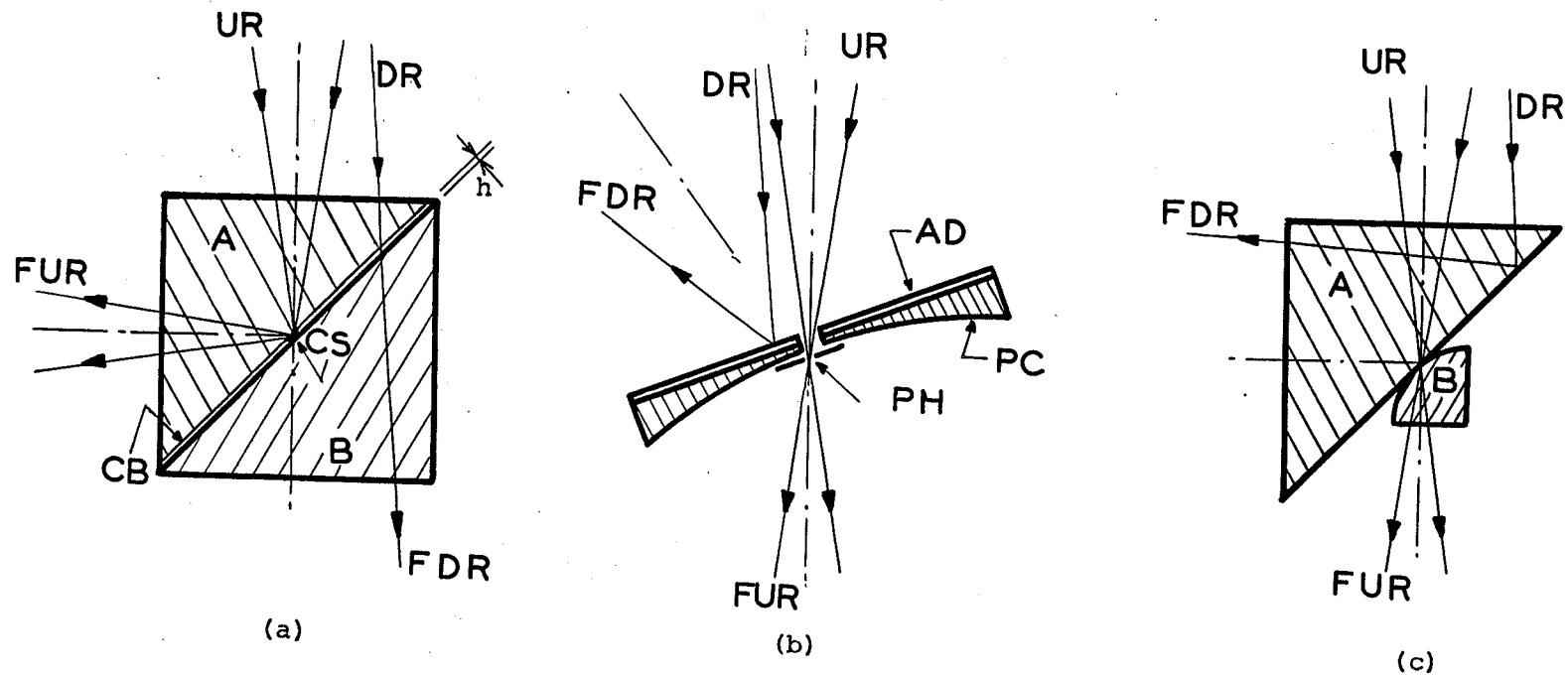


Fig. 3.5 Different devices that can be used as spatial filters. (a) A reflective central dot is deposited on the interface of the two halves of the prism; an index matching balsam is used to bind the two halves. (b) Spatial filter mirror; further filtering of the reference beam is performed by a pinhole. (c) Frustration of total reflection by a second surface; an apodized reference beam can be obtained. The notations are as follows: "UR" undiffracted ray, "DF" diffracted ray, "FUR" filtered undiffracted ray, "FDR" filtered diffracted ray, "A" and "B" prisms, "CS" central reflective spot, "CB" Canadian balsam, "AD" aluminum deposit and "PC" plano-convex lens.

this filter is extremely easy. SF is reflective everywhere except in the central region, where the low spatial frequency components are allowed to propagate through the pinhole PH. Such a filter gives a dark-field image. The filter consists of a plano-concave lens PC which has received a thin film of aluminum AD on its flat surface after a hole was made with an ultrasonic impact grinder; further filtering required for local generation of the reference wave is performed by the pinhole in a disk which is placed against the concave surface of the lens. This spatial filter will be used in most of the experiments reported in this thesis.

Another spatial filter of particular interest is shown in Fig. 3.5(c). This filter produces a central apodized transmissive disk when the angle of incidence on the internal surface of the prism A is larger than the critical angle. It is known that under critical incidence, there exists an evanescent wave in the less dense medium [39]. This evanescent wave gives rise to a real wave in the component B (this phenomenon is called frustration of total reflection), in other words, there is "tunneling" from A to B. The curvature of B determines the beam profile of the transmitted reference wave.

3.3.5 Holocameras

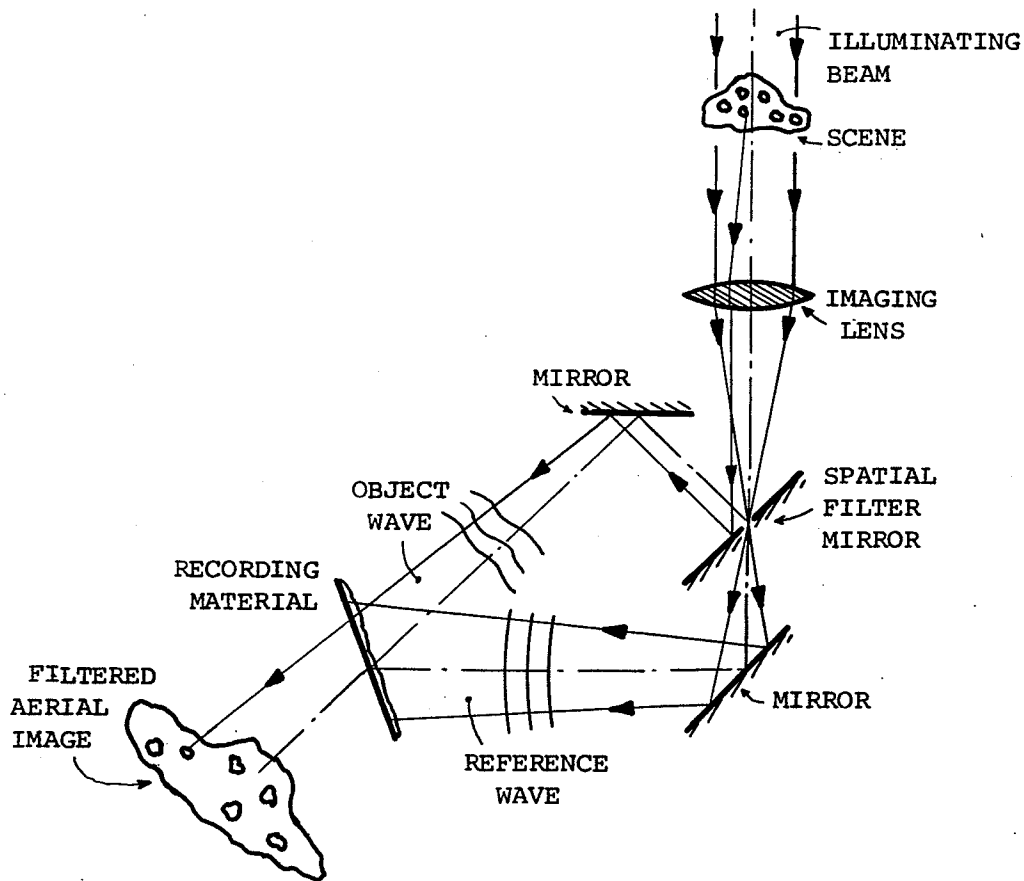
Two extremely interesting practical holocameras are now studied. They both use the spatial filter of Figs. 3.5(b) or (c). Invention of these apparatus has been reported to the Canadian Patents and Development Limited [36].

Single lens holocamera. This type of holocamera will be used to carry

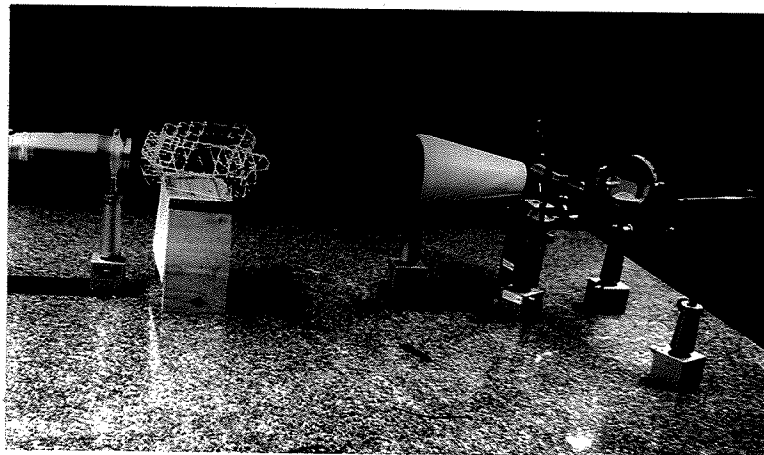
out all the experimental work. Laboratory investigations are facilitated since the embodiment requires a minimum of optical components (see Fig. 3.6). Another practical advantage is that the image magnification factor is a function of the object position, thus magnification may be adjusted within a wide range of values. The optical path matching of the reference and object waves is quite good, yet it is somewhat inferior to that obtained with the basic in-line techniques. The photograph of Fig. 3.6(b) gives a general view of the holocamera used in the experimental studies.

Telescope holocamera. Fig. 3.7 shows the embodiment, which is comprised of three lenses L_1 , L_2 and L_3 , a mirror M_3 , and two holographic gratings HG_1 and HG_2 . This holocamera requires more optical elements than the other, however the optical path matching between the reference and the object wave is now perfect if care is taken to adjust the optical paths by means of the holographic gratings HG_1 and HG_2 , the mirror M_3 , the angle α , and the position of the recording plane. The coherence requirements are exactly those of in-line holography. The space-invariance properties of holographic gratings [40] are employed, permitting ideal optical path matching by a ray to ray correspondence. This ray to ray correspondence no longer exists if a mirror M_2 is substituted for the holographic grating HG_2 . Although the difference in optical paths taken by the two interfering waves may still have zero value, it appears that the temporal coherence requirements are unchanged while the spatial coherence requirements are notably increased.

In these two holocameras, the reference-to-object wave intensity ratio may be adjusted by changing the characteristics of the spatial filter



(a)



(b)

Fig. 3.6 Single-lens holocamera: (a) schematic diagram, (b) photograph of the setup used to record a hologram of an architectural structure (refer to Section 5.2).

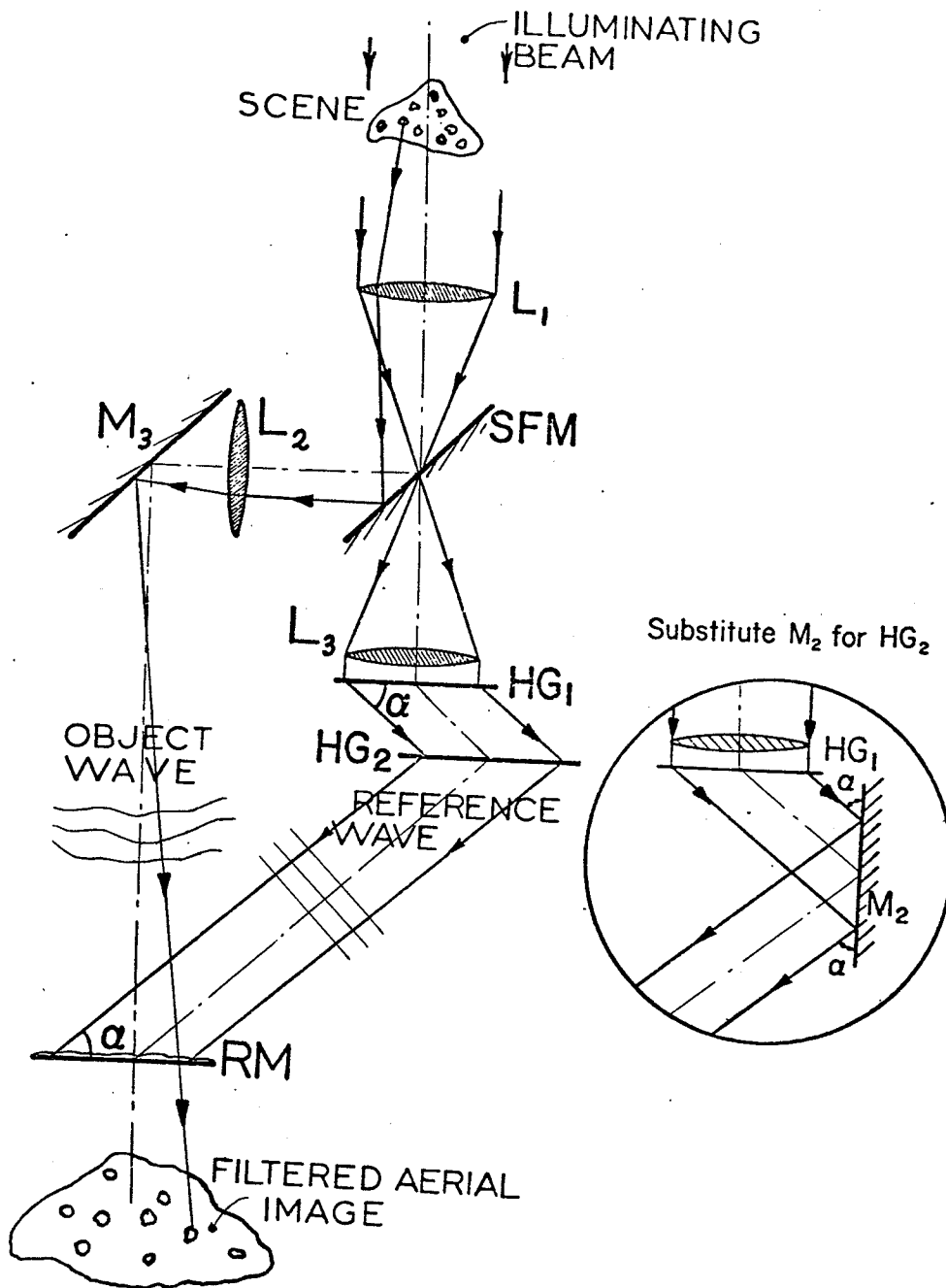


Fig. 3.7 Telescope holocamera using two holographic diffraction gratings to provide ideal optical path matching between the two interfering waves. A holographic grating and a mirror can be substituted for the two holographic gratings (circled diagram); although the optical path matching is still excellent, the spatial coherence requirements are notably increased. Notations are as follows: "L₁", "L₂" and "L₃" Fourier transform lenses, "SF" spatial filter mirror, "HG₁" and "HG₂" holographic gratings, "M₂" and "M₃" mirrors, and "RM" recording material.

and the reflectivity of the mirrors. If this is not sufficient, further adjustment may be made by means of an attenuator placed across the relevant wave. In addition, reflective objects may be holographically recorded with these two holocameras if most of the light diffracted by the objects propagates in a unique direction.

3.4 ANALYSIS OF THE BASIC HOLOGRAPHIC SYSTEMS

3.4.1 Two-lens Holographic System

Consider the scheme of Fig. 3.3 and let the three-dimensional amplitude distribution of the electric field radiated by the scene be expressed by the superposition of N planar distributions

$$O_0(x_0, y_0, d) = \sum_{n=1}^N O_0^{(n)}(x_0, y_0, d_n) = \sum_{n=1}^N \delta(d-d_n) O_0^{(n)}(x_0, y_0) \quad , \quad (3.2)$$

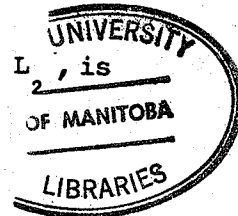
where d_n is the distance between the plane P_1 and the (n) th planar distribution. The fields engendered by $O_0^{(n)}(x_0, y_0, d_n)$ in the planes $\Pi_2^-, \Pi_2^+, \Pi_4^-$ and Π_4^+ are readily obtained by using the scalar theory of diffraction introduced in the appendix. Hence, in the plane Π_2^-

$$[\theta_2^{(n)}(x_2, y_2)]^- = H_{f_1^2/(f_1-d_n)}(x_2, y_2) \mathcal{F}_{1/\lambda f_1} O_0^{(n)}(x_0, y_0) \quad , \quad (3.3)$$

where the function $H_{f_1^2/(f_1-d_n)}(x_2, y_2)$ and the operator $\mathcal{F}_{1/\lambda f_1}(x_0, y_0)$ are defined in the appendix, and the vignetting introduced by the finite size of the aperture of the lens L_1 is neglected. The composite amplitude transmittance of the filter and of the lens L_2 , is

$$\Gamma_t(x_2, y_2) = F_t(x_2, y_2) H_{f_2}^*(x_2, y_2) \quad . \quad (3.4)$$

Therefore, the field in the plane Π_2^+ , just behind the lens L_2 , is



given by

$$[\theta_2^{(n)}(x_2, y_2)]^- = F_t(x_2, y_2) H_{f_2}^*(x_2, y_2) H_{f_1^2/(f_1 - d_n)}(x_2, y_2) \mathcal{F}_{1/\lambda f_1} \theta_0^{(n)}(x_0, y_0). \quad (3.5)$$

Thus, the field existing just before the hologram plane Π_4^- is given by

$$\begin{aligned} [\theta_4^{(n)}(x_4, y_4)]^- &= [\theta_2^{(n)}(x_2, y_2)]^+ * H_{z_h}(x_4, y_4) \\ &= [F_t(x_4, y_4) H_{f_2}^*(x_4, y_4) H_{f_1^2/(f_1 - d_n)}(x_4, y_4) \mathcal{F}_{1/\lambda f_1} \\ &\quad \theta_0^{(n)}(x_0, y_0)] * H_{z_h}(x_4, y_4). \end{aligned} \quad (3.6)$$

In virtue of the superposition theorem, the total field in the plane Π_4^- is given by

$$\begin{aligned} [\theta_4(x_4, y_4)]^- &= \sum_{n=1}^N [\theta_4^{(n)}(x_4, y_4)]^- \\ &= \sum_{n=1}^N [F_t(x_4, y_4) H_{f_2}^*(x_4, y_4) H_{f_1^2/(f_1 - d_n)}(x_4, y_4) \\ &\quad \mathcal{F}_{1/\lambda f_1} \theta_0^{(n)}(x_0, y_0)] * H_{z_h}(x_4, y_4). \end{aligned} \quad (3.7)$$

The holographic recording is a square-law recording medium which responds to the irradiance distribution $I_4(x_4, y_4)$ of the light impinging onto its surface. After recording and processing, the hologram is illuminated by a duplicate of the reference wave. Neglecting a constant phase factor and assuming that the hologram has an infinite aperture, the field in the plane Π_4^+ just behind the hologram is obtained by using the result of (2.13)

$$[\theta_4(x_4, y_4)]^+ = [\theta_4(x_4, y_4)]^- \quad (3.8)$$

Thus the total field in a plane Π_5 located at a distance z from the hologram yields:

$$\begin{aligned}
\theta_5(x_5, y_5) &= [\theta_4(x_4, y_4)]^+ * H_z(x_4, y_4) \\
&= \sum_{n=1}^N H_{z_h+z}^{(n)}(x_5, y_5) \mathcal{F}_{1/\lambda(z_h+z_n)} \{ F_t(x_2, y_2) H_{f_2}^*(x_2, y_2) \\
&\quad H_{f_1^2/(f_1-d_n)}^{(n)}(x_2, y_2) H_{z_h+z}^{(n)}(x_2, y_2) \mathcal{F}_{1/\lambda f_1} \{ O_0^{(n)}(x_0, y_0) \} \}. \quad (3.9)
\end{aligned}$$

Using the convolution theorem, it follows that

$$\theta_5(x_5, y_5) = \sum_{n=1}^N H_{z_h+z}^{(n)}(x_5, y_5) \left\{ \left[\mathcal{F}_{1/\lambda(z_h+z)} F_t(x_2, y_2) \right] * O_0(x_5/M', y_5/M') * H_e(x_5, y_5) \right\} \quad (3.10)$$

where

$$M' = -(z_h+z)/f_1, \quad (3.11)$$

and

$$e_n = \left[(z_h+z) f_1^2 + f_2^2 f_1 + f_2 (z_h+z) (f_1 - d_n) \right] / f_1^2 f_2 (z_h+z). \quad (3.12)$$

Examination of the RHS of (3.10) indicates that a reconstructed filtered image of the (n)th planar object distribution is reconstructed in a plane at a distance $z = z_n$ from the hologram, z_n being defined by the following relation

$$z_n = \left[f_1^2 (z_h + f_2) + f_2 z_h (f_1 - d_n) \right] / \left[(d_n - f_1) f_2 - f_1^2 \right] \quad (3.13)$$

which is obtained by writing that $\mathcal{F}_{1/\lambda f_2} H_e(x_5, y_5) = 1$. The magnification factor of the (n)th planar image distribution is given by

$$M'_n = -(z_h+z)/f_1 \quad (3.14)$$

Hence, the expression of the field for the three-dimensional reconstructed image is

$$\begin{aligned}
\theta_5(x_5, y_5, z) &= \sum_{n=1}^N \delta(z-z_n) H_{z_h+z_n}^{(n)}(x_5, y_5) \\
&\quad \{ O_0^{(n)}(x_5/M'_n, y_5/M'_n) * \mathcal{F}_{1/\lambda(z_h+z_n)} F_t(x_2, y_2) \} \quad (3.15)
\end{aligned}$$

Eq. (3.13) shows that the depth dimension is distorted by the two-lens imaging system, whereas (3.14) indicates that the transverse magnification factor M'_n is a function of the distance $(z_h + z_n)$. For a given planar distribution, the field of the filtered image is multiplied by the phase factor $H_{z_h+z_n}(x_5, y_5)$, which does not alter the appearance of the image when viewing is done with a square-law detector.

3.4.2 Single-Lens Holographic System

Considering now Fig. 3.2, it can be seen that the analysis of this system is essentially identical to that of the previous one if $(1/f_2) = 0$. Thus, (3.2) - (3.15) are representative of the one-lens holographic system when the value zero is substituted for $1/f_2$.

The position of the (n)th planar image distribution is given by

$$z_n = -z_h + f_1^2 / (d_n - f_1) \quad , \quad (3.16)$$

while the transverse magnification factor M''_n is

$$M''_n = -(z_h + z_n) / f_1 \quad . \quad (3.17)$$

The expression of the field for the three-dimensional image is

$$Q_5(x_5, y_5, z) = \sum_{n=1}^N \delta(z - z_n) H_{z_h+z_n}(x_5, y_5) \{ 0^{(n)}(x_5 / M''_n, y_5 / M''_n) * \mathcal{F}_{1/\lambda(z_h+z_n)} F_t(x_2, y_2) \} \quad . \quad (3.18)$$

3.4.3 Telescope Holographic System

The analysis based on the scalar theory of diffraction is used once more to obtain the relevant expression for the field of the filtered image, which is reconstructed upon illumination of the processed hologram.

Consider the scheme shown in Fig. 3.4. The fields engendered by $O_0^{(n)}$ (x_0, y_0, d_n) in the planes $P_1^-, P_1^+, P_2^-, P_2^+, P_3^-, P_3^+$ and P_4^- are readily obtained.

Hence,

$$[O_1^{(n)}(x_1, y_1)]^- = O_0^{(n)}(x_1, y_1) * H_{d_n}(x_1, y_1) \quad (3.19)$$

$$[O_1^{(n)}(x_1, y_1)]^+ = [O_0^{(n)}(x_1, y_1) * H_{d_n}(x_1, y_1)] H_{f_1}^*(x_1, y_1) \quad (3.20)$$

(the effect of the lens aperture is neglected),

$$[O_2^{(n)}(x_2, y_2)]^- = H_{\ell_n}(x_2, y_2) \left[\mathcal{F}_{1/\lambda f_1} O_0^{(n)}(x_1, y_1) \right] \quad (3.21)$$

$$[O_2^{(n)}(x_2, y_2)]^+ = H_{\ell_n}(x_2, y_2) F_t(x_2, y_2) \left[\mathcal{F}_{1/\lambda f_1} O_0^{(n)}(x_1, y_1) \right] \quad (3.22)$$

$$[O_3^{(n)}(x_3, y_3)]^- = H_{f_2}(x_3, y_3) \mathcal{F}_{1/\lambda f_2} \left\{ \left[\mathcal{F}_{1/\lambda f_1} O_0^{(n)}(x_1, y_1) \right] F_t(x_2, y_2) \right. \\ \left. H_{g_n}(x_2, y_2) \right\} \quad (3.23)$$

$$[O_3^{(n)}(x_3, y_3)]^+ = \left\{ \mathcal{F}_{1/\lambda f_2} \left[\mathcal{F}_{1/\lambda f_1} O_0^{(n)}(x_1, y_1) \right] \right\} * \\ \left[\mathcal{F}_{1/\lambda f_2} F_t(x_2, y_2) \right] * H_{f_2/g_n}^*(x_3, y_3) \quad (3.24)$$

and

$$[O_4^{(n)}(x_4, y_4)]^- = O_0^{(n)}(x_4/M''', -y_4/M''') * \\ \left[\mathcal{F}_{1/\lambda f_2} F_t(x_2, y_2) \right] * H_{z_h - f_2^2/g_n}^*(x_4, y_4) \quad (3.25)$$

In the above equations, $\ell_n = f_1^2/(f_1 - d_n)$, $g_n = f_2 \ell_n / (f_2 + \ell_n)$ and $M''' = -f_2/f_1$.

The total field in the plane P_4^- is found by using the superposition theorem

$$\begin{aligned} [O_4(x_4, y_4)]^- &= \sum_{n=1}^N [O_4^{(n)}(x_4, y_4)]^- \\ &= \sum_{n=1}^N O_0^{(n)}(x_4/M''', y_4/M''') * \left[\mathcal{F}_{1/\lambda f_2} F_t(x_2, y_2) \right] * \\ &\quad H_{z_h - f_2^2/g_n} \end{aligned} \quad (3.26)$$

After recording and processing of the hologram, the illumination by a readout wave identical to the reference wave generates a field defined by (2.3). Assuming that the hologram has an infinite aperture, it follows that

$$[O_4(x_4, y_4)]^+ = [O_4(x_4, y_4)]^- \quad (3.27)$$

and the total field in a plane P_5 located at the distance z from the hologram yields

$$\begin{aligned} O_5(x_5, y_5) &= \sum_{n=1}^N [O_5^{(n)}(x_5, y_5)] \\ &= \sum_{n=1}^N O_0^{(n)}(x_5/M''', y_5/M''') * \left[\mathcal{F}_{1/\lambda f_2} F_t(x_2, y_2) \right] * \\ &\quad H_{z_h + z - f_2^2/g_n}(x_5, y_5) \end{aligned} \quad (3.28)$$

Examination of the RHS of (3.28) indicates that a filtered image of the (n)th planar object distribution is reconstructed in a plane at a distance $z = z_n$ from the hologram plane, if the relation

$\mathcal{F}_{1/\lambda f_2} [H_{z_h + z - f_2^2/g_n}(x_5, y_5)] = 1$ is satisfied. This leads to

$$z_n = -d_n (f_2/f_1)^2 + (f_2 - z_h + f_1^2/f_2) \quad (3.29)$$

With z_n given by the last equation, it is now possible to write the expression for the three-dimensional distribution field of the reconstructed

filtered image as

$$O_5(x_5, y_5, z) = \sum_{n=1}^N \delta(z-z_n) \{O_0^{(n)}(x_5/M_n'', y_5/M_n'') * [\mathcal{F}_{1/\lambda f_2} F_t(x_5, y_5)]\} \quad (3.30)$$

in which

$$M_n'' = -f_2/f_1 \quad (3.31)$$

is the transverse magnification factor of the (n)th planar distribution of the reconstructed filtered image. Note that M_n'' does not depend on the location of the planar distribution, and thus constant transverse magnification is obtained by the telescopic system. From (3.29), it appears that the depth dimension is not distorted. The longitudinal magnification factor is

$$\mathcal{M}_n''' = -(f_2/f_1)^2 \quad (3.32)$$

In addition, when $f_1 = f_2 = f$, it follows that $\mathcal{M}_n''' = M_n'' = -1$ and that

$$z_n = -d_n - z_h + 2f.$$

3.4.5 Comments

The reconstructed filtered images generated by the holograms obtained with the three basic holographic systems have amplitude field distributions which are given by (3.15), (3.18) and (3.30). The mathematical form of these expressions differs only in the fact that (3.15) and (3.18) are multiplied by a phase factor that is not present in (3.30). The images will be either viewed or recorded with a square-law detector, the recorded irradiances being $[\theta_5(x_5, y_5, z)]^2$, $[Q_5(x_5, y_5, z)]^2$ and $[O_5(x_5, y_5, z)]^2$. The following equation holds

$$|\theta_5(x_5, y_5, z)|^2 = |Q_5(x_5, y_5, z)|^2 = |O_5(x_5, y_5, z)|^2 \quad (3.33)$$

Thus in the analysis, which follows, the phase factors of (3.15) and (3.18) will be neglected and common expressions will be used to represent the image field

$$O_5(x_5, y_5) = \sum_{n=1}^N \{ O_0^{(n)}(x_5/M, y_5/M) * \mathcal{F}_{1/\lambda u} F_t(x_2, y_2) * H_v(x_5, y_5) \} \quad (3.34)$$

and

$$O_5(x_5, y_5, z) = \sum_{n=1}^N \delta(z-z_n) \{ O_0^{(n)}(x_5/M, y_5/M) * \mathcal{F}_{1/\lambda u} F_t(x_2, y_2) \} \quad (3.35)$$

In these equations, M represents one of the transverse magnification factors (M' , M'' or M''') and u represents either $(z_h + z_n)$ or f_2 , depending upon which holographic system is used; v is a function of the position of the plane of observation.

3.4.5 Image Filtering

It is clear that the spatial filter plays a similar role in either type of holographic system. Eq. (3.35) indicates that the field of the aerial image generated in the absence of the filter is merely convolved with the Fourier transform of the amplitude transmittance of the filter. Filtering in the focal plane must be done in such a way that the low spatial frequency components may be used to generate the reference beam. A general type of filter satisfying this requirement has circular symmetry with amplitude transmittance

$$F_t(\rho_2) = \begin{cases} \alpha(\rho_2) & , \quad \text{for } 0 \leq \rho_2 < \epsilon \\ \beta(\rho_2) & , \quad \text{for } \epsilon \leq \rho_2 < \tau \\ \gamma(\rho_2) & , \quad \text{for } \tau \leq \rho_2 < \infty \end{cases} \quad (3.36)$$

and amplitude reflectance

$$F_r(\rho_2) = \begin{cases} 1 - \alpha(\rho_2) & , \quad \text{for } 0 \leq \rho_2 < r_p \\ 0 & , \quad \text{elsewhere} \end{cases} \quad (3.37)$$

($\rho_2^2 = x_2^2 + y_2^2$, and $\alpha(\rho_2)$, $\beta(\rho_2)$ and $\gamma(\rho_2)$ are real variables such that $0 \leq \alpha(\rho_2) < 1$, $0 \leq \beta(\rho_2) \leq 1$ and $0 \leq \gamma(\rho_2) \leq 1$). According to the filter variables, the filtered reconstructed images may be classified as follows

- (i) image with contrast enhancement $\{0 < \alpha(\rho_2) < 1, \beta(\rho_2) = 1, \gamma(\rho_2) = 0\}$
- (ii) dark-field image $\{\alpha(\rho_2) = \gamma(\rho_2) = 0, \beta(\rho_2) = 1\}$
- (iii) phase contrast image $\{\alpha(\rho_2) = i\alpha_0, \beta(\rho_2) = 1, \gamma(\rho_2) = 0\}$

where α_0 is a real constant such that $0 \leq \alpha_0 < 1$. Numerous other filters may be thought up, yet those producing the above mentioned images are relatively easily made and give effective filtering. Note that the smaller the value of $\alpha(\rho)$, the higher is the amount of energy available for generating the reference wave. The value of ϵ does not notably affect this amount of energy since the filtering of the reference beam requires an aperture radius which is much smaller than ϵ .

3.4.6 Reference Wave

The filtering of the reference wave is interwoven with the image filtering, since in both cases the spatial filtering is done in the common Fourier transform plane. Thus, the amplitude of the low spatial frequency components allocated to the processing of the reference wave is equal to

$(1-\alpha(\rho_2))$, and the radius r_p of the reflecting spot of the spatial filter is such that $r_p \leq \epsilon$.

The main problems encountered in local generation of the reference beam are caused by the propagation of the illuminating beam through an inhomogeneous random medium (turbulent gas or liquid) and by the transilluminated object scatterer. In the absence of diffraction effects caused by the finite extent of the lasing medium, the radial distribution of intensity in the TEM_{00} mode of most of the laser sources available has a truncated Gaussian profile. By using these sources as illuminating sources, the holographic recording apparatus can be remotely located, since divergence is reduced.

If the wave profile of the beam reaching the holographic system is "quasi" Gaussian, the magnitude of the amplitude distribution of the corresponding Gaussian function in the Fourier transform plane of the lens L_1 is

$$\left| \mathcal{F}_{1/\lambda f_1} [\exp(-\rho_1^2/w_1^2) H_{f_1}(\rho_1)] \right| = \text{const.} \exp(-\pi w_1 \rho_2 / \lambda f_1)^2, \quad (3.38)$$

where $\rho_1 = (x_1^2 + y_1^2)^{1/2}$, $\rho_2 = (x_2^2 + y_2^2)^{1/2}$ and w_1 is the beam half-width.

Effective filtering is provided if the radius r_p of the reflective spot is slightly larger than the beam half-width w_2 in the transform plane, i.e. $r_p > w_2 = \lambda f_1 / \pi w_1$. When the wave reaching the apparatus cannot be approximated by a wave having a Gaussian profile, maximum filtering with minimum blockage may be implemented if r_p is slightly larger than the diffraction-limited spot size in the transform plane, i.e. $r_p > 1.22 \lambda f_1 / r_a$ (r_a = radius of the lens aperture).

Considering the fact that the reference-to-object wave intensity ratio has to be larger than 1 (a trade-off between reconstruction efficiency and image resolution usually leads to a choice of a ratio of about 3), it is of importance that the spatial filter eliminates most of the object bearing information without noticeably attenuating the energy available for processing the reference beam. Very propitious filtering is encountered when the transilluminated object consists of a three-dimensional field of particles, because the object-bearing part of the wave will have very intense high order spatial frequency components and dim low order components.

If the illuminating beam propagates through a very long path before it reaches the scene, its beam half-width must be substantially increased in order to reduce the beam spread.

3.5 RECONSTRUCTED IMAGES

3.5.1 Position of the Reconstructed Filtered Images

From the results of (3.13), (3.16) and (3.29), it is seen that three different situations occur, depending upon the relative position of the hologram plane with respect to the aerial image $O_5(x_5, y_5)$:

(1) $z_n > 0$ with $n = 1, 2, 3 \dots N$; this situation gives rise to a three-dimensional image located entirely behind the hologram plane. Since this reconstructed image can be imaged onto a screen for viewing, or on photographic film for recording without the use of a lens, the image is real. Direct viewing with the eye or with other detectors such as cameras is possible by observing the field beyond the focussed image. It is of interest to note that the image is orthoscopic [41], that is to say, it has normal depth dimension.

(ii) $z_n < 0$ with $n = 1, 2, 3 \dots N$; the reconstructed orthoscopic image is now located before the hologram plane. It is impossible to focus the image onto a screen without a lens; the image must be intercepted with the eyes or another similar device. Therefore, the image is virtual.

(iii) $z_n \geq 0$ for $n = 1, 2, 3 \dots P$ and $z_n < 0$ for $n = (P+1), (P+2), (P+3) \dots N$; in this case, the image straddles the hologram plane [42]. Part of the image forms an orthoscopic real image, while the other part forms an orthoscopic virtual image. The very interesting properties of such holographic images will be discussed later in connection with the generation of a local reference beam.

3.5.2 Post-Recording Addition of the Central Ordinate

In theory, in virtue of the superposition principle, bright-field or phase contrast images may be obtained from the reconstructed images. Yet, experimental verification of this principle at optical frequencies is most critical and would require the use of highly sophisticated equipment, since the phase, amplitude and wavefront of the wave to be added to the reconstructed dark-field image must be carefully determined.

The optical arrangements which could be used are schematically represented in Figs. 3.8 and 3.9 in the case of holograms recorded with the single lens holocamera and with the telescope holocamera respectively.

3.6 SUMMARY

In the new method proposed, the separation of the spatial frequency

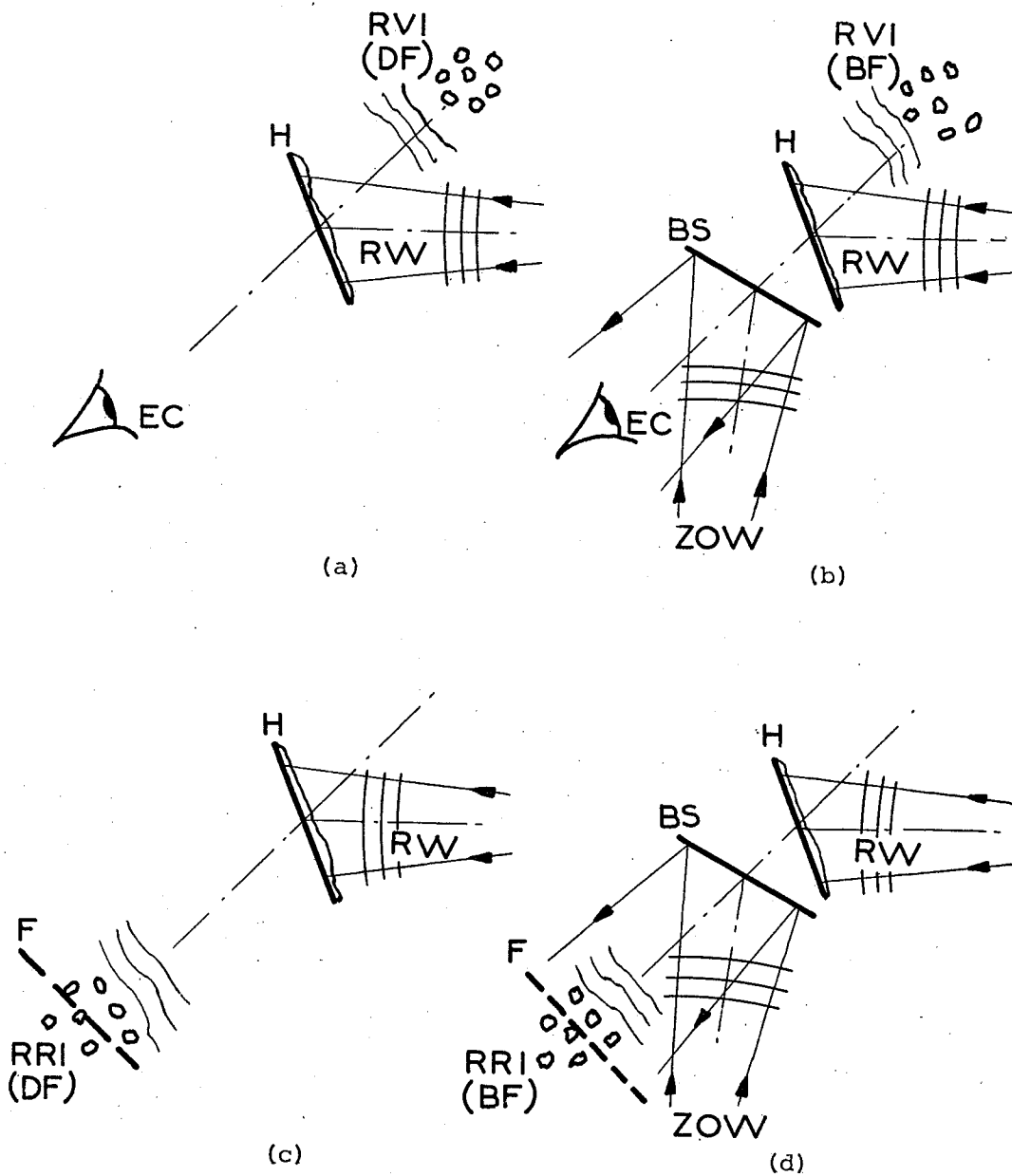


Fig. 3.8 Post-recording addition of the central ordinate in the case of holograms recorded with the single lens holocamera of Fig. 3.6: (a) and (c) conventional reconstruction of the dark-field images when $z < 0$ (virtual images) and when $z > 0$ (real images), (b) and (d) the central ordinate is superposed to the reconstructed waves when $z < 0$ (virtual images) and when $z > 0$ (real images). The notations are as follows: "RW" readout wave, "ZOW" zero order wave, "EC" eyes or photographic camera, "F" film, "BS" beam splitter, "RRI" reconstructed real image, "RVI" reconstructed virtual image, "BF" bright-field and "DF" dark-field.

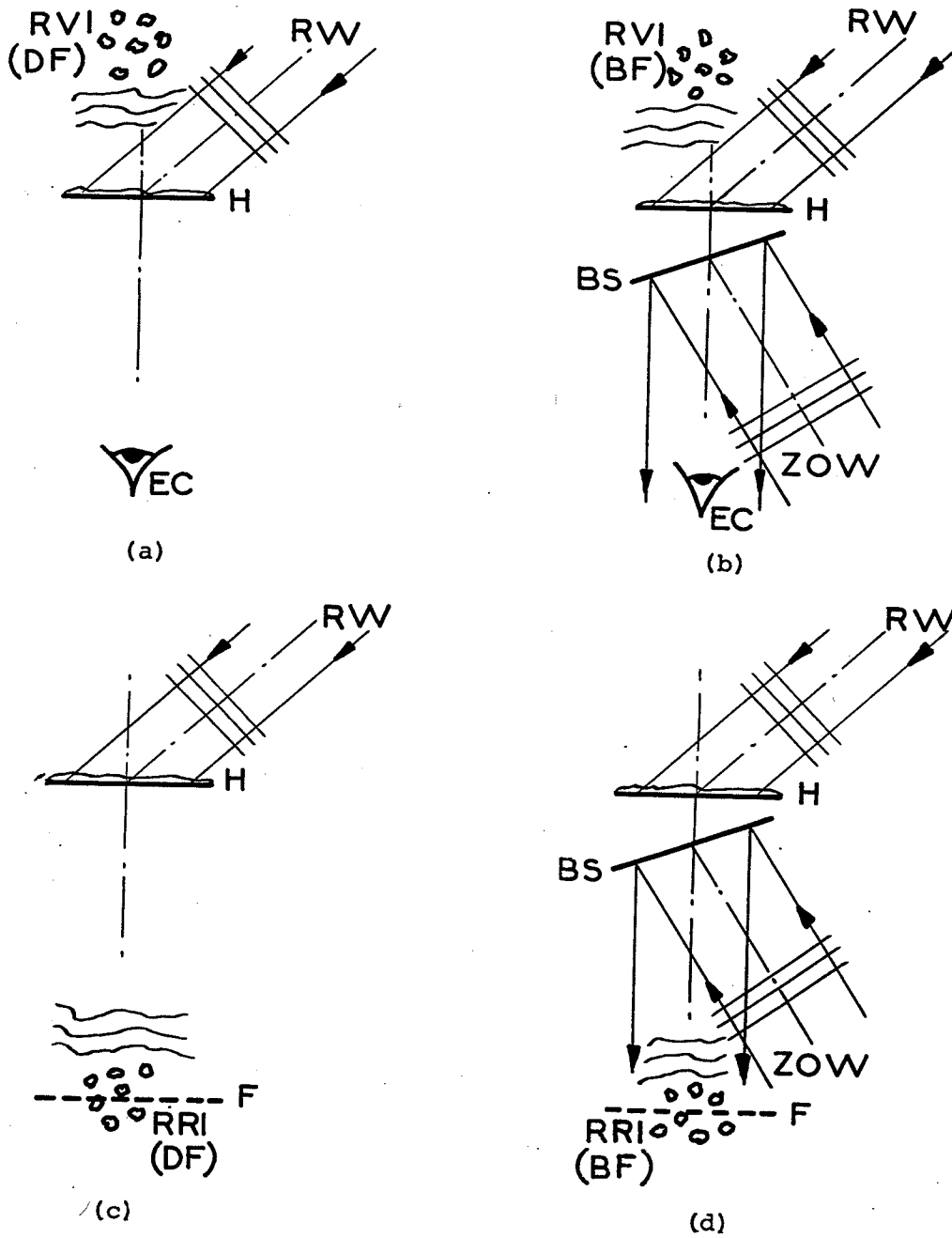


Fig. 3.9 Post-recording addition of the central ordinate in the case of holograms recorded with the telescope holocamera of Fig. 3.7: (a) and (c) conventional reconstruction of the dark-field images when $z_n < 0$ (virtual images) and when $z_n > 0$ (real images), (b) and (d) the central ordinate is superposed to the reconstructed waves when $z_n < 0$ (virtual images) and when $z_n > 0$ (real images). The notations are as follows: "RW" readout wave, "ZOW" zero order wave, "EC" eyes or photographic camera, "F" film, "BS" beam splitter, "RRI" reconstructed real image, "RVI" reconstructed virtual image, "BF" bright-field and "DF" dark-field.

components into an object bearing wave and a reference wave is done simultaneously. This feature allows recording of unattenuated diffracted rays and it permits recording of an interference pattern with a very high reference-to-object ratio. Thus, high resolution images can be reconstructed from holograms having high diffraction efficiency.

Although only the use of light waves has been mentioned, it must be said in passing that this new method is implementable when the illuminating wave is provided by a coherent source of any wavelength. Thus, application of the method in ultra-violet, infra-red or microwave holography is straightforward.

The two lens-assisted holocameras proposed permit imaging of a very wide range of transilluminated objects since the aerial images of the objects may be magnified or even demagnified prior to recording.

Due to the removal of a fraction of the central ordinate, the image contrast and detail visibility are enhanced. Dark-field images are of great interest when the objects have a very poor contrast; this is often the case with images obtained from phase objects (transparent objects).

Finally, it has been shown that a holocamera requiring a very low spatial and temporal coherence may be designed (telescope holocamera). This holocamera is best suited to remote sensing applications, since energy and coherence requirements are much smaller than those of the methods of amplitude/wavefront division.

*Chapter Four*MATHEMATICAL ANALYSIS OF THE RECONSTRUCTED FILTERED IMAGES4.1 INTRODUCTION

This chapter deals with the mathematical analysis of filtered images recorded by means of the new holographic method studied in the last chapter. As pointed out in that chapter, by neglecting a phase factor, a general expression for the field of three-dimensional reconstructed filtered images is given by (3.35).

The analysis is limited to two classes of transilluminated objects, namely: amplitude and phase gratings having amplitude transmittance discontinuities, and opaque disks. The choice of these two classes is justified by the specific intended use of the holocameras.

4.2 RECONSTRUCTED IMAGE OF A ONE-DIMENSIONAL OBJECT

A one-dimensional grating having transmittance discontinuities offers a relatively simple means of rapidly describing the properties of the holographically reconstructed filtered image. The general character of the analysis is not impaired, since most one-dimensional objects can be decomposed in a superposition of many grating-like structures.

Consider a one-dimensional grating having an amplitude transmittance $O_0^{(1)}(x_0, y_0, d_1)$, illuminated by a plane wave of amplitude 1. Assuming that $O_0^{(1)}(x_0, y_0, d_1)$ is a function of period $2L$ satisfying the Dirichlet

conditions, a series decomposition follows

$$O_0^{(1)}(x_0, y_0, d_1) = \delta(d-d_1) \sum_{k=-\infty}^{\infty} c_k \exp(-i\mu_k x_0) \quad (4.1)$$

where $c_k = (1/2L) \int_{-L}^L O_0^{(1)}(x_0, y_0, d_1) \exp(i\mu_k x_0) dx_0$ and $\mu_k = k\pi/L$ with $k = 0, \pm 1, \pm 2 \dots$. Substituting the explicit expression of $O_0^{(1)}(x_0/M, y_0/M, d_1)$ into (3.35), which gives the expression of the reconstructed filtered image, it follows that

$$O_5^{(1)}(x_5, y_5, z_1) = \delta(z-z_1) \sum_{k=-\infty}^{\infty} c_k \exp(i\mu_k x_5/M) F_t(x_5, y_5) \quad (4.2)$$

$F_t(x_5, y_5)$ is given by (3.34), thus

$$\begin{aligned} O_5^{(1)}(x_5, y_5, z_1) = & \delta(z-z_1) \{ \alpha(x_5) \sum_{k=-m_0}^{m_0} c_k \exp(i\mu_k x_5/M) \\ & + \beta(x_5) \sum_{k=-m_1}^{-m_0-1} c_k \exp(i\mu_k x_5/M) + \beta(x_5) \sum_{k=m_0+1}^{m_1} c_k \exp(i\mu_k x_5/M) \\ & + \gamma(x_5) \sum_{k=-\infty}^{-m-1} c_k \exp(i\mu_k x_5/M) + \gamma(x_5) \sum_{k=m_1+1}^{\infty} c_k \exp(i\mu_k x_5/M) \}, \quad (4.3) \end{aligned}$$

where m_0 and m_1 are the largest integers satisfying the inequalities $m_0 < 2\epsilon L/\lambda f_1$ and $m_1 < 2\tau L/\lambda f_1$.

4.2.1 Dark-Field Filter

It is of interest to study in detail the reconstructed image of an amplitude grating when $\alpha(\rho_2) = \gamma(\rho_2)$ and $\beta(\rho_2) = 1$. For an amplitude grating, the Fourier transform of $O_0^{(1)}(x_0, y_0, d_1)$ is a Hermitian function [43]; thus, evaluation of (3.3) or (3.21) indicates that if $c_k = a_k - ib_k$, then $c_{-k} = a_k - ib_k$. By substituting the values of the c_k 's into (4.3), and by using the values given to $\alpha(\rho_2)$, $\beta(\rho_2)$ and $\gamma(\rho_2)$, it follows that

$$O_5^{(1)}(x_5, y_5, z_1) = 2 \sum_{k=m_0+1}^{m_1} [a_k \cos(\mu_k x_5/M) + b_k \sin(\mu_k x_5/M)] \quad (4.4)$$

A physical interpretation of this result indicates that the image intensity is exactly the square of the real structure when $m_0 = 0$ and $m_1 \rightarrow \infty$. Yet, as m_1 decreases, a dark fringe appears where the amplitude transmittance of the object has discontinuities. This fringe is exactly located at the geometrical boundary of the grooves of the transilluminated grating. The dark fringe becomes wider as m_1 increases. The case of a grating, for which the amplitude transmittance is a square wave, is illustrated in Fig. 4.1. The occurrence of the dark fringe is a property of paramount importance, as dark-field images permit the study of the profile of objects with great accuracy [44]. The image contrast is enhanced when m_0 increases.

If the object is now a phase grating with $|O_0^{(1)}(x_0, y_0, d_1)| \sim 1$ (case of small changes of phase where the imaginary part only is dependent on x_0), evaluation of (3.3) or of (3.21) indicates that the c_n 's are such that $c_k = a_k + ib_k$ and $c_{-k} = -a_k + ib_k$, since the Fourier transform of $I_m[O_5^{(1)}(x_5, y_5, d_1)]$ is an anti-Hermitian function [43]. Using these values of the c_k 's and of the filter parameter defined above, (4.3) yields

$$O_5^{(1)}(x_5, y_5, d_1) = 2 \sum_{k=m_0+1}^{m_1} i [a_k \sin(\mu_k x_5 / M) + b_k \cos(\mu_k x_5 / M)] \quad (4.5)$$

From this equation, it is clearly seen that the observations concerning an amplitude grating hold for a phase grating as well.

4.2.2 Focussing Properties of Dark-Field Images

Considering (3.34) and substituting into it the expression of $O_0^{(1)}(x_0, y_0, d_1)$, it follows that

$$O_5(x_5, y_5) = \sum_{k=-\infty}^{\infty} c_k \exp(i\mu_k x_5 / M) H_{u^2/v}^* (\lambda u \mu_k / 2\pi) F_t(x_5, y_5) \quad (4.6)$$

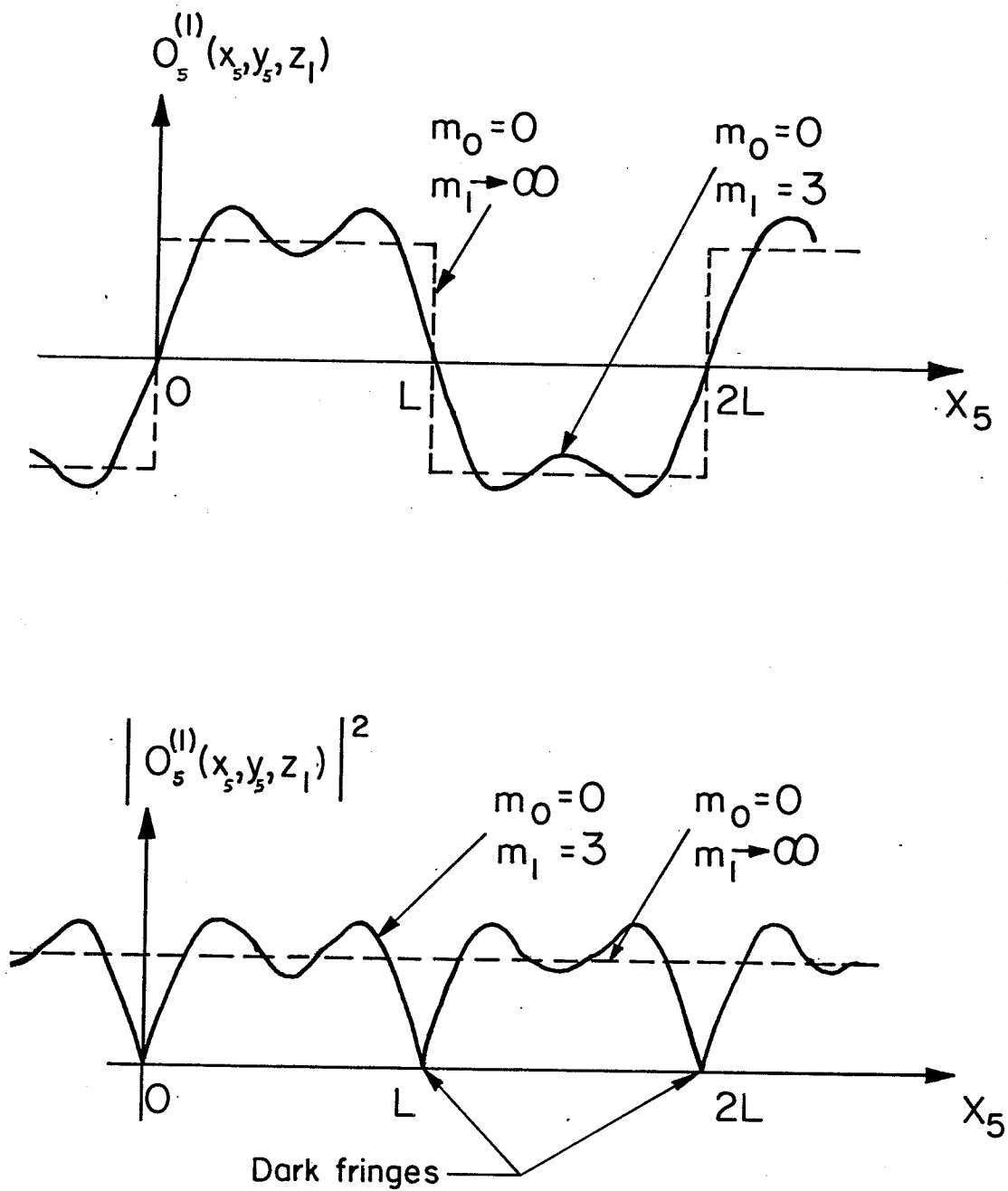


Fig. 4.1 Effect of dark-field filtering on a grating having an amplitude transmittance represented by a square wave. A distinctive dark fringe appears where the object transmittance is discontinuous.

The phase factor $H^*_{u^2/v} (\lambda u_k/2\pi)$ is a function of the position of the plane of observation, but it is also directly proportional to μ_k^2 .

Hence, although the effect of this phase factor is negligible for small values of k , it becomes important as k takes large values.

The effect on the image is readily understood. Thus, when the series expansion has small order terms, the position of the focussing plane is determined only approximately, whereas when the series expansion contains only high order terms, the plane of focus is accurately determined. This property is of extreme importance since accurate recovery of the depth dimension in the reconstructed image is possible by increasing m_0 .

4.2.3 Phase Contrast Filter

The object is the grating described earlier, and the filter is defined by $\{\alpha(\rho_2) = i\alpha_0, \beta(\rho_2) = 1, \gamma(\rho_2) = 0, m_0 = 0, m_1 \rightarrow \infty\}$. Hence

$$O_5^{(1)}(x_5, y_5, d_1) = \delta(z-z_1) \{i\alpha_0 + i2 \sum_{k=1}^{\infty} -a_k \sin(\mu_k x_5/M) + b_k \cos(\mu_k x_5/M)\} \quad (4.7)$$

and the image intensity is linearly related to the phase variation of the grating. It must be pointed out that the smaller α_0 is, the more intense the locally processed reference wave will be. In addition, the sensitivity of the method for showing very slight differences in phase is inversely proportional to α_0 .

4.3 RECONSTRUCTED DARK-FIELD IMAGE OF AN OPAQUE DISK

Although dark-field filtering has been used in microscopy for more than

half a century [45], and in spite of a recent recognition of the remarkable properties which characterize the dark-field images of opaque objects [46], no theory has yet been reported or published³ which substantiates the subjective observations in the specific and relevant case of imaging of circular opaque objects when spatial filtering with circular binary filters is performed.

It is therefore the object of this section to provide a mathematical analysis for the above mentioned case. The most significant property inherent in dark-field images of opaque objects is the existence of a dark line located on the contour of the Gaussian image of the object [47]. The relevance of this study is readily understood since holographic recording of dark-field images of particle fields corresponds to the case mentioned if the particles are assumed to be "quasi" circular opaque objects. This assumption is quite realistic and many mathematical models studying, for instance, the scattering properties of particles, have been based on it. Besides, the contour of each particle may always be defined in terms of the radii of curvature measured at different locations. Knowledge of the local radii of curvature and of the overall dimension of the particle is beneficial since it may determine the amount of interaction existing between one point of the contour and the rest of the contour. The importance of this interaction is implicitly linked to the slight displacement of the dark fringe from the exact position of the contour defined by the Gaussian image.

³Private communication with Dr. K. G. Birch, National Physical Laboratory, Teddington, Middlesex, GB, February 6, 1976.

4.3.1 Formulation

By using the convolution theorem, (3.35) may be rewritten in the following form

$$O_s(x_s, y_s, z) = \sum_{n=1}^N \delta(z-z_n) \mathcal{F}_{1/\lambda u} \left\{ \left[\mathcal{F}_{-1/\lambda u} O_0(x_s/M, y_s/M) \right] \right. \\ \left. [F_t(x_2, y_2)] \right\} \quad (4.8)$$

Let the object (an opaque disk) be represented by the one-dimensional planar distribution

$$O_0^{(1)}(\rho_0, z) = \delta(z-z_1) (1 - \text{circ}(\rho_0/a)) \quad (4.9)$$

$$\text{where } \rho_0 = \sqrt{x_0^2 + y_0^2}$$

$$\text{and } \text{circ}(\rho_0/a) = \begin{cases} 1 & \text{for } \rho_0 \leq a \\ 0, & \text{otherwise} \end{cases}$$

In addition, let the amplitude transmittance of the filter be defined by

$$F_t = \text{circ}(\rho_2/\tau) - \text{circ}(\rho_2/\epsilon) \quad (4.10)$$

Substituting the results of (4.9) and (4.10) into (4.8) and expressing the circular symmetry of the image, under illumination the following is obtained

$$O_s(\rho_s, z) = \delta(z-z_1) \mathcal{H}_{1/\lambda u} \left\{ \left[\mathcal{H}_{1/\lambda u} (1 - \text{circ}(\rho_s/|M|a)) \right] \right. \\ \left. [\text{circ}(\rho_2/\tau) - \text{circ}(\rho_2/\epsilon)] \right\}, \quad (4.11)$$

where $\mathcal{H}_{1/\lambda u}$ is the operator defining the Hankel transform.

$\mathcal{H}_{1/\lambda u} (1 - \text{circ}(\rho_s/|M|a))$ is now substituted into (4.11), and it follows that

$$O_s(\rho_s, z) = \delta(z-z_1) \mathcal{H}_{1/\lambda u} \left\{ \lambda u \left[\delta(\rho_2) - |M|a \frac{J_2(2\pi\rho_2|M|a/\lambda u)}{\rho_2} \right] \right. \\ \left. [\text{circ}(\rho_2/\tau) - \text{circ}(\rho_2/\epsilon)] \right\}, \quad (4.12)$$

where $J_1(2\pi\rho_2|M|a/\lambda u)$ is the Bessel function of the first kind and order one. The last equation simply indicates that the Hankel transforms of truncated Bessel functions remain to be evaluated. Hence, by using the definition of the Hankel transform [48], (4.12) yields:

$$O_5(\rho_5, z) = -|M|a\delta(z-z_1) \int_{\epsilon}^{\tau} J_0(2\pi\rho_5\rho_2/\lambda u) J_1(2\pi|M|a\rho_2/\lambda u) d\rho_2, \quad (4.13)$$

where $J_0(2\pi\rho_2\rho_5/\lambda u)$ is the Bessel function of the first kind and order zero. Knowing that $M = -u/f_1$ and neglecting a constant factor, the expression of the field of the focussed filtered image may now be written in the simplified form

$$O_5^{(1)}(\rho_5) = - \int_{\epsilon}^{\tau} J_0(2\pi\rho_5\rho_2/\lambda u) J_1(2\pi a\rho_2/\lambda f_1) d\rho_2. \quad (4.14)$$

Note that the field amplitude of a complementary aperture in an infinite plane would have the same magnitude, but opposite sign.

4.3.2 Evaluation of the Integral

There is no exact solution for (4.14). A numerical evaluation can be made by using polynomial approximations (for small arguments) and/or asymptotic expansions (for large arguments) of the Bessel functions [49].

A computer program permitting numerical calculations of the integral for any values of ϵ , τ and ρ_5 would be extremely intricate. However, since only the expression of the amplitude distribution of the field in the neighbourhood of the contour of the Gaussian image is of interest, it can be assumed that the Bessel functions have arguments with similar orders of magnitude. In addition, keeping in mind the significance of

the parameters in the arguments of the Bessel functions, it is expected that the extremely small value of λ (wavelength) at optical frequencies renders the arguments large enough to permit computation of the integral when the Bessel functions are expressed in terms of their asymptotic expansions.

Use of asymptotic expansions for large arguments. A realistic approach for finding the solution of (4.14) encompasses the above mentioned considerations (i.e. evaluation of the integral in the neighbourhood of the contour of the Gaussian image, and evaluation for only large arguments of the Bessel functions). It will be shown in a subsequent section that this approach is indeed justified.

Poisson's expansion [49] gives

$$J_0(\rho) = (2/\pi\rho)^{1/2} \{ \cos(\rho - \pi/4) [1 - (1^2 \cdot 3^2)/(2!(8\rho)^2) + \dots] \\ + \sin(\rho - \pi/4) [1/8\rho - (1^2 \cdot 3^2 \cdot 5^2)/(3!(8\rho)^3) + \dots] \}, \quad (4.15)$$

while Hansen's expansion [49] gives

$$J_1(\rho) = (2/\pi\rho)^{1/2} \{ \sin(\rho - \pi/4) [1 + (3 \cdot 5 \cdot 1)/(8 \cdot 16\rho^2) - \dots] \\ + \cos(\rho - \pi/4) [3/(8\rho) - (3 \cdot 5 \cdot 7 \cdot 1 \cdot 3)/(8 \cdot 16 \cdot 24\rho^3) + \dots] \}. \quad (4.16)$$

Hence, by keeping the first degree terms and substituting these expressions with their proper arguments into (4.14), the following is obtained

$$O_5^{(1)}(\rho_5) = - \int_{\epsilon}^{\Gamma} [(\lambda u)/(\pi^2 \rho_5 \rho_2)]^{1/2} \{ \cos(-\pi/4 + 2\pi \rho_5 \rho_2 / \lambda u) \\ + (\lambda u / 16\pi \rho_2 \rho_5) \sin(-\pi/4 + 2\pi \rho_5 \rho_2 / \lambda u) \} [(\lambda f_1) / \pi^2 a \rho_2]^{1/2} \\ \{ \sin(-\pi/4 + 2\pi a \rho_2 / \lambda f_1) + (3\lambda f_1 / 16\pi a \rho_2) \cos(-\pi/4 + 2\pi a \rho_2 / \lambda f_1) \} \\ \{ \dots \} d\rho_2, \quad (4.16)$$

which can be rewritten into

$$\begin{aligned}
O_5^{(1)}(\rho_5) = & - \int_{\epsilon}^{\tau} \lambda / (\pi^4 a \rho_5)^{1/2} \{ [\cos(-\pi/4 + 2\pi \rho_5 \rho_2 / \lambda u) \sin(-\pi/4 + 2\pi a \rho_2 / \lambda f_1)] / \rho_2 \\
& + [(3\lambda f_1 / 16\pi a) \cos(-\pi/4 + 2\pi \rho_5 \rho_2 / \lambda u) \cos(-\pi/4 + 2\pi a \rho_2 / \lambda f_1)] / \rho_2^2 \\
& + [(\lambda^2 u / 16\pi \rho_5) \sin(-\pi/4 + 2\pi \rho_5 \rho_2 / \lambda u) \sin(-\pi/4 + 2\pi a \rho_2 / \lambda f_1)] / \rho_2^2 \\
& + [(\lambda^2 u f_1 / (16\pi)^2 a \rho_5) \sin(-\pi/4 + 2\pi \rho_5 \rho_2 / \lambda u) \sin(-\pi/4 + 2\pi a \rho_2 / \lambda f_1)] / \rho_2^3 \\
& + [\dots] \} d\rho_2 \quad (4.17)
\end{aligned}$$

By neglecting the three last terms in the above equation, and by changing the function-products into function-sums, the following is obtained

$$\begin{aligned}
O_5^{(1)}(\rho_5) = & - \int_{\epsilon}^{\tau} \lambda / (\pi^4 a \rho_5)^{1/2} \{ - \cos[2\pi/\lambda (\rho_5/u + a/f_1) \rho_2] \\
& - \sin[2\pi/\lambda (\rho_5/u - a/f_1) \rho_2] \} (2\rho_2)^{-1} d\rho_2 \quad (4.18)
\end{aligned}$$

It is readily seen that the result obtained may now be expressed in terms of sine and cosine integrals, the definitions of which are [50]

$$\text{Si}(\rho) = \int_0^{\rho} [(\sin t)/t] dt = \text{si}(\rho) + \pi/2 \quad (4.19)$$

with

$$\text{si}(\rho) = - \int_{\rho}^{\infty} [(\sin t)/t] dt \quad (4.20)$$

and

$$\text{Ci}(\rho) = - \int_z^{\infty} [(\cos t)/t] dt \quad (4.21)$$

By breaking down the interval of integration and by using the definition of the sine and cosine integrals, (4.18) yields

$$\begin{aligned}
O_5^{(1)}(\rho_5) = & (\lambda/2\pi^2) \{ -\text{Ci}[2\pi a/\lambda f_1 (1-\rho_5/aM)\epsilon] + \text{Ci}[2\pi a/\lambda f_1 (1-\rho_5/aM)\tau] \\
& + \text{Si}[2\pi a/\lambda f_1 (1+\rho_5/aM)\epsilon] - \text{Si}[2\pi a/\lambda f_1 (1+\rho_5/aM)\tau] \} \quad (4.22)
\end{aligned}$$

It is interesting to compare the above result with the one given by Birch [51] in the case of an infinite slit filtered by a slit in the

Fourier transform plane. These two results differ only in that Birch's result has no cosine integral. However, (4.22) was obtained after simplifications had been made, the terms involving powers of λ larger than one being deleted. The expression of the image field would certainly be extremely more complicated if higher powers of λ were taken into account. It is not surprising to notice that for large arguments of the Bessel functions (i.e. $\arg = 2\pi a \rho_2 / \lambda f_1$), the mathematical expression of the field of the filtered image of a disk degenerates into that of a filtered image of a slit. As the radius a of the disk increases and as the value of λ decreases, according to Keller's ray theory of diffraction [52], the effective radius of curvature is increased, and therefore the circular edge looks more and more like a linear one. This increase in effective radius of curvature is followed by a proportional increase in the arguments of the Bessel functions.

Quantitative study. The result given by (4.22) can be easily evaluated numerically. A computer program using the expression of the sine and cosine integrals in terms of auxiliary functions has been successfully written.

The expressions used were [50]

$$\text{Si}(\rho) = \pi/2 - f(\rho) \csc \rho - g(\rho) \sin \rho \quad (4.23)$$

and

$$\text{Ci}(\rho) = f(\rho) \sin \rho - g(\rho) \csc \rho \quad (4.24)$$

The auxiliary functions are defined by

$$f(\rho) = (1/\rho) (\rho^4 + c_1 \rho^2 + c_2) / (\rho^4 + c_3 \rho^2 + c_4) + \epsilon_1(\rho) \quad (4.25)$$

and

$$g(\rho) = (1/\rho^2) (\rho^4 + c_5 \rho^2 + c_6) / (\rho^4 + c_7 \rho^2 + c_8) + \epsilon_2(\rho) \quad , \quad (4.26)$$

$$\text{with} \quad |\epsilon_1(x)| < 2.10^{-4} \quad , \quad |\epsilon_2(x)| < 10^{-4}$$

$$\text{and} \quad \begin{array}{ll} c_1 = 7.241163 & c_5 = 7.547478 \\ c_2 = 2.463936 & c_6 = 1.564072 \\ c_3 = 9.068580 & c_7 = 15.723606 \\ c_4 = 7.157433 & c_8 = 12.723684 \end{array}$$

It must be noted that these auxiliary functions are valid for $1 \leq \rho < \infty$. Therefore for small values of the argument, the sine integral was computed by substituting the power expansions of the sine function into (4.20) and by integrating term by term. Hence, for $\rho < 1$,

$$\begin{aligned} \text{Si}(\rho) \sim & \rho - \rho^3/(3 \cdot 3!) + \rho^5/(5 \cdot 5!) - \rho^7/(7 \cdot 7!) + \dots \\ & + (-1)^n \rho^{(2n+1)} / (2n+1) | (2n+1)! | + \dots \end{aligned} \quad (4.27)$$

Computation has been conducted for a given value of focal length, wavelength, particle size and various values of filter parameters.

Tables 4.1 and 4.2 give a list of numerical values for the amplitude and intensity distributions of the electric field in the image planes which have been obtained with the following parameters: $f_1 = 0.4\text{m}$, $u = 22\text{m}$, $a = 0.5\text{mm}$ and $\lambda = 0.5145\mu\text{m}$ (the wavelength chosen is the one of the strongest line obtained with the argon ion laser used in the experimental investigations). The values attributed to the filter parameters ($\tau = 1.25\text{mm}$, 2.50mm , 5.00mm , 7.50mm , 15.00mm and $\epsilon = 0.50\text{mm}$, 1.25mm) will be used in the qualitative studies of dark-field images (refer to Experiment A3). For these values the Bessel functions have arguments with magnitude ranging from 7.632 to 228.979, on the contour of

Table 4.1 Computation of (4.22): different values of τ and of the ratio ρ_5/aM are considered. The radius of the disk is $a = 0.5\text{mm}$, and ϵ is given the value 0.5mm . The amplitude and intensity distributions of the image field are listed.

$\tau =$	2.5mm		5.0mm		7.5mm		15.0mm		
	ρ_5/aM	$-0_5^{(1)}$	$ 0_5^{(1)} ^2$	$-0_5^{(1)}$	$ 0_5^{(1)} ^2$	$-0_5^{(1)}$	$ 0_5^{(1)} ^2$	$-0_5^{(1)}$	$ 0_5^{(1)} ^2$
0.67000		77.476	6002.555	91.844	8435.336				
0.67500		85.290	7274.445	96.334	9280.297	85.135	7247.895	80.752	6520.583
0.68000		93.324	8709.383	99.016	9804.215	84.121	7076.395	87.297	7620.707
0.68500		101.411	10284.210	99.844	9968.734	82.696	6838.668	89.734	8052.117
0.69000		109.373	11962.510	99.034	9807.650	82.339	6779.738	88.677	7863.574
0.69500		117.024	13694.550	97.055	9419.617	84.291	7104.977	89.056	7931.027
0.90000		124.173	15418.830	94.578	8945.035	89.139	7945.727	94.449	8920.617
0.90500		130.631	17064.420	92.401	8537.922	96.577	9327.098	102.591	10524.970
0.91000		136.216	18554.810	91.344	8343.766	105.431	11115.750	107.627	11583.550
0.91500		140.756	19912.330	92.144	8400.465	113.960	12986.760	106.948	11437.760
0.92000		144.094	20763.210	95.340	9099.727	120.356	14485.330	104.722	10966.670
0.92500		146.092	21342.820	101.188	10238.960	123.317	15206.970	107.479	11551.670
0.93000	→	146.631	21500.660	109.592	12010.350	122.515	15009.990	116.311	13528.260
0.93500		145.617	21204.300	120.083	14419.950	118.807	14115.170	124.865	15591.160
0.94000		142.979	20443.000	131.836	17380.830	114.103	13019.470	126.258	15940.980
0.94500		138.669	19229.110	143.731	20658.710	110.896	12298.020	121.580	14781.630
0.95000		132.662	17599.200	154.451	23855.100	111.563	12446.240	119.740	14337.660
0.95500		124.954	15613.430	162.607	26441.150	117.597	13829.030	127.576	15275.600
0.96000		115.501	13354.360	166.876	27847.760	129.008	16642.980	140.847	19837.900
0.96500		104.519	10924.230	166.123	27596.870	144.048	20749.940	147.366	21716.720
0.97000		91.869	8439.926	159.496	25438.820	159.391	25405.520	140.739	19807.340
0.97500		77.909	6069.813	146.467	21452.530	170.733	29149.770	130.076	16919.690
0.98000		63.761	4065.458	126.830	16085.940	173.687	30167.120	132.849	17644.750
0.98500		48.883	2389.534	100.663	10132.990	164.691	27123.050	155.103	24056.910
0.99000		33.496	1121.964	69.991	4898.684	141.599	20050.150	178.605	31899.560
0.99500		17.830	317.913	33.546	1125.321	103.775	10769.170	170.527	29079.540
0.99500		15.257	264.304	36.955	1365.687	55.707	3103.294	107.515	11559.540
0.99500		14.684	215.631	33.546	1125.321	50.585	2558.874	97.920	9589.355
0.99650		13.112	171.913	30.124	907.445	45.414	2062.433	88.287	7794.637
0.99700		11.539	133.143	26.692	712.457	40.200	1616.072	78.477	6158.684
0.99750		9.967	99.332	23.251	540.607	34.949	1221.441	68.344	4670.934
0.99800		8.395	70.480	19.803	392.174	29.667	880.124	57.932	3356.089
0.99850		6.825	46.576	16.351	257.366	24.360	593.425	47.286	2235.955
0.99900		5.256	27.621	12.896	166.302	19.034	362.303	36.451	1328.645
0.99950		3.688	13.600	9.440	89.105	13.696	187.585	25.477	649.055
1.00000		2.122	4.501	5.984	35.803	8.351	69.737	14.410	207.659
1.00050		0.557	0.312	2.530	6.401	3.005	9.031	3.303	10.911
1.00100		-1.003	1.006	-0.917	0.841	-2.331	5.436	-7.788	60.657
				-4.358	18.994	-7.656	58.617	-18.820	354.209

Table 4.1 Continued

τ =		2.5mm		5.0mm		7.5mm		15.0mm	
ρ_5/aM		$-O_5^{(1)}$	$ O_5^{(1)} ^2$	$-O_5^{(1)}$	$ O_5^{(1)} ^2$	$-O_5^{(1)}$	$ O_5^{(1)} ^2$	$-O_5^{(1)}$	$ O_5^{(1)} ^2$
0.99900		5.256	27.621	9.440	89.105	13.696	187.585	25.477	649.255
0.99950		3.688	13.600	5.984	35.803	8.351	69.737	14.410	207.550
1.00000		2.122	4.501	2.530	6.401	3.005	9.031	3.303	10.911
1.00050		0.558	0.312	-0.917	0.841	-2.331	5.436	-7.788	60.657
1.00100		-1.003	1.006	-4.358	18.994	-7.656	58.617	-18.820	354.209
1.00150		-2.552	6.563	-7.791	60.702	-12.963	168.035	-29.744	884.694
1.00200		-4.121	16.982	-11.221	125.909	-18.255	333.259	-40.530	1642.688
1.00250		-5.674	32.197	-14.633	214.112	-23.508	552.611	-51.091	2610.247
1.00300		-7.225	52.194	-18.031	325.109	-28.724	825.057	-61.400	3759.972
1.00350		-8.774	76.992	-21.420	458.829	-33.908	1149.733	-71.434	5102.773
1.00400		-10.318	106.460	-24.785	614.365	-39.034	1523.640	-81.112	6579.986
1.00450		-11.859	140.604	-28.134	791.512	-44.106	1945.368	-90.595	8207.512
1.00500		-13.393	179.384	-31.461	989.783	-49.129	2412.736	-100.027	10005.430
1.00550		-13.393	179.384	-31.467	990.180	-49.129	2413.670	-100.045	10008.000
1.00600		-10.492	811.803	-53.259	4001.740	-95.600	9139.387	-161.088	25949.490
1.01500		-42.954	1845.085	-92.004	8464.785	-131.176	17207.210	-167.404	28023.990
1.02000		-56.579	3201.150	-115.772	13403.160	-151.897	23072.670	-142.924	20427.160
1.02500		-69.183	4786.348	-132.839	17646.070	-158.847	25232.460	-120.054	14413.040
1.03000		-81.315	6612.195	-143.385	20550.510	-154.484	23865.410	-116.251	13514.220
1.03500		-91.951	8454.918	-147.865	21864.140	-142.468	20297.010	-125.319	15704.750
1.04000		-100.868	10174.290	-146.973	21600.920	-127.052	16142.190	-130.434	17012.960
1.04500		-104.391	11683.650	-141.670	20070.360	-112.230	12595.670	-123.121	15158.750
1.05000		-113.549	12916.130	-133.114	17719.420	-100.952	10191.270	-109.629	12018.500
1.05500		-117.591	13927.550	-122.561	15021.070	-94.634	8955.594	-101.393	10280.540
1.06000		-119.977	14394.540	-111.256	12377.940	-93.108	8669.188	-102.213	10447.390
1.06500		-120.898	14613.910	-100.324	10064.920	-94.931	9011.824	-105.638	11159.460
1.07000		-120.412	14500.480	-90.667	8220.516	-97.971	9598.258	-103.514	10715.140
1.07500		-119.677	14094.170	-82.902	6872.684	-99.744	9948.934	-94.966	9018.559
1.08000		-115.789	13407.160	-77.329	5979.730	-96.307	9275.039	-86.298	7447.410
1.08500		-111.893	12529.010	-73.939	5466.977	-90.156	8128.074	-83.181	6919.086
1.09000		-107.136	11478.050	-72.454	5249.531	-82.425	6793.893	-84.543	7147.535
1.09500		-101.671	10337.030	-72.389	5240.234	-74.602	5565.453	-84.559	7150.289
1.10000		-95.659	9150.602	-73.143	5349.953	-74.020	5565.453	-79.606	6337.086
1.10500		-89.258	7967.035	-74.080	5487.848	-68.055	4631.430	-72.030	5184.266
1.11000		-82.625	6826.965	-74.615	5567.457	-63.647	4050.978	-66.928	4479.371
1.11500		-75.910	5767.316	-74.287	5518.516	-61.540	3787.118	-66.207	4381.367
1.12000		-69.251	4795.734	-72.799	5299.734	-61.208	3746.450	-66.757	4456.473
1.12500		-62.776	3940.820	-70.049	4926.883	-61.666	3802.667	-64.385	4145.484
1.13000		-56.597	3203.182	-66.120	4371.836	-61.795	3818.582	-58.612	3435.397
1.13500		-50.644	2564.854	-61.091	3732.129	-60.530	3663.906	-52.731	2780.560
1.14000		-45.138	2037.479	-55.462	3076.002	-57.575	3314.891	-50.074	2507.392
1.14500		-40.176	1614.075	-49.685	2468.619	-53.088	2812.384	-50.040	2504.018

Table 4.2 Computation of (4.22): different values of τ and of the ratio ρ_5/aM are considered. The radius of the disk is $a = 0.5\text{mm}$, and ϵ is given the value 1.25mm . The amplitude and intensity distributions of the image field are listed.

ρ_5/aM	$\tau = 2.5\text{mm}$		$\tau = 5.0\text{mm}$		$\tau = 7.5\text{mm}$		$\tau = 15.0\text{mm}$	
	$-O_5^{(1)}$	$ O_5^{(1)} ^2$	$-O_5^{(1)}$	$ O_5^{(1)} ^2$	$-O_5^{(1)}$	$ O_5^{(1)} ^2$	$-O_5^{(1)}$	$ O_5^{(1)} ^2$
0.87000	-30.039	902.350	-15.671	245.588	-22.381	500.898	-26.763	716.276
0.87500	-22.613	511.363	-11.569	133.851	-23.782	565.602	-20.607	424.650
0.88000	-14.535	211.256	-8.843	78.190	-25.162	633.150	-18.125	328.521
0.88500	-5.966	35.583	-7.533	56.749	-25.038	626.878	-18.700	349.686
0.89000	2.918	8.514	-7.422	55.082	-22.164	491.258	-17.399	302.727
0.89500	11.930	142.318	-8.039	64.633	-15.955	254.572	-10.645	113.319
0.90000	20.879	435.924	-8.716	75.963	-6.717	45.118	-0.703	0.494
0.90500	29.574	874.637	-8.666	74.924	4.375	19.137	6.570	43.167
0.91000	37.830	1431.078	-7.042	49.595	15.573	242.519	8.561	73.289
0.91500	45.468	2067.339	-3.145	9.889	25.067	628.335	9.433	88.990
0.92000	52.326	2737.975	3.571	12.753	31.548	995.258	15.710	246.797
0.92500	58.257	3393.841	13.352	178.287	34.680	1202.707	28.476	810.876
0.93000	63.135	3986.023	26.096	680.980	35.311	1246.882	41.369	1711.353
0.93500	67.858	4469.945	41.124	1707.654	35.343	1249.161	47.498	2256.074
0.94000	69.349	4800.238	58.206	3387.939	37.266	1388.746	47.949	2299.142
0.94500	70.563	4979.180	75.626	5719.227	43.457	1888.498	51.634	2666.086
0.95000	70.165	4923.074	91.954	8455.477	55.100	3035.962	65.078	4235.207
0.95500	67.380	4621.260	105.633	11158.380	72.034	5188.852	83.873	7034.684
0.96000	64.303	4134.879	115.618	13357.550	92.790	8610.043	96.108	9236.723
0.96500	59.142	3497.767	120.746	14579.510	114.014	12999.130	95.361	9093.905
0.97000	52.505	2757.178	120.135	14432.460	131.373	17258.790	90.716	8227.728
0.97500	44.673	1995.655	113.231	12821.160	140.451	19726.380	99.613	9922.556
0.98000	36.726	1348.799	99.796	9959.160	137.656	18949.120	128.069	16401.400
0.98500	28.057	789.434	79.877	6380.313	120.813	14595.680	157.818	24906.640
0.99000	18.677	360.112	55.471	3077.045	89.256	7966.559	156.008	24338.530
0.99500	9.566	91.514	28.691	823.196	47.443	2250.876	99.252	9850.995
0.99550	8.617	74.258	25.006	671.104	42.945	1844.291	90.280	8150.480
0.99600	7.668	58.792	23.107	533.935	38.397	1474.347	81.270	6604.897
0.99650	6.718	45.125	20.298	412.003	33.806	1142.869	72.083	5195.992
0.99700	5.767	33.260	17.479	305.529	29.178	851.329	62.573	3915.338
0.99750	4.817	23.201	14.654	214.730	24.517	601.091	52.782	2785.942
0.99800	3.867	14.951	11.823	139.778	19.832	393.298	42.757	1828.189
0.99850	2.917	8.508	8.988	80.785	15.127	228.812	32.543	1059.035
0.99900	1.968	3.872	6.152	37.845	10.408	108.335	22.189	492.343
0.99950	1.019	1.039	3.315	10.991	5.683	32.292	11.742	137.876
1.00000	0.072	0.005	0.481	0.231	0.956	0.914	1.254	1.572
1.00050	-0.873	0.763	-2.349	5.517	-3.763	14.161	-9.220	85.007
1.00100	-1.818	3.304	-5.173	26.758	-8.471	71.755	-19.635	385.538

Table 4.2 Continued

$\rho_5 / \mu\text{M}$	2.5mm		5.0mm		7.5mm		15.0mm	
	$-0_5^{(1)}$	$ 0_5^{(1)} ^2$	$-0_5^{(1)}$	$ 0_5^{(1)} ^2$	$-0_5^{(1)}$	$ 0_5^{(1)} ^2$	$-0_5^{(1)}$	$ 0_5^{(1)} ^2$
0.99900	1.998	3.872	6.152	37.845	10.408	108.335	22.190	492.343
0.99950	1.919	1.039	3.315	10.991	5.583	32.292	11.742	137.876
1.00000	0.072	0.005	0.481	0.231	0.956	0.914	1.254	1.572
1.00050	-0.273	0.763	-2.349	5.517	-3.763	14.161	-9.220	85.007
1.00100	-1.818	3.304	-5.173	26.758	-8.471	71.755	-19.635	385.538
1.00150	-2.750	7.619	-7.990	63.833	-13.161	173.218	-29.942	896.535
1.00200	-3.703	13.710	-10.803	116.698	-17.837	318.164	-40.112	1608.958
1.00250	-4.641	21.542	-13.600	184.949	-22.475	505.114	-50.058	2505.765
1.00300	-5.578	31.112	-16.384	268.435	-27.077	733.164	-59.753	3570.458
1.00350	-6.514	42.425	-19.159	367.081	-31.647	1001.518	-69.173	4784.871
1.00400	-7.448	55.427	-21.913	480.196	-36.161	1307.603	-78.239	6121.270
1.00450	-8.373	70.115	-24.650	607.603	-40.622	1650.157	-87.111	7588.352
1.00500	-9.299	86.471	-27.366	748.919	-45.025	2027.258	-95.933	9203.117
1.00550	-9.301	86.504	-27.372	749.202	-45.034	2028.020	-95.949	9206.234
1.01000	-19.350	336.729	-53.117	2821.452	-85.458	7303.102	-150.947	22784.840
1.01500	-26.590	723.052	-75.939	5766.797	-115.112	13250.560	-151.339	22903.470
1.02000	-34.742	1207.002	-93.935	8823.359	-130.050	16915.650	-121.087	14662.000
1.02500	-41.751	1743.118	-105.406	1110.380	-131.415	17269.790	-92.622	8576.789
1.03000	-48.486	2350.931	-110.560	1223.600	-121.655	14800.020	-83.422	6959.191
1.03500	-53.949	2910.350	-109.862	12069.720	-104.465	10912.850	-87.316	7624.027
1.04000	-57.934	3356.360	-104.039	10824.070	-84.118	7075.883	-87.500	7656.258
1.04500	-60.480	3658.932	-94.068	8848.801	-64.629	4176.875	-75.519	5703.121
1.05000	-61.660	3801.952	-81.125	6581.316	-48.963	2397.357	-57.640	3322.359
1.05500	-61.236	3749.893	-66.206	4383.258	-38.290	1465.340	-45.039	2028.496
1.06000	-59.430	3531.882	-50.709	2571.352	-32.561	1060.202	-41.665	1735.965
1.06500	-56.587	3202.108	-36.023	1297.673	-30.630	938.179	-41.338	1708.790
1.07000	-52.787	2756.492	-23.036	530.667	-30.340	920.517	-35.883	1287.613
1.07500	-48.131	2316.610	-12.356	152.667	-29.548	873.055	-24.420	596.355
1.08000	-42.737	1826.452	-4.276	18.286	-26.692	712.464	-13.246	175.453
1.08500	-36.730	1349.531	1.218	1.484	-21.150	447.325	-8.024	64.384
1.09000	-30.270	916.262	4.412	19.469	-13.200	176.619	-7.677	52.938
1.09500	-23.483	551.467	5.798	33.623	-4.237	17.953	-6.371	40.595
1.10000	-16.528	273.169	5.988	35.852	4.529	20.513	-0.475	0.225
1.10500	-9.557	91.255	5.625	31.646	11.651	135.743	7.676	58.919
1.11000	-2.704	7.310	5.306	28.157	16.274	264.855	12.094	168.833
1.11500	3.981	15.266	5.505	30.302	18.252	333.130	13.584	184.536
1.12000	10.076	101.524	6.528	42.613	18.119	328.294	12.570	158.013
1.12500	15.766	248.574	8.493	72.132	16.876	284.813	14.157	200.414
1.13000	20.854	434.905	11.331	128.396	15.656	245.123	18.839	354.901
1.13500	25.263	636.233	14.817	210.529	15.377	236.466	23.177	537.157
1.14000	29.032	847.072	18.609	346.293	16.496	272.103	23.997	575.045
1.14500	31.822	1012.731	22.312	497.835	18.009	357.548	21.947	482.561

the Gaussian image, and therefore the considerations of Section 4.3.2 are justified.

By using the computed values in Tables 4.1 and 4.2, typical theoretical curves of the amplitude and intensity distributions of the electric field in the image plane can be plotted. Figs. 4.2, 4.4 and 4.3, 4.5 are obtained and the dip corresponding to the dark fringe located on the contour of the Gaussian image is clearly visible. It is most interesting to compare the width of this dip with the thickness of the dark fringe existing on the profile of the Gaussian images, shown in Figs. 5.6 and 5.7.

The results reported in Tables 4.1 and 4.2, along with other results gathered from further numerical computation (giving values to the filter parameters which cannot be attributed to the experimental filters) lead to the following conclusions:

- (i) The amplitude distribution of the field changes its sign on the Gaussian image. As a result, the image intensity is zero on the contour of the image. The observation of this dark fringe was reported for the first time by Lansraux [46]. Later the theory was published by Birch in the case of one-dimensional objects [51,53], and in Section 4.2.1 it has been shown that dark fringes appear at the location of the discontinuities.
- (ii) The dark fringe becomes narrower as the values of τ and a increase.
- (iii) The value of ϵ has only a small influence on the width of the dark fringe. However, an increase in the value of ϵ leads to an increase in the number of concentric rings. This phenomenon is a result of the fact that the influence of the low spatial frequency components becomes

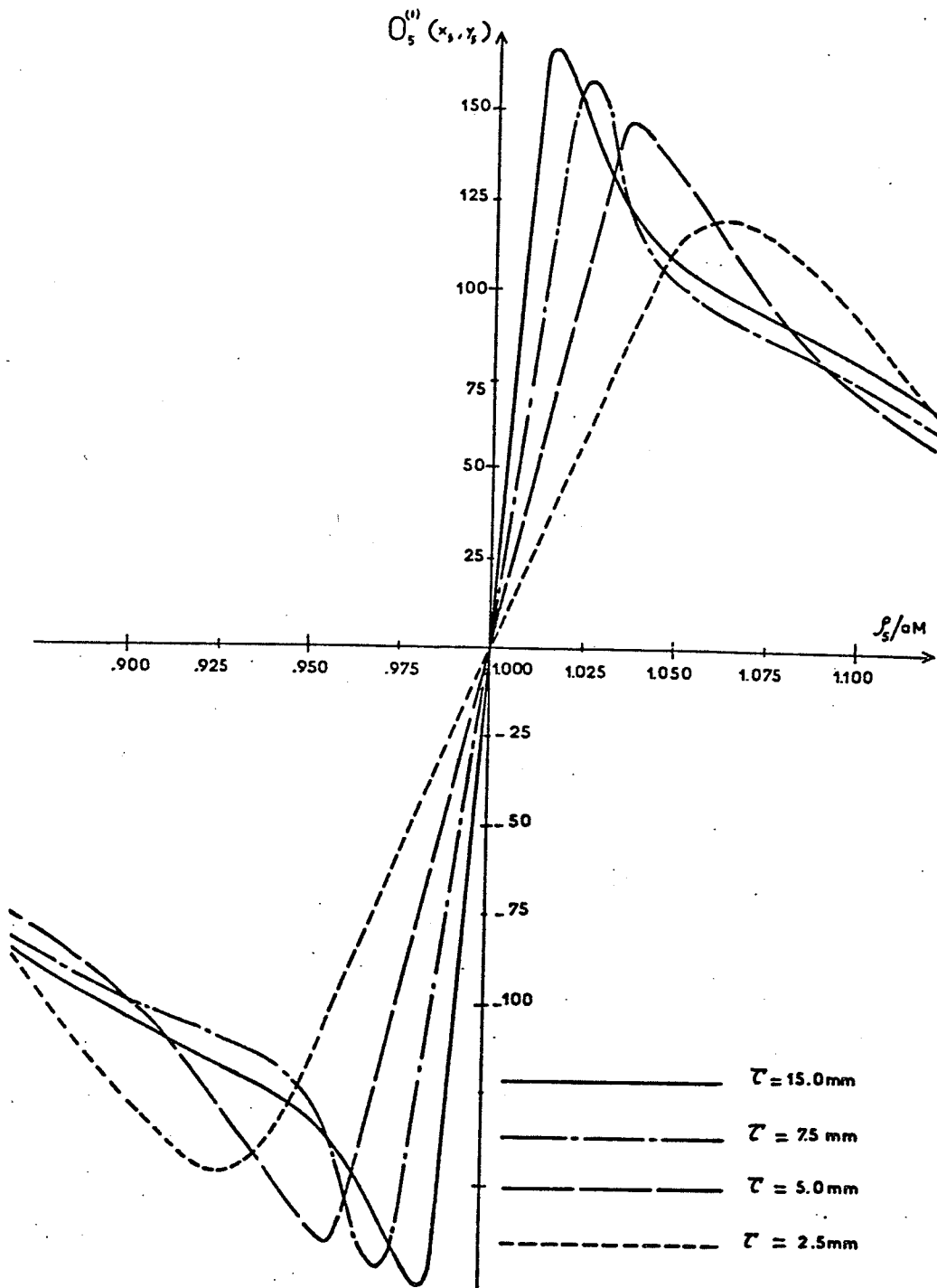


Fig. 4.2 Amplitude distribution of the image field. The computed values are given in Table 4.1. The change of sign of the amplitude distribution at the contour of the Gaussian image of the disk clearly proves the existence of a dark fringe for $\rho_5 = aM$.

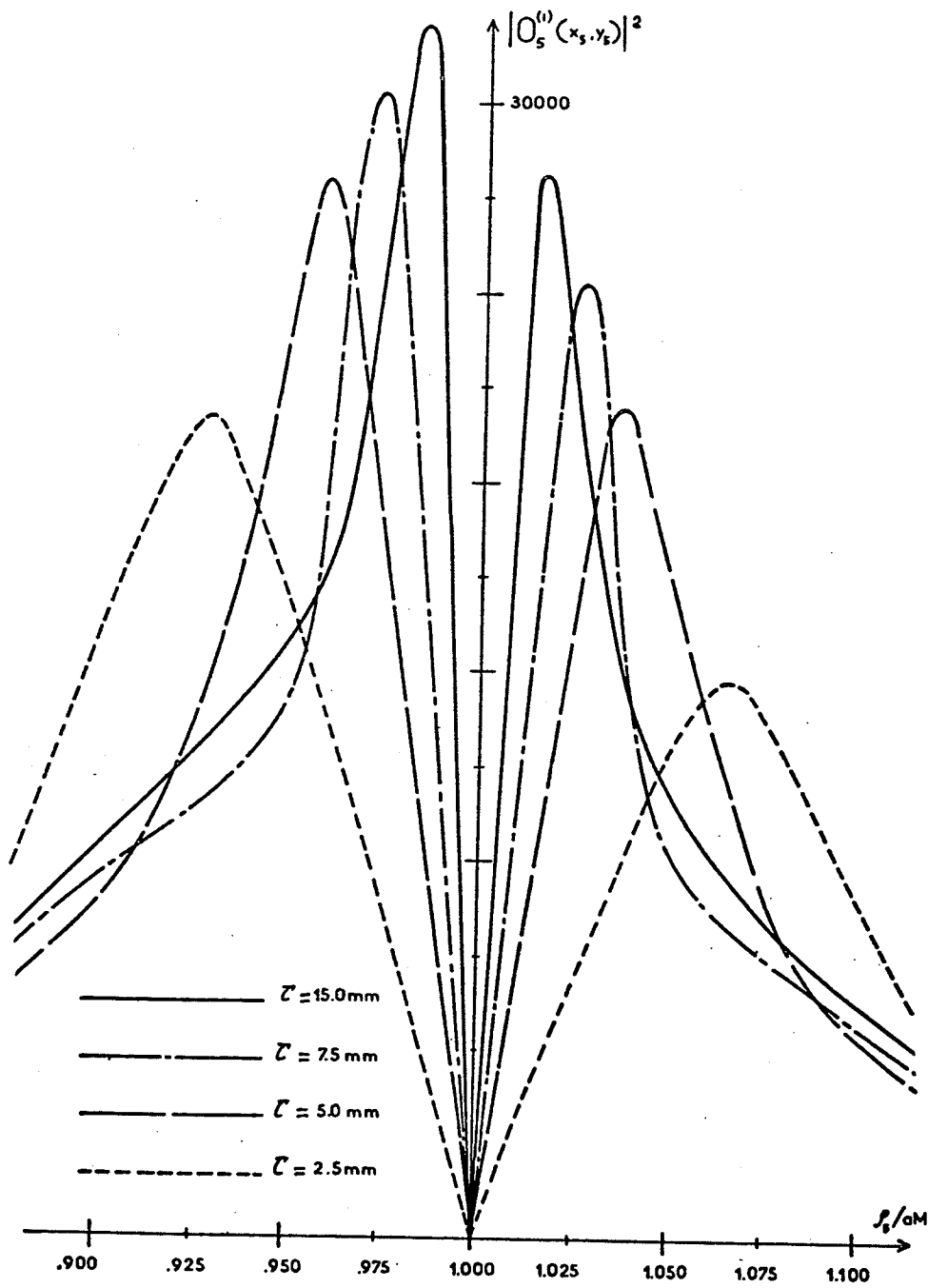


Fig. 4.3 Intensity distribution of the image field. The computed values are given in Table 4.1. Note the slight dissymmetry of the curves caused by mutual interference of rays diffracted by the edge of the disk. The width and depth of the dip centered at $\rho_s = aM$ is a function of the parameter τ .

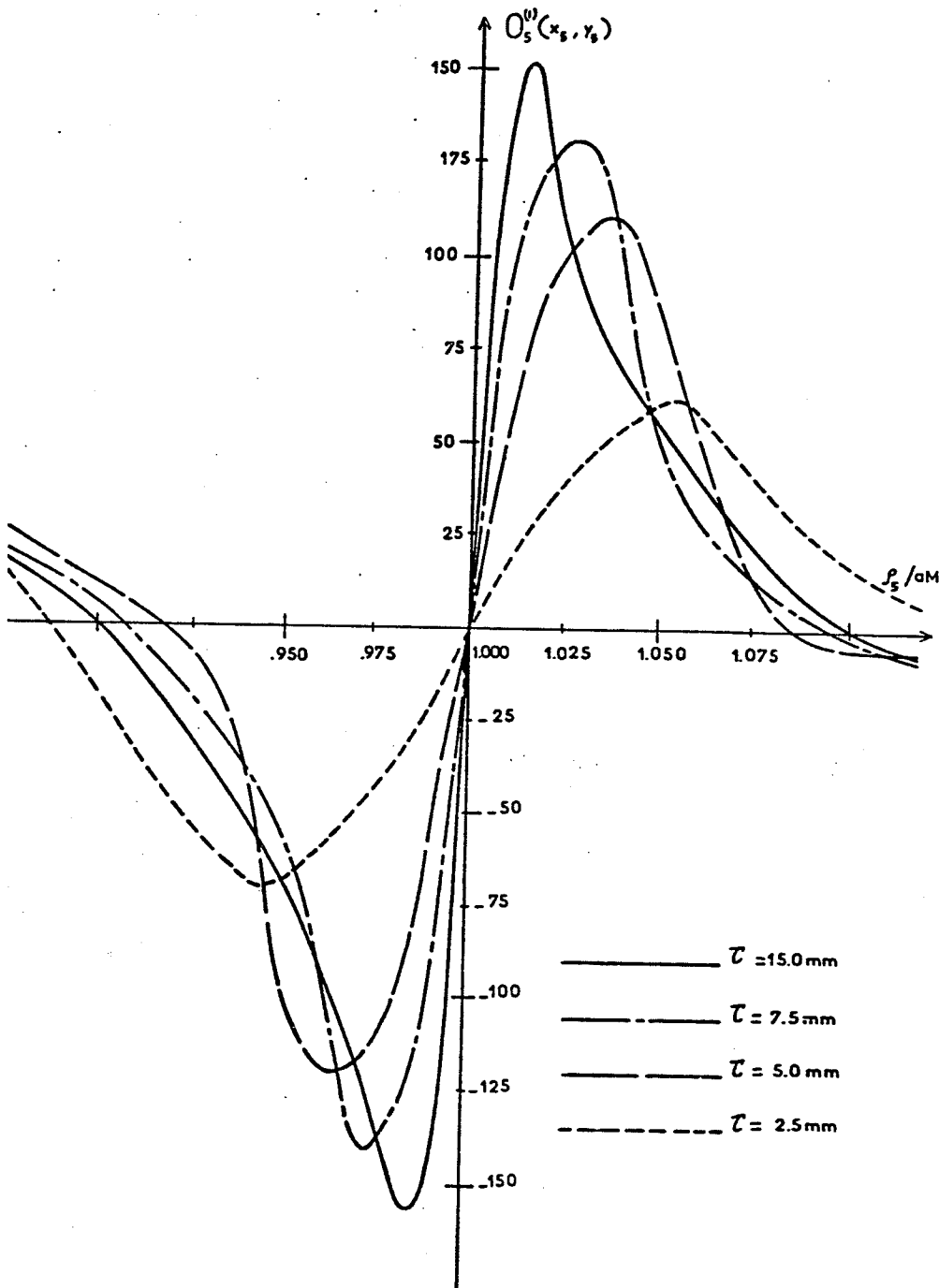


Fig. 4.4 Amplitude distribution of the image field. The computed values are given in Table 4.2. By comparing these curves with those of Fig. 4.2, it is seen that more circular fringes appear around the contour of the Gaussian image as ϵ becomes larger.

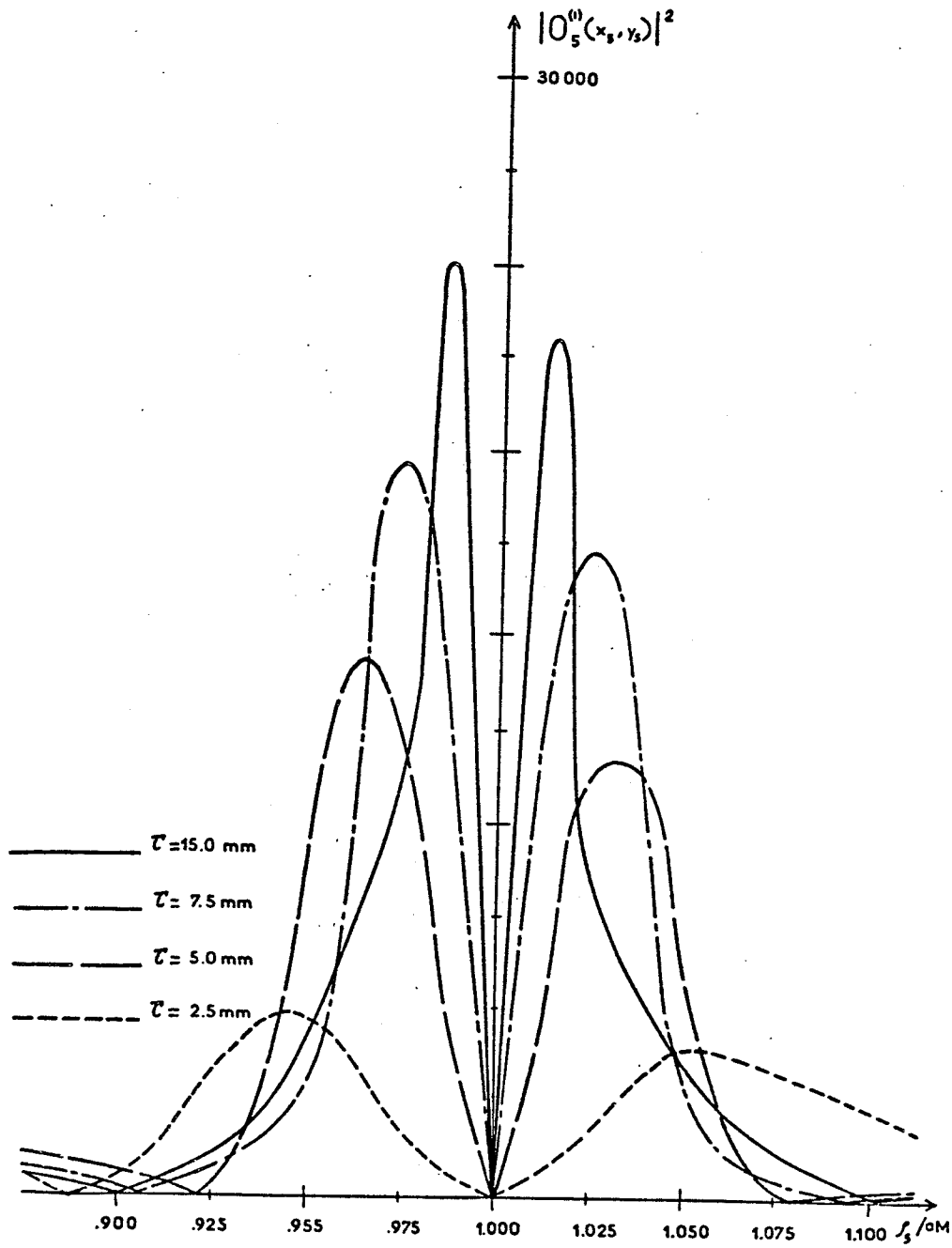


Fig. 4.5 Intensity distribution of the image field. The computed values are given in Table 4.2. By comparing these curves with those of Fig. 4.3, it is seen that ϵ has some influence on the width and depth of the dip centered at $\rho_s = aM$.

weaker as the value of ϵ increases, and thus mutual interference between the rays diffracted by the edge of the disk becomes more predominant.

4.3.3 Exact Value of the Field on the Profile of the Gaussian Image

It has been shown in the last section that, according to the numerical simulation, the sign of the field amplitude in the image plane changes as the value of ρ_5 approaches the value of Ma . In other words, a dark fringe appears on the contour defined in Gaussian optics. However, the numerical simulation only represents an approximated expression of the field amplitude.

A rigorous expression of the field amplitude on the exact profile of the Gaussian image is obtained by substituting the value $\rho_5 = -aM$ into (4.14). Hence

$$O_5^{(1)}(-aM) = - \int_z^T J_0(2\pi a \rho_2 / \lambda f_1) J_1(2\pi a \rho_2 / \lambda f_1) d\rho_2 \quad (4.28)$$

It must be noted that the arguments of the Bessel functions are identical.

Thus a change in variable gives

$$O_5^{(1)}(-aM) = - (\lambda f_1 / 2\pi a) \int_{2\pi a \epsilon / \lambda f_1}^{2\pi a T / \lambda f_1} J_0(t) J_1(t) dt \quad (4.29)$$

Substituting the well known relation $J_1(t) = -J_0'(t)$ into the last equation gives

$$O_5^{(1)}(-aM) = (\lambda f_1 / 2\pi a) \int_{2\pi a \epsilon / \lambda f_1}^{2\pi a T / \lambda f_1} J_0(t) dJ_0(t) \quad (4.30)$$

and integration of the above integral with respect to the variable t yields

$$O_s^{(1)}(-aM) = (\lambda f_1 / 4\pi a) \{ [J_0(2\pi a \tau / \lambda f_1)]^2 - [J_0(2\pi a \epsilon / \lambda f_1)]^2 \} . \quad (4.31)$$

This result is of utmost significance, since it shows that the field amplitude is in general not nil on the exact contour of the Gaussian image. However, it is seen that: firstly, for large values of the argument, the magnitude of the Bessel function of first kind of order zero becomes negligible; secondly, for the roots of (4.31) the dark fringe is exactly located on the boundary. It is, therefore, possible to study the exact microscopic profile of a circular disk (or circular aperture in an infinite plane) of known radius, since the values of τ , ϵ , λ and f_1 may be specifically chosen to give a zero value to the RHS of (4.31). An obvious set of values can be found from the knowledge of the set of arguments, which are zeros of the Bessel function of first kind of order zero.

The physical interpretation of the first result is immediate and can be expressed as follows: when the arguments are very large, the first result means that from a ray theory point of view the effective radius of curvature is very large and thus the result becomes comparable to the result obtained by imaging an infinite slit having the two edges very far apart from each other (this has been discussed previously in Section 4.3.2). Since the two edges are far apart, the mutual interference becomes negligible and the dark-fringe is exactly located on the Gaussian image contour. Birch has proved that in the case of an infinite half plane the dark fringe is rigorously centered on the Gaussian profile of the image [51]. Birch's result confirms the validity of the interpretation given.

4.4 IMPULSE RESPONSE

By using the common expression for the image field (refer to (3.35)), the impulse response, also called the point spread function, is readily obtained

$$H(x_5, y_5, z) = \sum_{n=1}^N \delta(z-z_n) \mathcal{F}_{1/\lambda u} F_t(x_2, y_2) \quad (4.32)$$

In the case of dark-field filtering, with filters of circular symmetry, the Fourier transform may be expressed in terms of its analogous Hankel transform [48]. Therefore (4.28) yields

$$H(\rho_5, z) = \sum_{n=1}^N \delta(z-z_n) \mathcal{H}_{1/\lambda u} F_t(\rho_2) \quad (4.33)$$

Substitution of the expression of $F_t(\rho_2)$ into the above equation gives

$$H(\rho_5, z) = \sum_{n=1}^N \delta(z-z_n) \left\{ \tau^2 \frac{[J_1(2\pi\tau\rho_5/\lambda u)]}{[2\pi\tau\rho_5/\lambda u]} - \varepsilon^2 \frac{[J_1(2\pi\varepsilon\rho_5/\lambda u)]}{[2\pi\varepsilon\rho_5/\lambda u]} \right\} \quad (4.34)$$

4.4 SUMMARY

The remarkable properties of the reconstructed filtered images have been analytically studied. It has been proved that:

- (i) With a dark-field filter, there exists a dark fringe which is located on the contours of the Gaussian images of disks and one-dimensional gratings having a square wave amplitude transmittance.
- (ii) Amplitude and phase objects (when the variation in phase is small) have identical dark-field images.
- (iii) Dark-field images permit accurate retrieval of the depth dimension.
- (iv) If the radius of a disk is known, it is possible to cancel out the

effect of mutual interference of a ray diffracted by one point of the contour with a ray diffracted by another point.

All these results are based on the assumption that the holographic process and the optical elements are perfect (i.e., they introduce no aberrations and there is no vignetting effect).

*Chapter Five*EXPERIMENTAL STUDIES OF THE METHOD5.1 INTRODUCTION

The experimental studies presented in this chapter allow verification of the properties of reconstructed dark-field images which have been obtained from the mathematical analysis of Chapter Four. The studies will be conducted with well defined objects (such as circular apertures of different radii) and also with more general objects (such as a transparency, amplitude and phase test targets, two clock wheels and an architectural structure).

It is also the object of this chapter to study the feasibility of the method when particle measurements are considered. In particular, a comparative study of the properties of dark-field and bright-field reconstructed images will be presented. This comparative study has great significance, since future development of this novel method will depend heavily on its ability to overcome the shortcomings of the other methods of holography (those which use local reference beam generation, and those which use conventional configurations).

Important remarks:

- (i) All the photographs of real images and reconstructed real images are direct contact prints of the negatives.
- (ii) The wavelength of the readout wave is the same as that of the recording wave. An argon-ion laser ($\lambda = .5145 \cdot 10^{-6} \text{m}$) is used in all the experiments reported in the thesis.

These two remarks emphasize the fact that the large magnification is obtained at the recording stage only.

(iii) When holograms are recorded, the filtered aerial image is formed behind the recording plane. Therefore real images are reconstructed upon illumination of the processed hologram by a duplicate of the reference wave. The recording of the reconstructed filtered images is done by placing a photographic film in the plane of interest.

5.2 QUALITATIVE STUDY OF DARK-FIELD IMAGES OF CIRCULAR APERTURES

5.2.1 Introduction

The aim of this study is to substantiate the theoretical quantitative analysis given in Section 4.3. The experimental work is conducted with circular apertures instead of a disk, yet, as it was pointed out in Section 4.3.1, the field amplitude of a circular aperture differs from that of the complementary disk only by its sign. Assuming that the illuminating wave is a plane wave of uniform profile, the above result can be easily determined by using either (4.11) or by using the superposition principle which is expressed as follows

$$U'_5(x_5, y_5) + U''_5(x_5, y_5) = U_5(x_5, y_5) \quad (5.1)$$

$U'_5(x_5, y_5)$ and $U''_5(x_5, y_5)$ denote respectively the values of the field when either the disk or its complementary aperture is placed in the object plane, and $U_5(x_5, y_5)$ is the value of the field when no screen is present in the object plane. Here the illuminating beam is a plane wave with uniform profile, and therefore the dark-field filter blocks the central ordinate. Hence, $U_5(x_5, y_5) = 0$ and

$$U_5^i(x_5, y_5) = -U_5^u(x_5, y_5) \quad (5.2)$$

Since photographic films are square-law detectors, the difference in sign does not affect the irradiance distribution in the image plane and, as a result, the visual aspect of the filtered images of a disk is identical to that of the complementary aperture.

A circular aperture is preferred to a disk for the following reasons:

i) pinholes of well known radii are readily available ii) it is practically impossible to hold a disk without changing the object content and iii) the illumination of a circular aperture only requires a collimated beam of reduced diameter, and thus the lens aperture is only determined according to the spatial frequency response which is needed for proper imaging.

The expression of the electromagnetic field of the reconstructed filtered image is identical to that of the filtered aerial image, since the holographic process has been assumed to be perfect. Therefore, the properties of the dark-field images can be directly studied from the dark-field aerial image generated by a conventional optical processor.

The optical processor used in the experiments is shown in Fig. 5.1. The object plane 0 is imaged onto the observation plane I by means of the lens L_1 of focal length f_1 . Filtering is performed by means of the dark-field spatial filter SF which is located in the back focal plane of L_1 . It is necessary to have a large magnification factor in order to be able to observe the very fine dark fringe which is located on the contour of the Gaussian image. Thus a transverse magnification

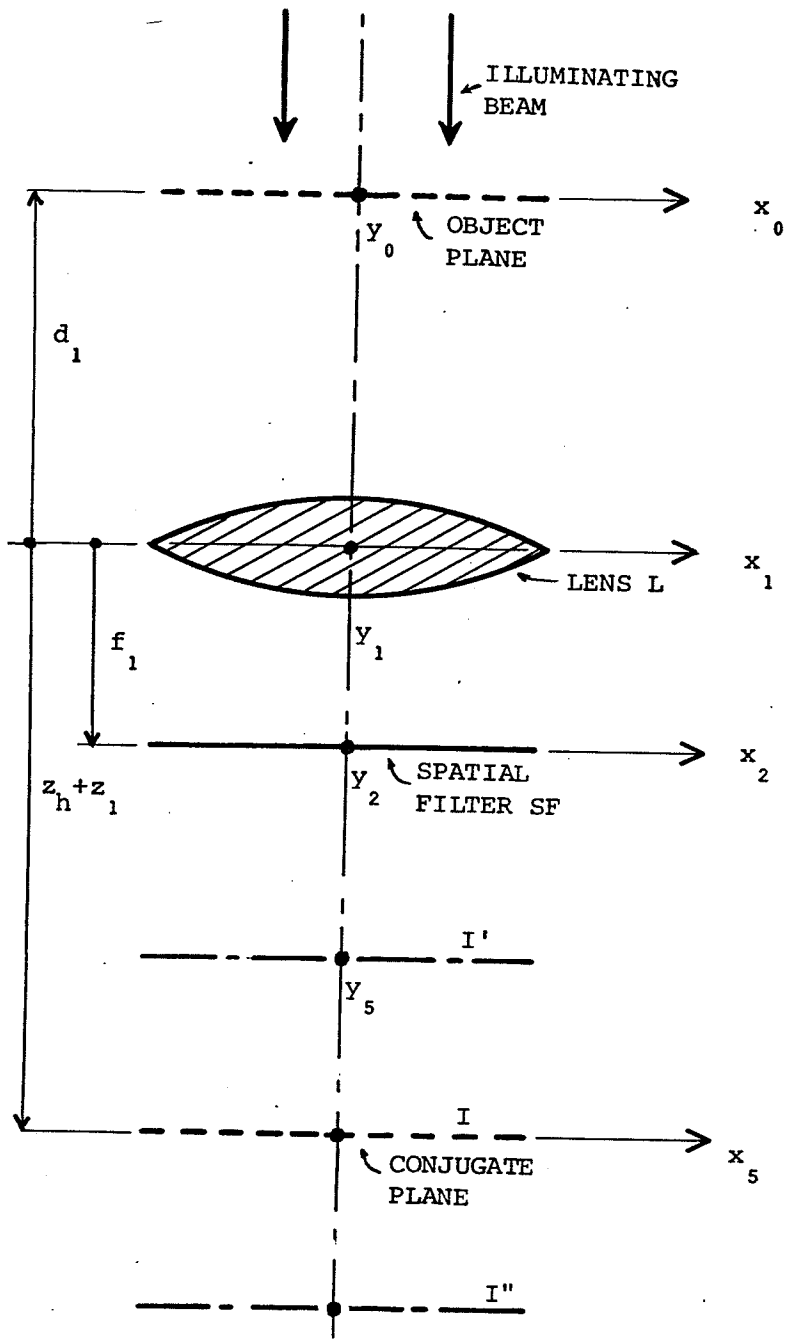


Fig. 5.1 Optical processor allowing photographic recording of a filtered image.

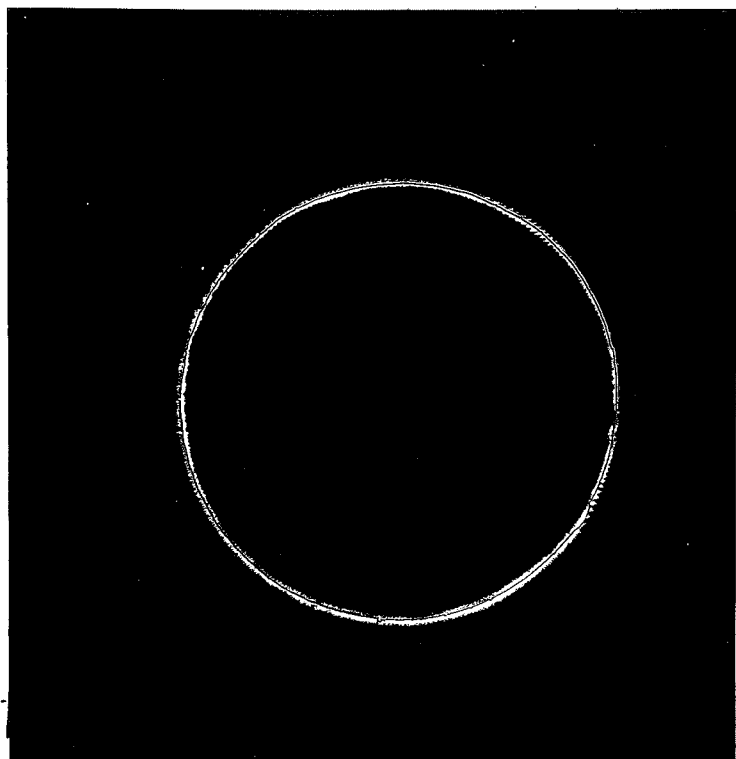
factor $M'' = -55$ is chosen. With a focal length $f_1 = 0.4\text{m}$, this magnification is achieved when the object plane is positioned slightly in front of the front focal plane of the lens at a distance $d_1 = 0.4074\text{m}$ from the lens, and the conjugate plane is at a distance $(z_h + z_1) = 22\text{m}$ behind the lens. The illuminating beam is provided by an argon-ion laser operated at the wavelength $\lambda = 0.5145 \cdot 10^{-6}\text{m}$.

5.2.2 QUALITATIVE STUDY OF DARK-FIELD IMAGES OF CIRCULAR APERTURES

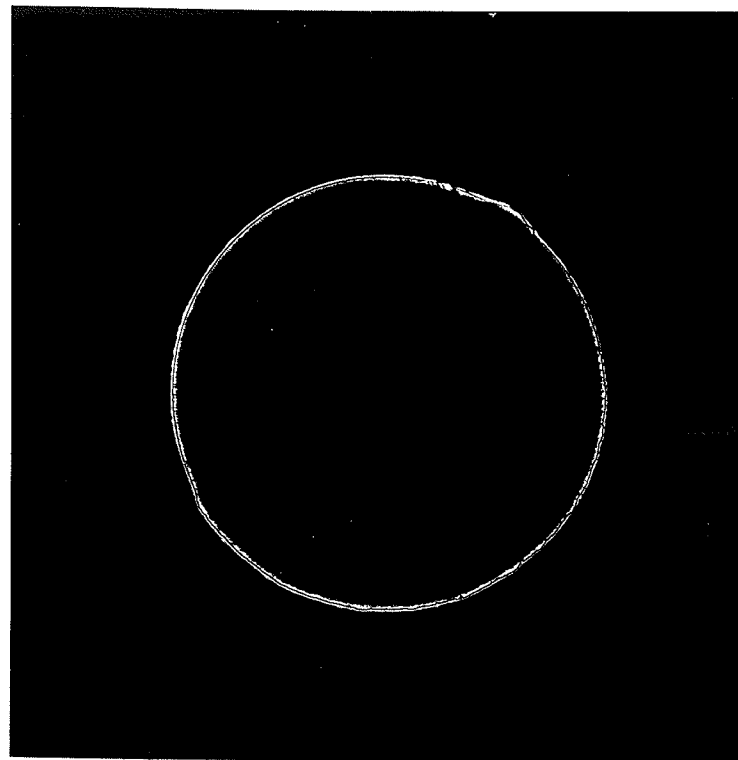
In this experiment it is shown that the intensity distributions of the dark-field images of a disk and its complementary aperture are identical. A desk paper punch is used for cutting the disk and its complementary circular aperture from a thin metallic sheet. The disk and its complementary aperture are sequentially placed in the object plane, and the dark-field images of the two objects are reconstructed in the conjugate plane.

Parameters: $a = 3 \cdot 10^{-3}\text{m}$, $\epsilon = 10^{-4}\text{m}$, $\tau = 15 \cdot 10^{-3}\text{m}$, $M'' = -10$ (note that for this experiment only, the magnification factor is $M'' = -10$).

Results: Although the objects were made in a very crude manner, the results are nevertheless quite convincing. Photographs (b) and (a) of Fig. 5.2 show the dark-field images of the disk and its complementary aperture. It can be seen that the intensity distributions about the Gaussian images differ only in the width of the bright zone. This difference occurs because the two negatives were not recorded under identical conditions. It is interesting to note that the microscopic profiles of the two objects are different. This experiment satisfactorily demonstrates the validity of (5.2).



(a)



(b)

Fig. 5.2 Dark-field images of complementary scenes: (a) filtered image of the circular aperture, (b) filtered image of the disk. $a = 3\text{mm}$, $\epsilon = 0.1\text{mm}$, $\tau = 15\text{mm}$ and $M'' = -10$.

5.2.3 Experiment A2

This experiment is intended to compare the amount of focussing error that may occur when viewing bright-field and dark-field images. The recording of the images is done in three different observation planes for two different filters. Figs. 5.3 and 5.4 show the recorded photographs.

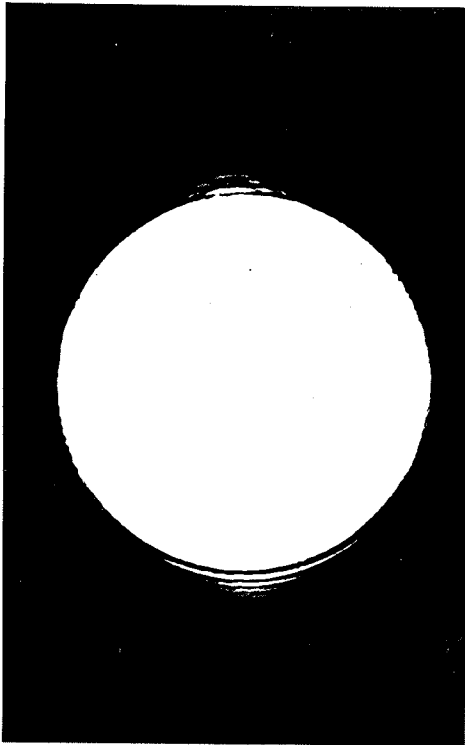
Parameters: $a = 0.5\text{mm}$, $\tau = 15\text{mm}$ and $d_1 = 0.4074\text{m}$. The recording planes are located at: (a) $z_h + z = 19.5\text{m}$; (b) $z_h + z_1 = 22\text{m}$ (this is the conjugate plane); (c) $z_h + z = 24.5\text{m}$.

For bright-field images, $\tau = 15\text{mm}$ and the central obstruction of the filter is removed. For dark-field images, $\epsilon = 0.1\text{mm}$ and $\tau = 15\text{mm}$.

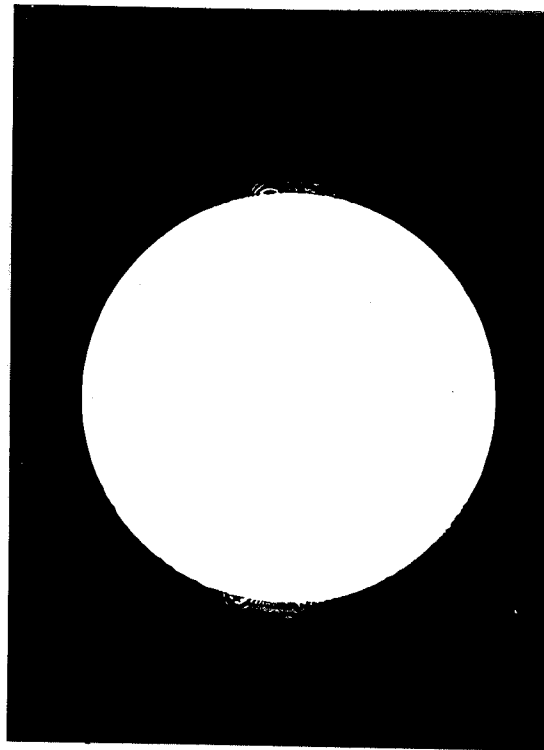
Results: By judging the recorded images of Fig. 5.3, it is impossible to determine which recording plane corresponds to the conjugate plane. However, on examination of the photographs of Fig. 5.4 it is readily seen that plane (b) is the conjugate plane. This result substantiates the argument of Section 4.2.2. It is seen that retrieval of the image depth dimension is greatly facilitated if a dark-field filter is used. A practical way for finding the conjugate plane is to observe the dark-fringe thickness. A minimum fringe thickness is obtained in the conjugate plane.

5.2.4 Experiment A3

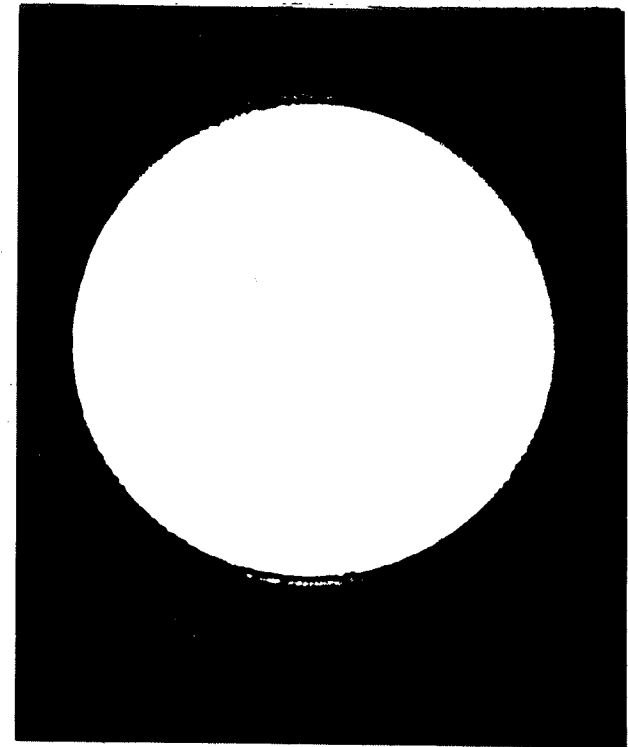
The object of this experiment is to qualitatively study the influence of the spatial filter parameters on the intensity distribution of the recorded dark-field images. The investigation is conducted for three different values of the circular aperture radius. Pinholes of well known



(a) $z_h + z = 19.5\text{m}$

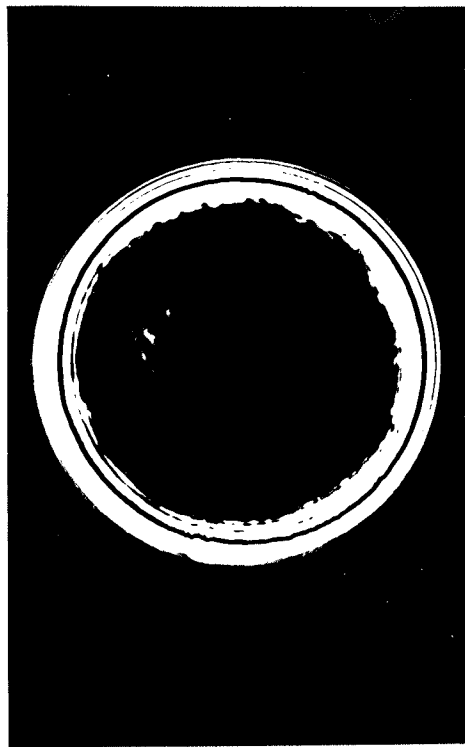


(b) $z_h + z_1 = 22\text{m}$

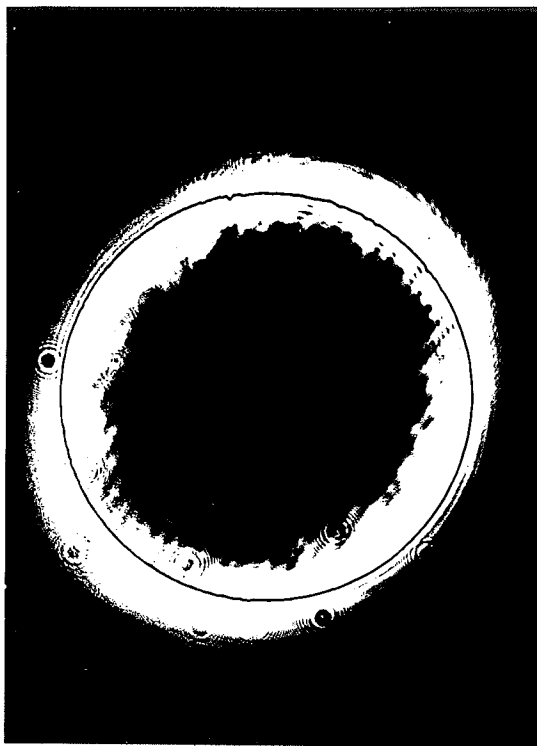


(c) $z_h + z = 24.5\text{m}$

Fig. 5.3 Bright-field images recorded in three different observation planes. From the three photographs it is not possible to determine the position of the conjugate plane which is located at $z_h + z_1 = 22\text{m}$. $a = 0.5\text{mm}$, $\tau = 15\text{mm}$ and $d_1 = 0.4074\text{m}$.



(a) $z_h + z = 19.5\text{m}$



(b) $z_h + z_1 = 22\text{m}$



(c) $z_h + z = 24.5\text{m}$

Fig. 5.4 Dark-field images recorded in three different observation planes. The plane located at $z_h + z = 22\text{m}$ is the conjugate plane. Note that the dark fringe thickness is minimum in the conjugate plane. $a = 0.5\text{mm}$, $\varepsilon = 0.1\text{mm}$, $\tau = 15\text{mm}$ and $d_1 = 0.4074\text{m}$.

sizes are placed in the object plane and the recording of the filtered images is made in the conjugate plane. The transverse magnification factor $M'' = -55$ is kept constant throughout the experiment. The recorded images are shown in Figs. 5.5 - 5.8, 5.9(a) and (b), and 5.10(b).

Parameters: $M'' = -55$; $a = 0.5\text{mm}$, 0.05mm and 0.005mm ; $\epsilon = 0.1\text{mm}$, 0.5mm , 1.25mm , 2.5mm , 5mm and 10mm ; $\tau = 1.25\text{mm}$, 2.5mm , 5mm , 7.5mm , 15mm and 50mm .

Results: Observation of the photographs gives the following information:

i) As τ increases, the dark fringe becomes thinner and conversely, as τ decreases, the dark fringe becomes thicker.

ii) As ϵ increases, the number of observable rings increases (this is best observed with the naked eye), and the image resolution seems to improve (compare Figs. 5.8(a), (b) and (c) with Figs. 5.10(b), 5.9(b) and (a) respectively).

iii) As τ decreases and as its value approaches that of ϵ , the dark fringe is no longer sharp and it becomes impossible to distinguish it from the other rings. Photograph (d) of Fig. 5.7 clearly shows this phenomenon.

iv) As a decreases, the effectiveness of the filter central obstruction decreases.

v) As a decreases, higher values of τ are required. Thus for $a = 0.005\text{mm}$, it was not possible to properly record any image (see Fig. 5.11(a)). However, Fig. 5.11(b) shows that an image may be obtained by placing the observation plane slightly away from the conjugate plane.

All these observations are in perfect agreement with the results obtained in Section 4.3.2. However, it is not possible to accurately determine

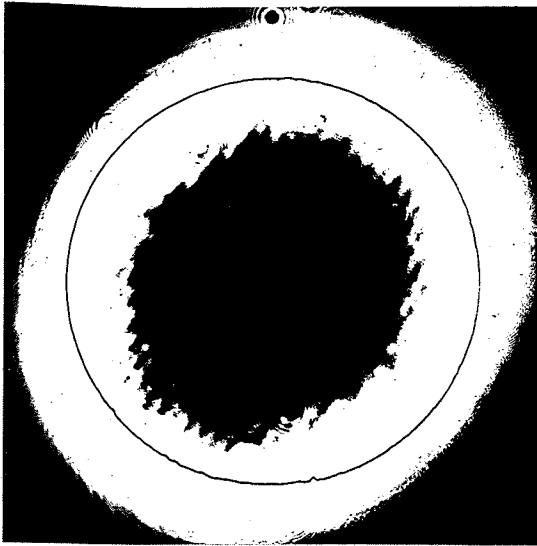
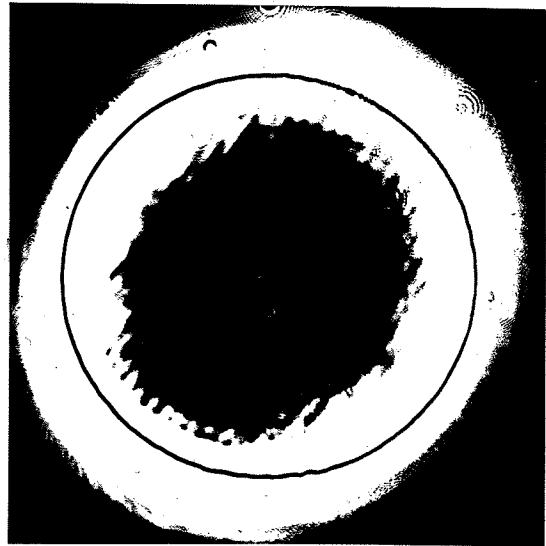
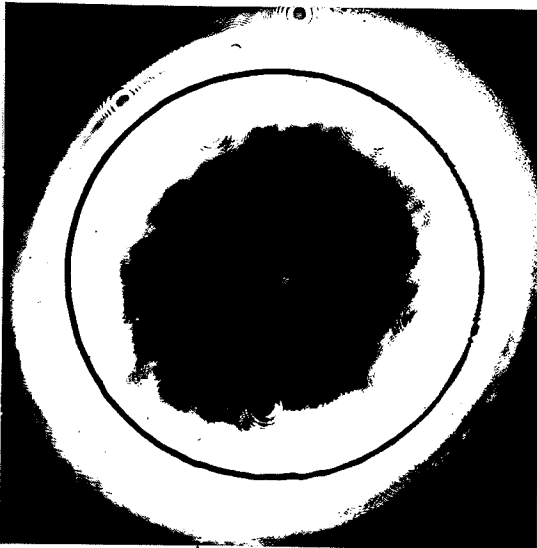
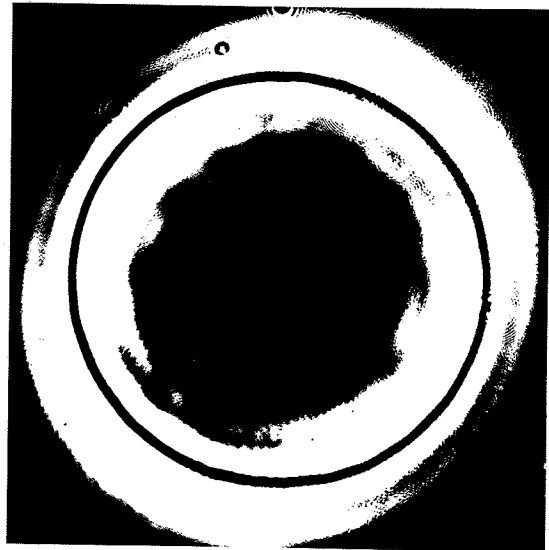
(a) $\tau = 15\text{mm}$ (b) $\tau = 10\text{mm}$ (c) $\tau = 7.5\text{mm}$ (d) $\tau = 2.5\text{mm}$

Fig. 5.5 Dark-field images recorded in the conjugate plane. Note that the central zone appears almost uniformly dark. $a = 0.5\text{mm}$, $\epsilon = 0.1\text{mm}$ and $M'' = -55$.

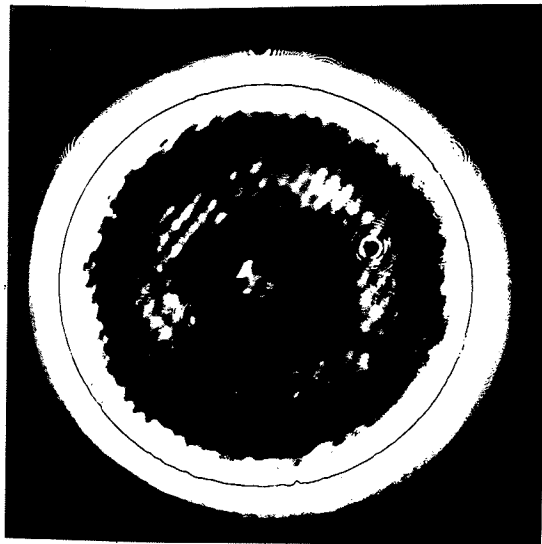
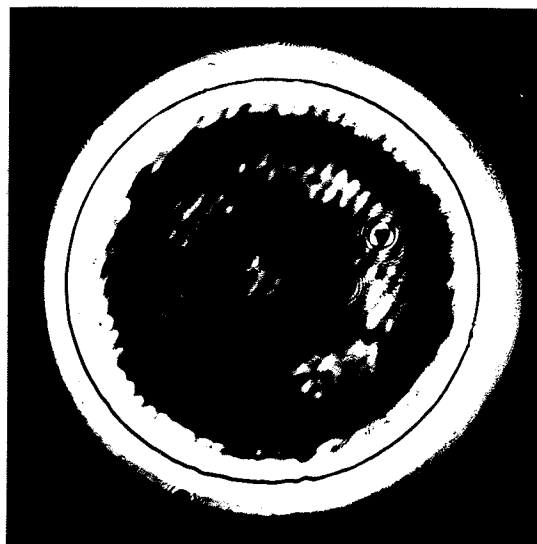
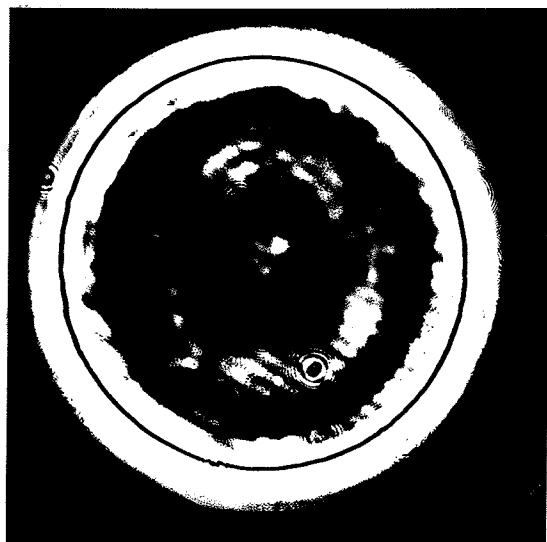
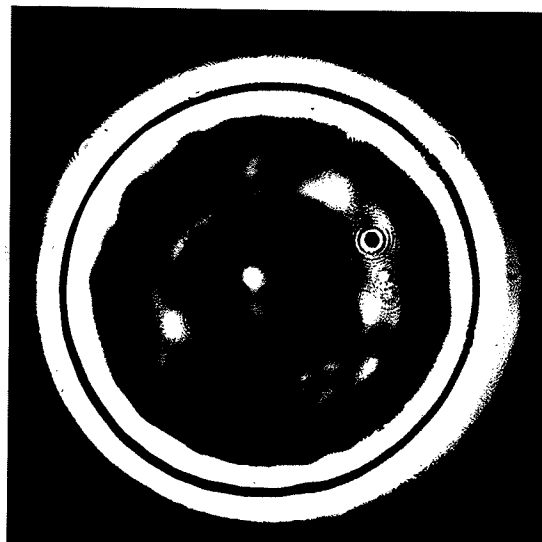
(a) $\tau = 15\text{mm}$ (b) $\tau = 7.5\text{mm}$ (c) $\tau = 5\text{mm}$ (d) $\tau = 2.5\text{mm}$

Fig. 5.6 Dark-field images recorded in the conjugate plane. Rings begin to be visible in the central region. Compare the thickness of the dark fringe with the width of the dip observed in the curves of Fig. 4.3. $a = 0.5\text{mm}$, $\epsilon = 0.5\text{mm}$ and $M'' = -55$.

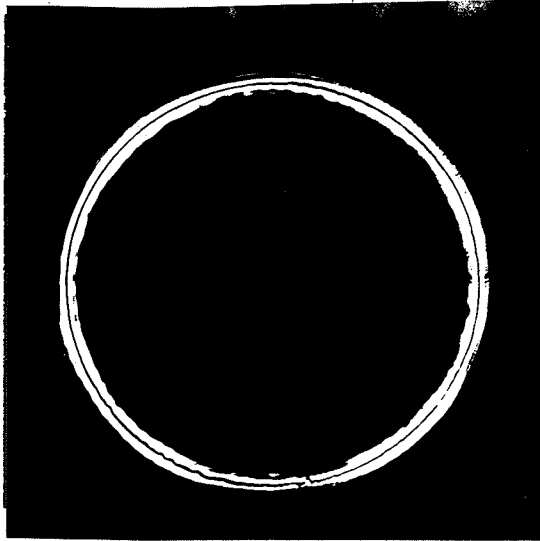
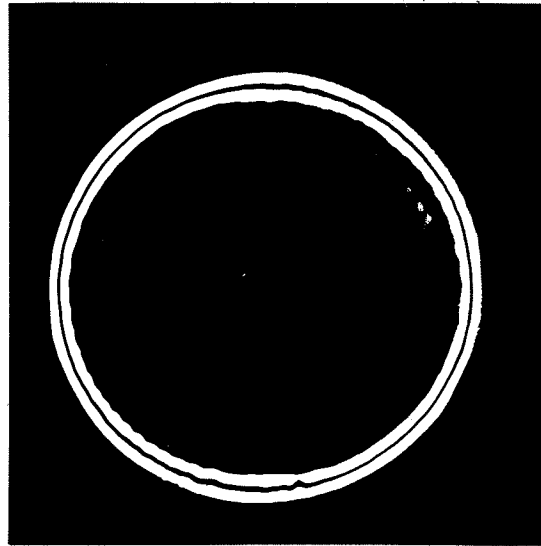
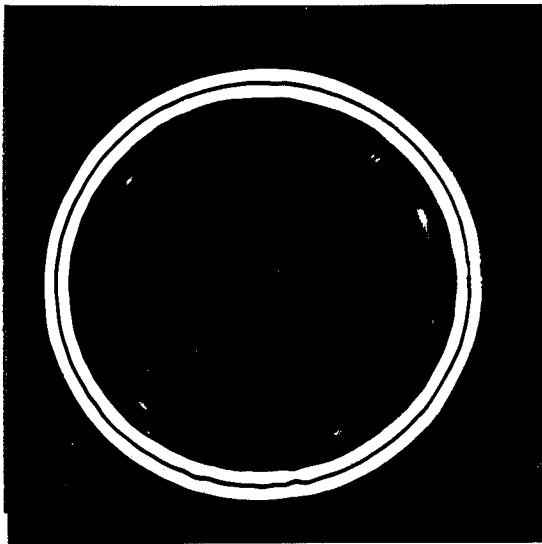
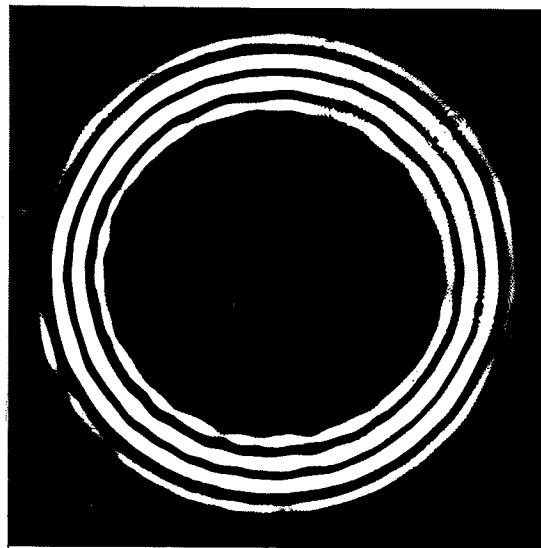
(a) $\tau = 15\text{mm}$ (b) $\tau = 7.5\text{mm}$ (c) $\tau = 5\text{mm}$ (d) $\tau = 2.5\text{mm}$

Fig. 5.7 Dark-field images recorded in the conjugate plane. Note that rings are clearly visible inside and outside the dark-fringe located on the Gaussian image. Compare the thickness of the dark fringe with the width of the dip observed in the curves of Fig. 4.5. $a = 0.5\text{mm}$, $\epsilon = 1.25\text{mm}$ and $M'' = -55$.

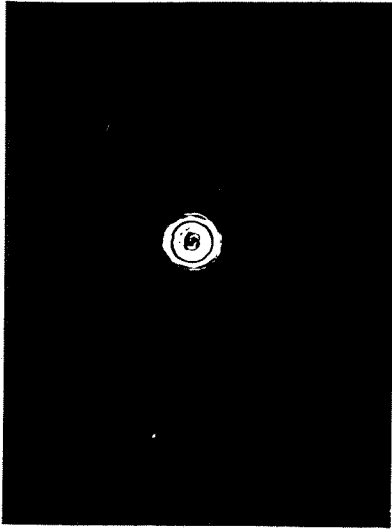
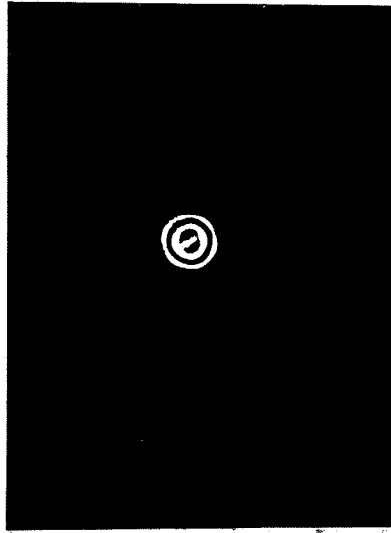
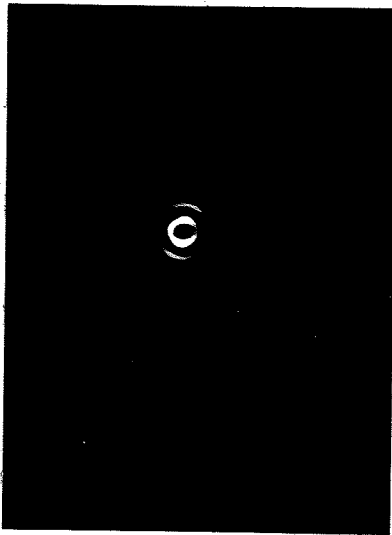
(a) $\tau = 15\text{mm}$ (b) $\tau = 7.5\text{mm}$ (c) $\tau = 5\text{mm}$ (d) $\tau = 2.5\text{mm}$

Fig. 5.8 Dark-field images recorded in the conjugate plane. Central rings are visible. Note that the resolution of the last two images is very poor. $a = 0.05\text{mm}$, $\varepsilon = 1.25\text{mm}$ and $M'' = -55$.

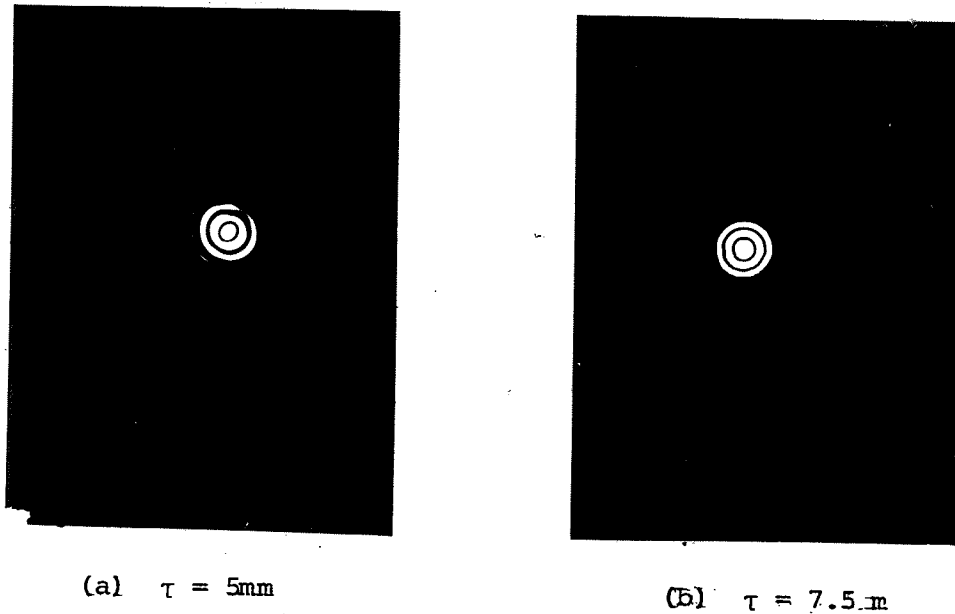
(a) $\tau = 5\text{mm}$ (b) $\tau = 7.5\text{mm}$

Fig. 5.9 Dark-field images recorded in the conjugate plane. The image resolution seems to be superior to that of the images of Fig. 5.8. $a = 0.05\text{mm}$, $\epsilon = 2.5\text{mm}$ and $M'' = -55$.

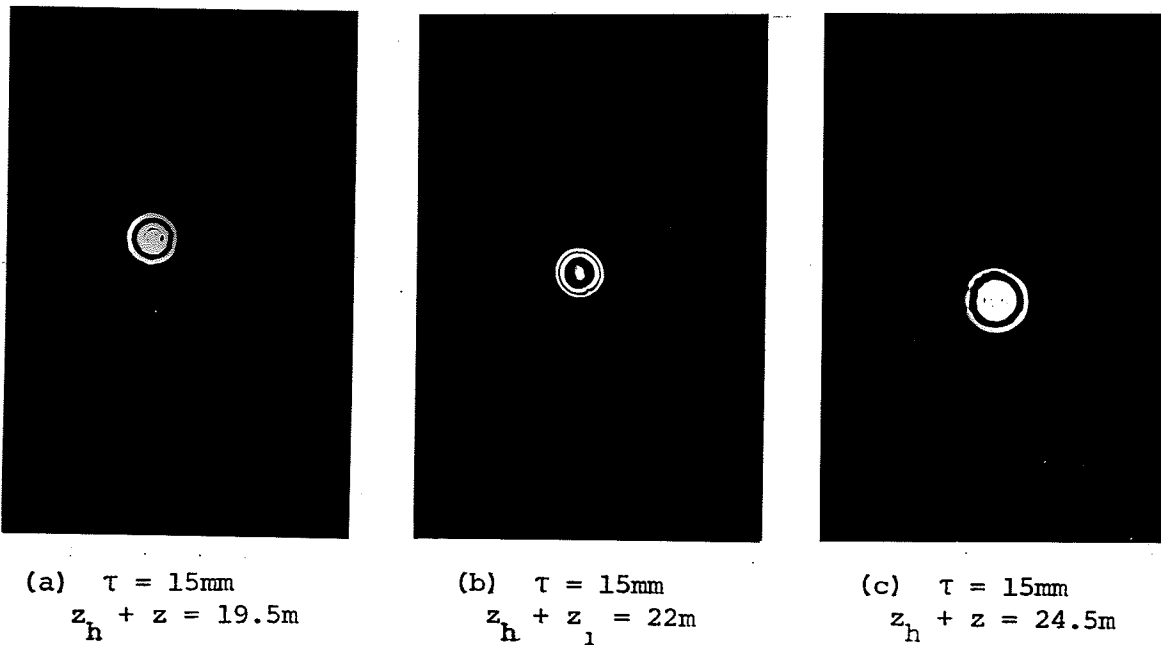
(a) $\tau = 15\text{mm}$
 $z_h + z = 19.5\text{m}$ (b) $\tau = 15\text{mm}$
 $z_h + z = 22\text{m}$
 1 (c) $\tau = 15\text{mm}$
 $z_h + z = 24.5\text{m}$

Fig. 5.10. (a) and (c) are dark-field images recorded in front of and behind the conjugate plane respectively. The thick dark fringe is characteristic of improper focussing. (b) is the dark-field image recorded in the conjugate plane. $a = 0.05$ and $\epsilon = 2.5\text{mm}$.

the position of the dark fringe, thus the results of Section 4.3.2 cannot be verified visually. Accurate measurement of the dark fringe position could be made by measuring directly the trace in the conjugate plane, using a photomultiplier detector. It is of interest to compare the photographs of the intensity distribution of the electric field in the image plane shown in Figs. 5.6 and 5.7 with the theoretical curves of the intensity distribution plotted in Figs. 4.3 and 4.5.

5.2.5 Experiment A4

This experiment is similar to Experiment A2. However, the aperture radius which was previously $a = 0.5\text{mm}$ is now $a = 0.05\text{mm}$. Figs. 5.10(a), (b) and (c), and 5.12(a), (b) and (c) show the recorded intensity distributions in three different planes for the dark-field and the bright-field images.

Parameters: $a = 0.05\text{mm}$, $\tau = 15\text{mm}$ and $d_1 = 0.4074\text{m}$. The recording planes are located at: (c) $z_h + z = 19.5\text{m}$; (d) $z_h + z_1 = 22\text{m}$ (this is the conjugate plane); (e) $z_h + z = 24.5\text{m}$.

For bright-field images $\tau = 15\text{mm}$ and the central obstruction of the filter is removed. For dark-field images, $\epsilon = 0.5\text{mm}$, $\tau = 15\text{mm}$.

Results: The results are similar to those observed in Experiment A2. Even though the aperture diameter is reduced, focussing properties are unchanged.

5.2.6 Experiment A5

In this final experiment the spatial frequency spectra of the three

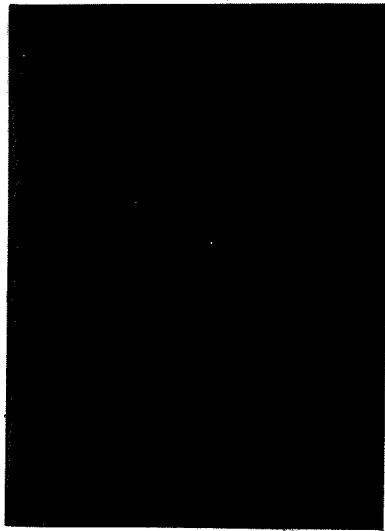
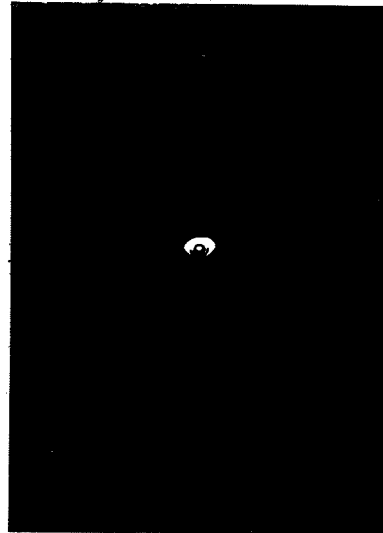
(a) $z_h + z_1 = 22\text{m}$ (b) $z_h + z = (22 + \delta)\text{m}$

Fig. 5.11 (a) is the dark-field image in the conjugate plane and (b) is the dark-field image in a plane slightly away from the conjugate plane. It seems that the image resolution is improved by a slight defocussing. $a = 0.005\text{mm}$, $\varepsilon = 10\text{mm}$ and $\tau = 50\text{mm}$.

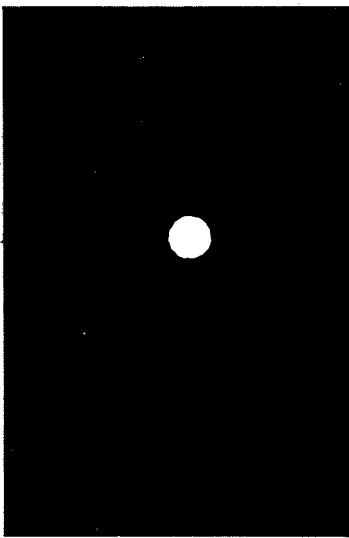
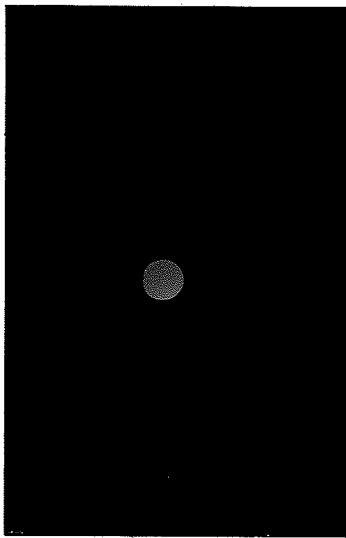
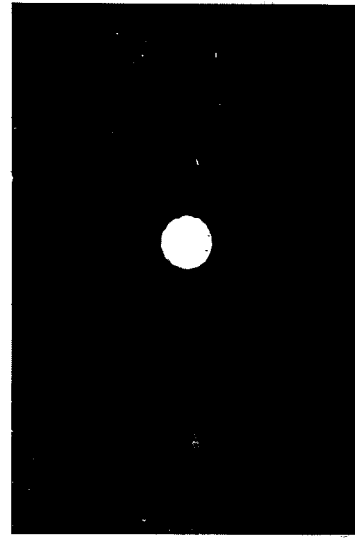
(a) $z_h + z = 19.5\text{m}$ (b) $z_h + z_1 = 22\text{m}$ (c) $z_h + z = 24.5\text{m}$

Fig. 5.12 Bright-field images recorded in three different planes. It is not possible to distinguish the focussed image from the others. Compare these photographs with those of Fig. 5.10. $a = 0.5\text{mm}$ and $\tau = 15\text{mm}$.

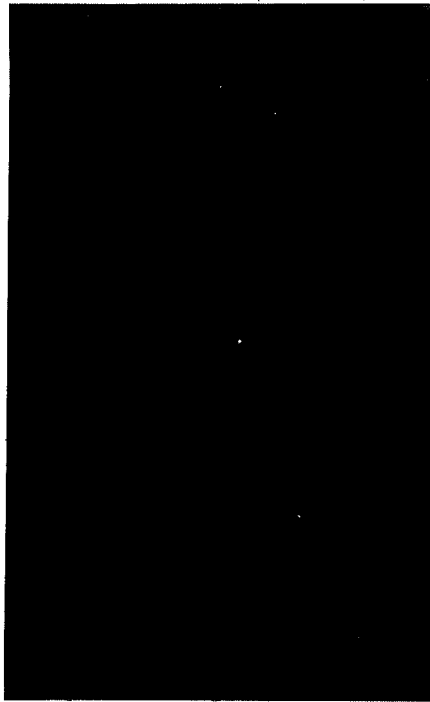
different apertures are compared. The intensity distributions recorded are referred to as the Airy patterns (after G.B. Airy who first derived them). The recording plane is now moved into the back focal plane of lens L_1 in front of the spatial filter and the Airy patterns are successively recorded (see Figs. 5.13(a), (b) and (c)).

Parameters: $a = 5.10^{-4}\text{m}$, 5.10^{-5}m and 5.10^{-6}m , $d_1 = 0.4074\text{m}$, and

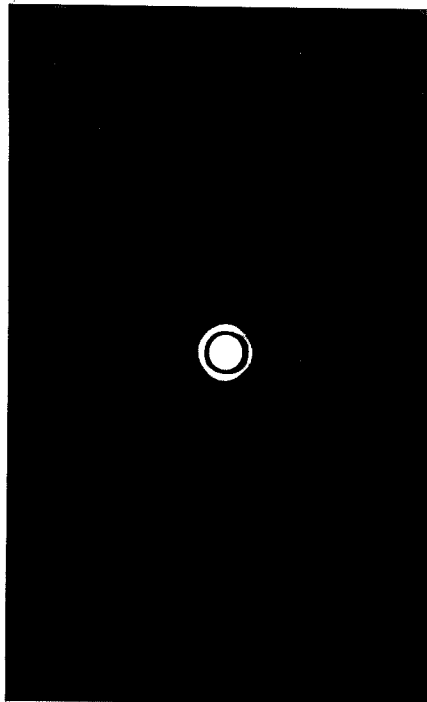
$$z_h + z = f_1 = 0.4\text{m}.$$

Results: The first zeros in intensity of the Airy patterns are obtained when $\rho_2 = 0.2512\text{mm}$, 2.512mm , 25.12mm and when $a = 0.5\text{mm}$, 0.05mm and 0.005mm respectively (these are calculated values). It is clearly seen from the photographs of Fig. 5.13 that the effectiveness of a given spatial filter is inversely proportional to the aperture radius. Thus, for an aperture radius $a = 0.5\text{mm}$, a filter with parameters $\epsilon = 0.1\text{mm}$ and $\tau = 15\text{mm}$ would have the same effect on the filtered image as another filter with parameters $\epsilon = 1\text{mm}$ and $\tau = 150\text{mm}$ would have on the filtered image of an aperture having a radius $a = 0.05\text{mm}$. This remark is readily confirmed by (4.22) in which the arguments of the sine and cosine integrals are proportional to either $a\epsilon$ or to $a\tau$ when $\rho_5 = aM''$ (on the boundary of the Gaussian image). A practical way for judging the effectiveness of a filter on the image would be to measure the dimensions of the obstruction and of the aperture of the filter in terms of the number of bright rings that are blocked and that are admitted, (i.e.) $\epsilon = 2.512\text{mm} = 1$ ring, $\tau = 14.917\text{mm} = 7$ rings, for $a = 0.05\text{mm}$).

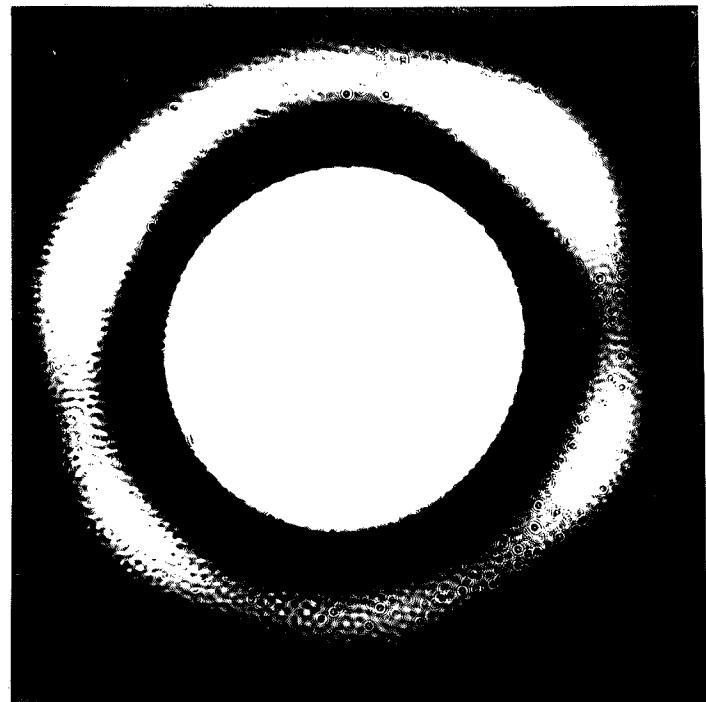
However, (4.22) is valid only if the arguments of the Bessels functions in (4.14) are large (i.e., $1 \ll (2\pi a\epsilon/\lambda f_1) < (2\pi a\tau/\lambda f_1)$). In addition,



(a) $a = 0.5\text{mm}$



(b) $a = 0.05\text{mm}$



(c) $a = 0.005\text{mm}$

Fig. 5.13 Spatial frequency spectra (Airy patterns) for circular apertures of different radii placed in the object plane.

(4.34) indicates that the spread of the impulse response of the optical system increases as $(2\pi\epsilon/\lambda u)$ and $(2\pi\tau/\lambda u)$ decrease, and thus the diffraction phenomenon drastically affects the intensity distribution of the filtered image. The effect of diffraction is best seen by choosing $a = 0.5\text{mm}$, $\epsilon = 0.1\text{mm}$ and $\tau = 2.5\text{mm}$ and observing the intensity distribution in the conjugate plane. A very fuzzy image is observed.

In conclusion, it can be said that the effectiveness of the spatial filter can be expressed very well in terms of the number of bright rings which propagate through the spatial filter, and in terms of the orders of these rings (i.e., when imaging an aperture of radius $a = 0.05\text{mm}$, the filter $\epsilon = 2.512\text{mm}$, $\tau = 14.917\text{mm}$ allows the 2nd, 3rd, 4th, 5th, 6th and 7th rings to propagate through), as long as the inequalities $1 \ll (2\pi a \epsilon / \lambda f_1) < (2\pi a \tau / \lambda f_1)$ and $1 \ll (2\pi \epsilon / \lambda u) < (2\pi \tau / \lambda u)$ are satisfied.

5.3 VERIFICATION OF THE GENERAL PROPERTIES

Many fundamental properties of both reconstructed dark-field images and aerial dark-field images have been pointed out in Chapter Four and in Section 5.1. It is the aim of this section to show experimentally that these properties are retained when a generalized transilluminated three-dimensional object is considered. The experiments performed on different objects substantiate further the theoretical results of Chapter Four and the qualitative study of Section 5.1, and confirm the usefulness of the method.

The single lens holocamera described in Section 3.3.5 and shown in the diagram of Fig. 3.2 is used. The spatial filter SF is reflective everywhere except in the central region where the low spatial components are allowed to propagate through a pinhole. This type of filter has been studied in Section 3.3.4 and is schematically represented in Fig.3.5 (b) . The dimensions are $\varepsilon = 0.3\text{mm}$, $\tau = 8\text{mm}$ and $r_p = 0.006\text{mm}$. Since the lens used in the setup has a focal length $f_1 = 0.4\text{m}$ and the wavelength of the laser source is 0.5145 m , the low cut-off spatial frequency is $40 \cdot 10^3 \text{ m}^{-1}$.

5.3.1 Experiment A6

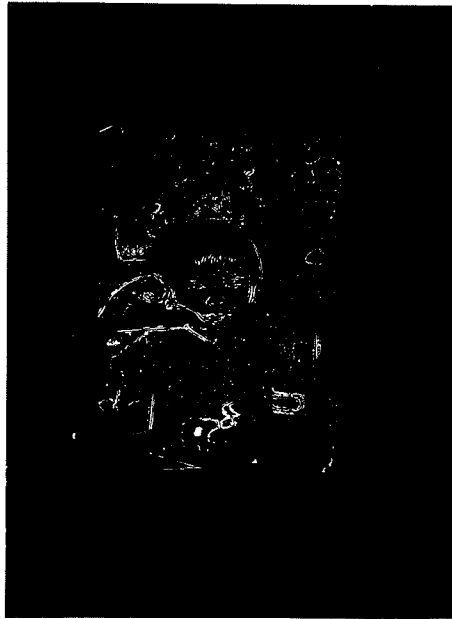
The aim of this experiment is to show that the reconstructed filtered image does not bear any of the finest object details when the low cut-off spatial frequency of the spatial filter is higher than the spatial frequencies of the finest object details. Fig. 5.14(a) represents a transparency of the author's son Pascal. This transparency has smooth and sharp intensity variations. Its reconstructed image, shown in Fig. 5.14(b), indicates that only the finest details are observable and that the profiles of Pascal's figure and other objects are enhanced.

5.3.2 Experiment A7

It was proved in Section 4.2.1 that dark-field filtering permits imaging of amplitude and phase objects. Fig. 5.15(a) represents an amplitude transparency of a resolution test target. The reconstructed dark-field images of the amplitude transparency (Fig. 5.15(b)), and of the

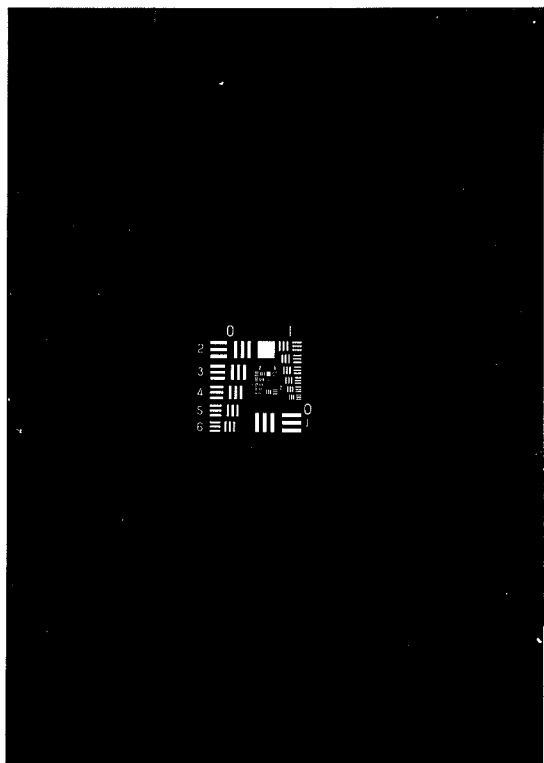


(a)

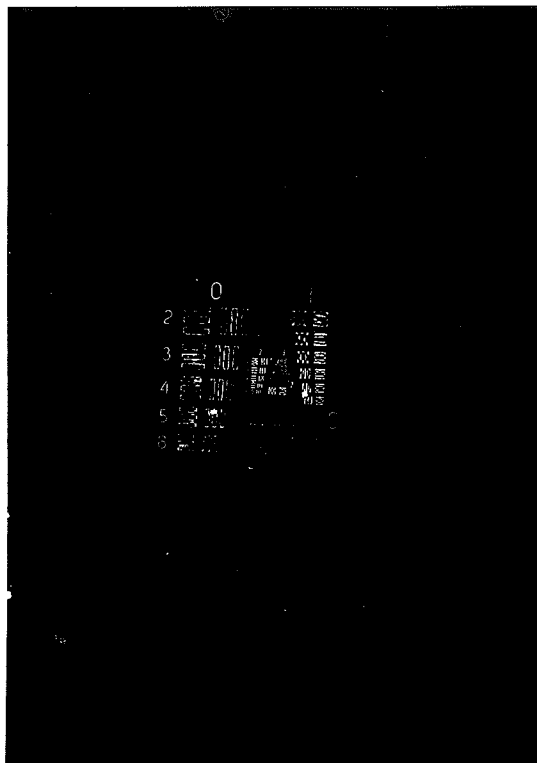


(b)

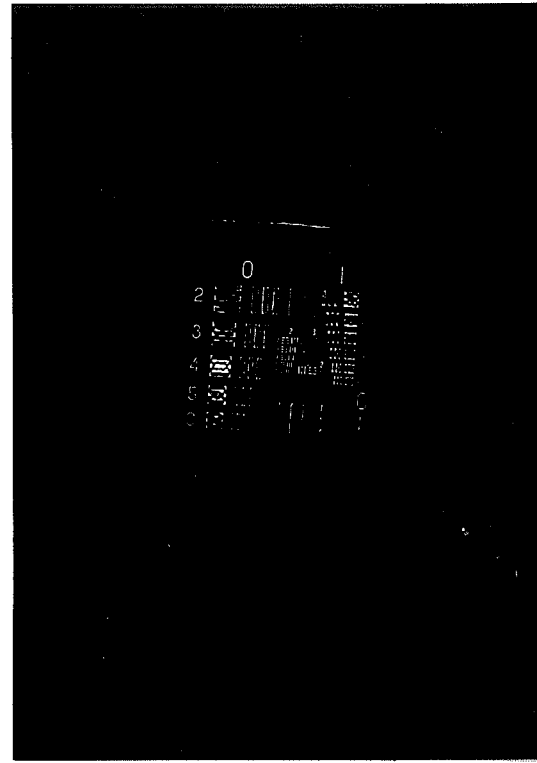
Fig. 5.14 Imaging of a continuous tone transparency: (a) the original of a transparency of the author's son, Pascal, (b) the reconstructed dark-field image.



(a)



(b)



(c)

Fig. 5.15 Imaging of amplitude and phase objects. (a) shows the original, (b) and (c) show the reconstructed dark-field images of the amplitude and the phase objects respectively.

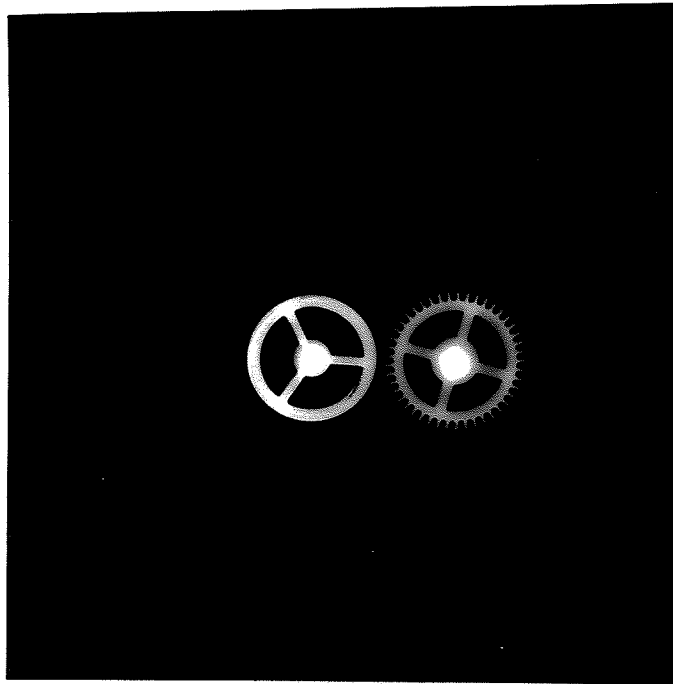
phase transparency (Fig. 5.15 (c)) of the same object, are identical, as predicted by (4.4) and (4.5).

5.3.3 Experiment A8

Photographs (a) and (b) of Fig. 5.16 represent the original and the hologram of opaque objects respectively. The photographs of Fig. 5.17 show the reconstructed dark-field image in (a) the plane which is the conjugate of the tooth wheel and (b) the plane which is the conjugate of the wheel with the spring. Clearly, the magnification properties and the three-dimensional character of the reconstructed image may be observed, as predicted in (3.18). The thin dark fringe along the profile of the focussed objects permits profile inspection [44,46,51].

5.3.4 Experiment A9

From (4.6) and from Experiments A2 and A4 of Section 5.2, it was found that dark-field images allow very accurate focussing. It is the intent of this experiment to show that reconstructed dark-field images permit very accurate recovery of the depth dimension of three-dimensional objects. Photographs (a) and (b) of Fig. 5.18 show the reconstructed bright-field image of an architectural model (the original can be seen in Fig. 3.6(b), where it is placed in the recording position). Although these two photographs were recorded in different planes, it is very hard to tell which beams are in focus. Photographs (a) and (b) of Fig. 5.19 show the reconstructed dark-field image of the same object. Clearly it becomes very easy to distinguish between the beams that are

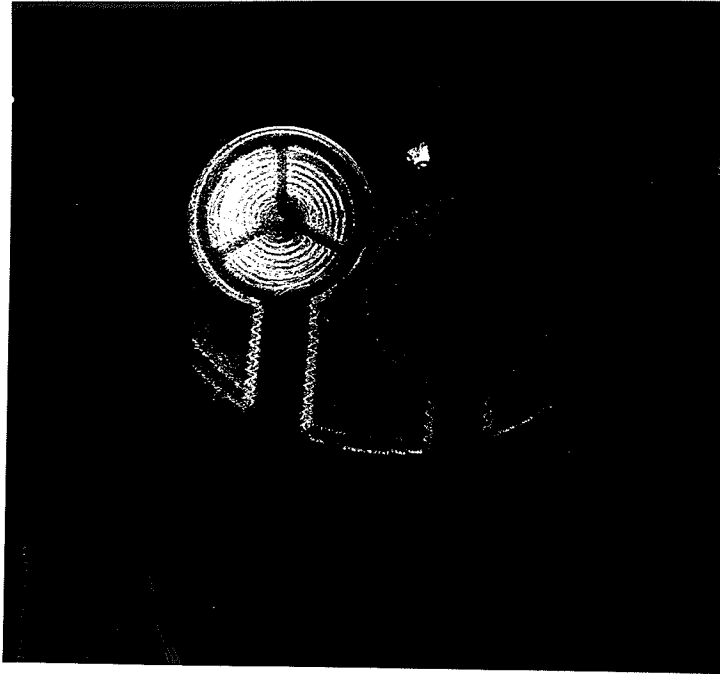


(a)

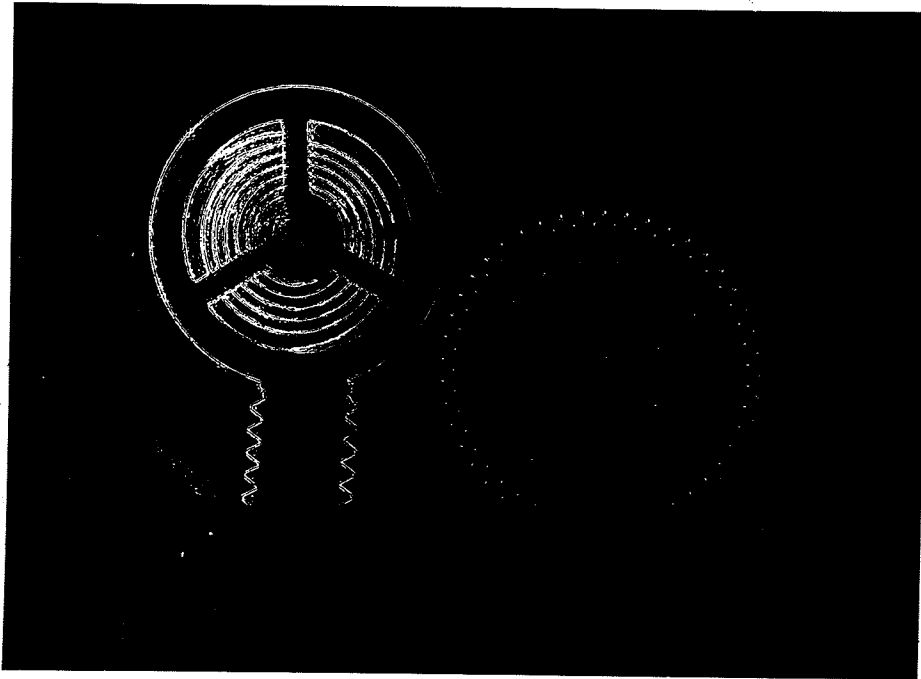


(b)

Fig. 5.16 Imaging of opaque objects: (a) the original clock wheels, (b) the hologram.

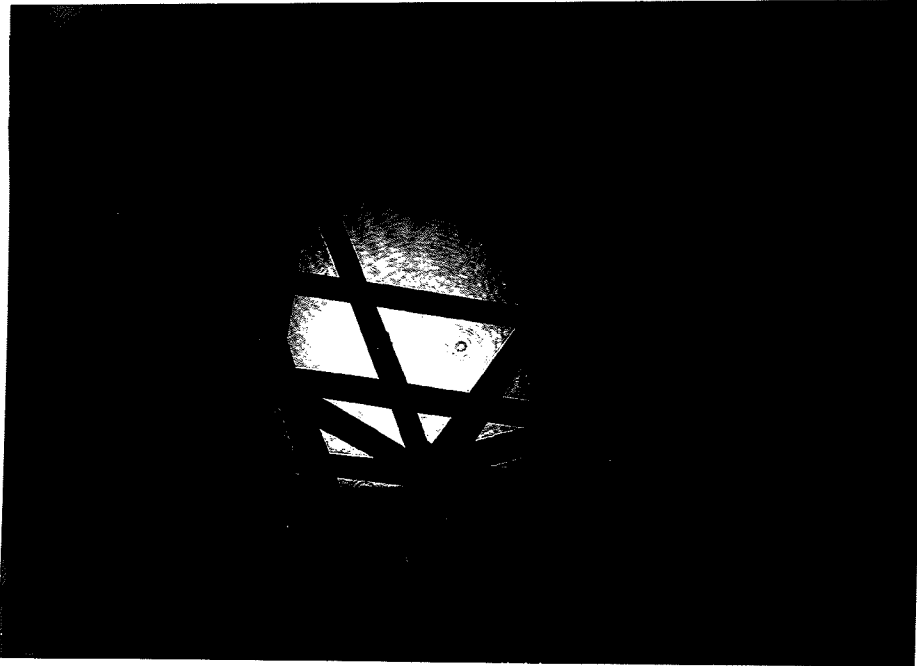


(a)

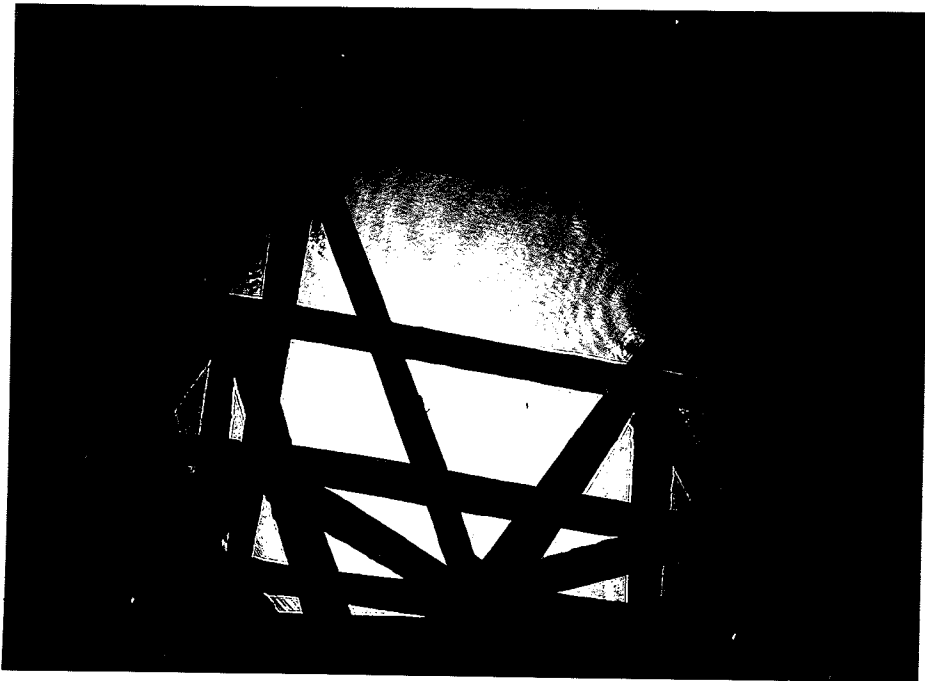


(b)

Fig. 5.17 Reconstructed dark-field images recorded in two different conjugate planes.

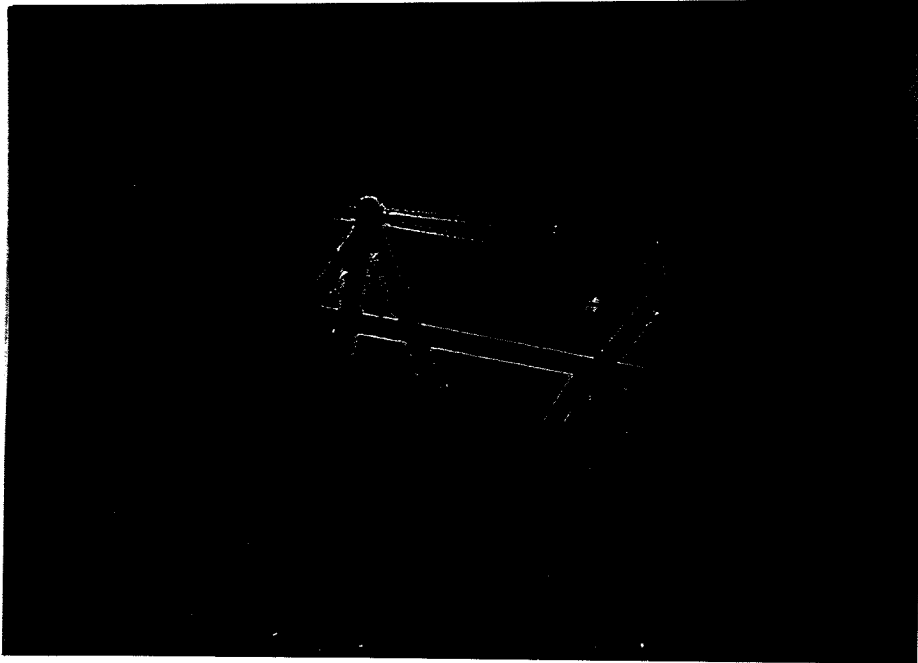


(a)

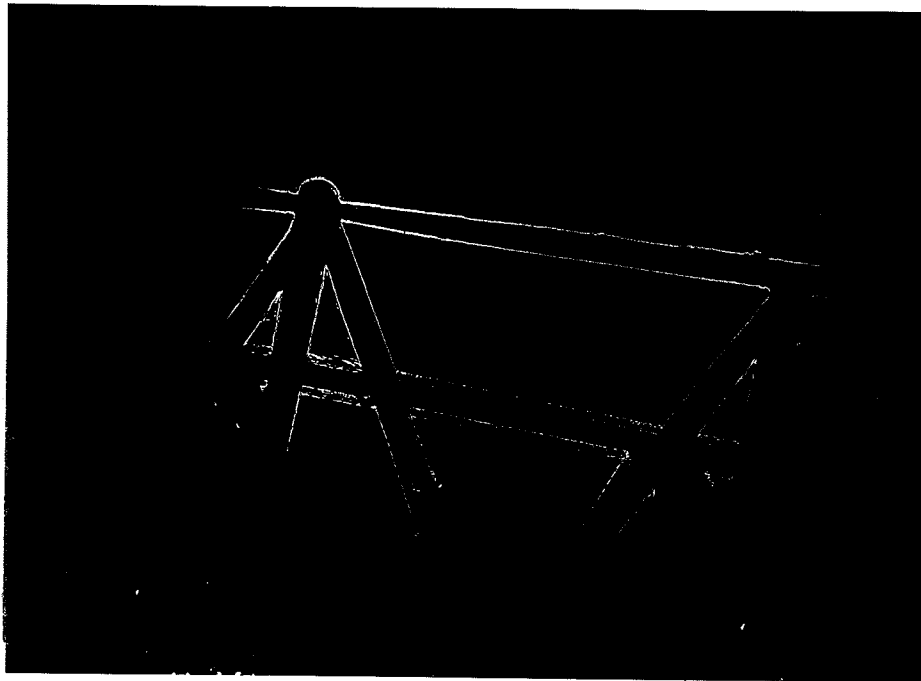


(b)

Fig. 5.18 Reconstructed bright-field images recorded in two different planes.



(a)



(b)

Fig. 5.19 Reconstructed dark-field images recorded in two different planes.

properly focussed and those which are not. A very thin dark fringe can be observed on the profile of the focussed beams.

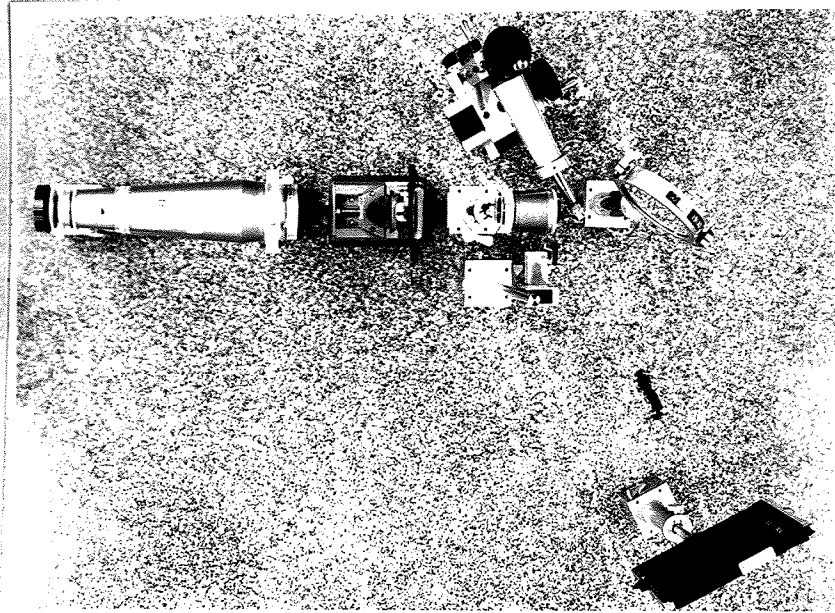
5.4 COMPARATIVE STUDY: BRIGHT-FIELD/DARK-FIELD IMAGES

This section will serve to demonstrate that retrieval of individual particle parameters (i.e., particle size, shape and canting angle) and of group parameters (i.e., spatial, size and density distributions) is rendered less cumbersome when the reconstructed images are of the dark-field type.

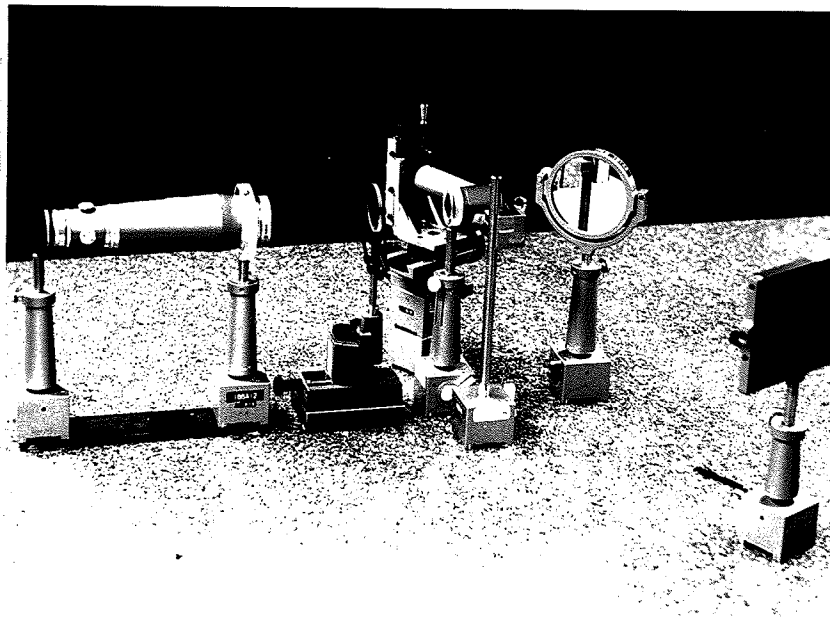
In order to perform a laboratory simulation of measurement of particle fields by using a continuous wave laser, it is necessary to image a time-invariant particle field. Far from being a limitation to the study, the time invariance of the particle field permits a systematic comparative study of different types of images, since images of the same sample volume can be compared after photographic or holographic recording.

5.4.1 Experiment A10

This experiment is conducted with the single lens holocamera (see Fig. 3.2) already used in Section 5.3. However a lens L_1 with a focal length $f_1 = 85\text{mm}$ is substituted for the previously used lens. Photographs (a) and (b) of Fig. 5.20 show the holocamera embodying the 85mm focal length lens, and Fig. 5.21(a) gives a close view of the object. In order to simulate a time-invariant particle field, a flat glass is sprayed on both sides with black paint. The region to be imaged

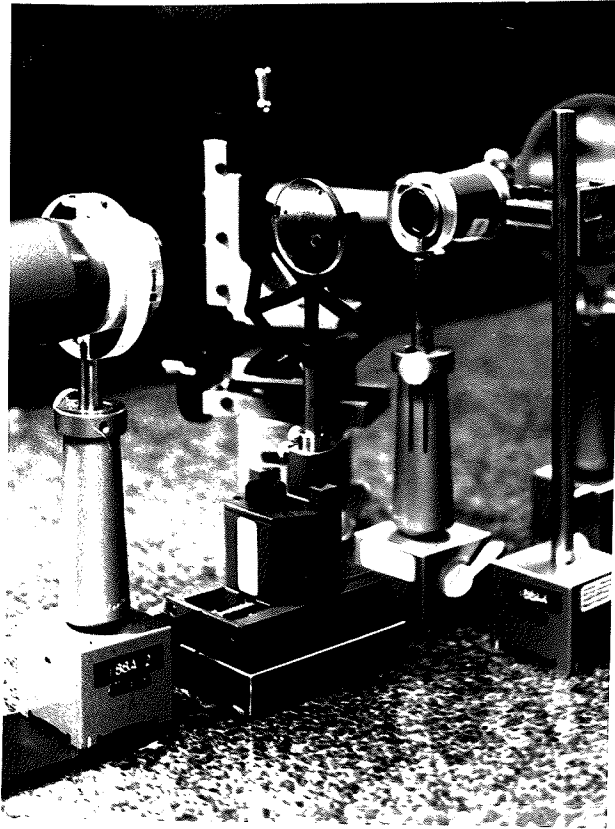


(a)

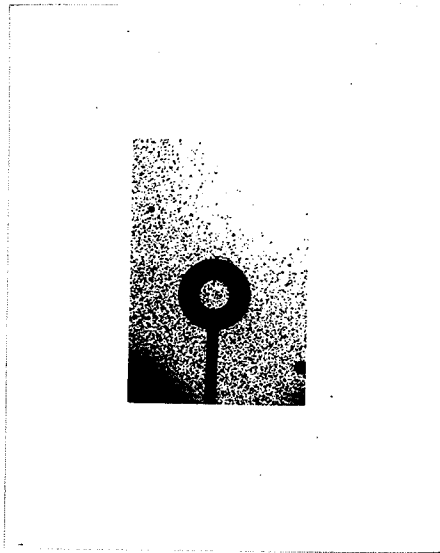


(b)

Fig. 5.20. (a) and (b) are two different views of the arrangement embodying the single-lens holocamera. Note that an 85mm focal length lens has been substituted for the 400mm focal length lens of Fig. 3.6. The equipment is identified as follows: "BC" beam collimator, "O" scene, "L" 85mm focal length lens, "SFM" spatial filter mirror, "M" mirror and "H" photographic plate holder.



(a)



(b)

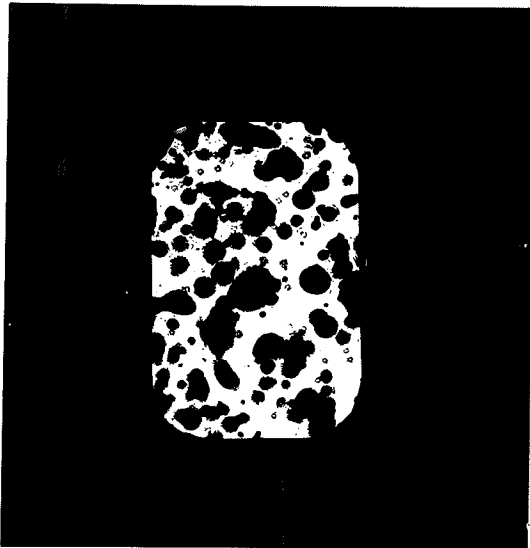
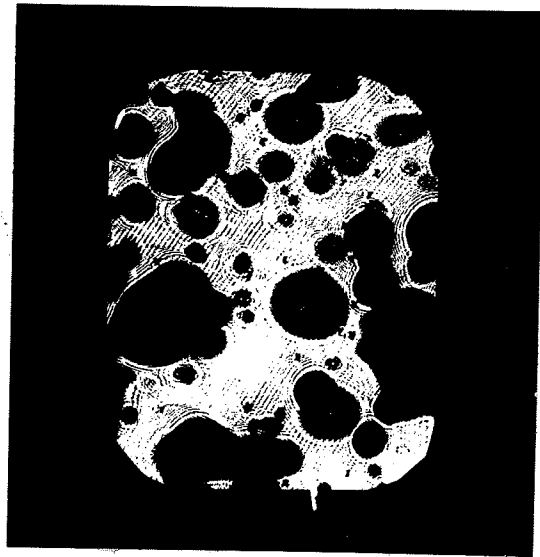
(c) $M'' \sim -15$ (d) $M'' \sim -25$

Fig. 5.21. (a) and (b) show the sprayed flat glass. (c) and (d) show the directly recorded bright-field images.

is within the circled area (see Fig. 5.21 (b) , which is a contact print of the sprayed flat glass). The experiment is conducted as follows:

- i) Direct recording of the bright-field and dark-field images (see Figs.5.21(c) and (d) , and Figs.5.22(a) and (b)). In these cases the reference wave is blocked.
- ii) Recording of the holograms of bright-field and dark-field scenes. The locally processed reference wave interferes with the object bearing wave in the recording plane, which is located in front of the conjugate planes.
- iii) Recording of the reconstructed dark-field images (see photographs (c) and (d) of Fig. 5.22.

Results: First, by comparing the directly recorded bright-field images (see Figs.5.21(c) and (d)) with the directly recorded dark-field images (see Figs. 5.22(a) and (b)), it appears that it is almost impossible to discriminate between the focussed particles and the out-of-focus ones when the images are of the bright-field type. The dark-field images show that the contour of the focussed particles is clearly outlined by a bright line (it is not possible to observe the dark fringe), whereas the out-fo-focus particles become almost invisible.

Second, by comparing the directly recorded dark-field images (see Figs.5.22(a) and (b)) with the recorded images of the holographically reconstructed field (see Figs.5.22(c) and (d)), it can be seen that the holographic process permits reconstruction of very good quality images. The content of the reconstructed images is slightly different from that of the directly recorded images. This is due to the fact that the flat glass was accidentally touched after the direct recording of the images.

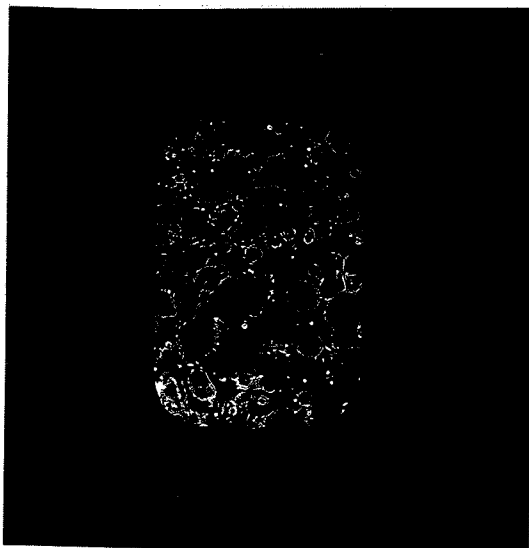
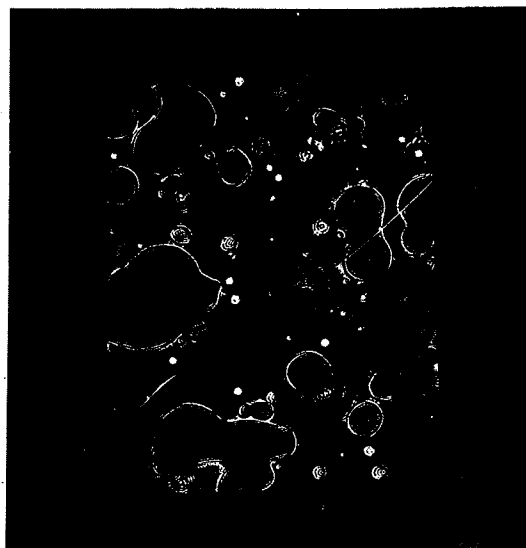
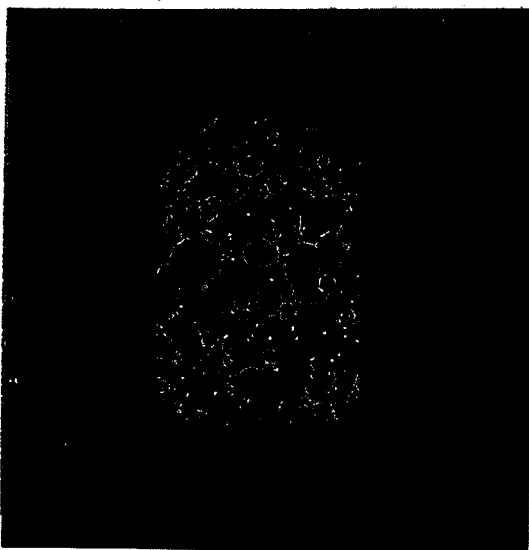
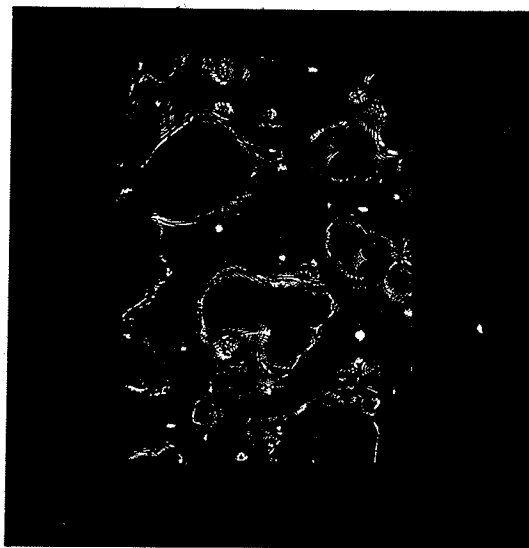
(a) $M'' \sim -15$ (b) $M'' \sim -25$ (c) $z_h + z_1 = .95m, M'' \sim -15$ (d) $z_h + z_2 = 2m, M'' \sim -25$

Fig. 5.22. (a) and (b) show the directly recorded dark-field images. (c) and (d) show the holographically reconstructed dark-field images. $z_h = .75m$.

It must be pointed out that the reconstructed images are recorded exactly in the planes of the directly recorded images.

5.4.2 Experiment A11

This experiment is conducted like Experiment A10. However, the 400mm focal length lens replaces the 85mm focal length lens.

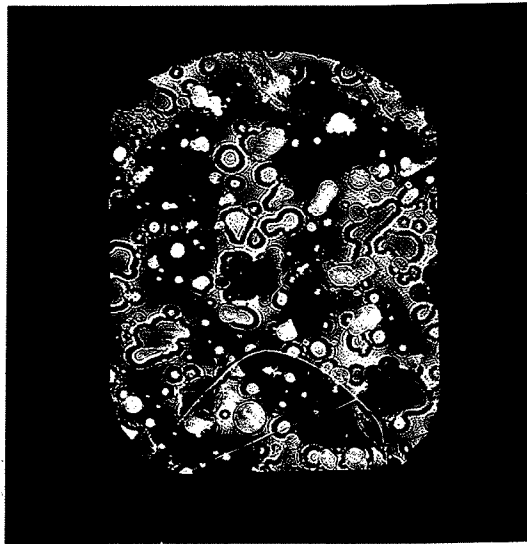
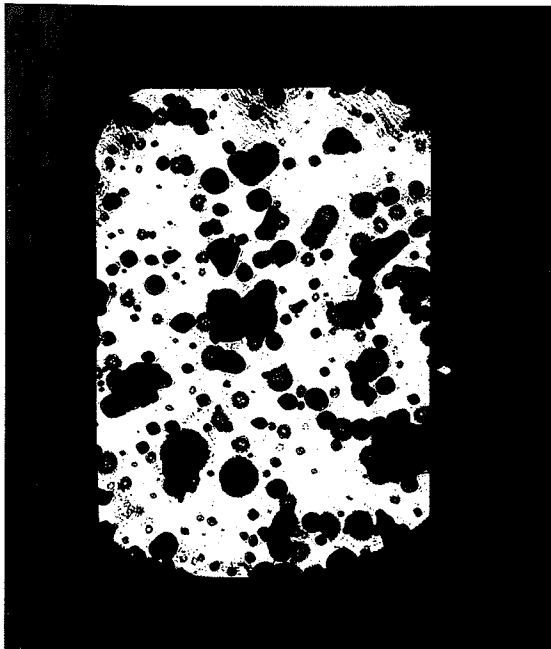
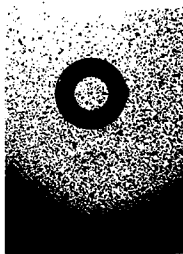
Photograph (e) of Fig. 5.23 shows a contact print of the flat glass.

(The sample region is circled.)

Results: Photographs (a), (b), (c) and (d) of Fig. 5.23 show directly recorded bright-field and dark-field images recorded in the two conjugate planes, while photographs (a), (b), (c) and (d) of Fig. 5.24 show the holographically reconstructed images.

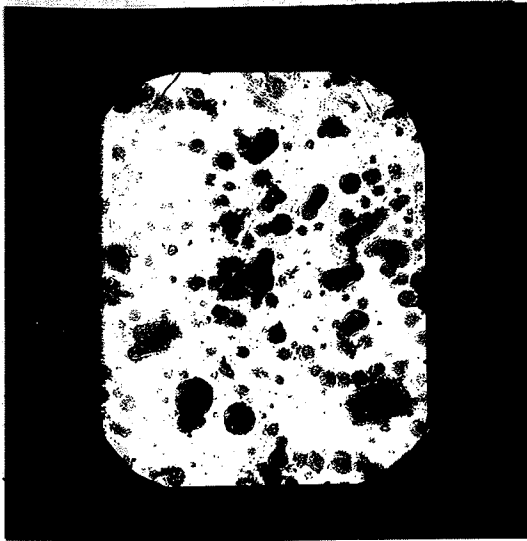
The quality of both the directly reconstructed and the holographically reconstructed dark-field images is much better than that obtained in Experiment A10. From the visual observations the following can be stated:

- i) The contours of the particles are well defined.
- ii) The out-of-focus particles are now clearly visible. There are very thick dark lines on their contours. Thus, it is extremely easy to distinguish between the focussed particles and the out-of-focus ones.
- iii) The quality of the holographically reconstructed images is really impressive.
- iv) By comparing the dark-field images with those dark-field images obtained in the previous experiment, it is readily observed that the

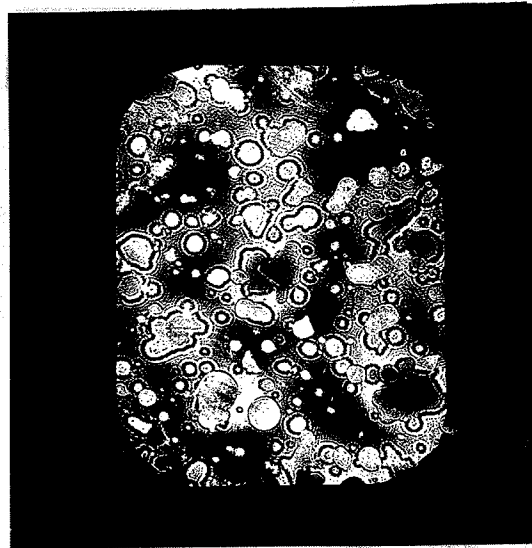
(a) $M'' \sim -15$ (b) $M'' \sim -15$ (c) $M'' \sim -18$ (d) $M'' \sim -18$ 

(e)

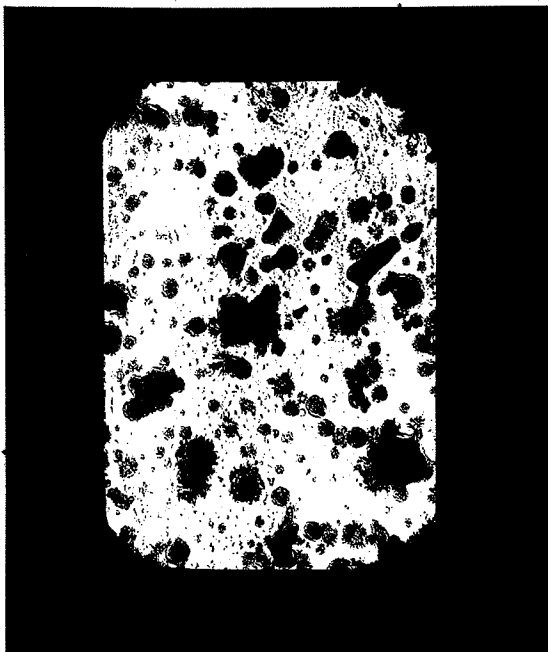
Fig. 5.23. (a), (c), (b) and (d) show the directly recorded bright-field and dark-field images. $z_h = 4.75\text{m}$. (e) shows a contact print of the sprayed flat glass. The sampled volume is circled.



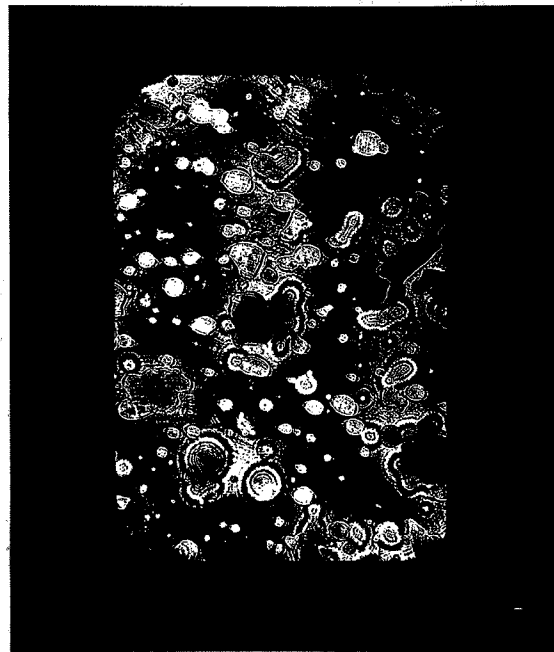
(a) $z_h + z_1 = 5\text{m}$, $M'' \sim -15$



(b) $z_h + z_1 = 5\text{m}$, $M'' \sim -15$



(c) $z_h + z_2 = 6.1\text{m}$, $M'' \sim -18$



(d) $z_h + z_2 = 6.1\text{m}$, $M'' \sim -18$

Fig. 5.24 Reconstructed bright-field and dark-field images in the two conjugate planes. $z_h = 4.75\text{m}$.

overall image visibility is now notably improved. Thus, it appears that the holocamera equipped with a 400mm focal length lens provides better imaging. In fact, the frequency spectrum is now spread over a larger area, since the focal length has been increased. It follows that the low and high cut-off spatial frequencies are reduced.

In conclusion, it must be emphasized that the visibility of dark-field images greatly depends on the design of the imaging system. Experiment All convincingly demonstrated the advantages of dark-field imaging.

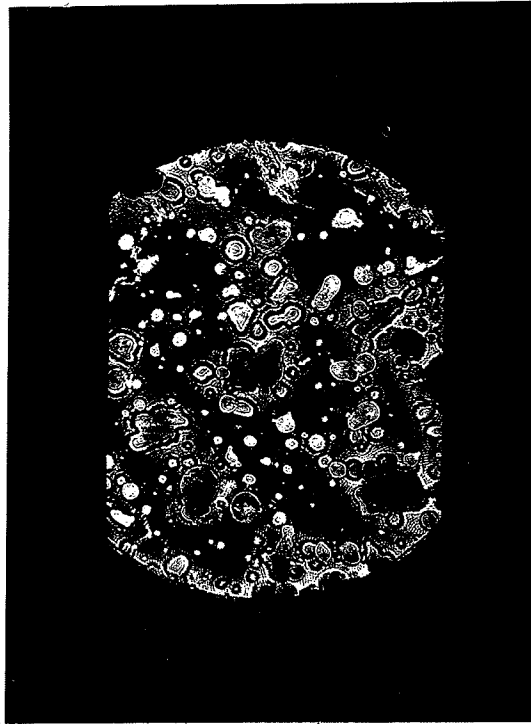
5.5 REDUCTION OF THE DISTANCE z_h

In Experiments A10 and All the distance z_h was very large indeed (z_h is the distance between the back focal plane of the lens L_1 and the hologram plane). In order to reduce the size of the holocamera, the recording plane can be placed closely to the back focal plane.

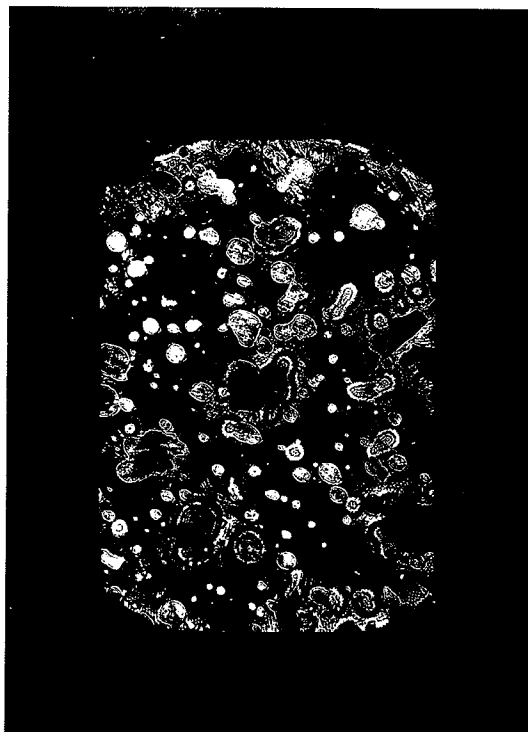
5.5.1 Experiment A12

The purpose of this experiment is to investigate the ability of a holocamera to record holograms which will reconstruct good quality images when z_h is reduced to a small value. The experimental arrangement used for Experiment All is altered by changing the position of the recording plane in such a way that $z_h = 0.5\text{m}$.

Results: The photographs of Fig. 5.25 show the reconstructed dark-field images in the two conjugate planes. The difference in quality between these images and those of the last experiment is hardly perceptible.



(a) $z_h + z_1 = 5\text{m}$, $M'' \sim -15$



(b) $z_h + z_1 = 6.1\text{m}$, $M'' \sim -18$

Fig. 5.25 Reconstructed dark-field images in the two conjugate planes
 $z_h = 0.5\text{m}$.

5.6

USE OF PARTIALLY FILTERED REFERENCE BEAMS

This section is of considerable interest because it investigates the feasibility of using an extended source in the generation of a local reference wave.

The reference wave spatial filter used in the experiments of Sections 5.2 to 5.5 was a pinhole having a radius $r_p = 6 \cdot 10^{-6}$ m. With such a small diameter the filtering is excellent and the object information is totally removed from the reference beam. However, a small pinhole requires a rigorous alignment of the holocamera with respect to the axis of propagation of the illuminating beam. If a pulsed laser source is used, a small pinhole might require frequent replacement. For a given lens and a given power density associated with the focussed spot, a small pinhole lowers the threshold breakdown of air which is approximately $7 \cdot 10^{11}$ W/cm² [54].

In the following, different filtering methods are experimentally studied. The single lens holocamera equipped with the 0.4m focal length lens is used throughout the experiments. The spatial filter mirror is still used. However, the small disk behind the fine pinhole is removed. Thus, the upper cut-off spatial frequency existing in the reference beam after propagation through the central hole of the spatial filter mirror is $1.5 \cdot 10^3$ m⁻¹.

It must be said in passing that the hologram reconstruction is done with a point source, since in field applications it would be impossible to obtain a duplicate of the partially filtered reference wave that would

allow reconstruction of unaberrated images.

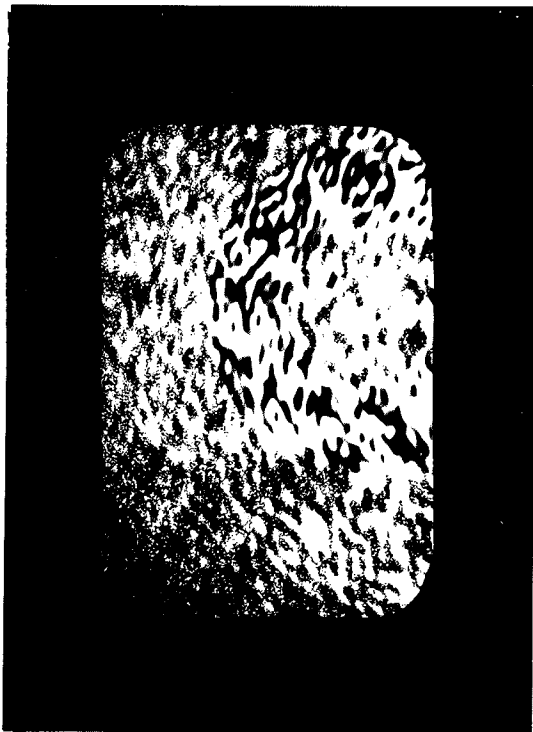
5.6.1 Experiment A13

In this experiment a very rough filtering of the reference beam is done, since the central hole of the spatial filter mirror has a radius $\epsilon = 0.3\text{mm}$. The partially filtered reference wave interferes with the object wave in a recording plane located at $z_h = 1.3\text{m}$ behind the focal plane of the lens.

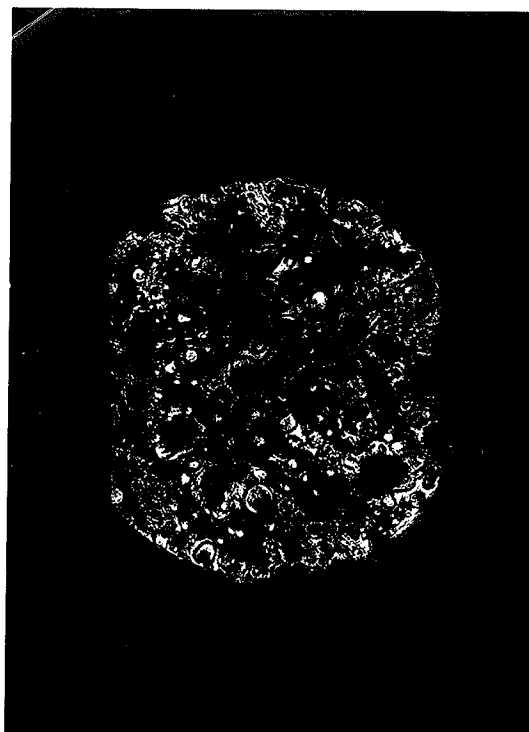
Results: Photograph (a) of Fig. 5.26 is a contact print of the hologram. It is easy to see that the very sharp white dots are due to the object bearing wave which has high spatial frequency components, while the smeary black dots are due to the reference wave which bears only the spatial frequency components smaller than $1.5 \cdot 10^6 \text{ m}^{-1}$. Note that each dot represents the out-of-focus image of a particle. Photographs (b) and (c) of Fig. 5.26 show the reconstructed dark-field images in the two conjugate planes located at $z_h + z_1 = 5\text{m}$ and $z_h + z_2 = 6.1\text{m}$. As expected, the results are not as good as those obtained when maximum filtering is imposed on the reference wave.

5.6.2 Experiment A14

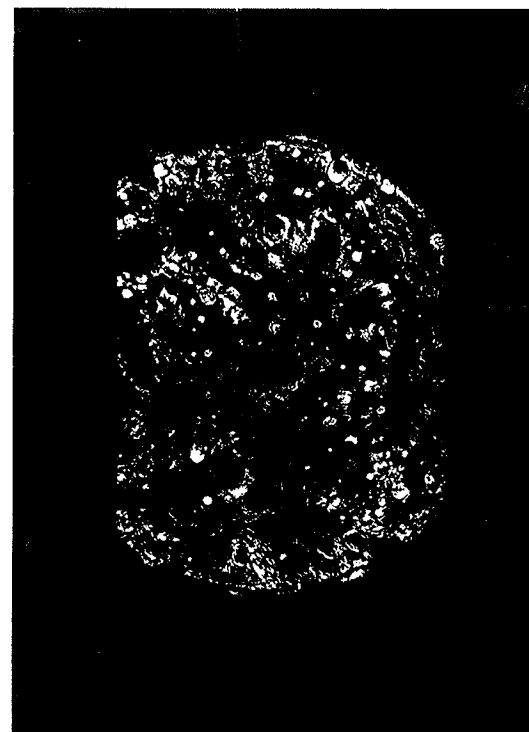
In order to improve the image quality, the reference wave is collimated by a lens after it passes through the spatial filter mirror. Nothing is changed in the path of the object bearing wave. The hologram is recorded in a plane positioned at $z_h = 1.3\text{m}$.



(a) $z_h = 1.3\text{m}$



(b) $z_h + z_1 = 5\text{m}, M'' \sim -15$



(c) $z_h + z_2 = 6.1\text{m}, M'' \sim -18$

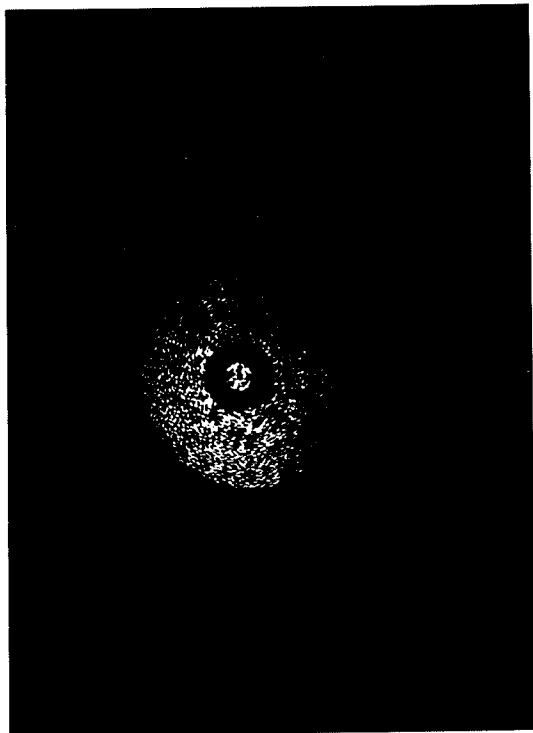
Fig. 5.26 (a) is a contact print of the hologram. The reference beam is partially filtered and not collimated. (b) and (c) are the reconstructed dark-field images in the two conjugate planes.

Results: Photograph (a) of Fig.5.27 is a contact print of the hologram. It is no longer possible to distinguish between the dots corresponding to the object bearing wave and those corresponding to the reference wave. In fact, by collimating the reference wave, the size of the smeary black dots has been reduced and the irradiance in the white regions has been increased. This reduction in size of the smeary black dots, and increase in irradiance of the background of the reference wave, increases the likelihood of an object bearing ray interfering with an intense reference ray. Thus, by having a somewhat higher reference-to-object wave intensity ratio, the reconstructed images should be of better quality than those reconstructed in Experiment A13. Figs.5.27(b) and (c) show that the image quality is now quite good, although still inferior to that obtained by recording holograms with a reference beam emerging from a point source.

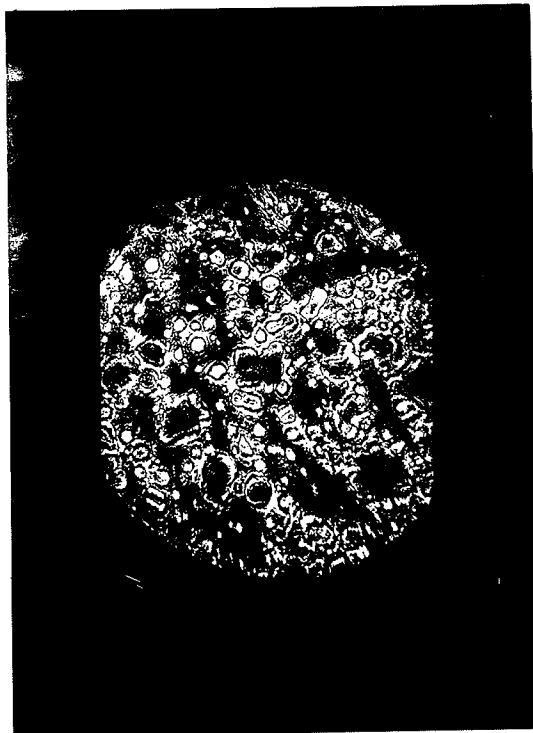
However, optimum quality could be obtained by reducing z_1 and z_2 , which represent the distance from the hologram to the two conjugate planes. In the limit, if z_1 or $z_2 = 0$, the hologram records the focussed image of one of the conjugate planes. This possibility had been mentioned in Section 3.5.1. Rosen [42] has shown that extended reference and reconstruction sources can be used when taking holograms of focussed images.

5.7 USE OF DIFFUSED REFERENCE BEAMS

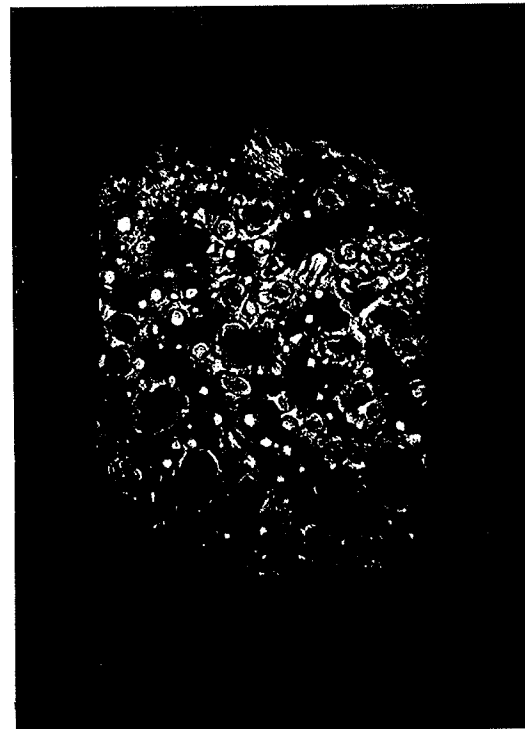
The main difficulty met in Experiments A13 and A14 was caused by the presence of dark smeary spots corresponding to the shadows cast by the particles. In an effort to make the alignment of the holocamera with



(a) $z_h = 1.3\text{m}$



(b) $z_h + z_1 = 5\text{m}, M'' \sim -15$



(c) $z_h + z_2 = 6.1\text{m}, M'' \sim -18$

Fig. 5.27 (a) is a contact print of the hologram. The reference beam is partially filtered and collimated. (b) and (c) are the reconstructed dark-field images in the two conjugate planes.

the reference beam less critical, it may be of interest to attempt recording holograms with a reference beam passing through a diffuser. Thus, all the object bearing spatial frequency components smaller than the high cut-off spatial frequency would be "broken down" by the diffuser, and a characteristic speckle pattern would interfere with the object bearing wave in the hologram plane. Som and Lessard [29] have conducted a comparable experiment, using a reference beam obtained by means of the amplitude division method. Such a procedure is very similar to the random bias recording technique described by Arsenault [55]. Arsenault reported some experimental results, by applying the technique to conventional off-axis recording of diffusing objects, and the author at a later time did some similar work by applying the technique to the holographic recording of diffusing objects by means of reflection type holograms (this work has not been published). The images obtained were of reasonably good quality. However, the objects were diffusing objects, and therefore the redundancy inherent in the holography of diffusing objects compensated for the lack of uniformity in amplitude of the reference beam in the recording plane. In measurements of particles and other transilluminated objects there is very little hologram redundancy, and as a result some regions of the image are not properly recorded. This phenomenon has been observed already in Experiment A13 (see Figs. 5.27 (b) and (c)).

In order to obtain an approximately uniform intensity distribution of the reference wave on the recording plane, the diffused source must be seen under a wide angle. However, the source size is proportional to this angle and thus image quality is expected to depend on a trade-

off between two conflicting parameters: uniformity of the reference wave on the recording plane, and source size. The two experiments that follow, clearly illustrate the problem.

5.7.1 Experiment A15

In this experiment a diffused reference source of 6mm diameter located at 0.75m from the recording plane is used. A hologram of a bright-field aerial image is recorded and then read out by means of a point source.

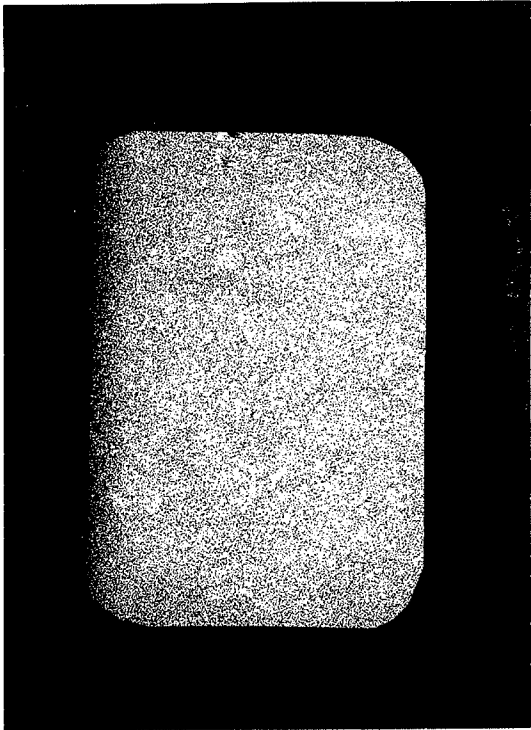
Results: Fig. 5.28(a) shows a contact print of the hologram. The characteristic speckle pattern of the diffused reference wave is clearly seen. This hologram looks quite different from, for example, the holograms that have been recorded in Experiment A11. Those holograms can be seen in Figs. 5.28(b) and (c).

The reconstructed images are of very poor quality with no details being distinguishable.

5.7.2 Experiment A16

In the attempt to obtain better image resolution, the size of the diffused reference source is now reduced to 0.2 mm and holograms of bright-field and dark-field images are recorded.

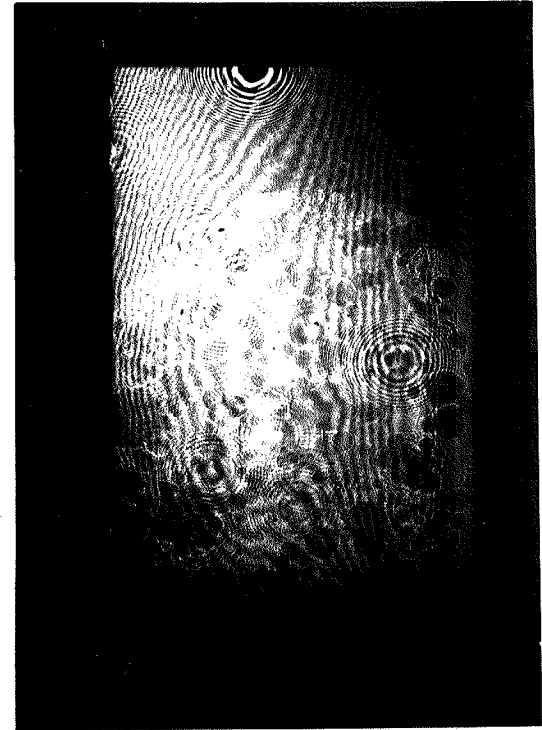
Results: Figs. 5.29(a) and (b) show the contact prints of the holograms. The speckle pattern of the reference wave is now composed of larger grains, a fact that is in agreement with the theory of speckle optics [56]. By reducing the size of the reference source, the resolution has



(a)

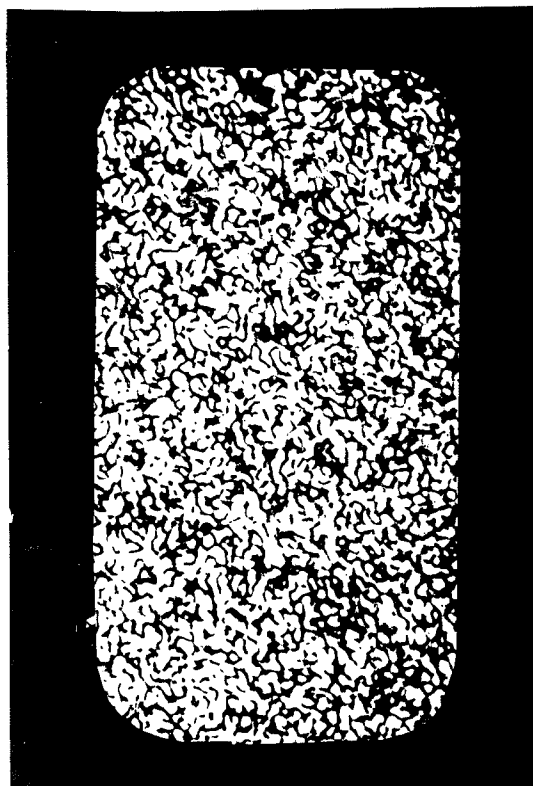


(b)

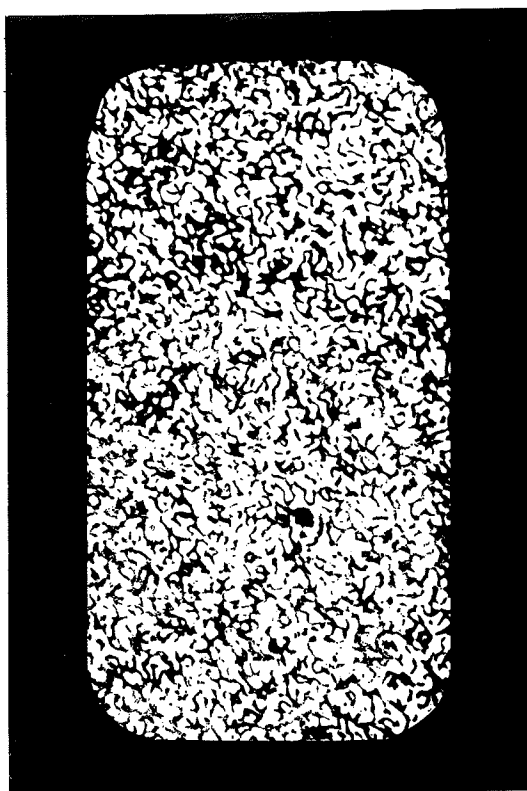


(c)

Fig. 5.28 (a) is a contact print of the recorded hologram. The diffused reference source of 6mm diameter is located 0.75m from the hologram plane. (b) and (c) are the contact prints of the holograms recorded in the Experiment All.



(a)



(b)

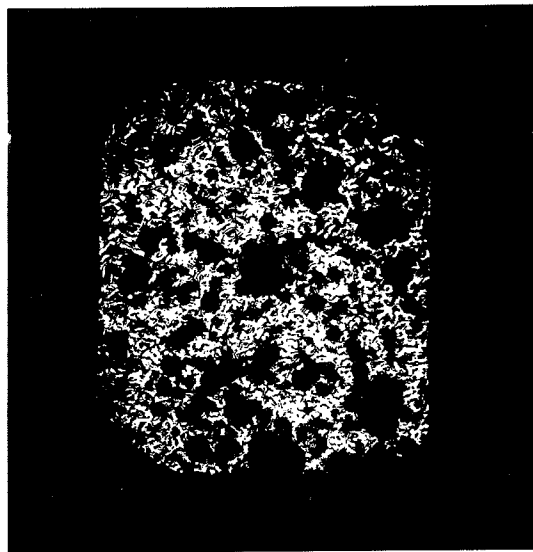
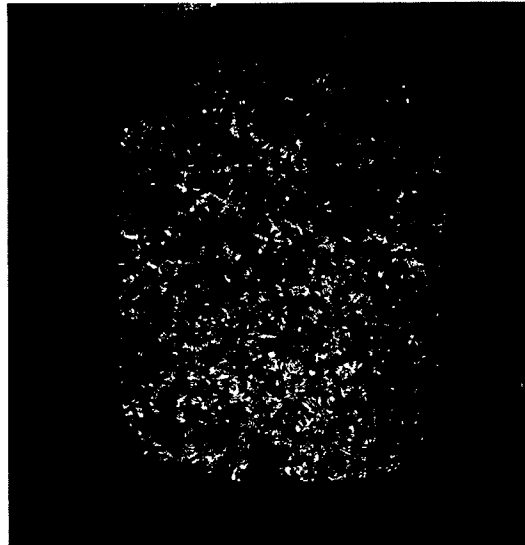
(c) $M'' \sim -15$ (d) $M'' \sim -15$

Fig. 5.29. (a) and (b) are the contact prints of the holograms of bright-field and dark-field images. The diffused reference source of .2mm diameter is located .75m from the hologram plane. (c) and (d) are the bright-field and dark-field reconstructed images.

been drastically increased and the results are shown in photographs (c) and (d) of Fig. 5.29.

5.8 SUMMARY AND COMMENTS

Throughout the experimental studies most of the properties inherent in holography of dark-field transilluminated objects have been distinctly observed, and a few alternative means of generating the reference waves have been discussed.

The holograms have all been recorded with a single lens holocamera, because it allows adjustment of the magnification over a wide range of values by simply changing the position of the objects with respect to the lens. Although the experimental setups were spread over a large area (two optical benches which are two meters apart were used for the configurations requiring a large magnification factor), this situation was not critical because of the original property of the methods using local reference beam generation. These methods automatically compensate for vibrations which are highly detrimental in conventional off-axis holography (refer to Section 6.4).

When recording bright-field images at least 10 times as much power was required from the laser source as was required for recording dark-field images. Only a relatively small amount of energy is required when using a holocamera based on the new method of local reference wave generation by spatial frequency component separation. This is due to the following reasons:

i) In recording a bright-field image the object-to-reference wave intensity ratio has to be larger than 3. It is readily seen that, if 75% of the incident energy is used to process the reference beam, the intensity of the object bearing wave will be reduced to one fourth of its initial value.

ii) The rays diffracted by the object have a relatively low intensity when compared with the intensity of the undiffracted rays. Thus, the removal of the undiffracted rays from the object bearing wave leads to a reduction in the object bearing wave intensity, and thus to a corresponding reduction in the intensity required from the reference wave. (Since the reduction in the object bearing wave is made without any attenuation of the diffracted rays, image details remain very bright.)

PART B

ORIGINAL PRINCIPLES IN HOLOGRAPHIC
INSTRUMENT DESIGN

*Chapter Six*THEORETICAL STUDIES6.1 INTRODUCTION

Holocameras based on the methods of local reference beam generation should in the near future drastically change the conception of holographic apparatus used in imaging of three-dimensional transilluminated objects [57,58]. However, a major drawback inherent in holography with a local reference beam is that it is difficult to maintain the required alignment between the optics of the holocamera and the illuminating beam, which is assumed to be an essentially collimated beam.

In remote measurements of particles, holocameras, which can be either air-borne or placed under water, can be illuminated by a pulsed laser source located and operated from the ground or the surface of the water (see Fig. 6.1). The idea of using holocameras with local optically processed reference beams in remote sensing applications was first put forward in 1975 [57]. The alignment of the holocamera is most critical, due to its relative motion with respect to the laser source and also due to the interaction of the propagation medium (turbulent air or water) with the wavefront of the illuminating beam.

Fortunately, in most of the applications of holographic imaging systems, the laser source can be located close to the holocamera. A typical configuration is shown in Fig. 6.2(a). If the disturbance introduced by the presence of a bulky laser source or holocamera in the vicinity of

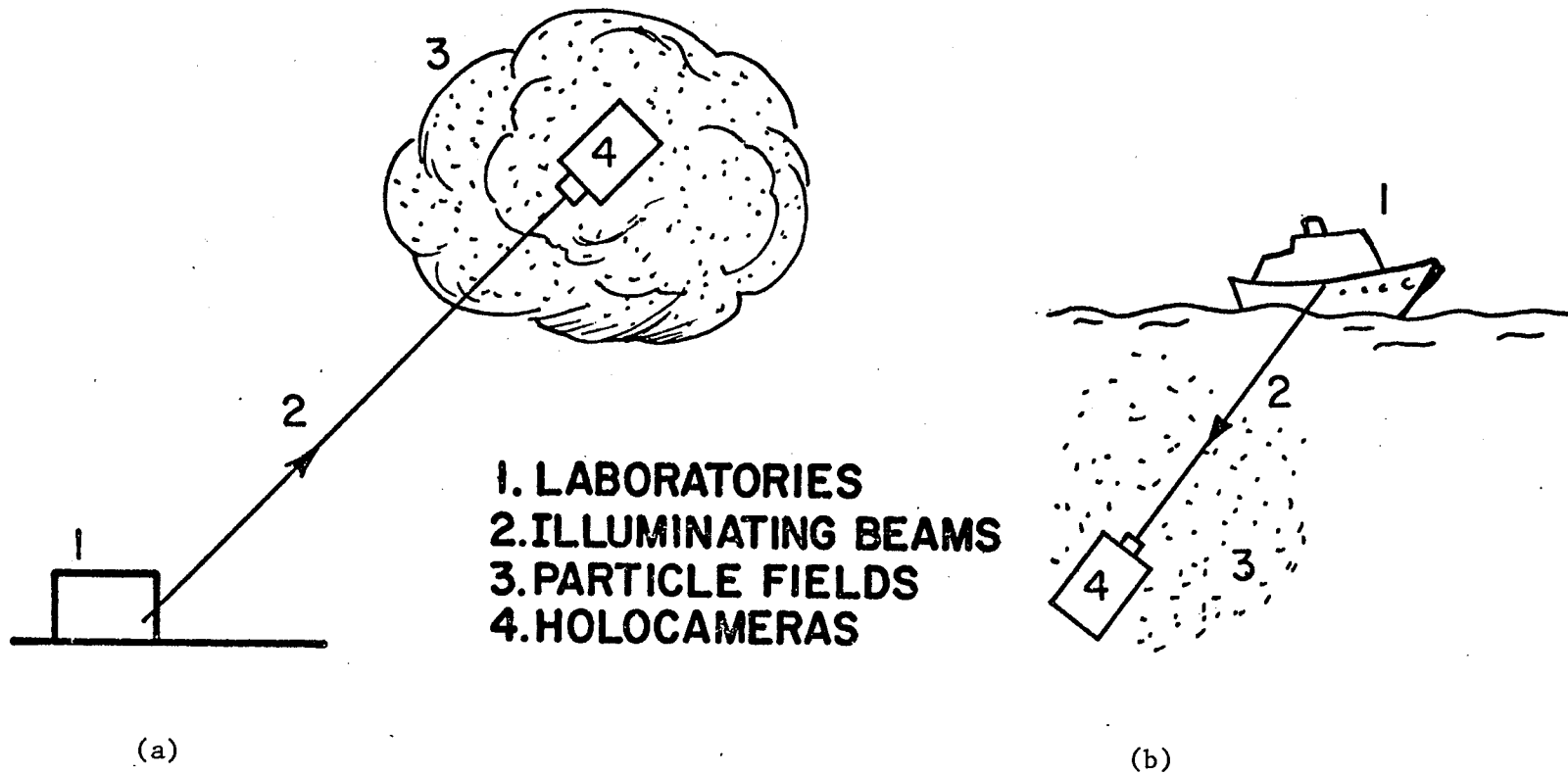


Fig. 6.1 Applications of holocameras with local optically processed reference beams to remote sensing: (a) atmospheric measurements and (b) underwater measurements.

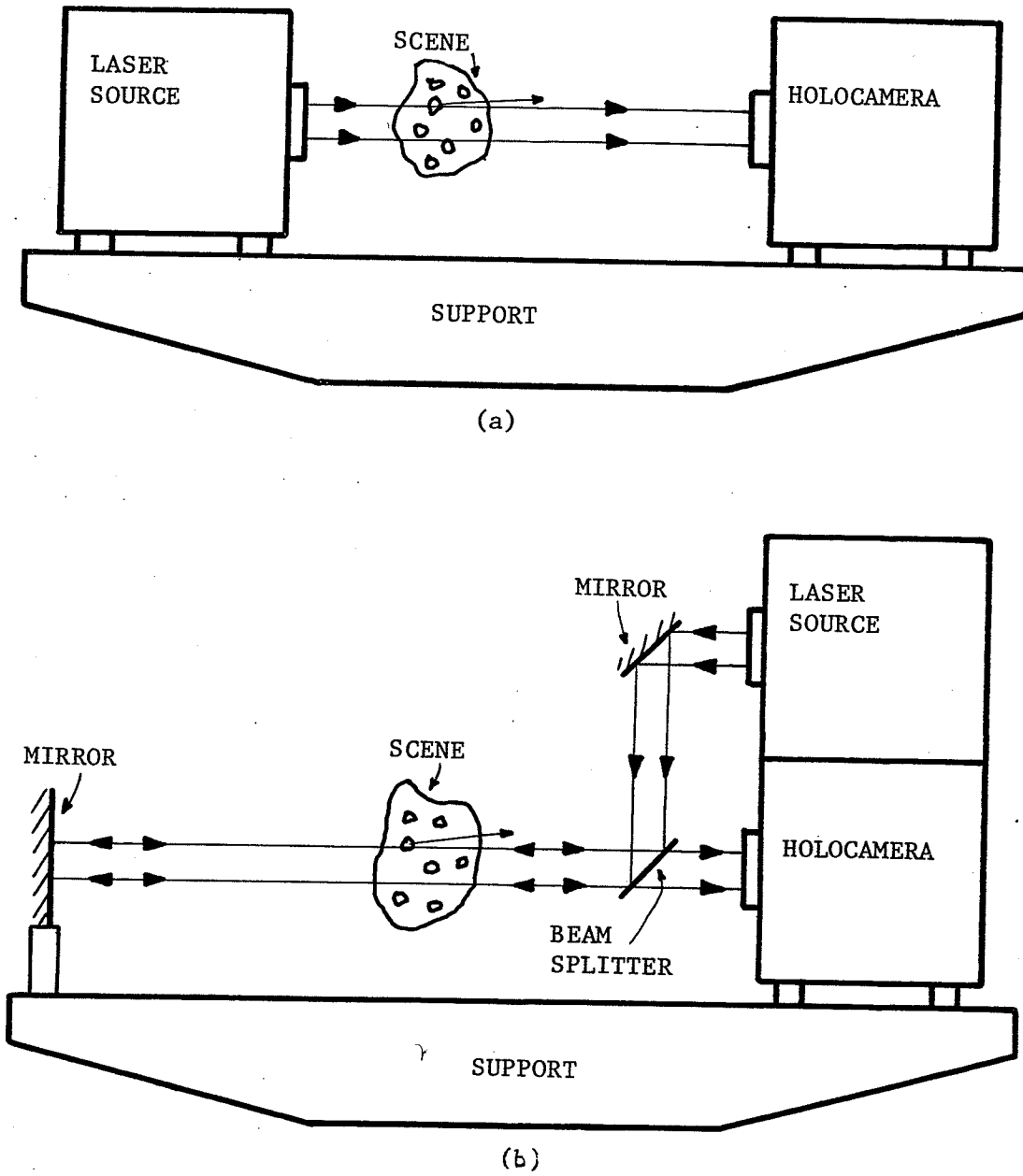


Fig. 6.2 Possible arrangements of the holocamera with respect to the laser source: (a) typical configuration, (b) beam-folded configuration.

the sample volume introduces changes in the physical parameters of the recorded scene, a more favorable configuration, using a mirror, can be implemented in order to limit those changes (see Fig. 6.2(b)). Alignment of the holocamera with the illuminating beam is now less critical than it was in the configuration of Fig. 6.1.

Holocameras with local optically processed reference beams are not practical unless special instruments embodying the holocameras are designed to alleviate the troublesome requirement concerning the alignment. It is the object of the following sections to analyse different instruments which would contribute to a drastic increase in the practicality of the holocameras. The holocameras will be treated as "black boxes" that require perfect alignment with the illuminating beams.

6.2 ELECTROOPTICAL TRACKING SYSTEM

The block diagram of Fig. 6.3 shows the different tasks that must be performed by the system. Since propagation of light through a randomly inhomogeneous medium results in a possible change in the illuminating beam characteristics, namely direction and divergence, and since the optical properties of the propagating medium are time-varying functions, the system must therefore provide an electrooptical feedback to the tracking and alignment equipment of the system. Such a sophisticated system is required in remote measurement applications illustrated in Fig. 6.1.

The implementable system proposed is sketched in Fig. 6.4(a). An auxiliary cw laser is used in connection with a mirror placed on the holo-

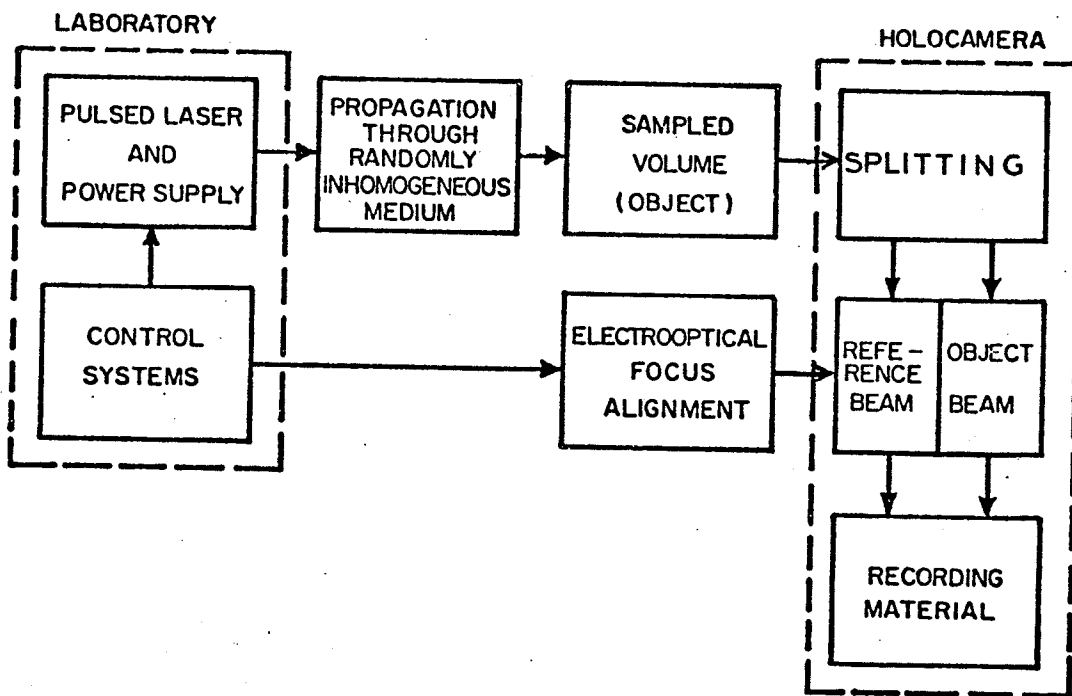
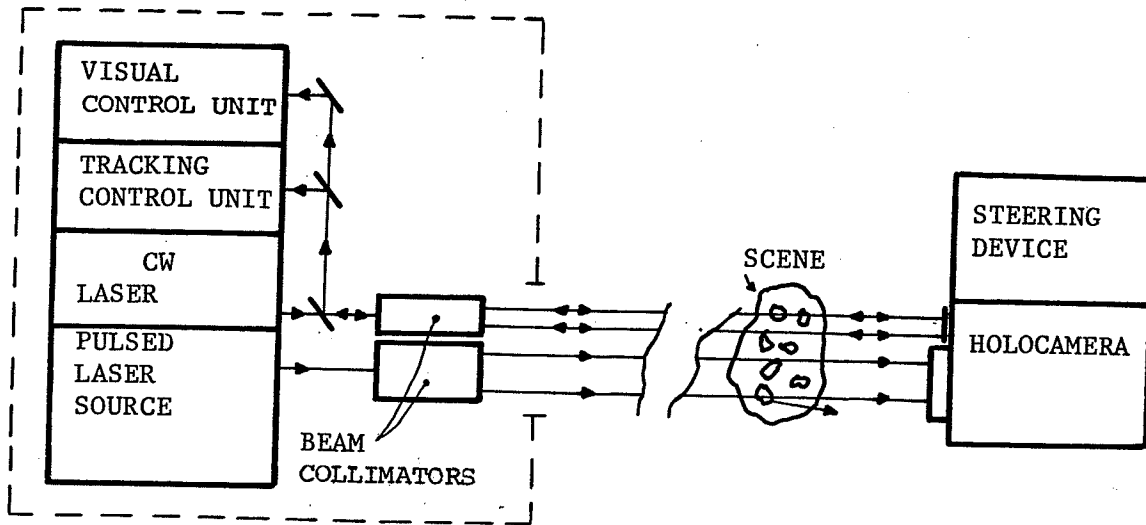
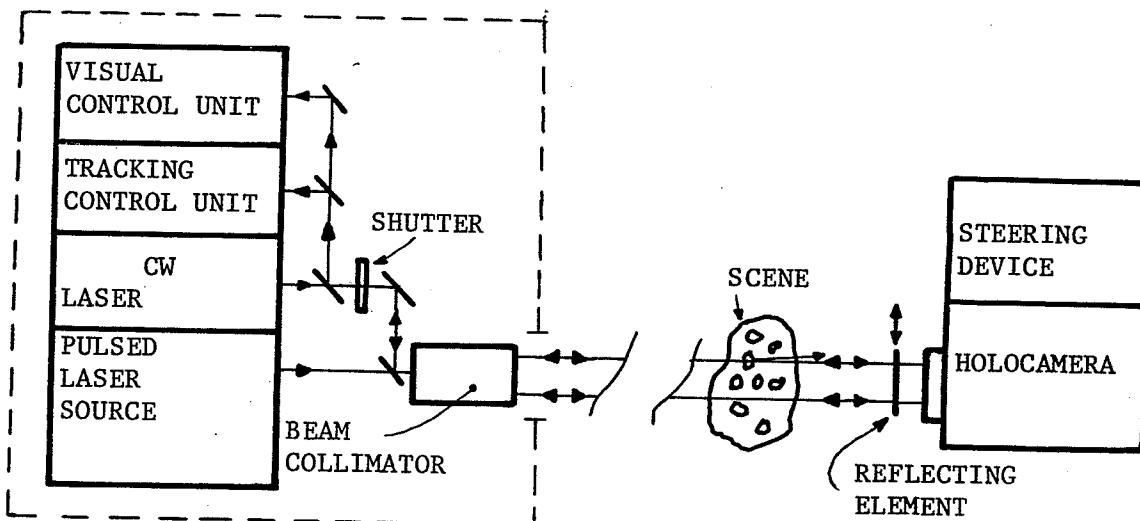


Fig. 6.3 Block diagram.



(a)



(b)

Fig. 6.4 Implementable systems for remote sensing applications: (a) using an auxiliary cw laser and two telescopes, and (b) using an auxiliary cw laser and a single telescope.

camera, and a tracking control device is used to continuously monitor and correct the alignment of the holocamera with the illuminating beam. Both the pulsed laser, which is flashed when holographic recording is desired, and the continuous wave laser propagate along almost identical optical paths. Assuming that the spatial variations in optical parameters of the medium are not appreciable over short distances, and that both laser sources radiate at the same frequency, it appears that the optical paths of the two beams are identical and efficient correction can be accomplished by means of electrooptical feedback. However, if it cannot be assumed that there are slow spatial variations in the medium optical parameters, it becomes necessary to modify the first scheme in such a way that the cw and pulsed laser share the same telescope. Fig. 6.4(b) shows the implementable system. It can be seen that a unique telescope is used for the two laser sources. The reflecting element, which is normally in front of the objective lens of the holocamera, is removed when the pulsed laser is flashed. In addition, a shutter placed in the optical path common to the visual and tracking control units is closed when flashing is triggered. (This prevents hazardous reflected light from entering these units.) The use of radiating sources of the same frequency permits continuous monitoring of the direction of the illuminating beams, since they also share a common optical path. The required exposure can be readily computed by knowing the exact attenuation of the auxiliary beam.

Although no prototype of these two instruments has been built, there is little doubt that future remote sensing holographic systems will be successfully devised. Possible applications of such systems in atmospheric precipitation and pollution measurements are numerous.

The feasibility of using retroreflectors to return a laser beam to the transmitting unit has been proved in recent years. Until the advent of the laser, retroreflectors were already widely used; however, their applications (in radar detection and ranging) were limited to the microwave region of the electromagnetic spectrum. With the availability of laser sources, which radiate in the visible and infrared spectra, the conventional techniques of detection and ranging using retroreflectors were joined by lidar techniques, and the development of Raman spectroscopic techniques for remote sensing. The use of retroreflectors in connection with optical interferometry and measurements, however, had been developed long before the appearance of the first lasers. In 1947 Peck [61] described an interferometer in which the two mirrors of a conventional Michelson interferometer were replaced by a triple set of plane front-surface mirrors mounted to form a corner right angle. Later, Peck used tetrahedral prism reflectors⁴ instead of the trihedral corner reflectors⁵ [62]. In spite of the growing number of applications of retroreflectors, only one experiment describing the use of retroreflectors in holography has so far been disclosed in the literature. In this experiment, Goodman, et al. [63] used a retroreflector attached to the object to provide a strong reflected signal from one zone of the object. This signal served as a reference beam in a lensless Fourier transform holographic arrangement. This section and the two following ones introduce new concepts that allow direct use of retroreflectors in holography.

⁴ Commonly called corner cube reflectors.

⁵ Also called three-mirror reflectors.

Retroreflectors are components that bend all the rays of incident radiation through exactly π rad. Although microwave retroreflectors are usually built from three reflecting metallic surfaces rigidly mounted at right angles to form a corner, there exist several other devices which are used in optics. Trihedral corner reflectors are similar to those used at microwave frequencies, the three conducting planes being replaced by three front-surface mirrors rigorously positioned at right angles to each other (see Fig. 6.5(a)). Positioning and mechanical rigidity of these retroreflectors are critical at optical frequencies, and for these reasons, tetrahedral prism reflectors are preferred. A tetrahedral prism reflector may be considered as simply a corner cut off from a cubical piece of glass, in which the three mutually perpendicular faces of the cube are the reflecting surfaces of the prism, and the cut surface is the face through which light enters and leaves the prism. Other less known but nevertheless effective retroreflector systems exist. The so-called cat's eye retroreflector of Fig. 6.5(b) consists of a convex lens with a spherical mirror at its focal plane. A modified version of the cat's eye consists of two concentric spherical mirrors, the outer one being a concave hemisphere and the inner one being a portion of a convex sphere with a radius roughly half that of the outer reflector (see Fig. 6.5(c)).

Trihedral corner reflectors are chosen in the theoretical investigations which follow. For the front surface mirrors, the law of reflection is directly applied to provide passage from the object space to the image space. The experimental setups, however, will embody tetrahedral prism reflectors. The reason for this choice lies in the fact that it is

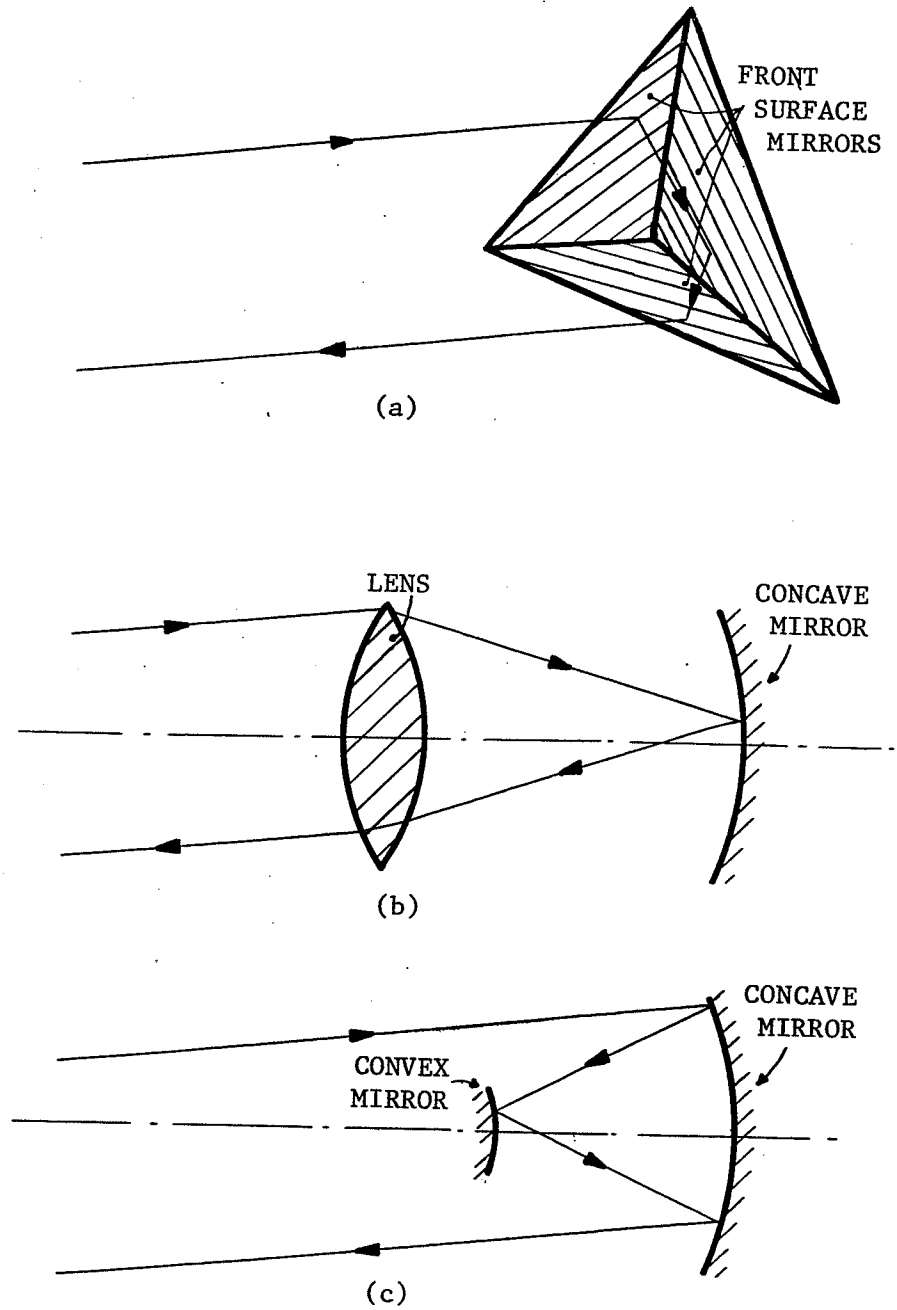


Fig. 6.5 Types of retroreflectors: (a) trihedral corner reflector, (b) cat's eye reflector, (c) modified cat's eye reflector.

feasible to produce tetrahedral prism reflectors of such good tolerances that an emerging ray can be assumed to be essentially antiparallel to the corresponding incident ray. The two properties of trihedral corner reflectors which are useful in the present studies are: firstly, the image space of a point object is found by reflecting the object in the corner point, and secondly, the emergent ray is parallel to the incident, but reversed in direction. These two properties are proved in the following manner.

Consider the general equation of a mirror surface in the rectangular coordinate system $\{x, y, z\}$

$$ax + by + cz + d = 0 \quad (6.1)$$

where a, b, c and d are constant values which characterize the mirror surface. If x_m, y_m and z_m are the coordinates of an object point M , the image point M' , having the coordinates x'_m, y'_m and z'_m , is simply the reflection of M in the mirror and the coordinates are readily obtained

$$\begin{aligned} x'_m &= x_m - 2(ax + by + cz + d)a/e^2 \\ y'_m &= y_m - 2(ax + by + cz + d)b/e^2 \\ z'_m &= z_m - 2(ax + by + cz + d)c/e^2 \end{aligned} \quad (6.2)$$

where $e^2 = a^2 + b^2 + c^2$. The set of Eqs. (6.2) can be arranged in the matrix form as follows

$$\begin{bmatrix} x'_m \\ y'_m \\ z'_m \\ 1 \end{bmatrix} = -e^{-2} \begin{bmatrix} 2a^2 - e^2 & 2ab & 2ac & 2ad \\ 2ab & 2b^2 - e^2 & 2bc & 2bd \\ 2ac & 2bc & 2c^2 - e^2 & 2cd \\ 0 & 0 & 0 & -e^2 \end{bmatrix} \begin{bmatrix} x_m \\ y_m \\ z_m \\ 1 \end{bmatrix} \quad (6.3)$$

Hence it is possible to write

$$[M'] = [T_1] [M] \quad , \quad (6.4)$$

where $[M']$, $[T_1]$ and $[M]$ correspond to the matrices of (6.3). Eq. (6.4) can be generalized for any number of reflections. If $[T_2]$, $[T_3]$, $[T_i]$ are the transform matrices for i mirrors, it follows that the successive reflections can be expressed in mathematical terms by the relation

$$[M'] = [T_i] [T_{i-1}] \dots [T_3] [T_2] [T_1] [M] \quad . \quad (6.5)$$

Hence, in the case of a retroreflector made of three mirrors, the matrix form is

$$[M'] = [T_3] [T_2] [T_1] [M] \quad . \quad (6.6)$$

By choosing a system of rectangular coordinates attached to the trihedral corner reflector such that the three axes lie on the lines of intersection of the three reflecting surfaces (see Fig. 6.6), the equations of the three reflecting surfaces can be simply written

$$\begin{aligned} \text{plane } \{y,z\} & : x = 0 \\ \text{plane } \{z,x\} & : y = 0 \\ \text{plane } \{x,y\} & : z = 0 \end{aligned} \quad (6.7)$$

Assuming that the reflections occur in the plane $\{y,z\}$ first, then in the plane $\{z,x\}$ and finally in the plane $\{x,y\}$, the transform matrices yield

$$[T_3] = \begin{bmatrix} 1 & 0 & 0 & 0 \\ 0 & 1 & 0 & 0 \\ 0 & 0 & -1 & 0 \\ 0 & 0 & 0 & 1 \end{bmatrix} , \quad [T_2] = \begin{bmatrix} 1 & 0 & 0 & 0 \\ 0 & -1 & 0 & 0 \\ 0 & 0 & 1 & 0 \\ 0 & 0 & 0 & 1 \end{bmatrix} , \quad [T_1] = \begin{bmatrix} -1 & 0 & 0 & 0 \\ 0 & 1 & 0 & 0 \\ 0 & 0 & 1 & 0 \\ 0 & 0 & 0 & 1 \end{bmatrix} \quad . \quad (6.8)$$

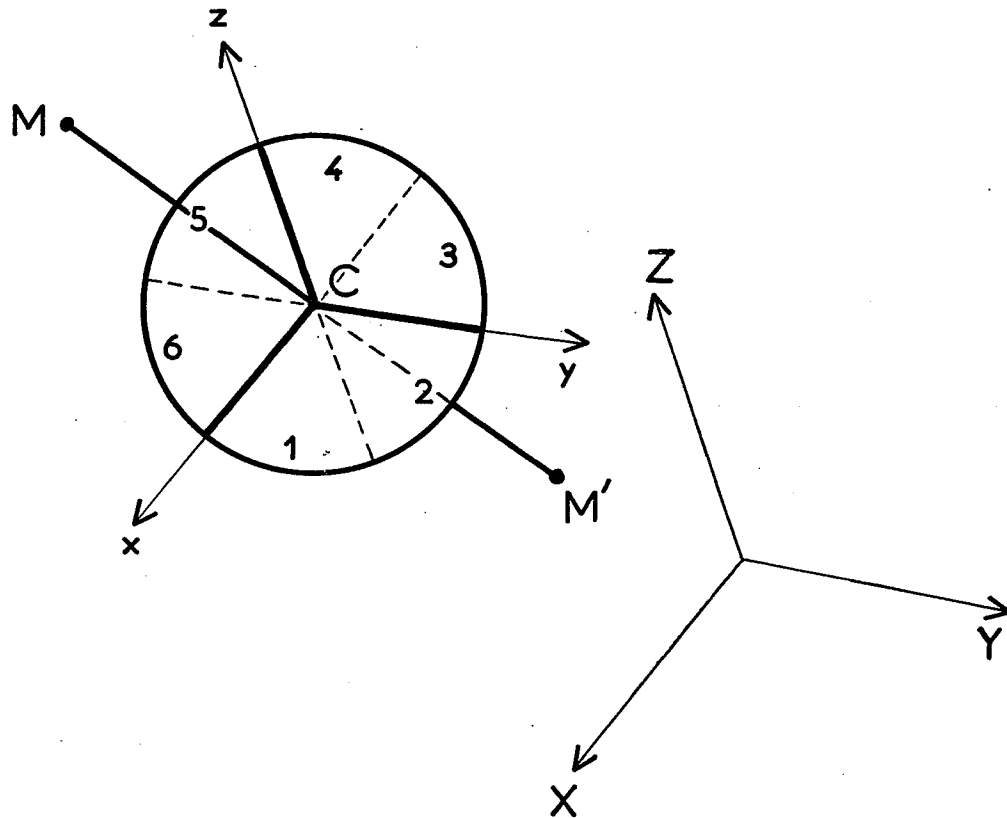


Fig. 6.6 Defining the coordinate systems. The axes of the rectangular system of coordinates x , y and z coincide with the lines of intersection of the three reflecting surfaces; the backward virtual reflections of these lines are shown in dotted lines. The rectangular system of coordinates X , Y and Z has a fixed position with respect to the holocamera.

By substituting the above results into (6.6), it follows that

$$\begin{bmatrix} x'_m \\ y'_m \\ z'_m \end{bmatrix} = \begin{bmatrix} -1 & 0 & 0 \\ 0 & -1 & 0 \\ 0 & 0 & -1 \end{bmatrix} \begin{bmatrix} x_n \\ y_n \\ z_n \end{bmatrix} \quad (6.9)$$

Thus $x'_m = -x_n$, $y'_m = -y_n$, and $z'_m = -z_n$, and the first property is proved. The components of a vector image $N'M'$, corresponding to a vector object NM , can be found by using (6.3)

$$\begin{bmatrix} x'_m - x'_n \\ y'_m - y'_n \\ z'_m - z'_n \end{bmatrix} = -e^{-2} \begin{bmatrix} 2a^2 - e^2 & 2ab & 2ac \\ 2ab & 2b^2 - e^2 & 2bc \\ 2ac & 2bc & 2c^2 - e^2 \end{bmatrix} \begin{bmatrix} x_m - x_n \\ y_m - y_n \\ z_m - z_n \end{bmatrix}, \quad (6.10)$$

where x_n, y_n, z_n and x'_n, y'_n, z'_n are the coordinates of an object point N and its image point N' . Consider again the case of a trihedral corner reflector. Successive multiplication of the matrix transforms of the surfaces $yz, zx,$ and xy leads to the matrix transform of the system. With the rectangular coordinate system of Fig. 6.6, it follows that

$$\begin{bmatrix} x'_m - x'_n \\ y'_m - y'_n \\ z'_m - z'_n \end{bmatrix} = \begin{bmatrix} -1 & 0 & 0 \\ 0 & -1 & 0 \\ 0 & 0 & -1 \end{bmatrix} \begin{bmatrix} x_m - x_n \\ y_m - y_n \\ z_m - z_n \end{bmatrix} \quad (6.11)$$

Eq. (6.11) shows that the vector image is antiparallel to the vector object; thus the second property is proved.

It is readily seen that the property of autoalignment of the emerging beam with respect to the incident beam will provide the starting point in the design of holographic instruments which will embody holocameras with local reference beam generation.

6.4 PRINCIPLE OF THE BEAM-FOLDED CONFIGURATION [59,60]

Consider the configurations shown in Figs.6.2(a) and (b). As pointed out earlier, the alignment of the illuminating beam with the holocamera is critical. Frequent resetting may be needed if vibrations, temperature gradients, and other environmental forces affect the instrument.

Replacing the mirror in the configuration of Fig. 6.2(b) by a trihedral corner reflector (see Fig. 6.5) provides a solution to the alignment problem. The support common to the holocamera, laser source and retro-reflector no longer has to ensure the perfect relative positioning required when using a mirror. The rigidity requirement of the instrument is confined to the ensemble holocamera/laser source. Hence the instrument becomes practical.

6.4.1 Analysis of the Configuration

It is seen in Fig. 6.7 that an expanded laser beam generated by the laser source is folded back by a trihedral corner reflector. After the direction of propagation has changed by π , the collimated beam illuminates the three-dimensional transilluminated scene, which is of interest, and the rays of light scattered by the scene, along with the

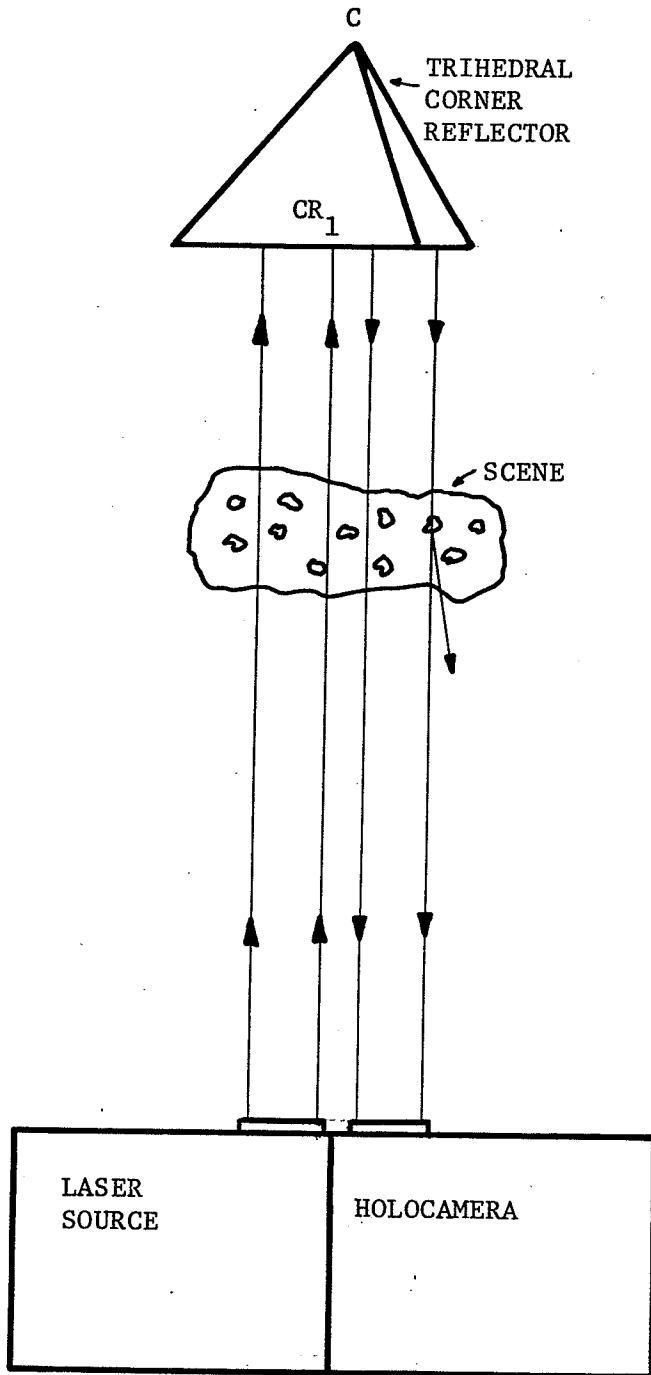


Fig. 6.7 Setup illustrating the basic beam-folded configuration. The undiffracted rays impinging onto the holocamera aperture are always antiparallel to the collimated beam generated by the laser source.

unscattered rays, impinge upon the holocamera. From the light gathered by the holocamera, two different light waves are obtained: first, the object bearing wave and second, the reference wave. The two waves are then brought to interfere in the recording plane where the holographic recording material is positioned. The distance between the retroreflector and the ensemble laser source/holocamera is not limited, and thus the imaged scene is not disturbed and not restricted in its depth dimension. Furthermore, the retroreflector can be moved away without changing the alignment of the laser source with respect to the holocamera. An arbitrary rotation of the retroreflector will not affect the direction of the folded beam. Regardless of angular motion, rotation, or shifting of the retroreflector during exposure of the recording material, stable interference fringes are formed in the recording plane. If there is a rapid translation of the retroreflector, a Doppler shift may be induced by the movement, but since both the object bearing wave and the reference wave are frequency shifted by the same amount, no disturbance in the interference pattern appears.

6.4.2 Effect of the Scene Motion on the Fringe Visibility

In holography it is important that the phase difference between the two interfering beams remain constant during exposure. In order to obtain a good fringe visibility, and therefore high diffraction efficiency during the reconstruction of the hologram, the change in the path difference at the recording plane must be very small. A change of π will shift the fringe position by half a fringe spacing, and if the change occurs during exposure, the recorded fringe modulation will fall to almost

zero and no hologram will be recorded. By scene motion, it is meant relative motion of the scene with respect to the recording medium. It is clear that other motion transferred to any optical element will affect in some way the recorded interference fringes, and motion of the recording material should be much smaller than the smallest fringe spacing (refer to Section 6.4.4).

Although the study of the scene motion may be conducted in many different ways, the present analysis will be based on Goodman's theory, which considers the hologram as being a temporal filter [64].

The total exposure $E(x_4, y_4)$ at a point $P\{x_4, y_4\}$ of the recording material is defined by the integral

$$E(x_4, y_4) = \int_{-T/2}^{T/2} I(x_4, y_4, t) dt \quad , \quad (6.12)$$

where $I(x_4, y_4, t)$ is the irradiance distribution in the recording plane and T represents the exposure time. The object and reference waves in the recording plane are represented by the following complex functions

$$a(x_4, y_4, t) = A(x_4, y_4, t) \exp [i\omega t] \quad (6.13)$$

and

$$b(x_4, y_4) = B(x_4, y_4) \exp [i\omega t] \quad , \quad (6.14)$$

where $\omega = 2\pi\nu$, ν being the optical frequency of the laser source.

Eq. (2.12) gives the expression of the transmission function of a phase hologram when the interfering waves are time-invariant. However, since the case of a time-varying object wave is now considered, the transmission function of a processed phase hologram can be rewritten as follows

$$\tau_1(x_4, y_4) = B^*(x_4, y_4) \int_{-T/2}^{T/2} A(x, y, t) dt \quad (6.15)$$

where a proportionality constant has been omitted, and the term $E(A, B; x_4, y_4)$ in (2.12) is assumed to be unity. By using the definition of the rectangle function

$$\text{rect}(t) = \begin{cases} 1 & |t| \leq 1/2 \\ 0 & \text{otherwise} \end{cases} \quad (6.16)$$

(6.15) can be rewritten as follows

$$\tau_1(x_4, y_4) = B^*(x_4, y_4) \int_{-\infty}^{\infty} \text{rect}(t/T) A(x_4, y_4, t) dt \quad (6.17)$$

The generalized Parseval's formula [65] which is expressed by

$$\int_{-\infty}^{\infty} F_1(t) F_2(t) dt = \int_{-\infty}^{\infty} \mathcal{F}_1[F_1(t)]^* \mathcal{F}_1[F_2(t)] d\omega' \quad (6.18)$$

can be used to rewrite (6.17) in the frequency domain. Hence,

$$\tau_1(x_4, y_4) = B^*(x_4, y_4) T \int_{-\infty}^{\infty} \text{sinc}(\pi T \omega') \mathcal{F}_1[A(x_4, y_4, t)] d\omega' \quad (6.19)$$

The interpretation of the above result is that the effect of uniform exposure of the recording material is entirely equivalent to that of a linear filter having a transfer function

$$H(\omega') = \text{sinc}(\pi T \omega') \quad (6.20)$$

The amplitude of the reconstructed image will be reduced by a factor $\text{sinc}(\pi T \omega')$ if the difference in optical frequencies of the reference and object beams $(\omega'/2\pi)$ is uniform over the recording plane.

A typical recording configuration which can be considered in a systematic study of object motion in holocameras with local optically processed reference beams is shown in Fig. 6.8. This configuration represents a

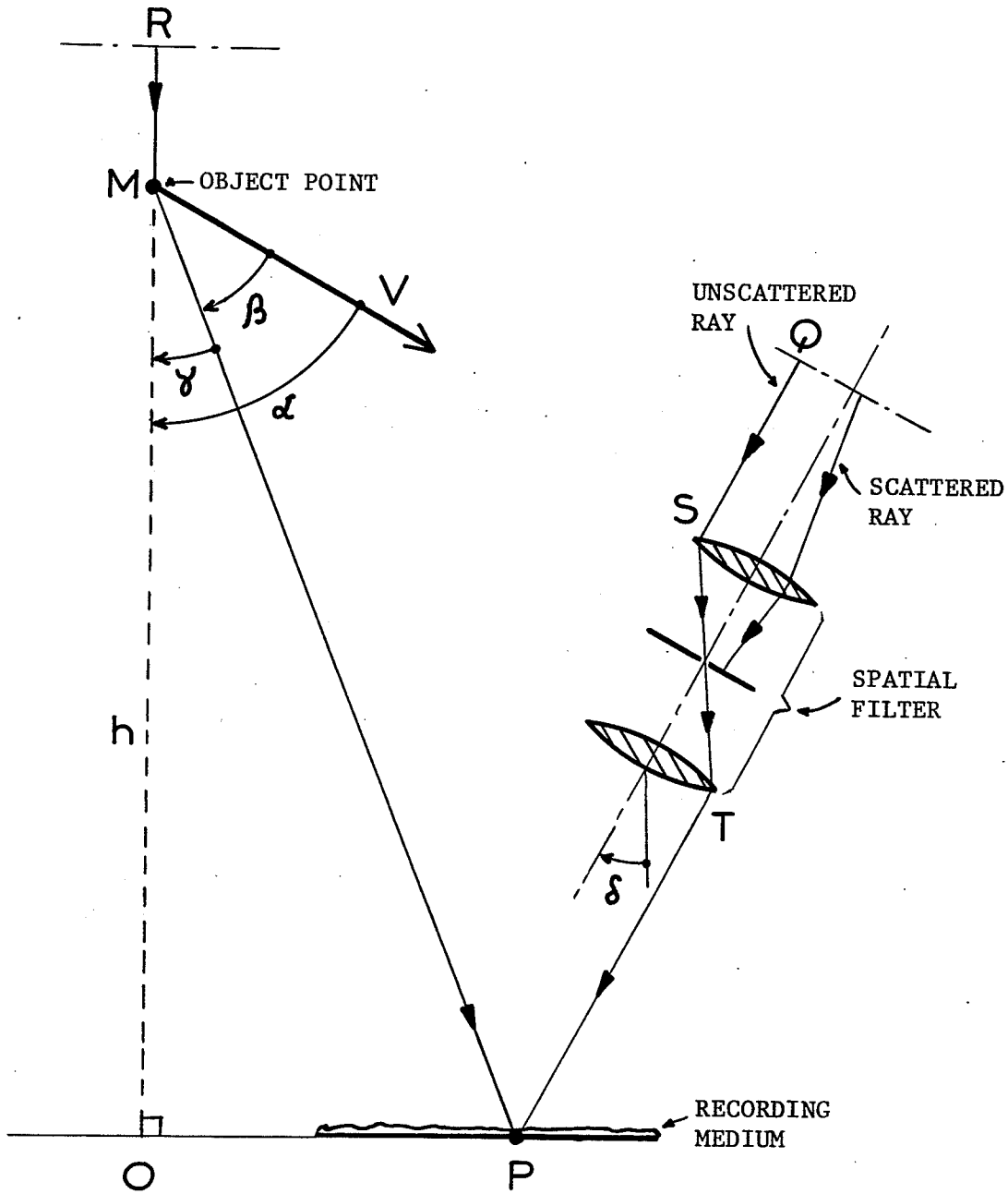


Fig. 6.8 Recording geometry.

holocamera in which the scene is not imaged by any lens prior to recording. It is also representative of the telescope holographic system in which the aerial image is not distorted by a spherical phase factor, and thus a linear motion in the object space is imaged by another linear motion in the aerial image space (refer to (3.29)). However, the configuration of Fig. 6.8 does not represent the two-lens or the single-lens holographic system, since images are affected by a quadratic phase factor, and thus a linear object motion in the object space does not correspond to a linear motion in the aerial image space (as predicted by (3.13) and (3.16)). Fortunately, both the scene and the illuminating beam aerial images are affected by the same quadratic phase factor. Therefore, the overall effect of motion is similar to that encountered in the telescope lens.

Consider now an undiffracted ray TP provided by the reference wave, and a ray MP scattered by a point M of the scene, interfering in a point P of the recording plane $\{x_4, y_4\}$ (see Fig. 6.8). By assuming that the points R and Q are both in phase and are illuminated by two coherent plane waves, the directions of which are parallel to RM and QS respectively, the phase difference between the unscattered and scattered rays at point $P\{x_4, y_4\}$ is given by

$$\Delta[P\{x_4, y_4\}] = (2\pi/\lambda) (\overline{QSTP} - \overline{RMP}) \quad (6.21)$$

If the motion of point M is linear, with velocity v and orientation as shown in Fig. 6.8, it follows that

$$\Delta[P\{x_4, y_4\}] = [\phi_r(x_4, y_4) - \phi_0(x_4, y_4) - (2\pi/\lambda)vt(\cos\beta - \cos\alpha)] \quad (6.22)$$

where $\phi_0(x_4, y_4)$ and $\phi_r(x_4, y_4)$ are the phases of the object and reference

rays at point $P\{x_4, y_4\}$ when $t = 0$.

The phasors $A(x_4, y_4, t)$ and $B(x_4, y_4)$ can be expressed as follows

$$A(x_4, y_4, t) = A_0(x_4, y_4) \exp i[-(2\pi vt/\lambda)(\cos\beta - \cos\alpha) - \phi_0(x_4, y_4)] \quad (6.23)$$

$$B(x_4, y_4) = B_0(x_4, y_4) \exp i[-\phi_r(x_4, y_4)] \quad (6.24)$$

where the angles α and β are shown in Fig. 6.8. Substituting the values of the above phasors into (6.19) gives

$$\tau_1(x_4, y_4) = TB_0(x_4, y_4)A_0(x_4, y_4) \exp i[\phi_r(x_4, y_4) - \phi_0(x_4, y_4)] \int_{-\infty}^{\infty} \text{sinc}(\pi T\omega') \mathcal{F}_1[\exp i(2\pi vt/\lambda)(\cos\alpha - \cos\beta)] d\omega' \quad (6.25)$$

Using the expression of the Dirac delta function

$$\delta(az) = (2\pi)^{-1} \int_{-\infty}^{\infty} \exp(iaz) dt = (1/a)\delta(z) \quad (6.26)$$

(6.25) can be rewritten as follows

$$\tau_1(x_4, y_4) = TB_0(x_4, y_4)A_0(x_4, y_4) \exp i[\phi_r(x_4, y_4) - \phi_0(x_4, y_4)] \int_{-\infty}^{\infty} \text{sinc}(\pi T\omega') \delta[(v/\lambda)(\cos\alpha - \cos\beta) - \omega'] d\omega' \quad (6.27)$$

Finally, using the shifting property of the Dirac delta function, (6.27)

yields

$$\tau_1(x_4, y_4) = TB_0(x_4, y_4)A_0(x_4, y_4) \exp i[\phi_r(x_4, y_4) - \phi_0(x_4, y_4)] \text{sinc}[(\pi Tv/\lambda)(\cos\alpha - \cos\beta)] \quad (6.28)$$

From the above equation, it is readily seen that the fringe visibility on the hologram will be maximum when the sinc function has maximum value, that is, for an argument

$$b = (\pi Tv/\lambda)(\cos\alpha - \cos\beta) = 0 \quad (6.29)$$

In other words, when there is no motion ($v=0$) and when $(\cos\alpha - \cos\beta) = 0$, the fringe contrast will have a maximum value. A case of interest is when the point on the hologram is exactly in the projection of the unscattered ray. For this point (see point $O\{x'_4, y'_4\}$ in Fig. 6.8) the fringe visibility is maximum for any motion vectors. However, as the point of observation in the recording plane is moved away from point $O\{x'_4, y'_4\}$, the visibility decreases until it reaches the value zero (first zero of the sinc function occurs for $b = \pm\pi$), it is therefore possible to retrieve the position of the observation point for which the fringe visibility is zero, and which corresponds to the first zero of the sinc function.

Eq. (6.29) can be transformed by writing

$$\begin{aligned}\cos\beta &= \cos[\alpha - (\alpha - \beta)] \\ &= \cos\alpha \cos(\alpha - \beta) + \sin\alpha \sin(\alpha - \beta)\end{aligned}\quad (6.30)$$

If h is the distance from the scattering point $M\{x_4, y_4\}$ to the recording plane, and if the angles α and β are very small, (6.29) can be transformed, using the relation

$$\begin{aligned}\cos\beta &= \cos[\alpha - (\alpha - \beta)] = \cos\alpha \cos(\alpha - \beta) + \sin\alpha \sin(\alpha - \beta) \\ &\approx \cos\alpha \{1 - [(x_4 - x'_4)^2 + (y_4 - y'_4)^2] / 2h^2\} \\ &\quad + \sin\alpha \{[(x_4 - x'_4)^2 + (y_4 - y'_4)^2]^{1/2} / h\}\end{aligned}\quad (6.31)$$

Hence

$$b = (\pi Tv / \lambda) \{ \cos\alpha - [(1 - g^2 / 2) \cos\alpha] / h^2 - [g \sin\alpha] / h \}, \quad (6.32)$$

where $g = [(x_4 - x'_4)^2 + (y_4 - y'_4)^2]^{1/2} / h$ is a function which represents the effective numerical aperture of the hologram when the point $O\{x'_4, y'_4\}$

is located at the center of the recording plane [66].

For an axial movement (i.e., $\alpha = 0$) (6.32) yields

$$b = (\pi Tv/\lambda) (g^2/2) \quad (6.33)$$

whereas for a transverse motion (i.e., $\alpha = \pi/2$) (6.32) yields

$$b = (\pi Tv/\lambda) (-g) \quad (6.34)$$

By writing $b = \pm\pi$, it is now possible to determine the value of g which gives zero fringe visibility, and thus to obtain the expression for the effective numerical aperture of the hologram. (The effective numerical aperture determines the diffraction-limited image resolution.)

Therefore, it is of importance to know its value when determining the performance of an optical system. Eqs. (6.33) and (6.34) give

$$\begin{aligned} g_a &= \pm [2\lambda/(Tv)]^{1/2} \\ g_t &= \pm \lambda/Tv \end{aligned} \quad (6.35)$$

where g_a and g_t are related to the effective numerical aperture of the hologram in the cases of axial and transverse movements respectively.

Fig. 6.9 shows the variations of g_a and g_t plotted against (vT/λ) , which represents the number of wavelengths the scattering point M moves during the exposure time T .

6.4.3 Effect of Linear Motion on the Image Sharpness

On considering that the transmission function of the processed phase hologram (refer to (6.28)) contributes to the reconstruction of the virtual image, it follows that by illuminating the hologram with a dupli-

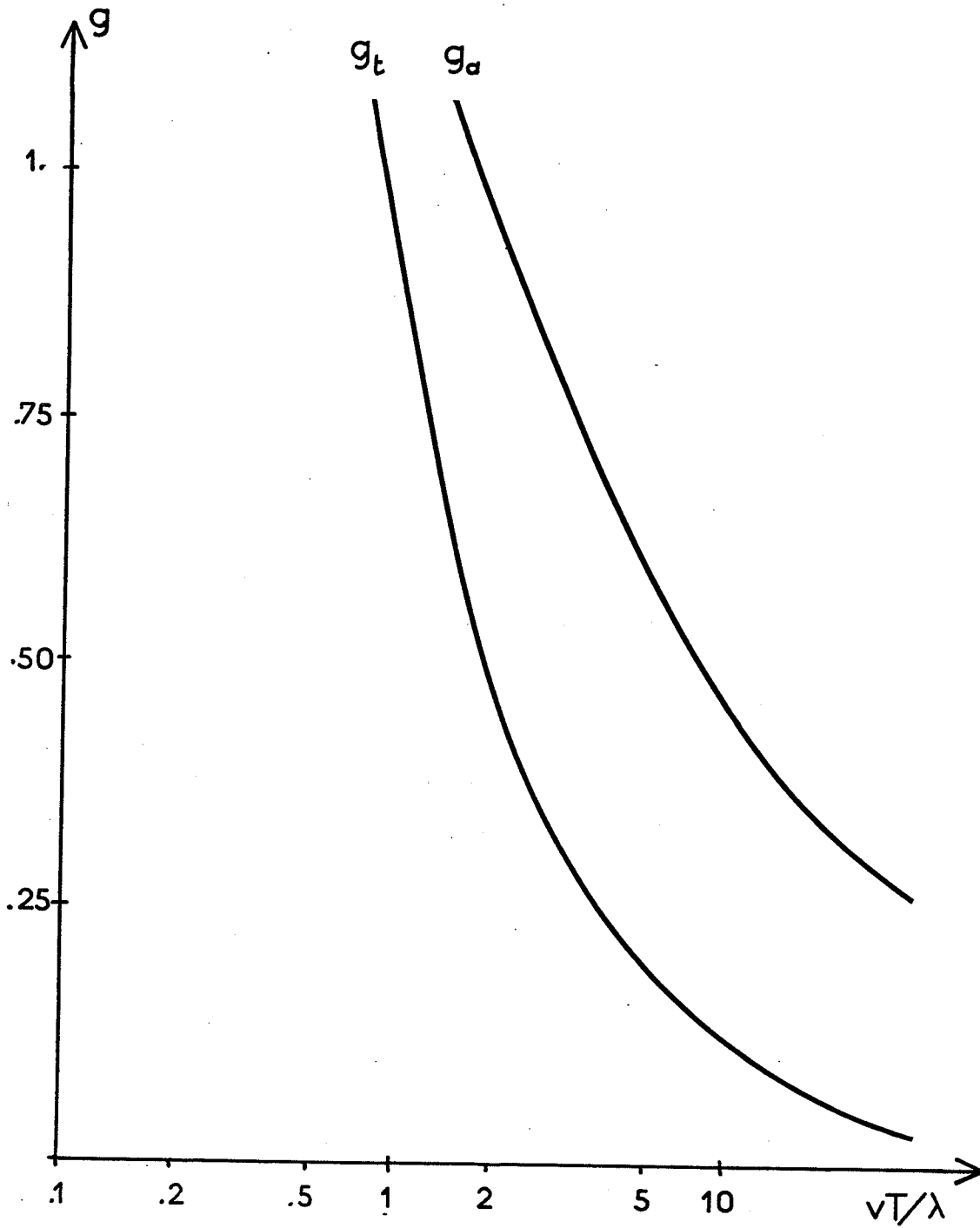


Fig. 6.9 Effective numerical aperture of the hologram as a function of the number of wavelengths of scene motion (g_a for axial motion and g_t for transverse motion).

cate of the reference wave $B(x_4, y_4)$, the expression of the image field distribution is given by

$$O(x_4, y_4) \propto |B(x_4, y_4)|^2 A_0(x_4, y_4) \exp[-i\phi_0(x_4, y_4)] \text{sinc}\left[\frac{\pi T v}{\lambda} (\cos\alpha - \cos\beta)\right] \quad (6.36)$$

It is desirable to determine a source that would give such a field distribution on the hologram. Neumann [66] found that a line source of length $\ell = vT$, centered at $t=0$, lying in the direction of the velocity vector v (see Fig. 6.10) and having a linear phase variation $(2\pi z/\lambda)(-\cos\alpha)$ gives rise to a field distribution which is expressed as

$$\psi(x_4, y_4) \propto vT \exp(-i2\pi p_0/\lambda) \text{sinc}\left[\frac{\pi T v}{\lambda} (\cos\alpha - \cos\beta)\right] \quad (6.37)$$

where p_0 is the distance between the middle of the line and the point P , and $p_0 \gg \ell$.

Comparing (6.36) with (6.37), it can be seen that they are similar. Thus, the reconstructed image of the moving scattering point M is a line image of length (vT) .

In conclusion, object motion affects the spatial modulation of the recorded fringe contrast and therefore limits the effective numerical aperture of the hologram. In addition, the image of a scattering point is seen as if the recorded scene were that of a line of length (vT) . The overall effects on the reconstructed image quality are: firstly, a reduction in the diffraction-limited image resolution and secondly, a loss of image sharpness identical to that of a conventional photograph of a moving scene. However, in spite of a reduction in image quality, under normal experimental conditions, object motion does not jeopardize the holographic

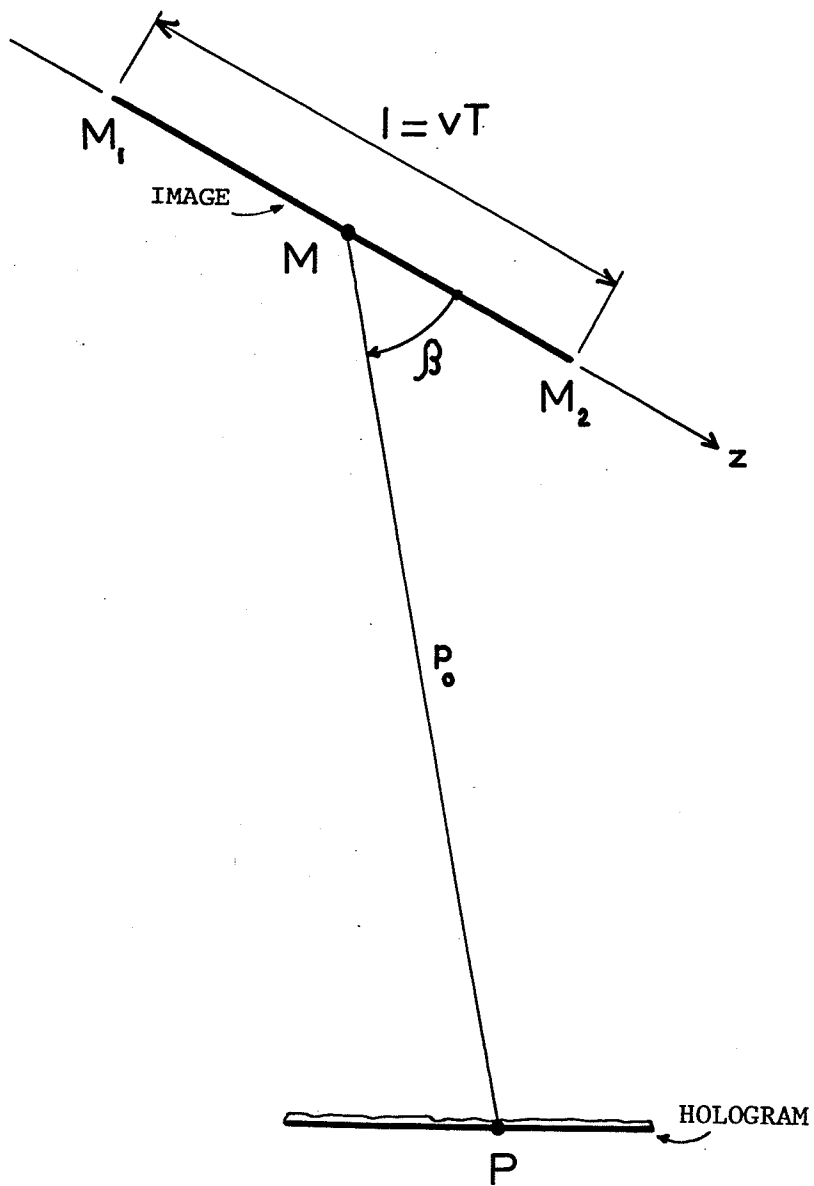


Fig. 6.10 Reconstructed image of a point object having a linear motion.

process. This point will be substantiated by the experimental investigations in Chapter Seven. A theoretical comparison of the sensitivity to object motion of holograms of transilluminated objects with the sensitivity of holograms of diffusely reflecting objects shows that the former type of hologram is much less sensitive to object motion, and that maximum-contrast fringes are recorded regardless of the direction of motion [66].

6.4.4 Effect of Linear Recording Medium Motion

An analysis similar to that of Section 6.4.2 is repeated. However, in the present situation, the phase of the reference wave in one point of the recording medium $P\{x_4, y_4\}$ is no longer constant. According to Fig. 6.8 the phases of the waves at a point $P\{x_4, y_4\}$ in the recording medium are

$$\phi_0(x_4, y_4, t) = \phi_0(x_4, y_4) + (2\pi tv/\lambda) \sin\gamma \quad (6.38)$$

for the object wave and

$$\phi_r(x_4, y_4, t) = \phi_r(x_4, y_4) - (2\pi tv/\lambda) \sin\delta \quad (6.39)$$

for the reference wave ($\phi_0(x_4, y_4)$ and $\phi_r(x_4, y_4)$ being the phases of the object and reference beams at $t=0$). Therefore, the expression of the phasors are

$$A(x_4, y_4, t) = A_0(x_4, y_4) \exp[-i\phi_0(x_4, y_4) - i(2\pi tv/\lambda) \sin\gamma] \quad (6.40)$$

and

$$B(x_4, y_4, t) = B_0(x_4, y_4) \exp[-i\phi_r(x_4, y_4) + i(2\pi tv/\lambda) \sin\delta] \quad (6.41)$$

Since both the reference and the object waves have a time-varying phase at point $P\{x_4, y_4\}$, it follows that the transmission function of the

processed hologram can now be expressed as

$$\tau_1(x_4, y_4) = \int_{-\infty}^{\infty} \text{rect}(t/T) B^*(x_4, y_4, t) A(x_4, y_4, t) dt \quad (6.42)$$

where the definition of $\text{rect}(t/T)$ is given by (6.16). By using again the generalized Parseval's formula [65], (6.42) can be rewritten in the frequency domain, giving

$$\tau_1(x_4, y_4) = \int_{-\infty}^{\infty} \text{sinc}(\pi T \omega') \int_1^2 [A(x_4, y_4, t) B^*(x_4, y_4, t)] d\omega' \quad (6.43)$$

After substitution of the expressions of the phasors $A(x_4, y_4, t)$ and $B(x_4, y_4, t)$ into the last equation, the integration is carried on as in Section 6.4.2 and the final result is given by

$$\tau_1(x_4, y_4) = TB_0(x_4, y_4) A_0(x_4, y_4) \exp i[\phi_r(x_4, y_4) - \phi_0(x_4, y_4)] \text{sinc}[(\pi T v / \lambda) (\sin \delta - \sin \gamma)] \quad (6.44)$$

Eqs. (6.44) and (6.28) have a similar form. Thus, the sinc function will modulate again the fringe visibility over the hologram aperture. It is worthwhile to mention that the first zero of the sinc function occurs when

$$(\sin \delta - \sin \gamma) / \lambda = (T v)^{-1} \quad (6.45)$$

that is, when the spatial frequency of the recorded fringes is $(T v)^{-1}$.

In conclusion, maximum-contrast fringes at point $P\{x_4, y_4\}$ are recorded only if the displacement $(T v)$ of the recording medium during exposure is much smaller than the fringe spatial period at $P\{x_4, y_4\}$.

6.4.5 Effect of the Retroreflector Motion

Since both the object and the reference waves are derived from the same illuminating beam, and since the illuminating beam is folded by the retroreflector prior to the separation of the reference wave from the object wave, an axial displacement of the corner point of the retroreflector induces an identical phase shift into the two interfering waves. Thus, in the absence of any other motion, the phasors $A(x_4, y_4, t)$ and $B(x_4, y_4, t)$ can be expressed as follows

$$A(x_4, y_4, t) = A_0(x_4, y_4) \exp i[-\phi_0(x_4, y_4) - \phi_i(t)] \quad (6.46)$$

and

$$B(x_4, y_4, t) = B_0(x_4, y_4) \exp i[-\phi_r(x_4, y_4) - \phi_i(t)] \quad (6.47)$$

where $\phi_0(x_4, y_4)$ and $\phi_r(x_4, y_4)$ have been defined earlier and where $\phi_i(t)$ represents the phase shift created by the retroreflector motion. The change of path length in the object wave is matched by a similar change of path length in the reference wave. By substituting the last two expressions into (6.42), the transmission function of the processed phase hologram is readily obtained. Its expression is given by

$$T_1(x_4, y_4) = TB_0(x_4, y_4) A_0(x_4, y_4) \exp i[\phi_r(x_4, y_4) - \phi_0(x_4, y_4)] \quad (6.48)$$

Hence, by assuming that the retroreflector is perfect, and that the extent of the plane wave constituting the reference beam is much larger than the retroreflector displacement during exposure (Tv), it follows that the effect of the retroreflector motion does not affect the fringe visibility. This is shown in (6.48). It must be pointed out that the above statement is true for any type of retroreflector motion (transverse,

axial, rotating). In addition, the Doppler frequency shift induced in the object wave by an axial displacement of the retroreflector is exactly matched by a similar frequency shift in the reference wave, and therefore the mutual coherence of the interfering waves is preserved. For a non-linear motion, the frequency shift is a time-varying function. However, for very small frequency shifts, the change in fringe spacing is unnoticeable; thus the fringe contrast is unaffected by a non-linear retroreflector motion.

6.5 PRINCIPLE OF THE TWO-RETROREFLECTOR CONFIGURATION [67,60]

It is clear that although the beam-folded configuration provides better fringe contrast than any other configuration, regardless of the direction of the scene motion, the fringe contrast is nevertheless modulated over the surface of the hologram when scene motion occurs. The detrimental effects of this fringe contrast modulation are: firstly, a loss in diffraction-limited image resolution, secondly, a loss of brightness of the reconstructed image and, thirdly, a blurring of the reconstructed image similar to the usual blurring resulting from time integration of a moving image.

In 1967, a method of reducing the fringe contrast modulation by adjusting the path length of the reference wave in order to match any change in path length of the object wave, was proposed by Neumann and Rose [68]. The success of this method was only partial, as adjustments could be performed only for a change in optical path of the order of a few wavelengths, and only over a limited area about the hologram center. Thus, since the correction was achieved for only the hologram center, the detrimental

effects listed above were diminished but not cancelled.

A new holographic configuration which uses the synchronized motion of one or two retroreflectors to compensate totally for the scene motion in any direction, is disclosed in the section which follows.

6.5.1 Analysis of the Configuration

The holographic configuration is shown in Fig. 6.11. The laser source provides an expanded collimated beam which is steered by the first front surface mirror M_1 onto the first retroreflector CR_1 . Assuming that the retroreflector CR_1 is a perfect element, the emerging beam is laterally shifted and the direction of propagation is opposite to that of the incident beam. The second retroreflector CR_2 , in its turn, shifts and changes the direction of propagation of the incident beam. Finally, the second front surface mirror M_2 steers the beam emerging from CR_2 onto the holocamera in which the reference wave is separated from the object bearing wave, and where the object wave is eventually filtered prior to recording. It must be added that if the scene is extended over a large volume, the illuminating beam will propagate twice across the scene, but along different paths (because the retroreflector CR_1 shifts the beam).

As it will be shown in the next section, total scene motion compensation is obtained by synchronizing the motion of at least the retroreflectors CR_2 in such a way that the direction of motion is exactly that of the scene, and the magnitude of the vector velocity is one-half that of

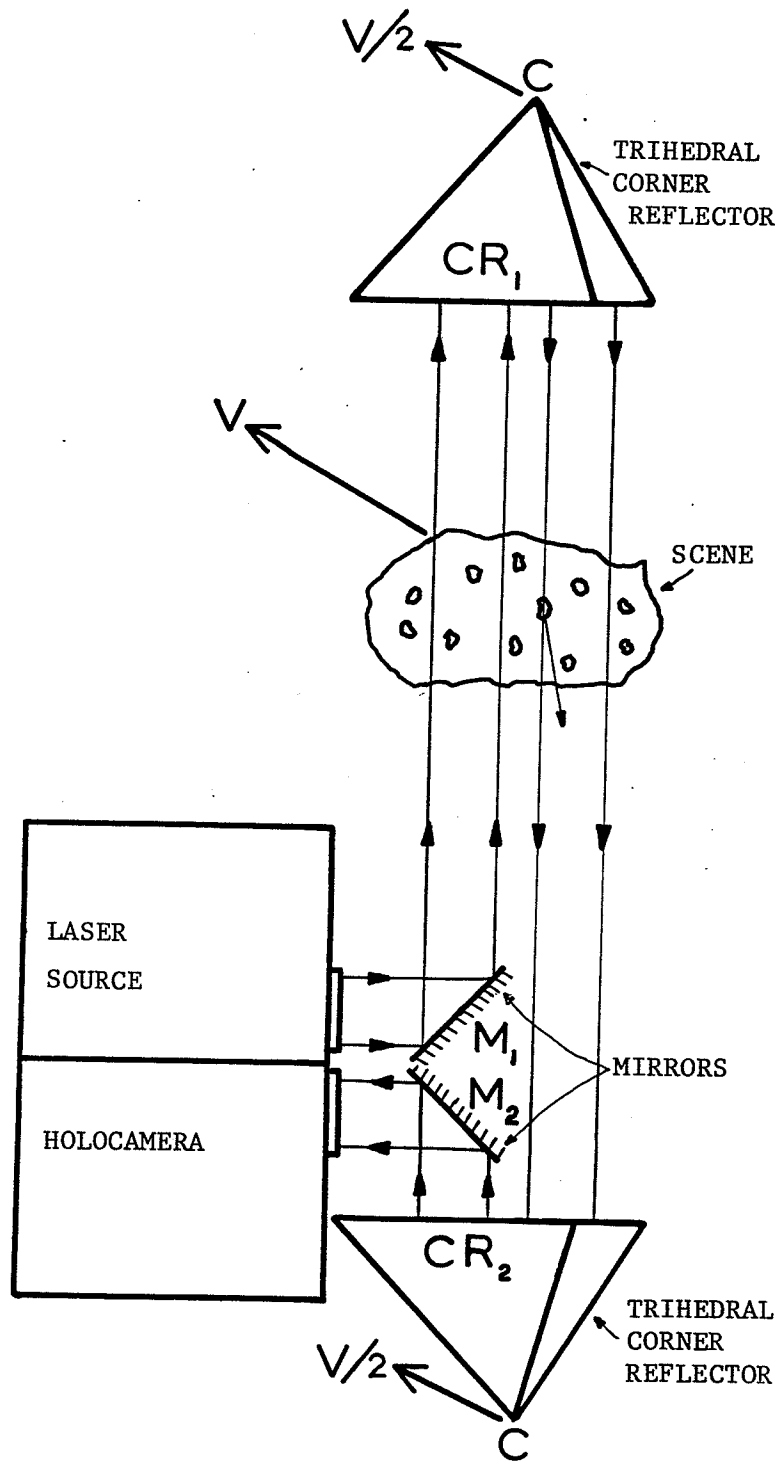


Fig. 6.11 Modified beam-folded configuration. This configuration is well suited to holographic imaging of moving scenes. The scene motion is compensated for by synchronizing the motion of the retroreflectors with that of the scene.

the scene. An electro-optical feedback control system may be devised to provide the required synchronization.

6.5.2 Total Compensation of the Object Motion

Consider the schematic diagram of Fig. 6.6. The mobile rectangular system of coordinates $\{x,y,z\}$ is attached to the three lines which result from the intersection of the three reflecting surfaces of the retroreflector CR_2 . The rectangular coordinate system $\{X,Y,Z\}$ has a fixed position with respect to the holocamera, the laser source and the two mirrors M_1 and M_2 (see Fig. 6.11), and its axes are parallel to the axes x,y and z respectively. The system $\{x,y,z\}$ can translate in any direction, however it cannot rotate around C . The coordinates of the points M , M' and C are defined as follows

$$M \begin{cases} X_m = X_{m0} + \int_0^t \dot{X}_m dt \\ Y_m = Y_{m0} + \int_0^t \dot{Y}_m dt \\ Z_m = Z_{m0} + \int_0^t \dot{Z}_m dt \end{cases} \quad (6.49)$$

$$M' \begin{cases} X'_m = X'_{m0} + \int_0^t \dot{X}'_m dt \\ Y'_m = Y'_{m0} + \int_0^t \dot{Y}'_m dt \\ Z'_m = Z'_{m0} + \int_0^t \dot{Z}'_m dt \end{cases} \quad (6.50)$$

and

$$C \begin{cases} X_c = X_{c0} + \int_0^t \dot{X}_c dt \\ Y_c = Y_{c0} + \int_0^t \dot{Y}_c dt \\ Z_c = Z_{c0} + \int_0^t \dot{Z}_c dt \end{cases} \quad (6.51)$$

where the dot on a variable is the operator (d/dt) , and $X_{m0}, Y_{m0}, Z_{m0}, X'_{m0}, Y'_{m0}, Z'_{m0}, X_{c0}, Y_{c0}$ and Z_{c0} are the values of the coordinates at $t=0$. Eq. (6.9) can be directly used to provide a relationship between the coordinates of object point M and the image point M' . Making use of the relations

$$\begin{aligned}x_m &= X_m - X_c \\y_m &= Y_m - Y_c \\z_m &= Z_m - Z_c\end{aligned}\tag{6.52}$$

and

$$\begin{aligned}x'_m &= X'_m - X'_c \\y'_m &= Y'_m - Y'_c \\z'_m &= Z'_m - Z'_c\end{aligned}\tag{6.53}$$

it follows that

$$\begin{bmatrix} X'_{m0} + \int_0^t \dot{X}'_m dt - X_{c0} - \int_0^t \dot{X}_c dt \\ Y'_{m0} + \int_0^t \dot{Y}'_m dt - Y_{c0} - \int_0^t \dot{Y}_c dt \\ Z'_{m0} + \int_0^t \dot{Z}'_m dt - Z_{c0} - \int_0^t \dot{Z}_c dt \end{bmatrix} = \begin{bmatrix} -1 & 0 & 0 \\ 0 & -1 & 0 \\ 0 & 0 & -1 \end{bmatrix} \begin{bmatrix} X_{m0} + \int_0^t \dot{X}_m dt - X_{c0} - \int_0^t \dot{X}_c dt \\ Y_{m0} + \int_0^t \dot{Y}_m dt - Y_{c0} - \int_0^t \dot{Y}_c dt \\ Z_{m0} + \int_0^t \dot{Z}_m dt - Z_{c0} - \int_0^t \dot{Z}_c dt \end{bmatrix}\tag{6.54}$$

There is total compensation for the object point motion only if

$$\dot{X}'_m = \dot{Y}'_m = \dot{Z}'_m = 0\tag{6.55}$$

By differentiating (6.54) with respect to t , and by using (6.55), the

following is obtained

$$\begin{aligned}\dot{X}_m &= 2\dot{X}_c \\ \dot{Y}_m &= 2\dot{Y}_c \\ \dot{Z}_m &= 2\dot{Z}_c\end{aligned}\tag{6.56}$$

It is seen that there is perfect compensation for the point object motion when the vector velocity of the corner point c is parallel to the velocity vector of the object point but with a magnitude one-half that of the object point. Consequently, perfect compensation for the scene motion can be achieved if the scene translates (in any direction) but does not rotate.

6.5.3 Comments

- i) It is seen from Fig. 6.11 that for large transverse object displacements when the illuminating beam has a Gaussian profile, the object irradiance is a time-varying function. In order to maintain a time-invariant scene irradiance, it is necessary to synchronize the transverse motion of translation of the retroreflector CR_1 with that of the retroreflector CR_2 . Thus, it is seen that transverse object displacements are only limited by the dimensions of the retroreflectors. An electrooptical feed back system capable of monitoring the displacement of the object is, however, required when the scene motion is unknown.
- ii) When large transverse scene displacements are not required, a front surface mirror can be substituted for the retroreflector CR_1 . However, alignment of the holocamera with the illuminating beam is then more critical.

iii) Axial object displacements are limited only by the positions of the retroreflectors; thus, very large axial displacements can easily be compensated for.

iv) In order to improve the practicality of moving the retroreflectors at high speed, it may be preferable to rotate them around an axis which does not coincide with the corner point (see Fig. 6.12). Compensation for the transverse scene displacements is complete; however, there is no compensation for the axial scene displacements. From (6.56) it is found that for a transverse scene displacement $\int_0^t \dot{z}_t dt$, the corner point C of the retroreflector CR_2 must have a transverse displacement

(1/2) $\int_0^t \dot{z}_t dt$. Now

$$\int_0^t \dot{z}_t dt = 2\rho_c \{ \sin[\theta_0 + \int_0^t \dot{\theta} dt] - \sin(\theta_0) \} \quad (6.57)$$

where ρ_c is the distance from the corner point C to the axis O, θ is the angle shown in Fig. 6.12 and θ_0 is the value of θ at $t=0$. Assuming that $\theta_0 \ll 1$ and that $[\theta_0 + \int_0^t \dot{\theta} dt] \ll 1$, (6.57) gives

$$\dot{\theta} = \dot{z}_t / (2\rho) \quad (6.58)$$

It can easily be shown that the induced relative axial image motion with respect to the holocamera is

$$\begin{aligned} \int_0^t \dot{z}_a dt &= 2\rho_c \{ \cos(\theta_0) - \cos[\theta_0 + \int_0^t (\dot{z}_t / 2\rho_c) dt] \} \\ &= (1/4\rho_c) \left[\int_0^t \dot{z}_t dt \right]^2 + \theta_0 \int_0^t \dot{z}_t dt \quad (6.59) \end{aligned}$$

This last result indicates that the transverse scene displacement is changed into a much smaller axial image displacement. This situation is quite favorable since axial image motion does not noticeably affect the

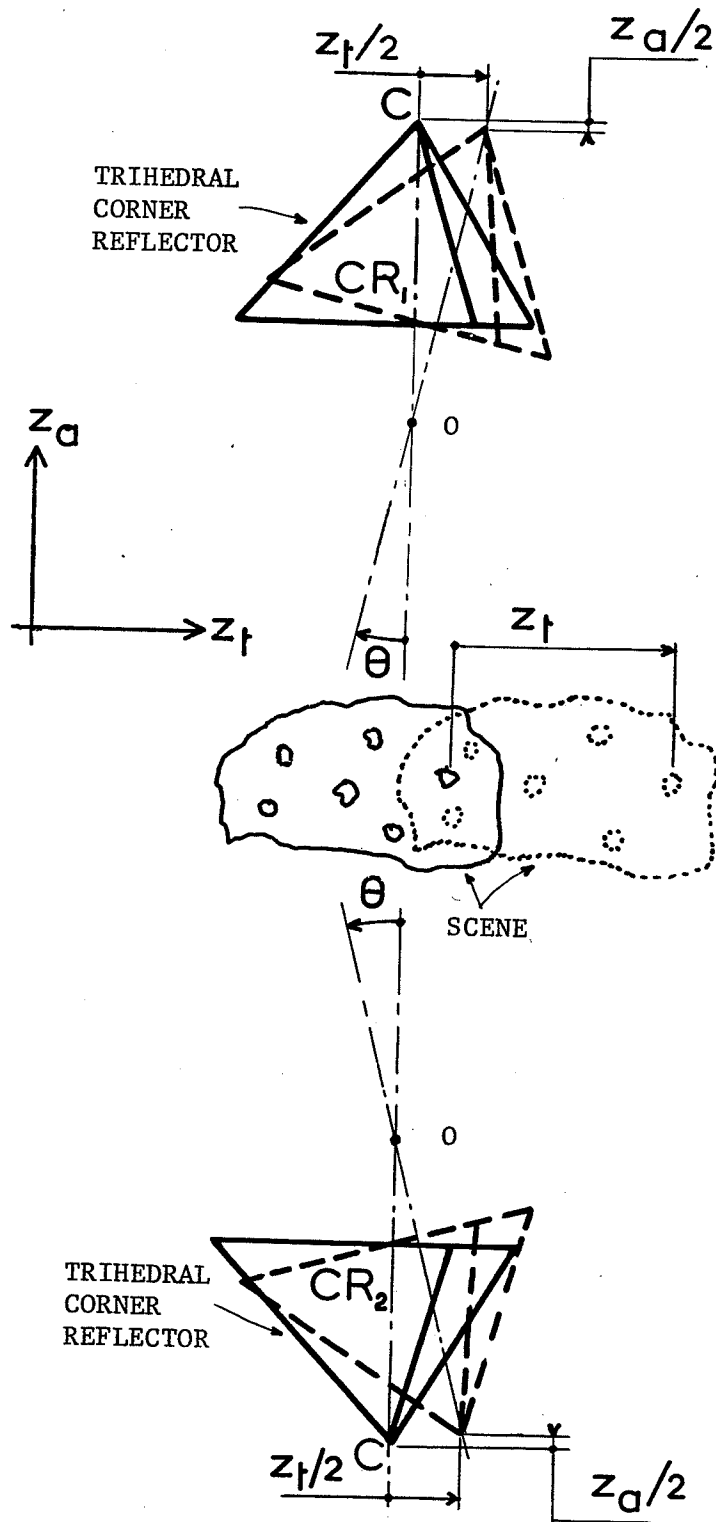


Fig. 6.12 Compensation for transverse scene displacements can be implemented by synchronizing the rotation of the retroreflectors around points which do not coincide with the corner points.

sharpness of the reconstructed image (see Section 6.4.3), and since the effective diffraction-limited image resolution is better than that of a similar transverse image displacement (see Fig. 6.9).

In order to keep the scene irradiance constant during exposure, the retroreflector CR_1 must be rotated in such a way that its angular velocity is equal but opposite in direction to that of the retroreflector CR_2 .

The configuration encompassing rotating retroreflectors may be preferred to the one equipped with translating retroreflectors when only transverse scene displacements are to be compensated for and when the velocity of the scene motion is relatively large.

Note that vibrating transilluminated objects could be holographically recorded by using a cw laser if the period of revolution were exactly that of the vibrating object. This could be done by chopping the illuminating beam in such a way that the total exposure time T would be equal to the sum of (n) successive short exposures ΔT . Thus,

$$T = (n)\Delta T \quad , \quad (6.60)$$

where (n) is an integer larger than or equal to one. If T_1 is the period of vibration, the inequality $\Delta T \ll T_1$ must hold.

6.6

PRINCIPLE OF THE CONFIGURATION ALLOWING IMAGING OF HYPER-
VELOCITY TRANSILLUMINATED SCENES [69,70]

Holography of hypervelocity transilluminated scenes is a field of great interest because of its potential applications in connection with imaging of atmospheric particle fields from aircraft, and monitoring of aerosols emitted, for instance, by rocket injectors. Holographic recording of moving scenes [5] requires the use of pulsed lasers generating a pulse of very short duration. Although pulsed laser units generating a pulse of $\sim 10\eta$ sec are commercially available, technological advances are presently limited. For particle fields having a relative velocity of 150m sec^{-1} with respect to holocameras mounted in aircraft, the magnitude of the relative displacement occurring during a pulse duration of 10η sec would be $1.5\mu\text{m}$. At first sight this value may appear extremely satisfactory when the particle sizes are $5\mu\text{m}$ and up. Yet this displacement is not acceptable for the recording of holograms by the conventional off-axis method, because any change in optical path of one of the interfering beams is fatal when its magnitude is as large as the wavelength of the light produced by the source. A holocamera with an in-line configuration [5], or a holocamera with a local optically processed reference beam recording bright-field [27-29] or dark-field [36-38] images (see Part A), would make this displacement acceptable since a displacement perpendicular to the direction of propagation of the illuminating beam induces an effect similar to object motion observed in photography (see Section 6.4.3). In the example considered above, a pulsed laser source generating pulses with pulse duration of 10η sec was used. In fact, most of the pulsed lasers commonly available generate a pulse with a pulse duration of the order of 1μ sec, and therefore a streaked image

would be recorded, due to a relative displacement of $150\mu\text{m}$ during the exposure. A displacement of $150\mu\text{m}$ no longer permits imaging of particles as small as $5\mu\text{m}$.

Although three-dimensional imaging of hypervelocity transilluminated scenes is of importance, it is surprising to note that until now only one holographic method of accomplishing such imaging has been disclosed in the literature [71]. In this method, the velocity synchronized Fourier transform holocamera permits recording of individual particles only because it is the particle itself that is responsible for generating a local reference beam. This method is of some theoretical interest; however, it seems very impractical to use such a holocamera for atmospheric particle measurements.

6.6.1 Analysis of the Configuration

The holographic configuration is schematically represented in Fig. 6.13. It can be seen that the collimated beam generated by the pulsed laser is successively deflected by the rotating mirror RM, reflected by the retroreflector CR, deflected again by the rotating mirror RM and finally received by the holocamera. The angular velocity of the rotating mirror RM is synchronized with the velocity of the particles within the region of interest, and the holocamera generates a local reference beam (either amplitude/wavefront division or spatial frequency separation methods can be used) which interferes with the image bearing wave in the hologram plane. As it will be shown in Section 6.6.3, the images of the particles within the region of interest have no relative motion with

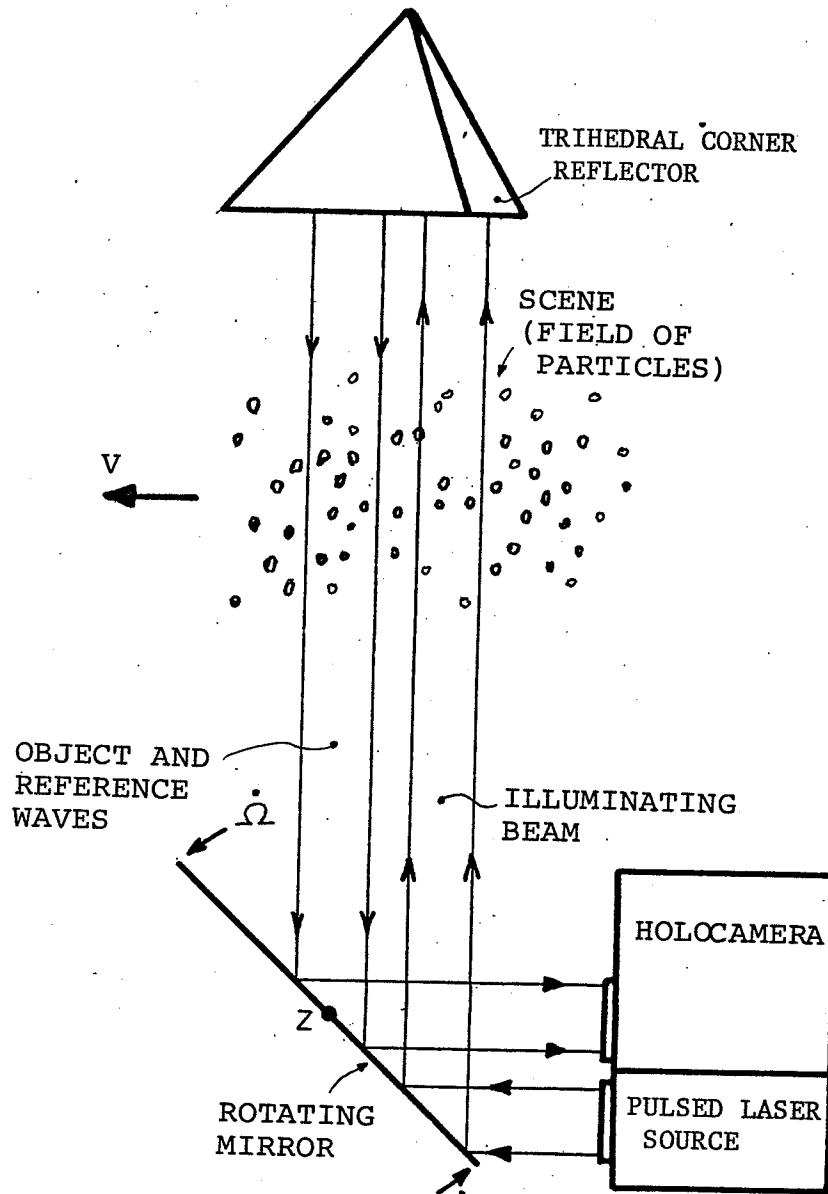


Fig. 6.13 Holographic configuration. The axis of the rotating mirror is perpendicular to the scene velocity vector and to the collimated beam generated by the pulse laser source.

respect to the recording medium, whereas the images of the other particles have a relative motion which is a function of their locations in the propagation path. It must be pointed out that the optical paths of both reference and object waves are identical (refer to the next section). Thus, no relative length variation can occur, and moreover, the undiffracted rays of light impinging onto the holocamera remain parallel to the collimated beam generated by the pulsed laser, in spite of the air turbulence and the changing positions of the rotating mirror RM.

6.6.2 Effect of the Rotation of the Illuminating Beam

Eqs.(6.9) and (6.11) describe the reflection properties of three-mirror reflectors. Firstly, an object point in the object space is imaged into an image point which is symmetrically placed with respect to the corner of the retroreflector (refer to (6.9)). Secondly, an emerging ray is antiparallel to the incident ray (refer to (6.11)). The illuminating beam, generated by the laser source and expanded by a telescope arrangement, is collimated. It follows from these two properties that the beam emerging from the retroreflector is also a collimated beam, and its direction is exactly antiparallel to the incident collimated beam. Since the collimated beam propagates twice through the scene, the beam reflected by the retroreflector contains a certain amount of diffracted rays. However, it will be established in Section 6.6.5 that the rays diffracted by the region of the scene not located around the point for which the rotation of the mirror is synchronized, are not coherent, and they do not interfere with the locally filtered reference wave.

Fig. 6.14 shows the path followed by the illuminating beam under two different angular positions of the rotating mirror RM. It is readily seen that since the incident and emerging beams are antiparallel but shifted, the beams propagating toward the holocamera will remain antiparallel to the beam emerging from the laser source. This provides perfect control over the alignment of the holocamera with respect to the illuminating beam, regardless of the angular positions of the rotating mirror RM and the retroreflector. As RM rotates, there is a Doppler frequency shift of the illuminating beam, but this shift is by no means detrimental to the fringe contrast of the recorded hologram, because the frequencies of both the reference and the object waves are shifted by exactly the same amount.

In order to obtain a time-invariant irradiance of the scene, it is necessary to have a collimated beam with a uniform beam profile. An illuminating beam with a Gaussian beam profile can, however, be successfully used if the lateral shift of the illuminating beam is much smaller than its beam half-width. The lateral shift of the illuminating beam can be compensated for either by rotating the retroreflector around an axis that does not go through its corner point, or by moving the mirror in a direction transverse to the incident illuminating beam.

6.6.3 Partial Compensation for the Object Motion

Consider the diagram of Fig. 6.15. The reflecting surface rotates around the Z axis, and the rectangular coordinate system $\{X, Y, Z\}$ is attached to the holocamera. The problem is to find the image point M' of the

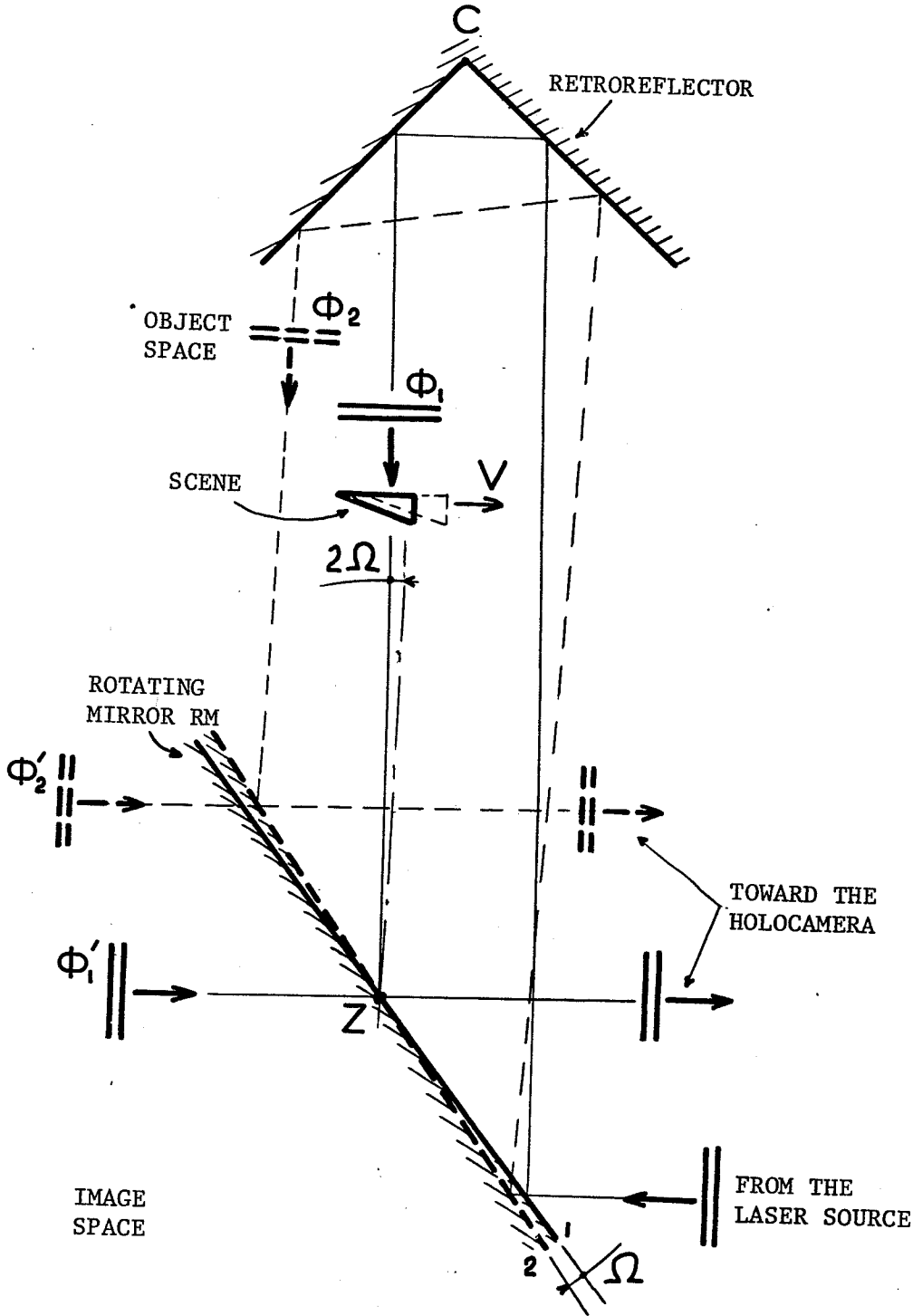


Fig. 6.14 Two-dimensional representation. In the image space the illuminating beam, regardless of the position of the rotating mirror, is antiparallel to the illuminating beam generated by the laser source.

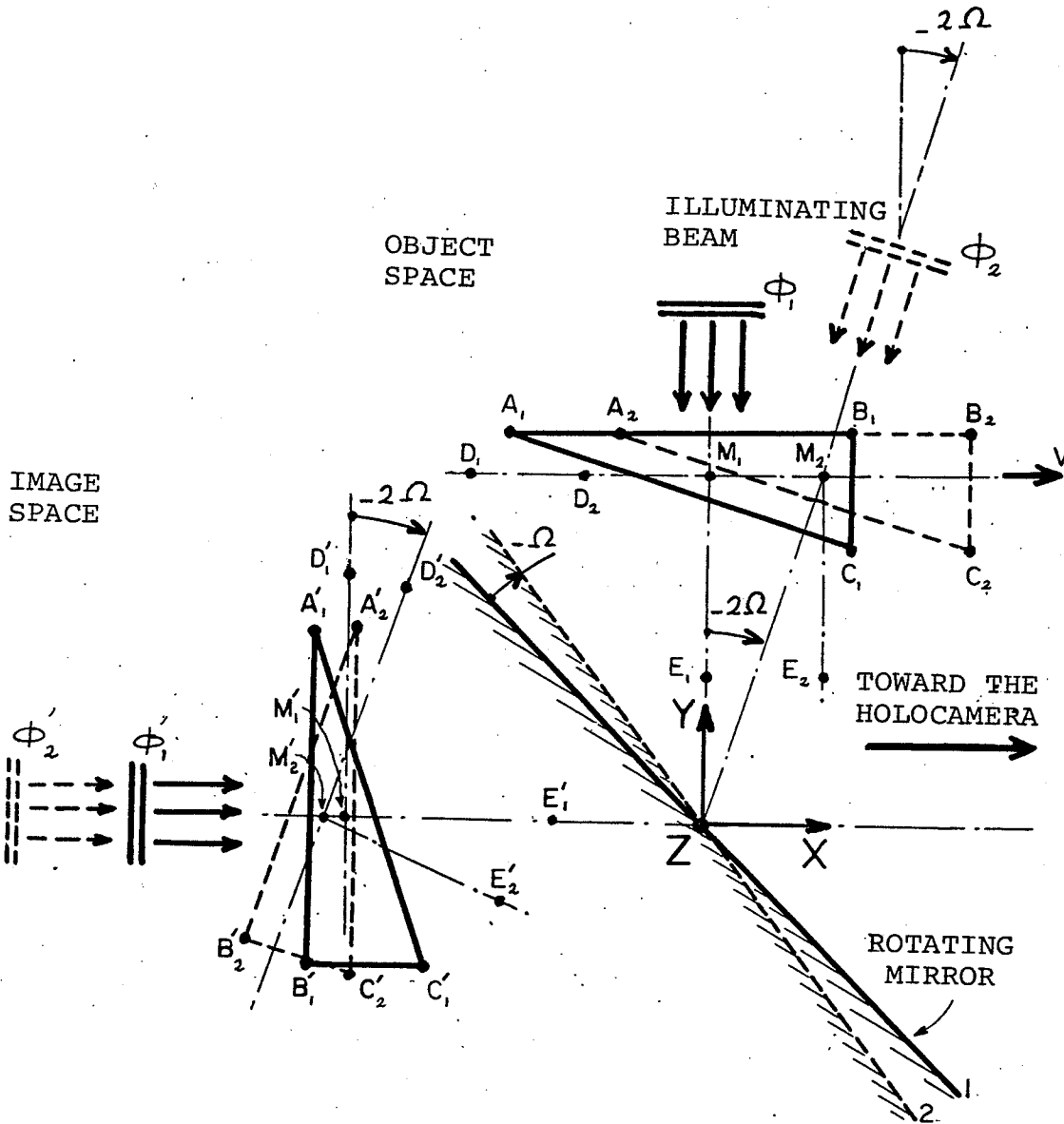


Fig. 6.15 Image motion with respect to the holocamera. The rectangular coordinate system X, Y and Z is attached to the holocamera. The reflecting surface rotates around the Z axis. The angular motion of the rotating mirror is synchronized with the transverse motion of the object point M . As a result, the image point M' only has a small axial displacement and the image points A', B' and C' are seen from the holocamera aperture as if they rotated around the image point M' .

object point M in the plane XY . The equation of the reflecting surface is simply

$$X \cos(\pi/4 + \Omega) + Y \sin(\pi/4 + \Omega) = 0 \quad , \quad (6.61)$$

where $\Omega = \Omega_0 + \int_0^t \dot{\Omega} dt$ is the angle between the first bisector and the normal to the reflecting surface. Eq. (6.61) is similar to (6.1).

Therefore, the matrix form of the transformation is readily obtained

$$[M'] = [T_1] [M]$$

$$\begin{bmatrix} X'_m \\ Y'_m \end{bmatrix} = \begin{bmatrix} 1 - 2\cos^2(\pi/4 + \Omega) & -2\cos(\pi/4 + \Omega)\sin(\pi/4 + \Omega) \\ -2\cos(\pi/4 + \Omega)\sin(\pi/4 + \Omega) & 1 - 2\sin^2(\pi/4 + \Omega) \end{bmatrix} \begin{bmatrix} X_m \\ Y_m \end{bmatrix} \quad , \quad (6.62)$$

where the coordinates of M and M' are defined by (6.49) and (6.50).

For small values of angle Ω , the sine and cosine functions can be approximated in the following manner (neglecting terms involving powers of Ω larger than 2)

$$\cos(\pi/4 + \Omega) \sim (1 - \Omega - \Omega^2/2)/\sqrt{2} \quad (6.63)$$

$$\sin(\pi/4 + \Omega) \sim (1 + \Omega - \Omega^2/2)/\sqrt{2} \quad (6.64)$$

These results are substituted into (6.62) which then yield these two relations

$$X'_m = -X_m (-2\Omega + \Omega^3 + \Omega^4/4) - Y_m (1 - 2\Omega^2 + \Omega^4/4) \quad (6.65)$$

and

$$Y'_m = -X_m (1 - 2\Omega^2 + \Omega^4/4) - Y_m (2\Omega - \Omega^3 + \Omega^4/4) \quad (6.66)$$

By using the explicit expressions for Ω and the coordinates of M and M' , and by neglecting powers of Ω larger than 1, (6.65) and (6.66) can be rewritten as follows

$$(\dot{X}'_{m_0} + \int_0^t \dot{X}'_m dt) = 2(X_{m_0} + \int_0^t \dot{X}_m dt) (\dot{\Omega}_0 + \int_0^t \dot{\Omega} dt) - (Y_{m_0} + \int_0^t \dot{Y}_m dt) \quad (6.67)$$

$$(\dot{Y}'_{m_0} + \int_0^t \dot{Y}'_m dt) = -(X_{m_0} + \int_0^t \dot{X}_m dt) - 2(Y_{m_0} + \int_0^t \dot{Y}_m dt) (\dot{\Omega}_0 + \int_0^t \dot{\Omega} dt) \quad (6.68)$$

Differentiating (6.67) and (6.68) with respect to time gives

$$\dot{X}'_m = 2[\dot{X}_{m_0} \dot{\Omega} + \dot{\Omega}_0 \dot{X}_m + \dot{X}_m \int_0^t \dot{\Omega} dt + \dot{\Omega} \int_0^t \dot{X}_m dt] - \dot{Y}_m \quad (6.69)$$

$$\dot{Y}'_m = \dot{X}_m + 2[\dot{Y}_{m_0} \dot{\Omega} + \dot{\Omega}_0 \dot{Y}_m + \dot{Y}_m \int_0^t \dot{\Omega} dt + \dot{\Omega} \int_0^t \dot{Y}_m dt] \quad (6.70)$$

The last two equations can be simplified if the object point is assumed to have a transverse motion only. Thus $\dot{Y}_m = 0$, and (6.69) and (6.70) yield

$$\dot{X}'_m = 2[\dot{X}_{m_0} \dot{\Omega} + \dot{\Omega}_0 \dot{X}_m + \dot{X}_m \int_0^t \dot{\Omega} dt + \dot{\Omega} \int_0^t \dot{X}_m dt] \quad (6.71)$$

$$\dot{Y}'_m = \dot{X}_m + 2\dot{Y}_{m_0} \dot{\Omega} \quad (6.72)$$

It appears that the above system of two equations with two unknowns provides solutions which indicate that complete motion compensation cannot be achieved. However, (6.72) indicates that there is compensation for the transverse image point motion if $\dot{\Omega} = -\dot{X}_m / (2Y_{m_0})$. Clearly, there is not complete compensation for the axial image point motion. Yet (6.69) shows that this displacement is small for small values of X_{m_0} ; moreover, a small axial displacement of an image does not noticeably affect the image sharpness (refer to Section 6.4.3), but reduces slightly the diffraction-limited image resolution and the brightness of the reconstructed image (refer to Section 6.4.2).

6.6.4 Effect of Partial Compensation on the Sharpness of the Reconstructed Image

By considering an extended object, it can be shown that the image point for which the RHS of (6.72) equals zero has a small axial motion indicated by (6.71), and the image formed by the rotating mirror simply rotates around this image point. Fig. 6.15 shows the motion of a three-point object (ABC), and the motion of the corresponding three-point image (A'B'C'), in the space object and in the space image respectively. The rotation of the rotating mirror RM is synchronized with the transverse motion of the image point M, namely $\dot{\Omega} = -\dot{x}_m / (2Y_{m0})$, where \dot{x}_m is the transverse velocity of the three-point object. It is seen that the image point M' has only a small axial displacement and that the image of the three-point object rotates around point M' by an angle of 2Ω . The three-point object is seen from the holocamera aperture as if it were an object that rotates around a point which has a small axial displacement. Thus, there is very little loss in image sharpness of the reconstructed image for the region of the scene that is centered around point M. In addition, the object points located in a plane passing through point M and parallel to the transverse displacement, will be very sharp in spite of the fact that they are not very close to point M (case of the point D shown in Fig. 6.15). Also, the image points located on a plane passing through point M and normal to the transverse displacement will have a reconstructed image that is considerably blurred (case of the point E shown in Fig. 6.15).

6.6.5 Comments

From what has been said above, it follows that:

i) The depth-of-field of the reconstructed image is limited by the maximum allowable transverse motion of the recorded image. It must be mentioned that the definition of the depth-of-field in holography is somewhat different from that of photographic depth of field.

In the case of the present configuration, the depth-of-field defines a depth beyond which it is no longer possible to distinguish a given detail of an object, because the image is blurred by the object motion and because the brightness of the reconstructed detail is reduced.

In the case of a photographic setup equipped with a rotating mirror, the depth-of-field would be defined as the depth beyond which a given detail of an object is no longer distinguishable because the image is blurred by the object motion and because the camera lens is not focussed on this detail.

ii) Since the object points located in planes parallel to the direction of the scene motion (for example, point E) have images which have a large motion with respect to the recording plane, the Doppler frequency shift induced by the motion of the points will not permit any coherent contribution to the interference fringes in the hologram (refer to (6.19)).

Thus these points will give a constant bias exposure on the hologram and they will not be reconstructed by the hologram.

Hence, the overall imaging properties of the holographic configuration

are of the utmost interest because it is now possible to reconstruct images of very dense particle fields, and to be able to observe a slice of the sample volume without having the view obstructed by the particles contained in the other planes. Note that the last property is similar to that of tomographic images. However, the depth-of-field of the reconstructed images, although reduced by the rotation of the image, is still considerably larger than that obtainable with a similar set-up equipped with a photographic camera.

iii) Due to the Doppler frequency shift mentioned above, the temporal filtering properties of the recorded hologram permit total suppression of the noise caused by the propagation of the illuminating beam from the rotating mirror to the retroreflector. Clearly, spatial filtering of the reference wave is needed only to remove the object information which comes from the scene slice, the motion of which is synchronized with the rotation of the mirror. Thus, spatial filtering is greatly improved, since all rays with low spatial frequency components which have been scattered by the region of the scene situated away from the slice of interest, are incoherent and do not have to be removed by a pinhole aperture of very small diameter. Note that since filtering can be performed by a relatively larger pinhole aperture, the alignment of the holocamera is less critical. In addition, the air breakdown threshold is increased and the likelihood of burning the pinhole aperture is decreased; this is particularly true in pulsed holography⁶ [54].

iv) The three-dimensional velocity vector of any particle with respect to another one can be easily recovered by recording a double exposure

⁶ Private communication with J.D. Trolinger, Spectron Development Laboratories, Inc., Costa Mesa, Cal., USA, May 26, 1976.

hologram. Since the average velocity of the particles is almost completely compensated for by the angular motion of the rotating mirror, the particle displacement visible in the reconstructed image merely represents the relative displacement of the particle between the two exposures.

Another way to recover the three-dimensional velocity vector of each particle is to use a relatively long exposure time and to desynchronize slightly the angular motion of the rotating mirror. The velocity vector of each particle can be determined from the knowledge of the length of the streak which is visible on the image of each particle.

At the present time, no other method allows recovery of the three-dimensional velocity vector of each particle when the magnitude of the average velocity vector of the particles is much larger than that of the relative velocity vector of one particle with respect to another one.

It must be noted that the focussing properties of dark-field images permit accurate recovery of the third dimension of the velocity vector of each particle.

6.7 HOLOGRAPHIC TOMOGRAPHY

In photographic tomography (Greek τόμος: slice) only a slice of a three-dimensional scene is properly imaged. The camera and the illuminating source, or the scene, are moved in such a way that the motion of the slice with respect to the camera is minimized, while the motion of the rest of the scene with respect to the camera is maximized. (The imaging

system of the camera is focussed on the slice.)

It was indicated in the last section that the configuration in which a rotating mirror is used permits holographic imaging of a slice of a given depth of a scene having a transverse motion. It is readily seen that an easy way to perform holographic tomography is to use the beam folded configuration studied in Section 6.4, and to rotate the scene around an image point which determines the center of the slice. Another way to obtain similar results is to keep the scene motionless and to rotate the whole apparatus (holocamera, laser source and retroreflector) around an image point. However, the shortcoming of these two methods is that they require either rotation of the scene or of the bulky recording holographic instrument, and this is not always feasible.

6.7.1 Principle of the Configuration Allowing Holographic Tomography of Motionless Scenes

Substitute a silvered prism for the two mirrors M_1 and M_2 in the configuration of Fig. 6.11. A new configuration, illustrated in Fig. 6.16, is obtained. It can be easily seen that by translating the retroreflector, and by rotating in a determined way the silvered prism around the Z axis, a steady interference pattern is formed in the recording plane of the holocamera using local reference beam generation. In addition, the rays undiffracted by the scene, which are incident on the holocamera aperture, remain antiparallel to the rays emerging from the laser source, regardless of the angle of rotation of the silvered prism around the Z axis.

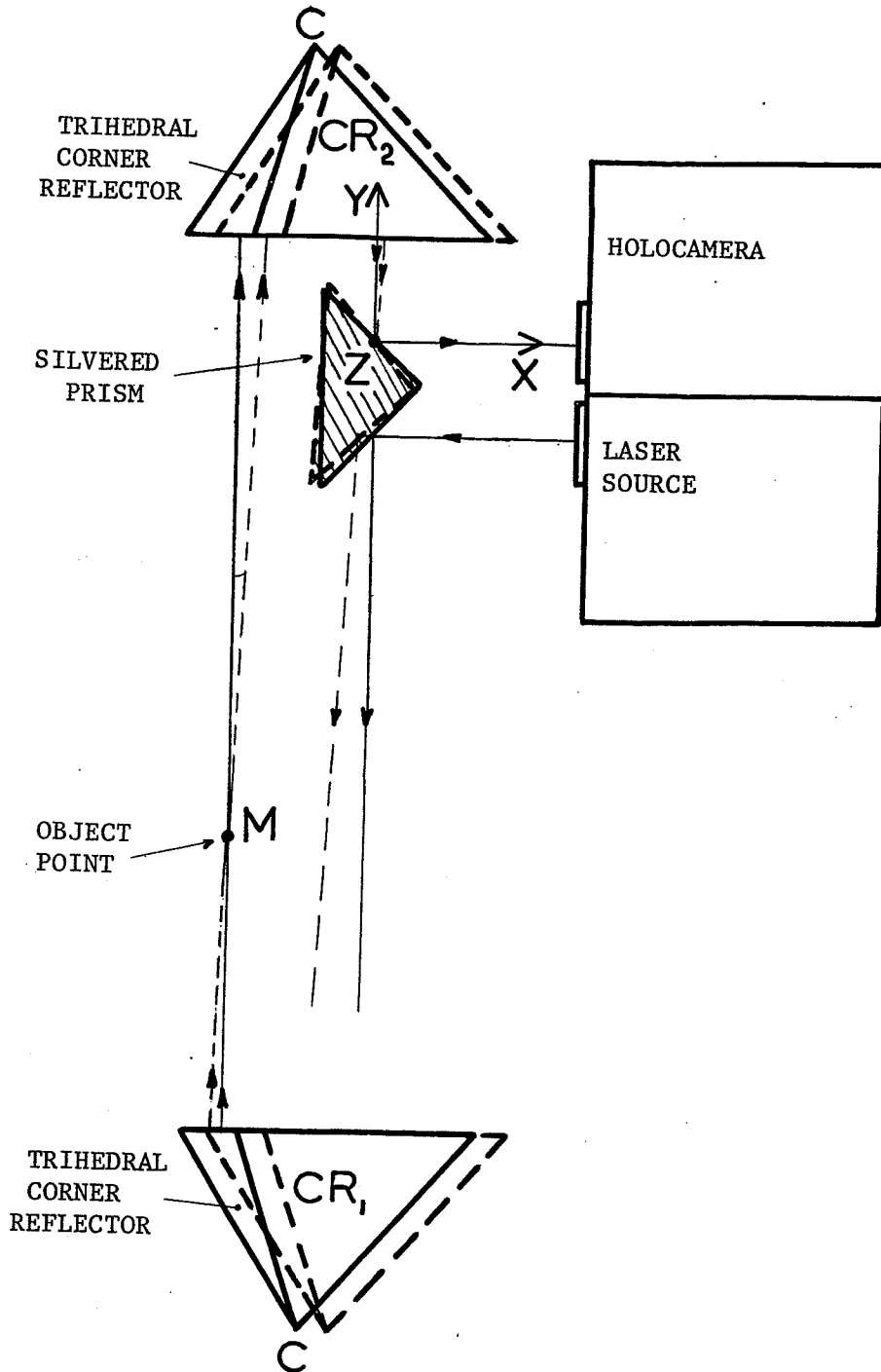


Fig. 6.16. Holographic tomography: the silvered prism rotates around the Z axis which is parallel to the line of intersection of the two reflecting surfaces.

By considering the rectangular coordinate system (X, Y, Z) shown in Fig.

6.16, it is possible to use (6.54) once more. With the coordinates of the points M, M' and C defined by (6.49) - (6.51), and with the assumption that $\dot{X}_m = \dot{Y}_m = \dot{Z}_m = \dot{Y}_c = \dot{Z}_c = 0$, (6.54) gives

$$\begin{bmatrix} X'_{m0} + \int_0^t \dot{X}'_m dt - X_{c0} - \int_0^t \dot{X}_c dt \\ Y'_{m0} + \int_0^t \dot{Y}'_m dt - Y_{c0} - \int_0^t \dot{Y}_c dt \\ Z'_{m0} + \int_0^t \dot{Z}'_m dt - Z_{c0} - \int_0^t \dot{Z}_c dt \end{bmatrix} = \begin{bmatrix} -1 & 0 & 0 \\ 0 & -1 & 0 \\ 0 & 0 & -1 \end{bmatrix} \begin{bmatrix} X_{m0} - X_{c0} - \int_0^t \dot{X}_c dt \\ Y_{m0} - Y_{c0} \\ Z_{m0} - Z_{c0} \end{bmatrix} \quad (6.73)$$

Thus, the coordinates of the image point M' are

$$M' \begin{cases} X'_m = -Y_{m0} + 2X_{c0} + 2 \int_0^t \dot{X}_c dt \\ Y'_m = -Y_{m0} + 2Y_{c0} \\ Z'_m = -Z_{m0} + 2Z_{c0} \end{cases} \quad (6.74)$$

and the vector velocity of the image point M' has the components

$$\begin{cases} \dot{X}'_m = 2\dot{X}_c \\ \dot{Y}'_m = 0 \\ \dot{Z}'_m = 0 \end{cases} \quad (6.75)$$

when the object point M is motionless. The vector velocity of the image point is parallel to the vector velocity of the corner point but has a magnitude twice that of the corner point. Hence, when the object

scene is motionless, a displacement of the retroreflector creates a displacement of the image scene. Fig. 6.17 shows the position of the images for two different positions of the corner point. The image scene erected by the retroreflector becomes the object scene of the rotating silvered prism. By analogy with Fig. 6.15, it appears that the transverse motion of the image scene, created by translating the corner point, can be compensated for by rotating the silvered prism. Eq. (6.72) can be used again to provide the relationship between the transverse motion of the corner point and the angular motion of the silvered prism. If the image point M' is transformed into an image point M'' by the rotating prism, and if the coordinates of the point M'' are

$$M'' \begin{cases} X''_{m_0} + \int_0^t \dot{X}''_m dt \\ Y''_{m_0} + \int_0^t \dot{Y}''_m dt \\ Z''_{m_0} + \int_0^t \dot{Z}''_m dt \end{cases} \quad (6.76)$$

on replacing the indices m' and m in Eq. (6.72) by, respectively, m'' and m' , and by using the expressions of the coordinates of M' given by Eq. (6.74), it follows that

$$\dot{Y}''_m = 2\dot{X}'_c + 2\dot{\Omega}(-Y'_{m_0} + 2Y'_{c_0}) \quad (6.77)$$

The condition for compensation of the translation of the retroreflector is therefore

$$\dot{\Omega} = -\dot{X}'_c / (2Y'_{c_0} - Y'_{m_0}) \quad (6.78)$$

The image of the object scene is seen from the aperture of the holocamera as if it rotated by an angle of 2Ω (see Fig. 6.16) around a point that has a very small axial motion in the image space. (This axial motion can be

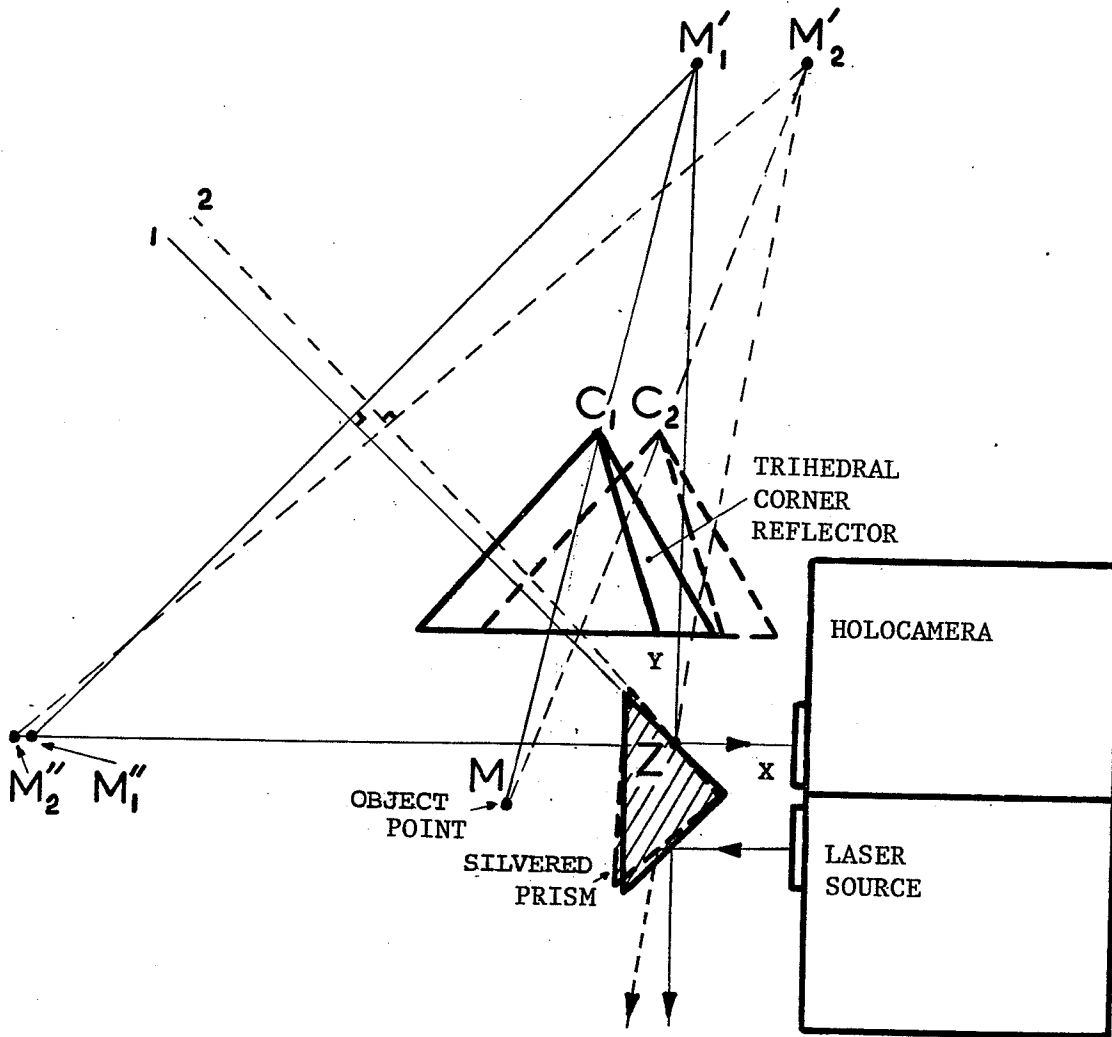


Fig. 6.17 Holographic tomography: correspondence between the object space and the image space that can be seen from the holocamera objective.

easily compensated for by an axial motion of the three-mirror reflector). Hence, all the comments of Section 6.6.5 are applicable to the tomographic images obtained by synchronizing the translation of the retro-reflector CR_2 with the rotation of the silvered prism around the Z axis.

6.8

SUMMARY

Chapter Six has introduced several holographic configurations, the principles of which are new. It has been shown that retroreflectors provide the rigorous alignment required for generating local reference beams in the holocameras. The holocameras which have been considered had local reference waves, and the theoretical studies considered in this chapter are valid for the two basic methods of local reference beam generation, namely: amplitude/ wavefront division, and spatial frequency separation.

The ability of two of the four configurations to compensate for scene motion is, of course, of significant importance. It is now feasible to holographically record a three-dimensional transilluminated scene with a continuous wave laser source. Finally, the remarkable imaging properties of the configurations using rotating mirrors should not be overlooked, since they permit recovery of the three-dimensional velocity vector of each particle, and also permit holographic tomography.

*Chapter Seven*EXPERIMENTAL INVESTIGATIONS7.1 INTRODUCTION

These experimental investigations are intended to substantiate the theoretical studies of Chapter Six. In addition, interesting comparisons between bright-field and dark-field reconstructed images permit greater appreciation of the remarkable properties of dark-field images. The order of presentation of the experimental investigations corresponds to that of the subsections of Chapter Six. The remarks of Section 5.1 still apply to this chapter. The theoretical studies were carried on by assuming that the retroreflectors were trihedral corner reflectors. However, this type of retroreflector is not readily available for applications at optical frequencies. Thus, all the experiments are performed with tetrahedral prism reflector (ray deviation: 1-5 arc seconds, aperture: 65mm). Tetrahedral prism reflectors have the advantage over trihedral corner reflectors of permanence of adjustment within the mirror set, and it is feasible to produce tetrahedral prism reflectors with good tolerances at a reasonable cost. However, in a tetrahedral prism reflector, the reflections on the interfaces of the prism (glass/air) are at angles larger than the critical angle and thus there is total reflection at the interface glass/air. Total reflection on the faces of the prism causes phase shifts in the polarization of the electric vector [71], and since the prism is filled with dielectric material (glass), the optical corner of the retroreflector does not coincide with the point corner of the prism [62]. The change in state of polarization is particularly

large at total internal reflection far from the critical angle. It is seen that if the collimated beam impinging onto the retroreflector is linearly polarized, the state of polarization of the emerging beam will be different from one sextant to another, but will remain constant over the area of each sextant. In order to maintain a high fringe contrast, it becomes necessary to have a ray to ray correspondence between the interfering rays in the recording plane (i.e., a diffracted ray must interfere with the ray that illuminates the diffracting point). It must be pointed out that the telescope holocamera allows a ray to ray correspondence. In practice, the experimental investigations are conducted with the single lens holocamera and the useful aperture of the tetrahedral prism reflector is reduced to one sextant. (The difference in the electric vector angular positions measured in two adjacent sextants is approximately 40° .)

7.2 BEAM-FOLDED CONFIGURATION

7.2.1 Experiment B1

It is the intent of this experiment to demonstrate the effectiveness of the beam-folded configuration. In particular, the property of the corner cube reflector to maintain vigorous alignment of the holocamera with respect to the illuminating beam, is closely examined. The retroreflector used is visible in Fig. 7.1. It is mounted on a holder which permits small transverse and axial displacements (maximum displacements: 25mm), and also rotation around the corner point of the retroreflector. For large axial displacements, the ensemble retroreflector/holder is moved

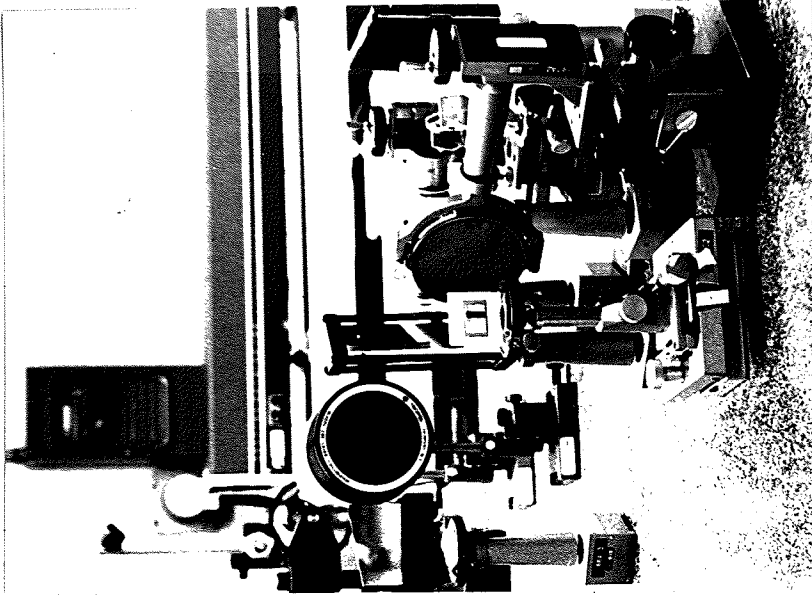


Fig. 7.2 Photograph of the setup. The prism is used as a beam splitter, thus dividing the illuminating beam into a reference and an object wave.

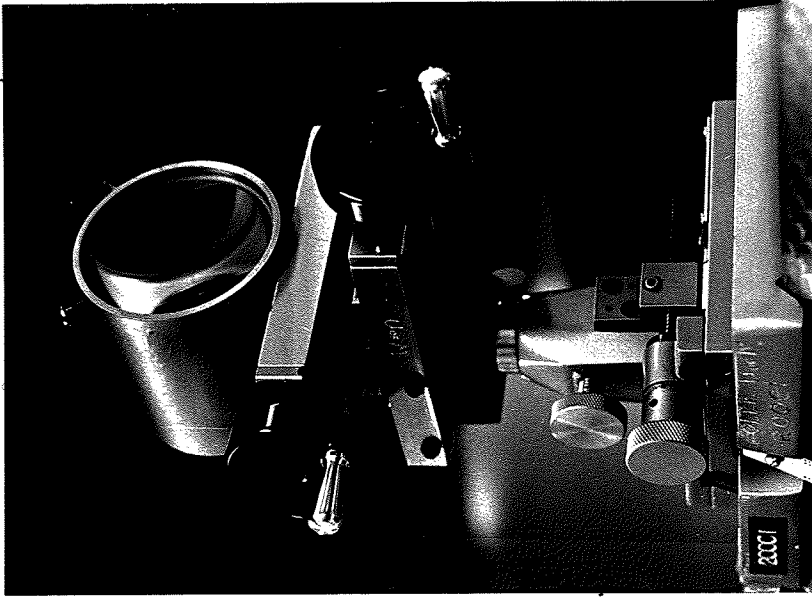


Fig. 7.1 Close-up of one of the tetrahedral prism reflectors used in the experiments. Note that its holder permits rotation around the corner point and also transverse and axial displacements in the horizontal plane.

on an optical bench (maximum axial displacement: 1.50m) which can be seen in Fig. 7.4. The holocamera used generates a reference beam by amplitude/wavefront division (no imaging lens is used). The prism, which plays the role of a beam splitter, is visible in Figs.7.2 and 7.3. The schematic diagram of the beam-folded configuration is found in Fig. 6.7, and the general view of the experimental arrangement is depicted in Fig. 7.3. The optical components of the holocamera are all placed on the same optical bench and can be seen in the background of the photograph of Fig. 7.4. The distance between this bench and the retroreflector optical rail is approximately 12m, and the optical rail is supported by an ordinary office desk. Spatial filtering is performed by a 12 μ m diameter pinhole placed in the back focal plane of an 85mm focal length lens. The object consists of an etched metallic sheet, representing the "UM" sign, which is mounted on a holder that permits both axial and transverse displacements. The exposure time varies from 5 to 10 sec.

Results: (i) Effect of the object motion on the image sharpness: the effect of transverse and axial displacements of approximately 3mm is shown in Figs.7.5(a) and (b) respectively. It can be seen that the deleterious effect of motion on the reconstructed image is identical to that occurring in photography under similar object displacements (see Section 6.4.3).

(ii) The effect of the object motion on the diffraction-limited image resolution cannot be observed.

(iii) Effect of the retroreflector motion: the reconstructed images are shown in Figs.7.5(c)-(e) for a transverse displacement of 10mm, an axial displacement of 1.5m and a rotation of $\pm 15^\circ$ around the corner

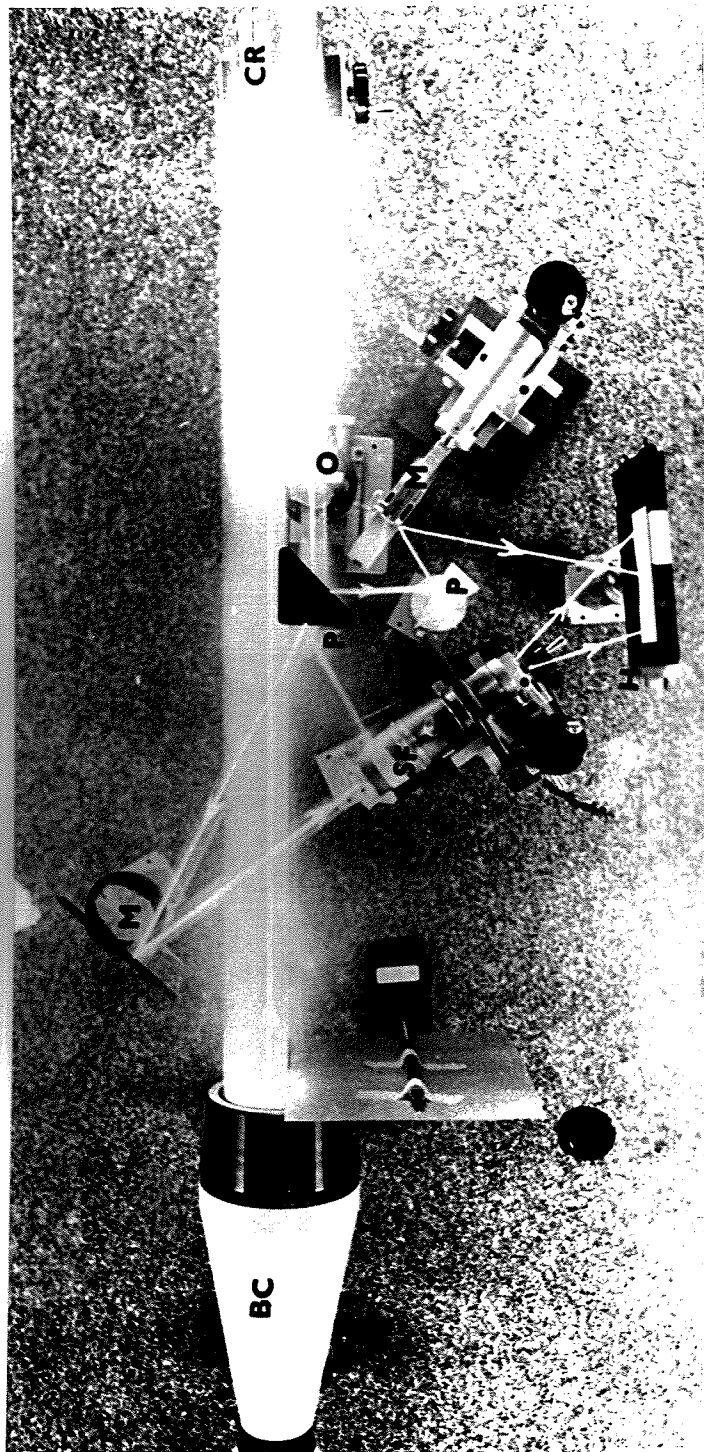


Fig. 7.3 General view of the setup of the beam-folded configuration. In order to show all the optical components, the retroreflector has been placed on the bench. The equipment is identified as follows: "BC" beam collimator, "CR" tetrahedral prism reflector, "O" object, "P" prism, "M" mirror, "SF" spatial filter and "H" photographic plate holder.

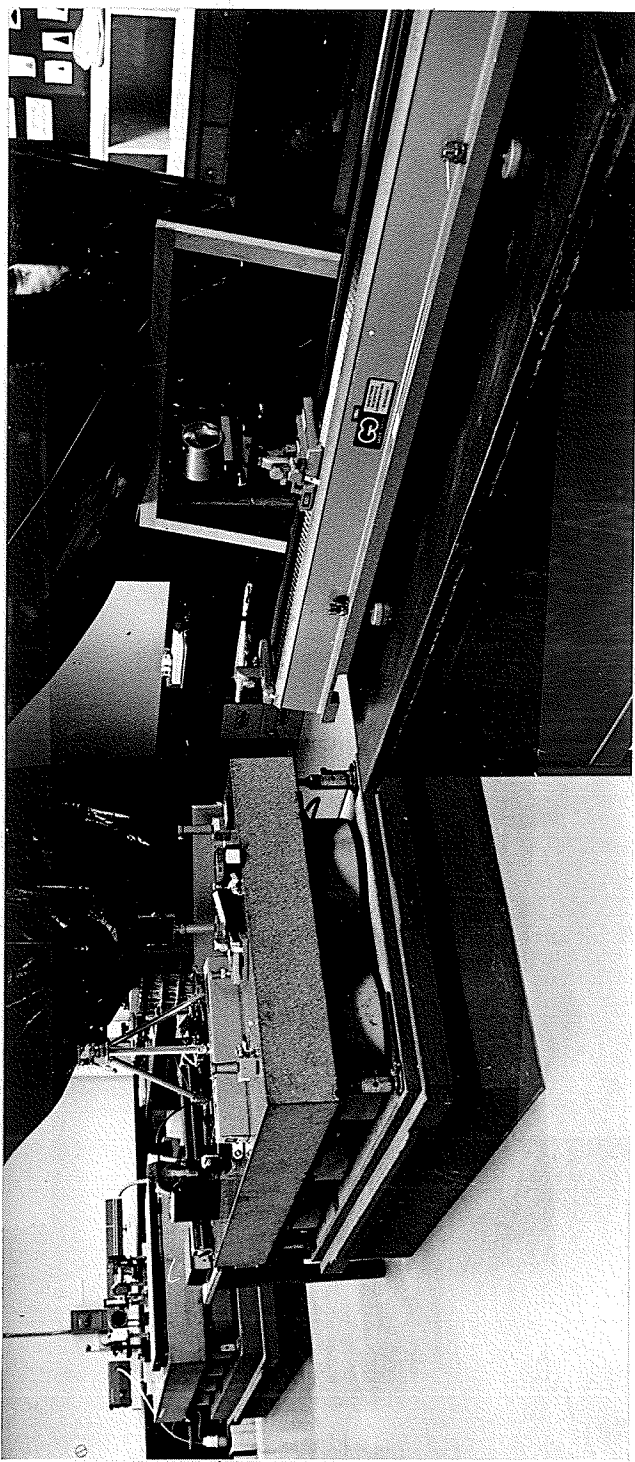
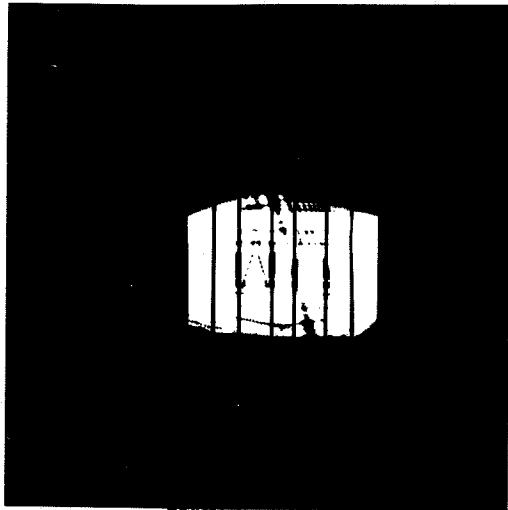
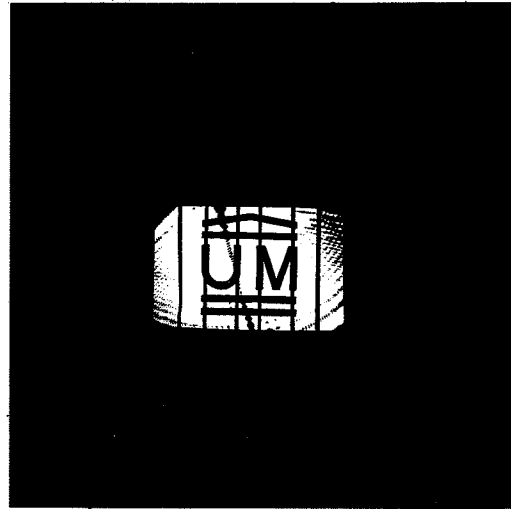


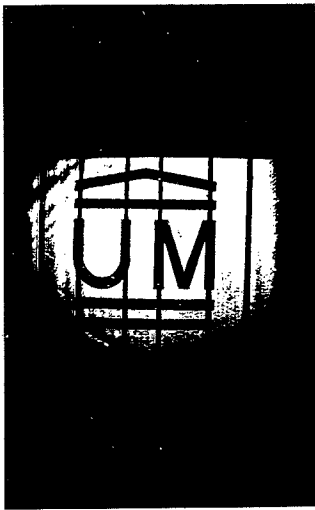
Fig. 7.4 Overall view of the setup. Some of the optical components of Fig. 7.3 are identifiable on the optical bench in the background. The retroreflector is visible in the foreground. It is mounted on an optical rail that permits axial displacements of about 1.5m. The distance separating the retroreflector from the holocamera setup is approximately 12m.



(a)



(b)



(c)



(d)



(e)

Fig. 7.5. (a) and (b), effect of the object motion on the reconstructed images for transverse and axial displacements of $\sim 3\text{mm}$ respectively. (c), (d) and (e), effect of the retroreflector motion on the reconstructed images for a transverse displacement of 10mm , an axial displacement of 1.5m and a rotation of $\pm 15^\circ$ around the corner point of the retroreflector respectively.

point of the retroreflector respectively. The reconstructed images reveal no noticeable degrading effect on the image quality. (The photograph of Fig. 7.5(e) is noisy because the hologram was bleached with a depleted bleaching solution.) Transverse motion and rotation of the retroreflector are in practice limited by the effective aperture of the retroreflector. When transverse displacement and/or rotation of the retroreflector is large with respect to the aperture of the retroreflector, there is a reduction in the section of the illuminating beam which emerges from the retroreflector, and therefore the object is only partially illuminated for a certain time during the exposure of the recording material. As a result, if the rays of the intensity distribution of the reference wave in the recording plane are inverted with respect to the image from which they are derived, the illuminated region of the image and the reference wave move away from each other as the effective aperture of the retroreflector is further reduced. Figs. 7.6(a) and (b) are photographs taken in the recording plane representing the interfering waves (the reference wave has been attenuated for clarity). In (a), both reference and object beams correctly overlap, ensuring a good reference-to-object intensity ratio over the hologram. In (b), the effective aperture of the retroreflector is reduced because the cross section of the emerging beam decreases; the unilluminated part of the object wave no longer corresponds to the illuminated part of the reference wave. Thus, the two waves no longer overlap. In order to provide a good reference-to-object intensity ratio for any position of the retroreflector, an additional lens must be placed in either arm of the holographic arrangement. Fig. 7.6(c) shows a photograph taken in the recording plane when an additional lens is used. It can be seen that the two beams still overlap, although the effective

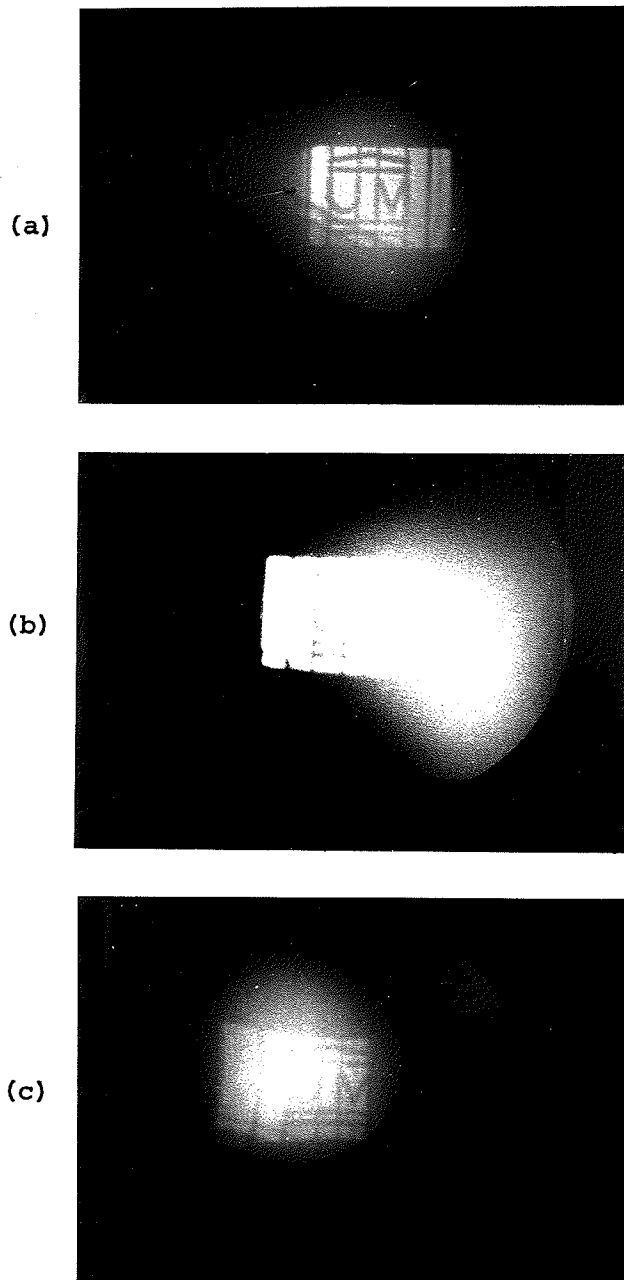


Fig. 7.6 Compensation for a reduction in illuminating beam cross section. In (a), the reference and object beams properly overlap. In (b), due to a reduction in the cross section of the illuminating beam, the two interfering waves no longer overlap. In (c), compensation is provided by adding a lens in one of the arms of the holographic arrangement.

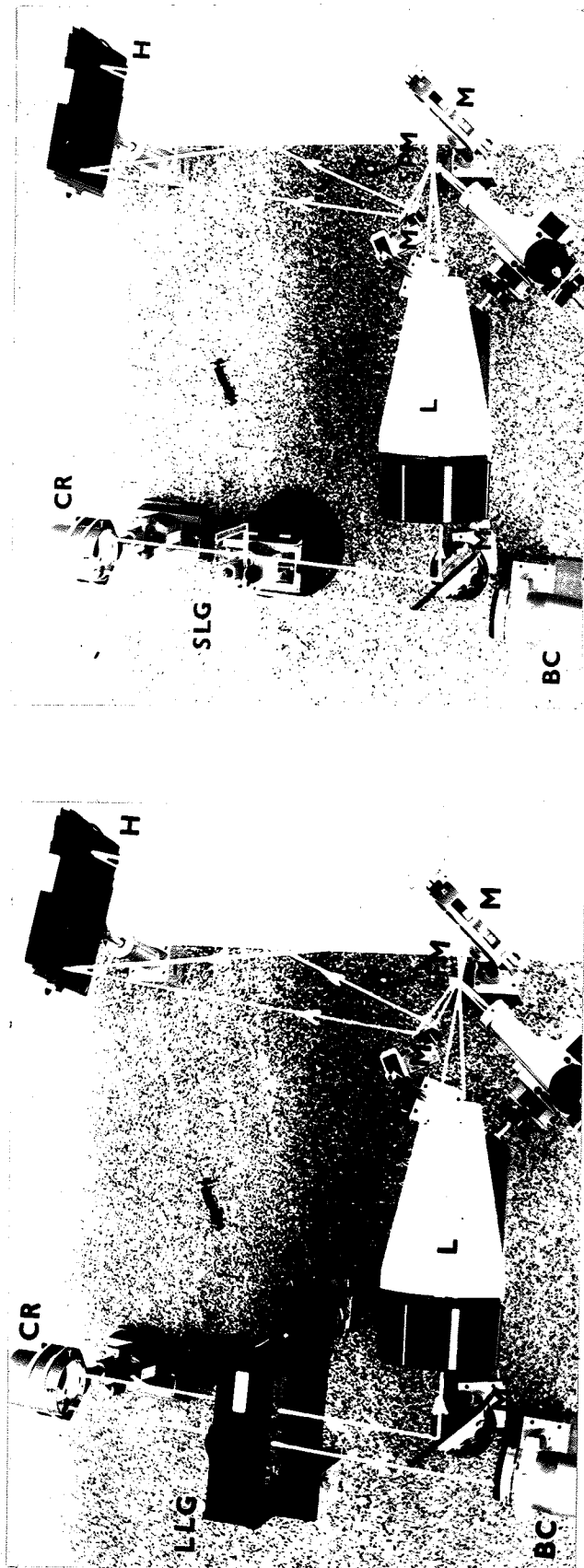
aperture of the retroreflector does not allow illumination of the entire object. Such a compensation is provided by the holocameras described in Section 3.3.5.

7.3

MEASUREMENT OF TIME VARYING FIELDS OF PARTICLES WITH THE
BEAM-FOLDED CONFIGURATION

So far it has been a question of imaging only time-invariant fields of particles (see Chapter Five). It is now the object of this section to image time-varying particle fields. Since the laboratory is not equipped with a pulsed laser, which would normally be required for such investigations, the beam of a continuous wave argon-ion laser is simply blocked with a conventional photographic shutter. The shortest exposure available with such a device is 1/200 sec, which is, by all means, considerably larger than the pulsed width which can be obtained with currently available pulsed lasers. However, any displacement of the object during the exposure does not impair the fringe visibility of the recorded hologram (refer to Section 6.4.2), it merely makes the reconstructed image look blurred, as would be the case if a photograph had been taken with similar object motion during exposure (see photographs (a) and (b) of Fig. 7.5). In order to have minimum blur, the particle fields to be imaged will be restricted to fields containing slowly moving particles.

The two experiments which follow will be concerned with imaging of glass beads falling through water, and algae. Photographs (a) and (b) of Fig. 7.7 show, respectively, the arrangements used for holographic recording of glass beads falling through a large liquid gate filled with water,



(a) Holographic recording of glass beads

(b) Holographic recording of algae

Fig. 7.7 Arrangements used for dark-field holographic recording of particle fields. The optical components are identified as follows: "BC" beam collimator, "LLG" large liquid gate; "SLG" small liquid gate, "CR" tetrahedral prism reflector, "L" imaging lens, "SFM" spatial filter mirror, "M" mirror and "H" photographic film holder.

and algae in suspension in a small liquid gate of 1.25mm thickness. The single lens holocamera (see Fig. 3.6(a)) is used. In the photographs of Fig. 7.7 the retroreflector and the film holder are seen on the bench where the lens and the spatial filter are set up. In practice however, in order to demonstrate the effectiveness of the beam-folded configuration, and to obtain large transverse magnification prior to holographic recording (refer to (3.16)), the retroreflector and the photographic plate holder are placed on other benches. The use of a telescope holocamera (see Fig. 3.7) would not require remote positioning of the film holder since the transverse magnification factor would then be determined by the ratio between the focal lengths of the lenses used in the telescope system (refer to (3.29)). Finally, it must be said that the illuminating beam propagates twice through the scene.

7.3.1 Experiment B2

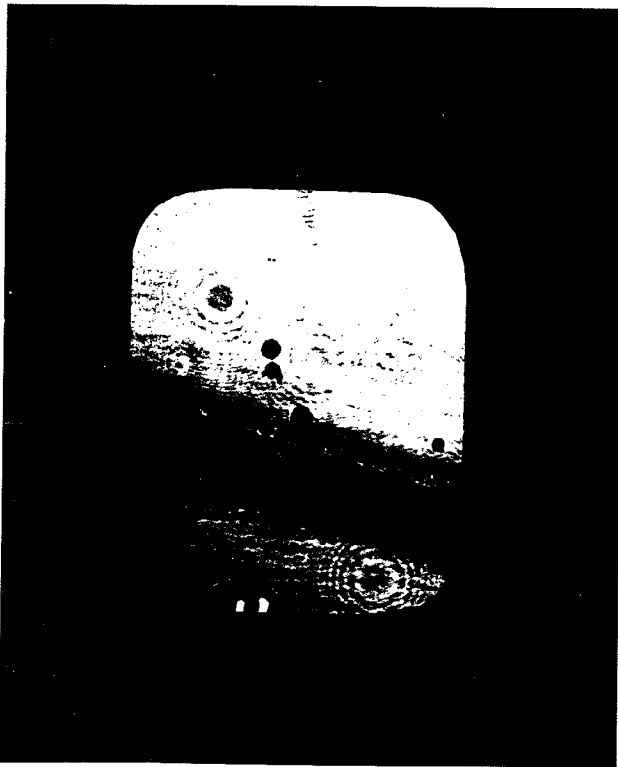
In this experiment, glass beads of diameters smaller than $50\mu\text{m}$ are allowed to fall from the top of the liquid gate filled with water. The shutter which controls the exposure time is set at $1/200$ sec, and in order to improve the energy efficiency of the configuration, the spatial filter mirror is not backed by a small pinhole (see Fig. 3.5). Thus the reference wave is filtered by the 0.3mm radius hole of the spatial filter mirror placed in the back focal plane of the 400mm focal length lens. The reference wave of the bright-field configuration is filtered by the same aperture.

Results: With a transverse magnification factor of approximately 20, glass beads as small as $20\mu\text{m}$ can be recorded. However, smaller particles

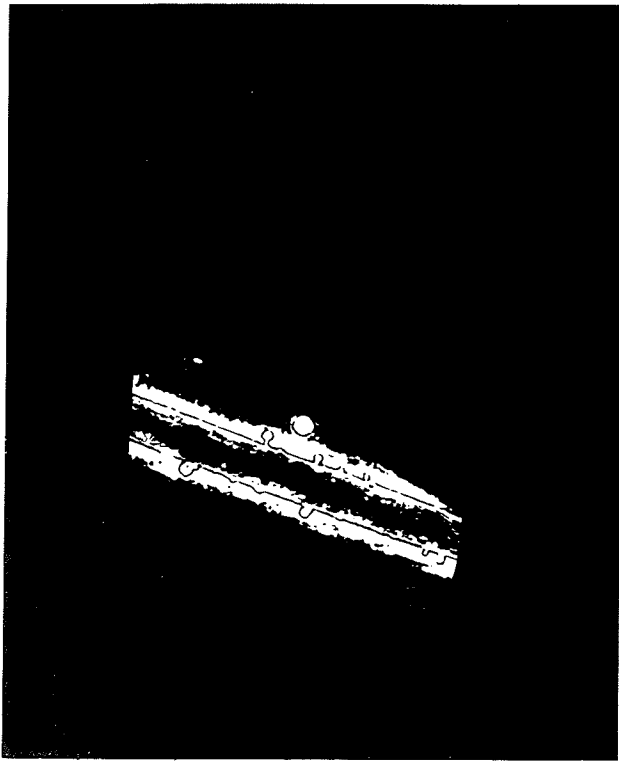
cannot be properly imaged because of the limited numerical aperture of the lens used.

i) Holograms of bright-field and dark-field images are recorded for small density distributions of falling glass beads. Photographs (a) and (b) of Fig. 7.8 show the reconstructed bright-field and dark-field images. Note that the wire diameter is $250\mu\text{m}$. The background of the bright-field image is noisy, and diffraction patterns of out-of-focus particles are identifiable, whereas that of the dark-field image is absolutely noise-free because the spatial frequency filter has cut off the low frequency components of the out-of-focus particles. The two photographs do not correspond in their content because their holograms are not recorded simultaneously. It must be pointed out that in this experiment, the energy requirement of holographic recording by the amplitude/wavefront division method is approximately 15 times that of holographic recording by spatial frequency component separation. This is of course due to fact that the amplitude/wavefront of the undiffracted rays is divided before generation of the reference wave. In addition, the bright-field image irradiance is superior to that of the dark-field image, and therefore higher reference wave intensity is needed to maintain an appropriate reference-to-object wave intensity ratio.

ii) The photograph of Fig. 7.9(a) shows a typical reconstructed dark-field image of relatively dense spatial distribution of glass beads. The dark fringe located on the Gaussian image is clearly visible around the glass beads (pointed out with an arrow) and on the profile of the wire. Other glass beads are not in focus and no sharp dark fringe is perceptible.

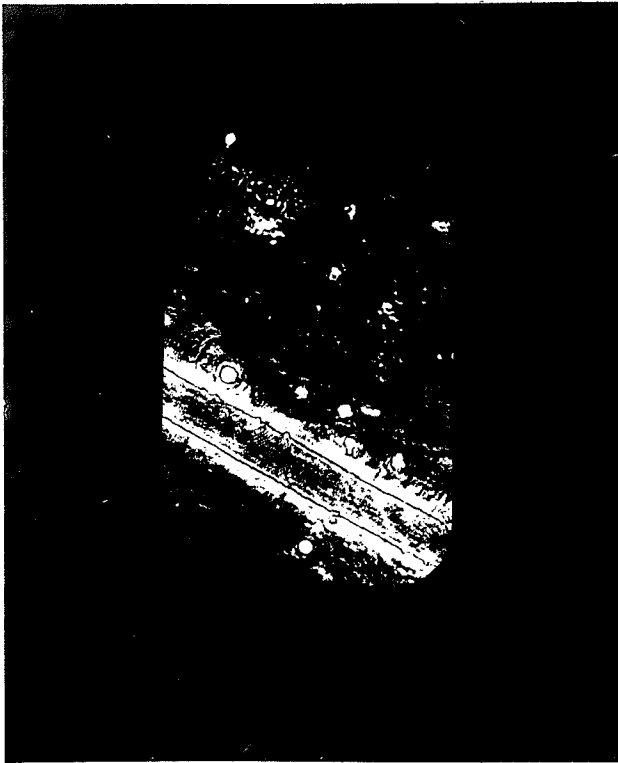


(a) Reconstructed bright-field image

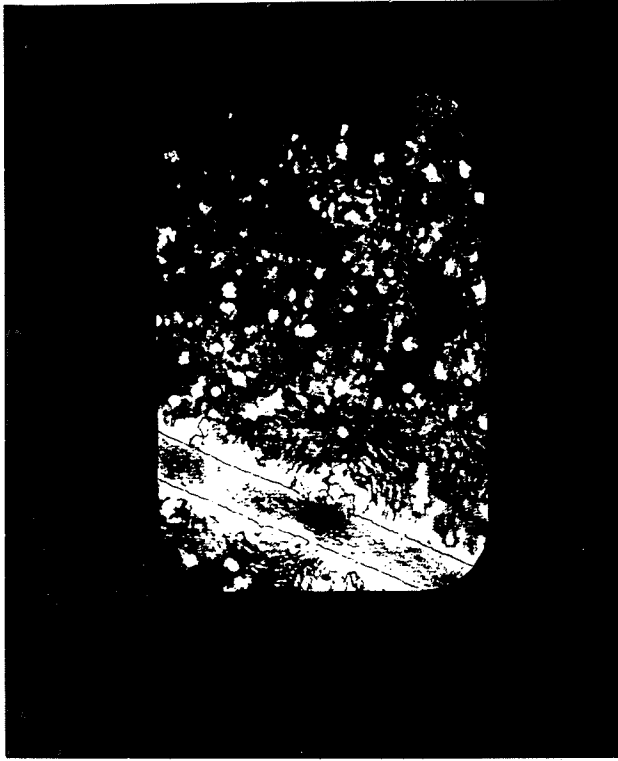


(b) Reconstructed dark-field image

Fig. 7.8 Reconstructed images of glass beads falling freely in the water-filled liquid gate. The dark-field image is free of noise caused by the out-of-focus particles. $f_1 = 400\text{mm}$, $r_p = \epsilon = 0.3\text{mm}$, $\tau = 8\text{mm}$ and $M'' \sim -20$.



(a) From a single exposure hologram. Observe the dark fringe on the Gaussian image.



(b) From a double exposure hologram. The arrows point out the beads in their two positions.

Fig. 7.9 Reconstructed dark-field images of relatively dense spatial distributions of glass beads. $f_1 = 400\text{mm}$, $r_p = \epsilon = 0.3\text{mm}$, $\tau = 8\text{mm}$ and $M'' \sim -20$.

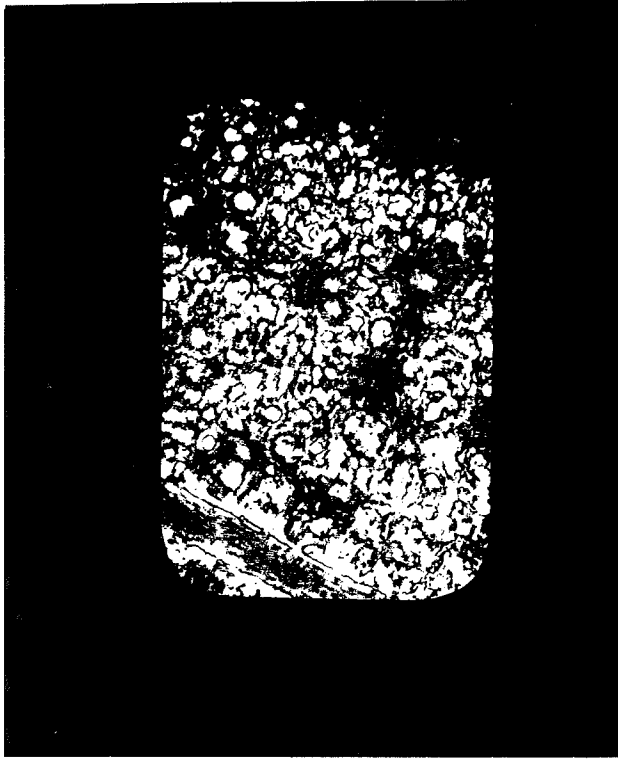
The photograph of Fig. 7.9(b) shows the image reconstructed from a double exposure hologram. The density distribution is approximately the same as above, and the time between exposures is about 1 sec. Several glass beads (pointed out by arrows) can be identified in their positions at the two different instants when the shutter is opened. The time lapse between exposures is relatively large; a shorter time lapse would facilitate retrieving of the bead displacements and instant velocities.

iii) Photographs (a) and (b) of Fig. 7.10 distinctly indicate the property of the reconstructed dark-field image to provide accurate recovery of the depth dimension. These photographs show the reconstructed images in two different planes. The arrows point out the glass beads which are in focus. Note that the spatial density distribution of the glass beads is now very high.

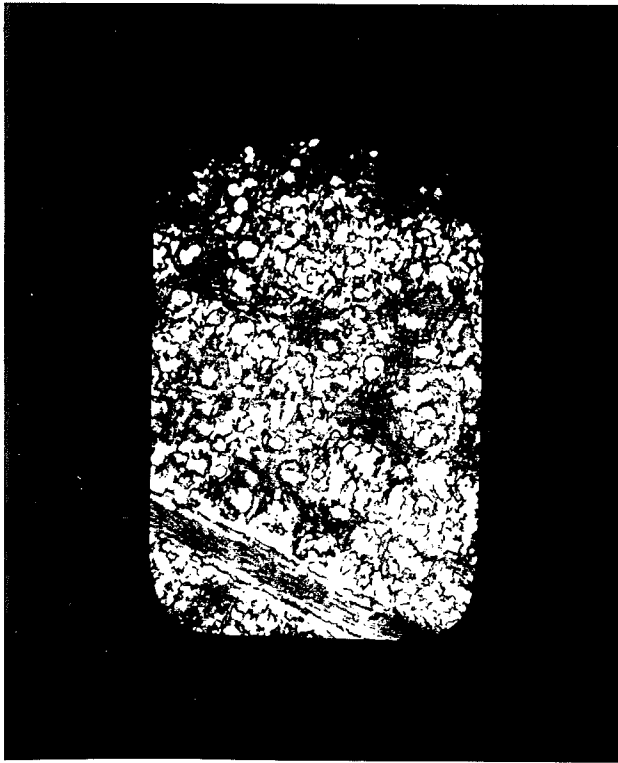
7.3.3 Experiment B3

The purpose of this experiment is to demonstrate the usefulness of the new holographic method generating a local reference wave by means of spatial frequency component separation. A solution of the diatom Melosira⁶ constitutes the scene to be imaged. The practical setup is similar to the one used for recording images of glass beads. However, preamplification of the recorded image is now $M \sim -50$. With this magnification, an exposure duration of 1/200 sec is insufficient for the type of recording material used (the laser source being used at maximum output). For this reason, the shutter is set at 1/25 sec and a 1.25mm thin liquid gate (see Fig. 7.7(b)) is substituted for the large liquid gate formerly

⁶ Provided by Dr. P. Healey, Fresh Water Institute, Winnipeg, Man., Canada.



(a) In the plane of the wire



(b) In another plane

Fig. 7.10 Two dark-field images reconstructed from the same hologram. The spatial density distribution of the glass beads is very high. The arrows point out the glass beads which are in focus. $f_1 = 400\text{mm}$, $r_p = \epsilon = 0.3\text{mm}$, $\tau = 8\text{mm}$ and $M'' \sim -20$.

used. Such a small liquid gate limits the convection currents and therefore reduces the agitation of the diatoms. In field measurements a pulsed laser source would be used, and thus agitation would not affect the image sharpness.

Holograms of bright-field and dark-field images are recorded at two different instants, then the reconstructed images are recorded in three different planes for each type of image. The three planes are defined as follows

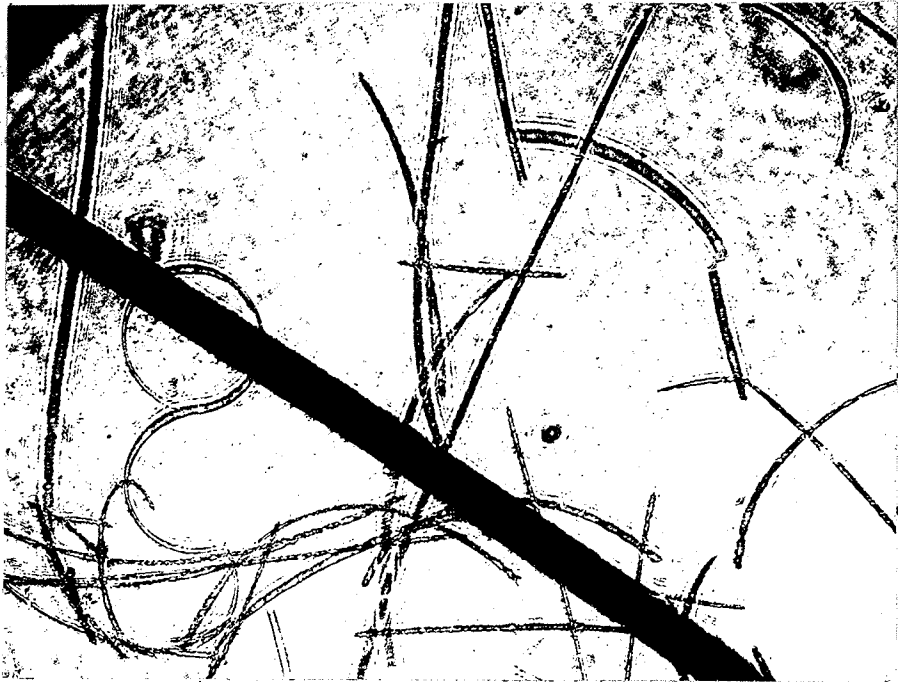
$$\text{first plane} \quad z_h + z_1 = 19\text{m}$$

$$\text{second plane} \quad z_h + z_2 = 20.2\text{m}$$

$$\text{third plane} \quad z_h + z_3 = 21.6\text{m}$$

The average transverse magnification factor is $M' \sim -20$.

Results: The recorded images shown in photographs (a) and (b) of Fig.7.11 indicate that a depth of 1.25mm in the object space corresponds to about 2.6m in the image space. The 100 μm wire visible on all the photographs indicates the size of these diatoms. This particular species of diatoms (Melosira) is about 5 μm in diameter and several millimeters long. The numerical aperture of the lens used does not allow analysis of the finest details in the dark-field images. Note that although the coherent background of the dark-field images is suppressed, the character of the focused diatoms is not altered. The background is free from the noise produced by the diffraction pattern of the out-of-focus diatoms. Again, the energy saved in recording dark-field images is really appreciable, not only because a more economical laser source is required, but because intense irradiation of living cells can be lethal. This latter consideration is most significant in biological applications in which continuous

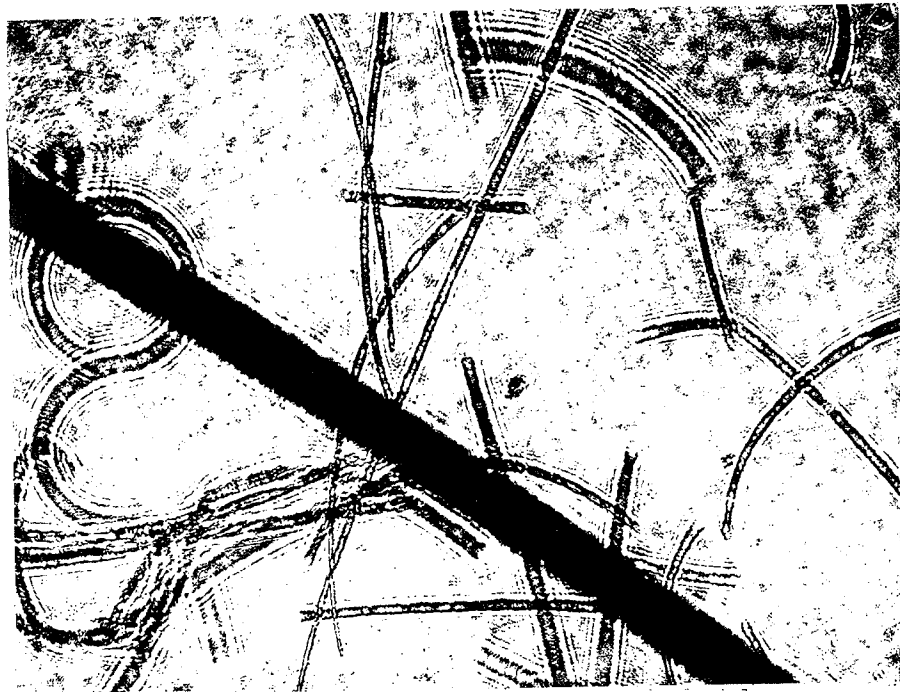


(a) Reconstructed bright-field image. $z_h + z_1 \sim 19\text{m}$

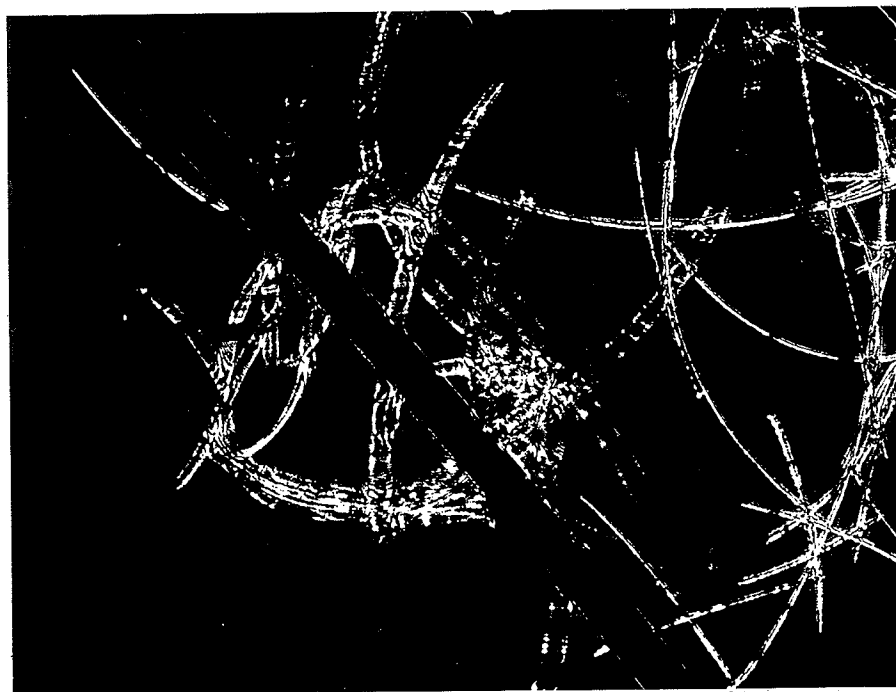


(b) Reconstructed bright-field image. $z_h + z_2 \sim 20.2\text{m}$

Fig. 7.11 Holographic imaging of diatoms. $f_1 = 400\text{mm}$, $r_p =$
 $\epsilon = 0.3\text{mm}$, $\tau = 8\text{mm}$ and $M'' \sim -50$.

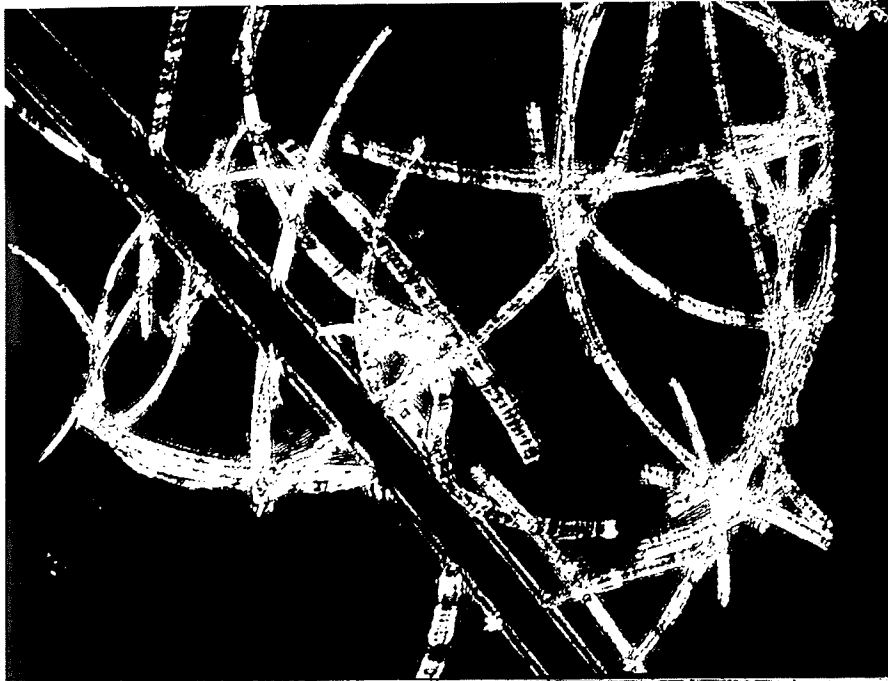


(c) Reconstructed bright-field image. $z_h + z_3 \sim 2.16\text{m}$

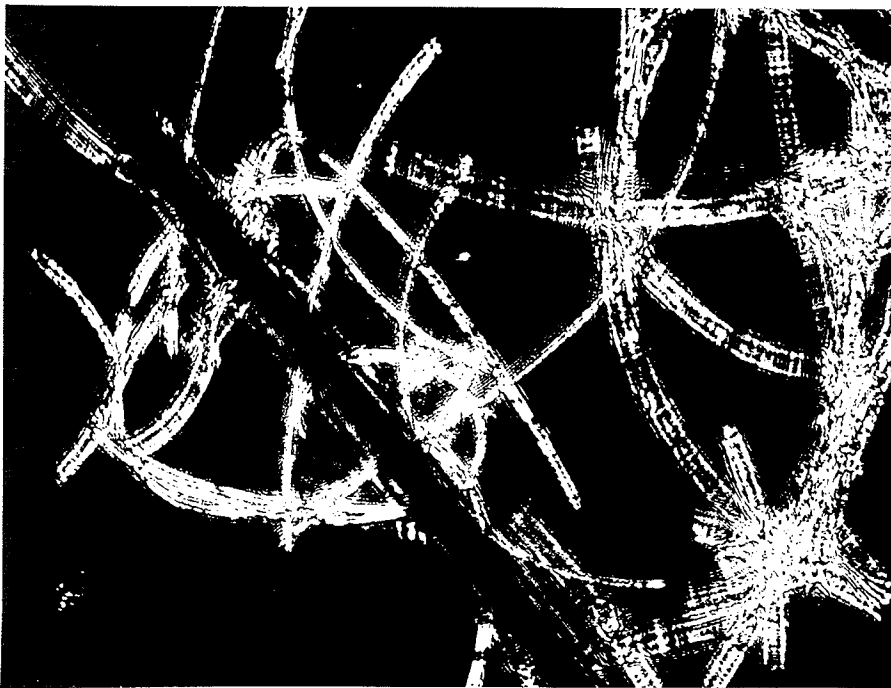


(d) Reconstructed dark-field image. $z_h + z_1 \sim 19\text{m}$

Fig. 7.11 Holographic imaging of diatoms. $f_1 = 400\text{mm}$, $r_p = \epsilon = 0.3\text{mm}$, $\tau = 8\text{mm}$ and $M'' \sim -50$.



(e) Reconstructed dark-field image. $z_h + z_2 \sim 20.2\text{m}$



(f) Reconstructed dark-field image. $z_h + z_3 \sim 21.6\text{m}$

Fig. 7.11 Holographic imaging of diatoms. $f_1 = 400\text{mm}$, $r_p = \epsilon = 0.3\text{mm}$, $\tau = 8\text{mm}$, $M'' \sim -50$.

monitoring of living organisms is desirable.

Finally, it must be pointed out that imaging through a deep sample volume is feasible; however such an investigation requires more power from the laser source, for the amount of scattering increases.

7.4 TWO RETROREFLECTOR CONFIGURATIONS

The schematic diagram of the experimental setup is found in Fig. 6.11, and general views of the setup are shown in the photographs of Fig. 7.12. Two tetrahedral prism reflectors are used, and they are placed in such a way that the sextants of one of the retroreflectors correspond to the sextants of the other one. Hence, the full area of a sextant over which the state of polarization is uniform can be used for recording the holograms.

Three identical slides are linked by a chain, and the sprockets fixed on the slides holding the retroreflectors have twice as many teeth as the sprocket fixed on the slide holding the scene. This arrangement compensates for transverse scene motion (transverse motion is more detrimental than axial motion - compare Fig. 7.5(a) with Fig. 7.5(b)).

Bright-field and dark-field holocameras are used. The experimental setups are shown in Fig. 7.13. In each holocamera an imaging lens forms an aerial image which is later reconstructed by the hologram. Filtering of the reference waves is performed in both holocameras by a 50 μ m diameter pinhole placed in the back focal plane of the 400mm focal length lens, and filtering of the dark-field images is done by means of the spatial filter

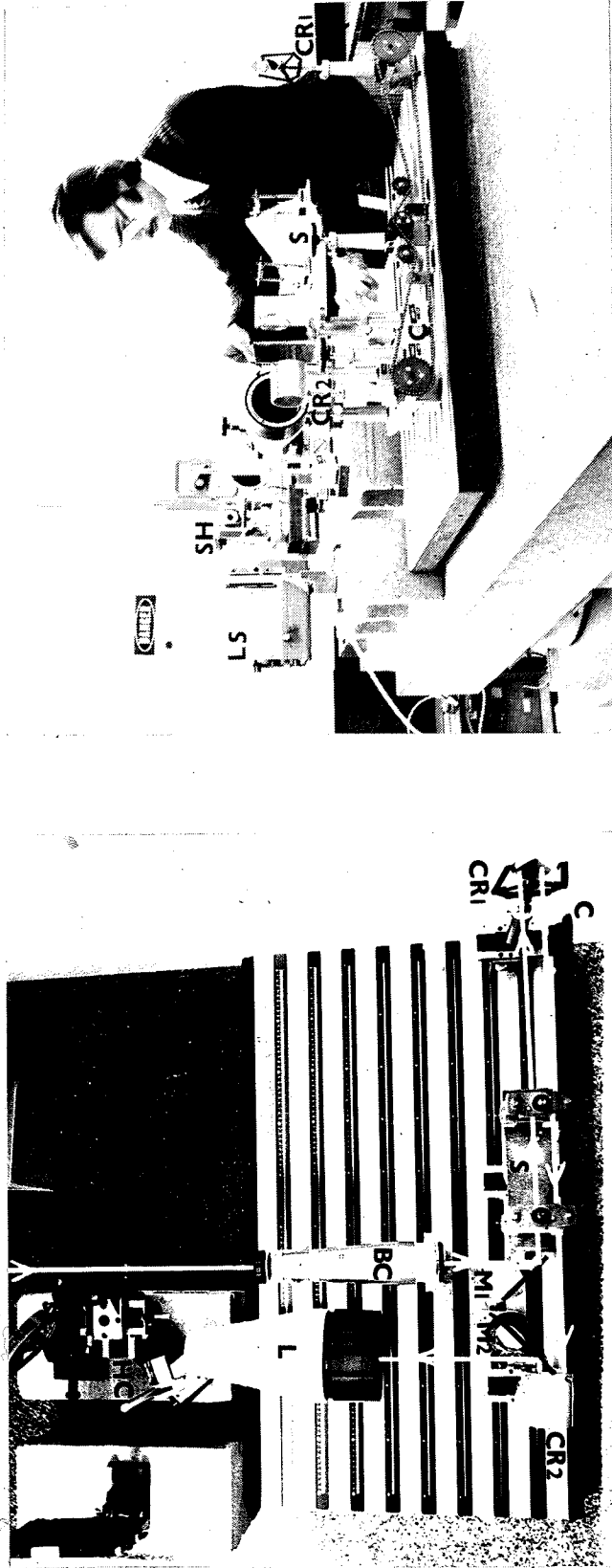


Fig. 7.12 General views of the experimental setup. The motion of the retroreflectors is synchronized with the transverse motion of the scene by means of a chain and sprocket system linking the slides holding the scene and the retroreflectors. The equipment is identified as follows: "BC" beam collimator, "CR₁" and "CR₂" tetrahedral prism reflectors, "S" scene, "M₁" and "M₂" mirrors, "L" 400mm focal length lens, "HC" holocamera, "C" chain, "LS" laser and "SH" shutter.

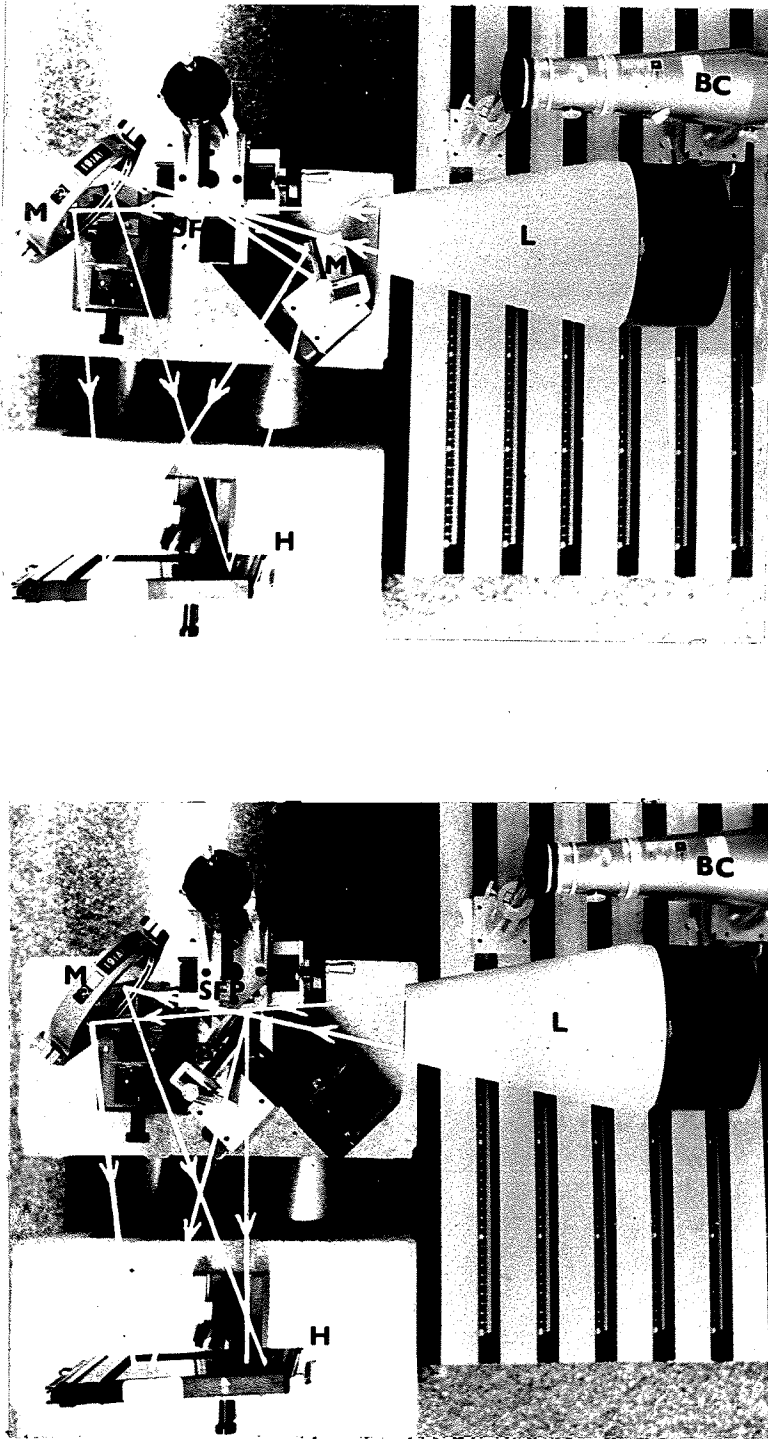


Fig. 7.13 Experimental setups of the bright-field hologcamera (on the left) and of the dark-field hologcamera (on the right). The equipment is identified as follows: "BC" beam collimator, "L" 400mm focal length lens, "SFP" spatial filter pinhole, "SFP" spatial filter mirror, "BS" beam splitter, "M" mirror and "H" photographic plate holder.

mirror (see Fig. 3.5(b)), with $\epsilon = 0.3\text{mm}$ and $\tau = 8\text{mm}$.

7.4.1 Experiment B4

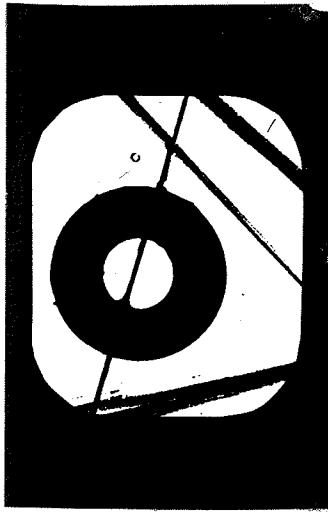
The aim of this experiment is to photographically record the focussed images of the bright-field and dark-field images of the object (a washer held by a .25mm vertical wire). Recording is done under three different conditions: firstly, there is no scene displacement; secondly, there is a $\sim 7\text{mm}$ transverse scene displacement, but no synchronization of the retroreflectors; and thirdly, there is a $\sim 7\text{mm}$ transverse scene displacement and synchronization of the two retroreflectors. The exposure time is 10 sec and the transverse magnification factor is $M'' \sim -2$.

Results: The photographs directly recorded in the conjugate planes of the objects are shown in Fig. 7.14. It is seen that compensation for transverse object displacements is most effective.

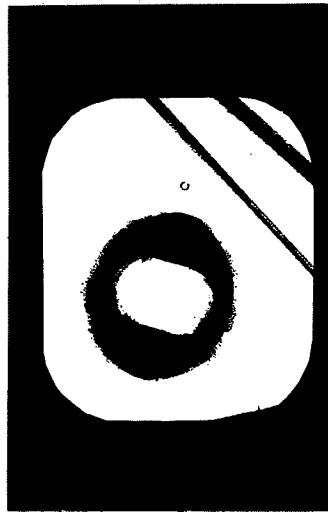
7.4.2 Experiment B5

The purpose of this experiment is to holographically record the aerial filtered images of the object by means of the bright-field and dark-field holocameras of Fig. 7.13. Recording is done under the three conditions of Experiment B4.

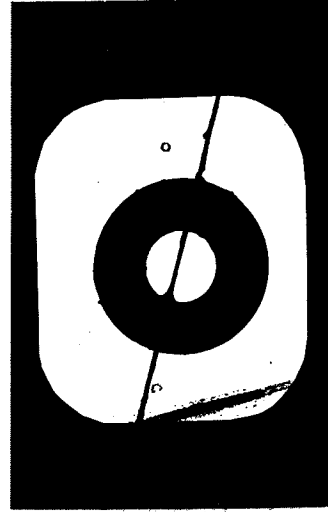
Results: The photographs of the reconstructed images are shown in Fig. 7.15. It is readily seen that object motion does not jeopardize the holographic process. These results are comparable to those obtained by direct recording of the aerial images in the conjugate plane of the object (the



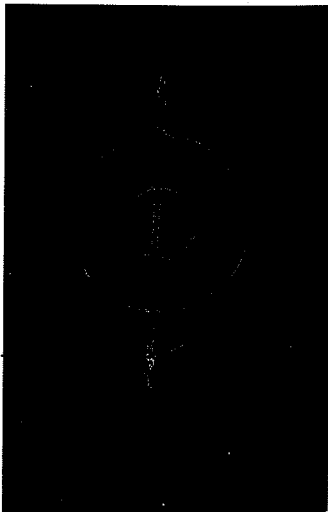
(a)



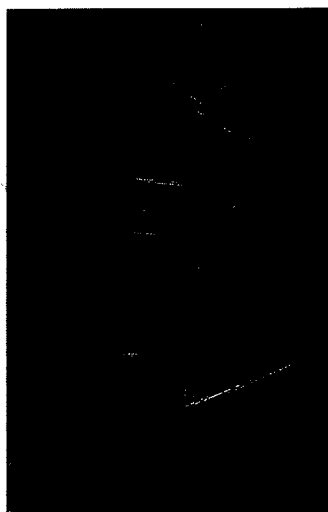
(b)



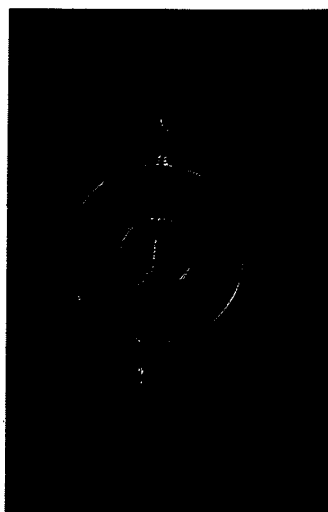
(c)



(d)

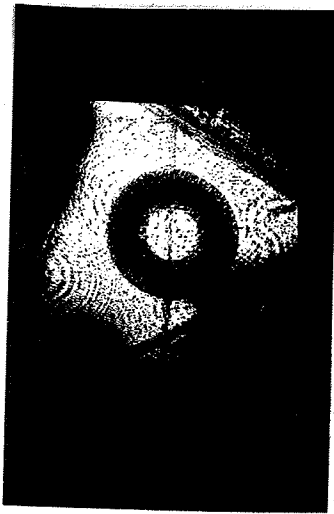


(e)

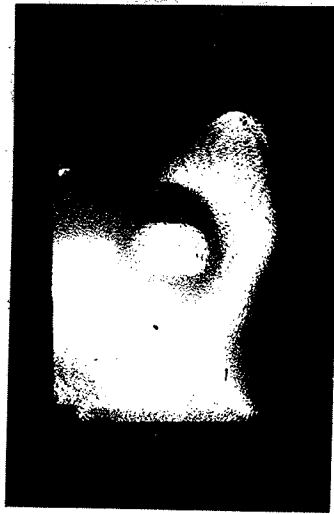


(f)

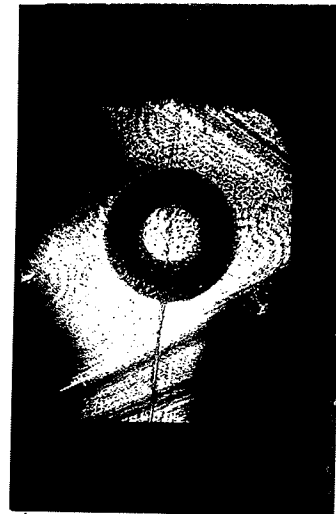
Fig. 7.14 Photographs directly recorded in the conjugate plane of the object. (a) - (c) are the bright-field images, while (d) - (f) are the dark-field images. In (a) and (d) the scene displacement is zero; in (b) and (e) the scene displacement is $\sim 0.7\text{mm}$ and the chain linking the sprockets is removed; in (c) and (f) the scene displacement is again $\sim 0.7\text{mm}$ but the chain now links the three sprockets. Exposure time: 10 sec in all cases. Transverse magnification factor: $M'' \sim -2$.



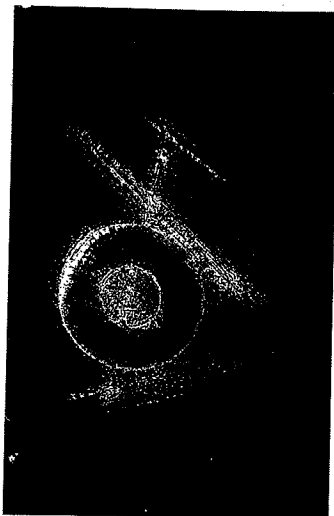
(a)



(b)



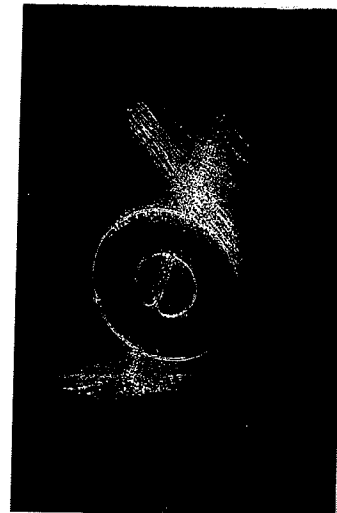
(c)



(d)



(e)



(f)

Fig. 7.15 Photographs of the holographically reconstructed images. (a) - (c) are the reconstructed bright-field images, while (d) - (f) are the reconstructed dark-field images. In (a) and (d) the scene displacement is zero, in (b) and (e) the scene displacement is $\sim 7\text{mm}$ and the chain linking the sprockets is removed; in (c) and (f) the scene displacement is again $\sim 7\text{mm}$ but the chain now links the three sprockets. Exposure time: 10 sec in all cases. Transverse magnification factor: $M'' \sim -2$.

reconstructed images are noisy because the holograms are bleached). The sharpness of the images recorded when there is no object motion, and when the motion of the object is synchronized with that of the retro-reflectors, can be appreciated by observing the vertical wire.

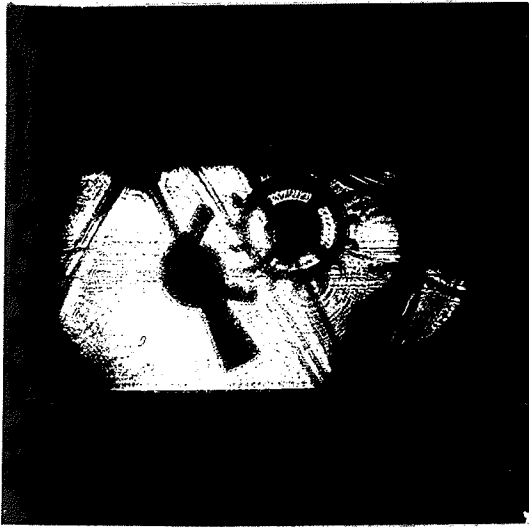
7.4.3 Experiment B6

The aim of this experiment is to holographically record the aerial filtered image of a three-dimensional scene by means of the bright-field and dark-field holocameras. Recording is done with a transverse scene displacement of $\sim 7\text{mm}$, and the chain links the three sprockets. Exposure time: 10 sec and transverse magnification factor $M'' \sim -1.7$ to -3.2 .

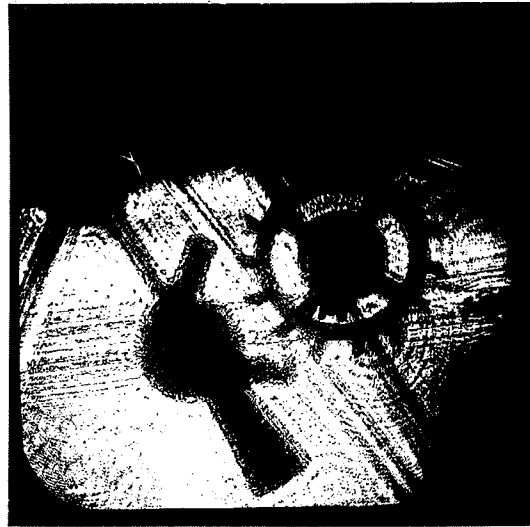
Results: The photographs of the reconstructed images are shown in Fig. 7.16. The depth dimension of the reconstructed images indicates that the scene motion is compensated for at any depth of the region of the scene which is illuminated by the beam emerging from the retroreflector CR_1 .

7.5 SIMULATION WORK RELATIVE TO THE CONFIGURATION ALLOWING IMAGING OF HYPERVELOCITY TRANSILLUMINATED SCENES

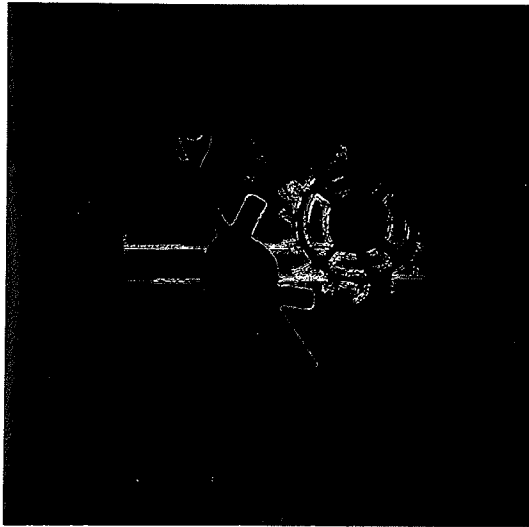
The principles established in Section 6.6 are verified by means of an experimental simulation conducted with slowly moving objects. The schematic diagram of the setup is found in Fig. 6.13. Holocameras recording bright-field and dark-field images are used; the corresponding arrangements can be seen in photographs (a) and (b) of Fig. 7.17. Filtering of the reference waves is performed in both holocameras by a $50\mu\text{m}$ diameter pinhole placed in the back focal plane of the 400mm focal length



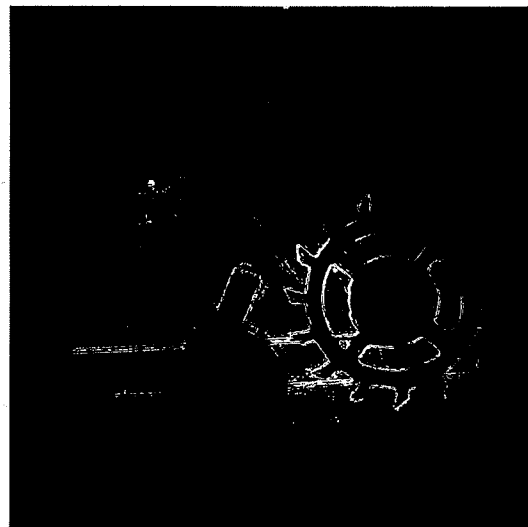
(a)



(b)

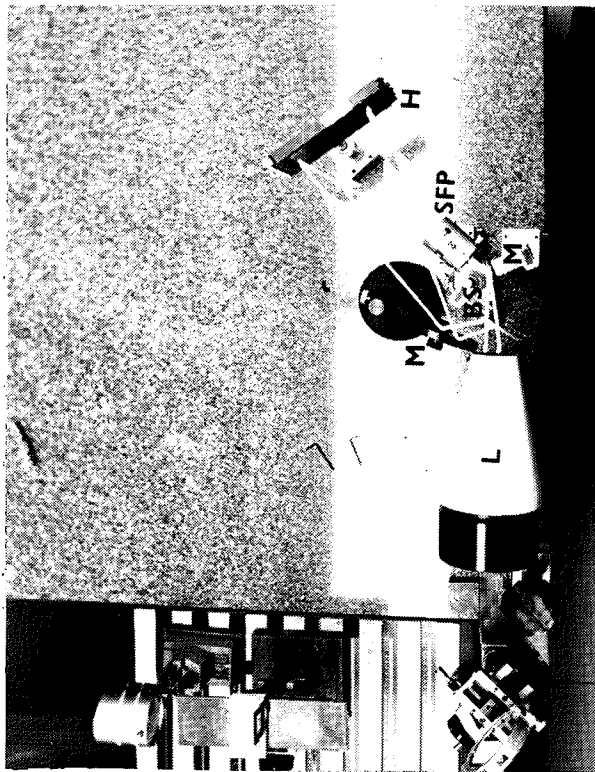


(c)

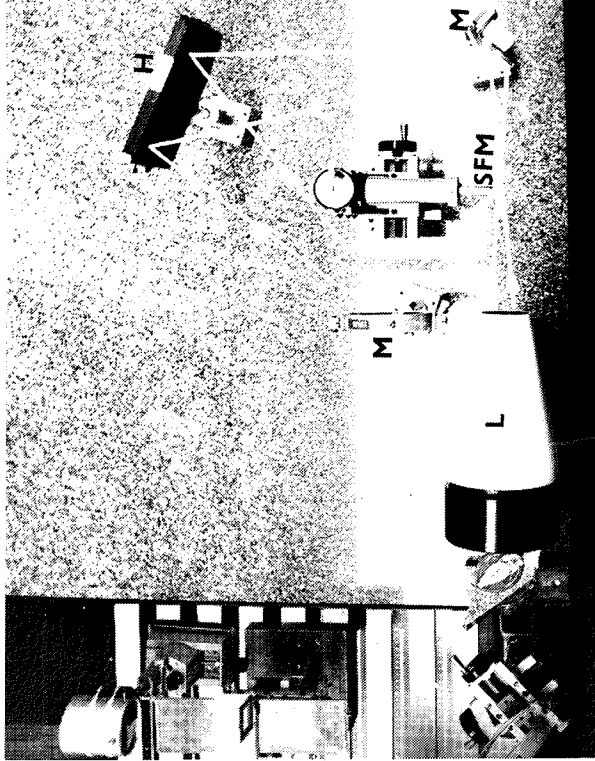


(d)

Fig. 7.16 Holographically reconstructed images of the three-dimensional moving scene when the scene motion is compensated for: (a) and (b) are the reconstructed bright-field images, (c) and (d) are the reconstructed dark-field images. In both cases the exposure time is 10 sec and the transverse scene displacement is $\sim 3\text{mm}$. The transverse magnification factor is $M'' \sim -1.7$ to -3.2 .



(a) Recording of bright-field images



(b) Recording of dark-field images

Fig. 7.17. Holocameras used in the experimental simulation of the configuration allowing imaging of hypervelocity transilluminated scenes. The equipment is identified as follows: "L" imaging lens, "SFP" spatial filter pinhole, "SFM" spatial filter mirror, "M" mirror and "H" photographic plate holder.

lens, and filtering of the dark-field images is done by means of the spatial filter mirror (see Fig. 3.5(b)), with $\epsilon = 0.3\text{mm}$ and $\tau = 8\text{mm}$. The simulation setup is shown in the photographs of Figs. 7.18 and 7.19. The angular motion of the rotating mirror is linked to the transverse scene motion by means of a steel string attached at one end to the transverse slide holding the scene, and at the other end to the lever of the rotation carrier base. In order to achieve proper synchronization, the length of the lever is chosen to be half the distance separating the object of interest from the axis of the rotating mirror. The scene is composed of three objects placed in three different planes. The first and the last objects are screws placed 150mm apart (they are not visible on the photographs) and the central object (the one for which proper synchronization is achieved) is a metallic disk held by two .25mm diameter cross-wires. An exposure time of 10 sec permits a displacement of $\sim 7\text{mm}$ of the manually operated transverse slide.

7.5.1 Experiment B7

The purpose of this experiment is to photographically record the focussed images corresponding to the three objects positioned in three different planes. Bright-field and dark-field images are thus directly recorded. Recording is done under the three different conditions: firstly, there is no scene displacement; secondly, there is a transverse scene displacement, but no synchronization of the rotating mirror; thirdly, there is a transverse scene displacement and synchronization of the rotating mirror.

Results: The photographs directly recorded in the conjugate planes of the three objects are shown in Figs. 7.20 to 7.25. The following obser-

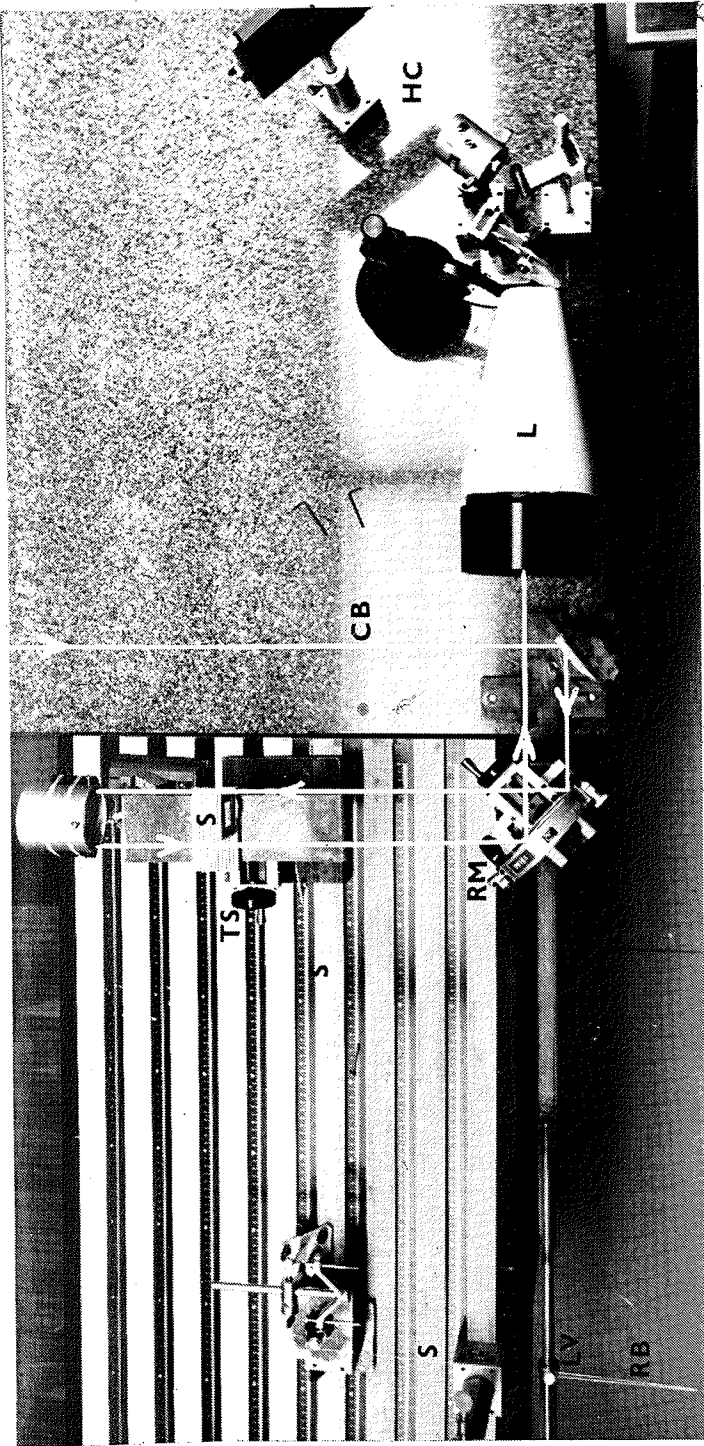


Fig. 7.18 General view of the simulation setup enabling synchronization between the angular motion of the rotating mirror and the transverse scene motion. The equipment is identified as follows: "S" steel string, "RB" rubber band, "LV" lever, "RM" rotating mirror, "TS" transverse slide, "S" scene, "CR" tetrahedral prism reflector, "M" mirror, "L" imaging lens, "CB" collimated beam and "HC" holocamera.

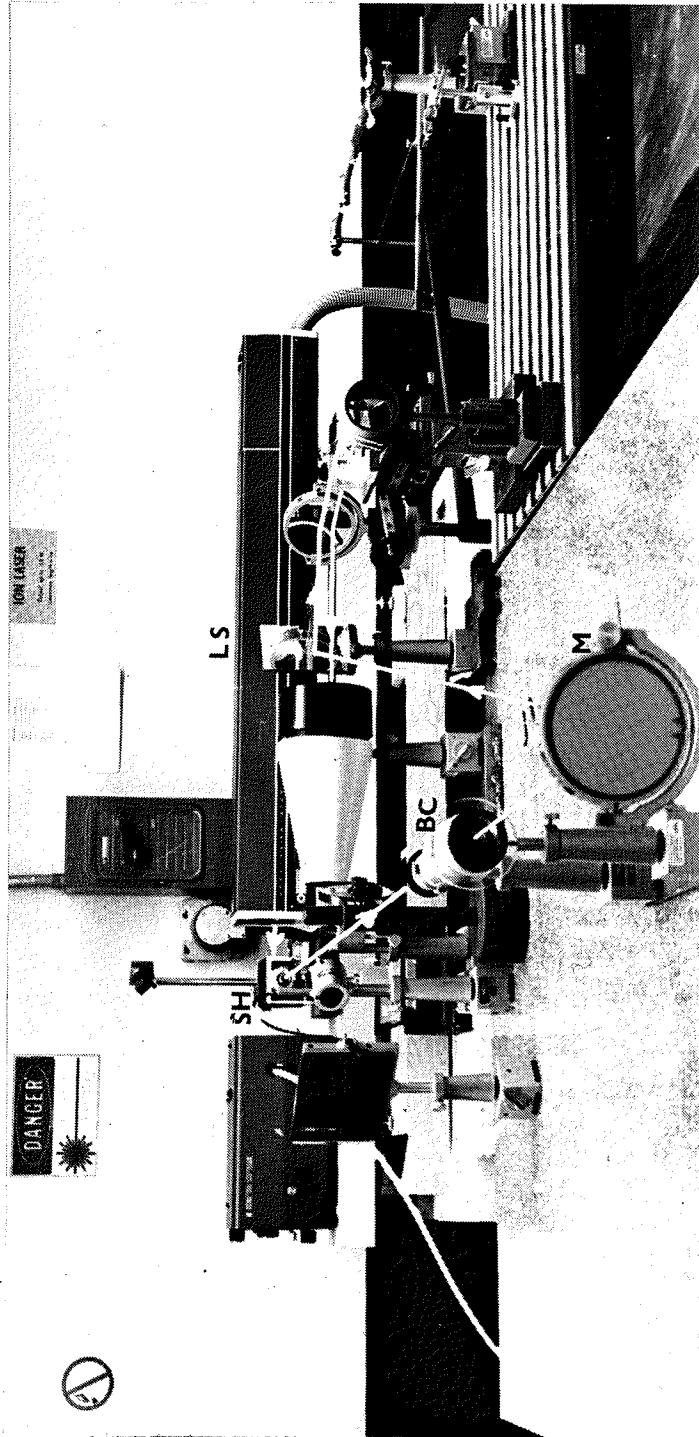


Fig. 7.19 General perspective of the simulation setup. Note that the scene and the retro-reflectors are mounted on an optical bench resting on a desk. The equipment which is not visible in Figs. 7.17 and 7.18 is identified as follows: "LS" cw argon-ion laser source, "SH" shutter, "BC" beam collimator and "M" mirror.

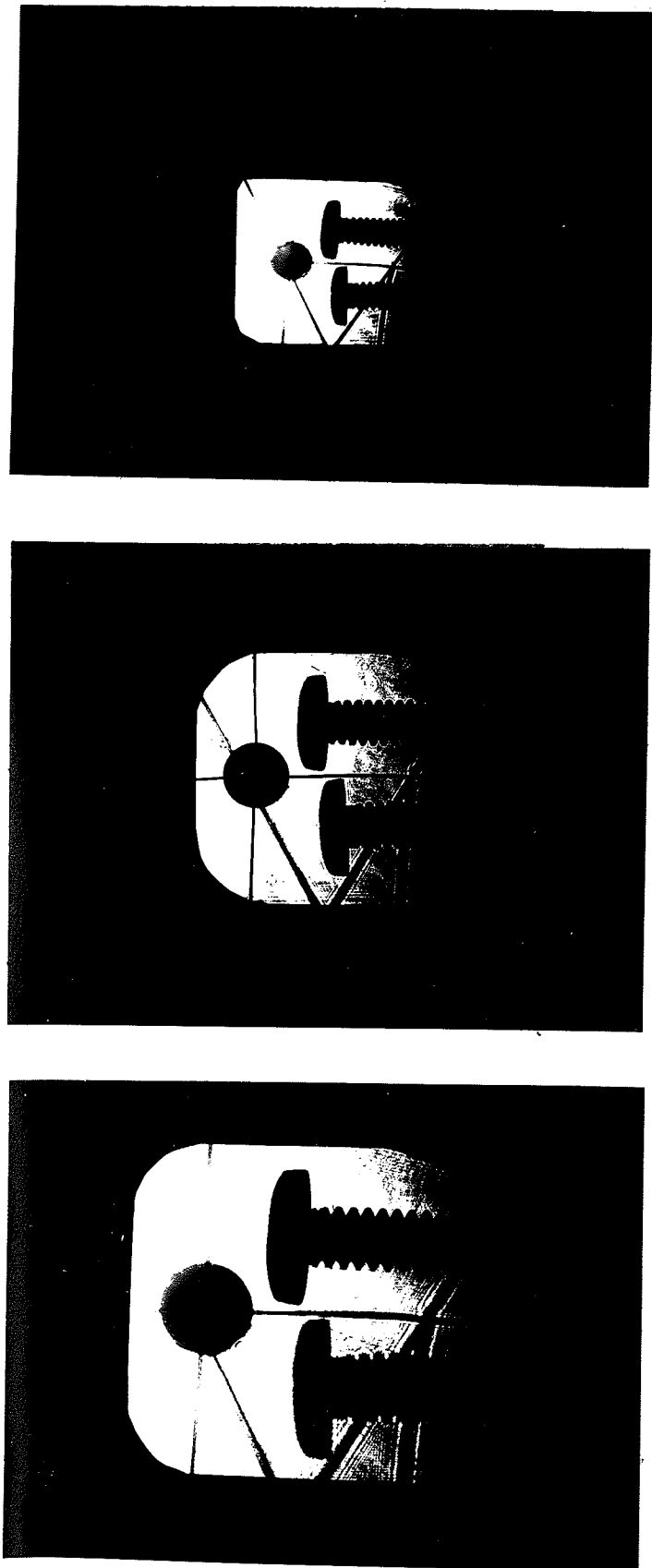


Fig. 7.20 Bright-field photographs recorded in the conjugate planes of the three objects. Exposure time: 10 sec , transverse displacement: 0. The focussed objects are easily recognized.

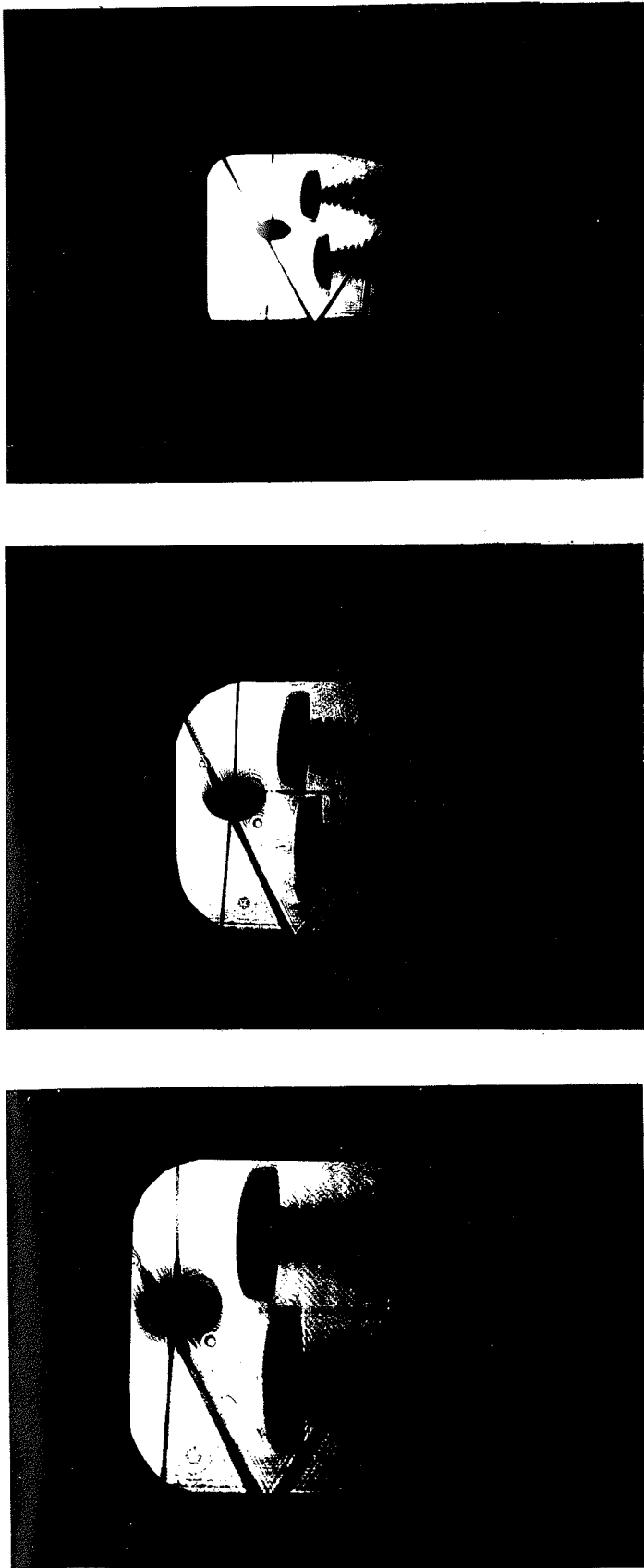


Fig. 7.21 Bright-field photographs recorded in the conjugate planes of the three objects. Exposure time: 10 sec , transverse displacement: $\sim 7\text{mm}$, the mirror rotation is not linked with the transverse scene motion. The images of the three objects are blurred by the displacement. The image of the horizontal wire, however, remains sharp.

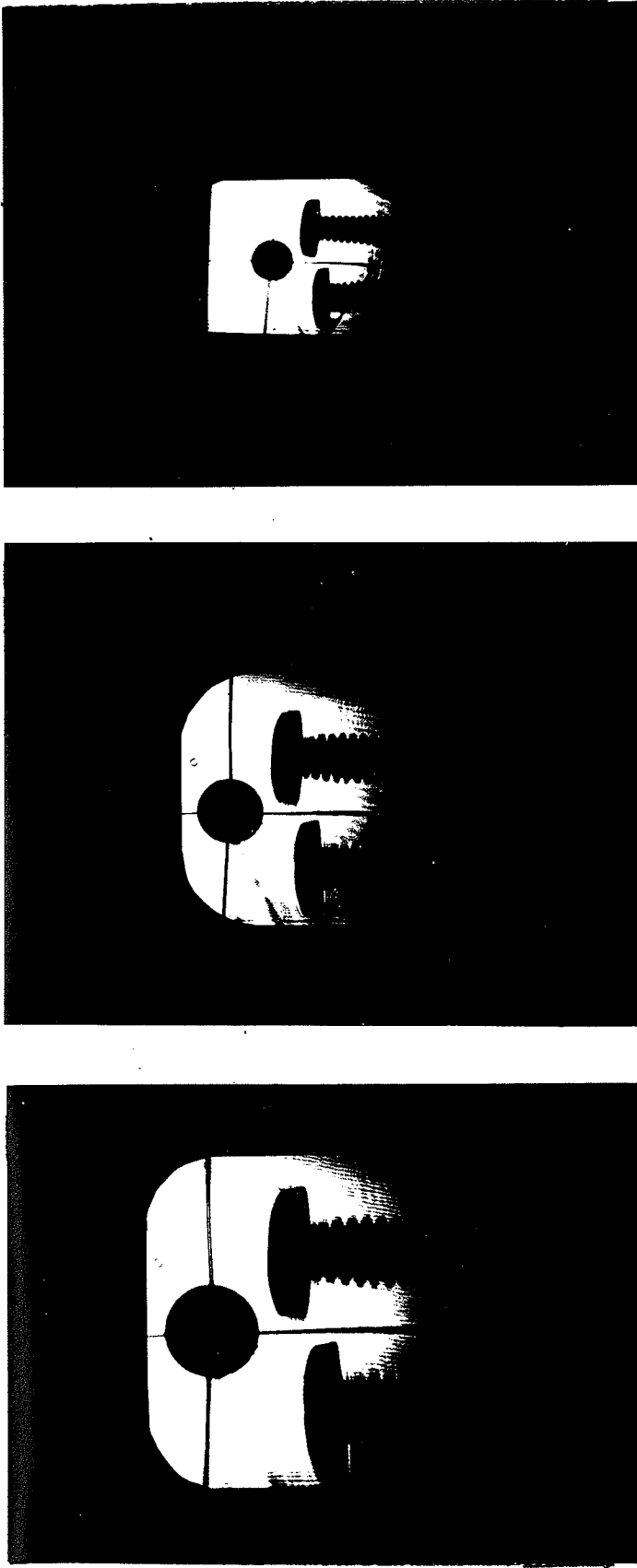


Fig. 7.22 Bright-field photographs recorded in the conjugate planes of the three objects. Exposure time: 10 sec, transverse displacement: $\sim 7\text{mm}$, the mirror rotation is linked with the transverse scene motion. The image of the central object is not blurred by the displacement (observe the vertical wire).

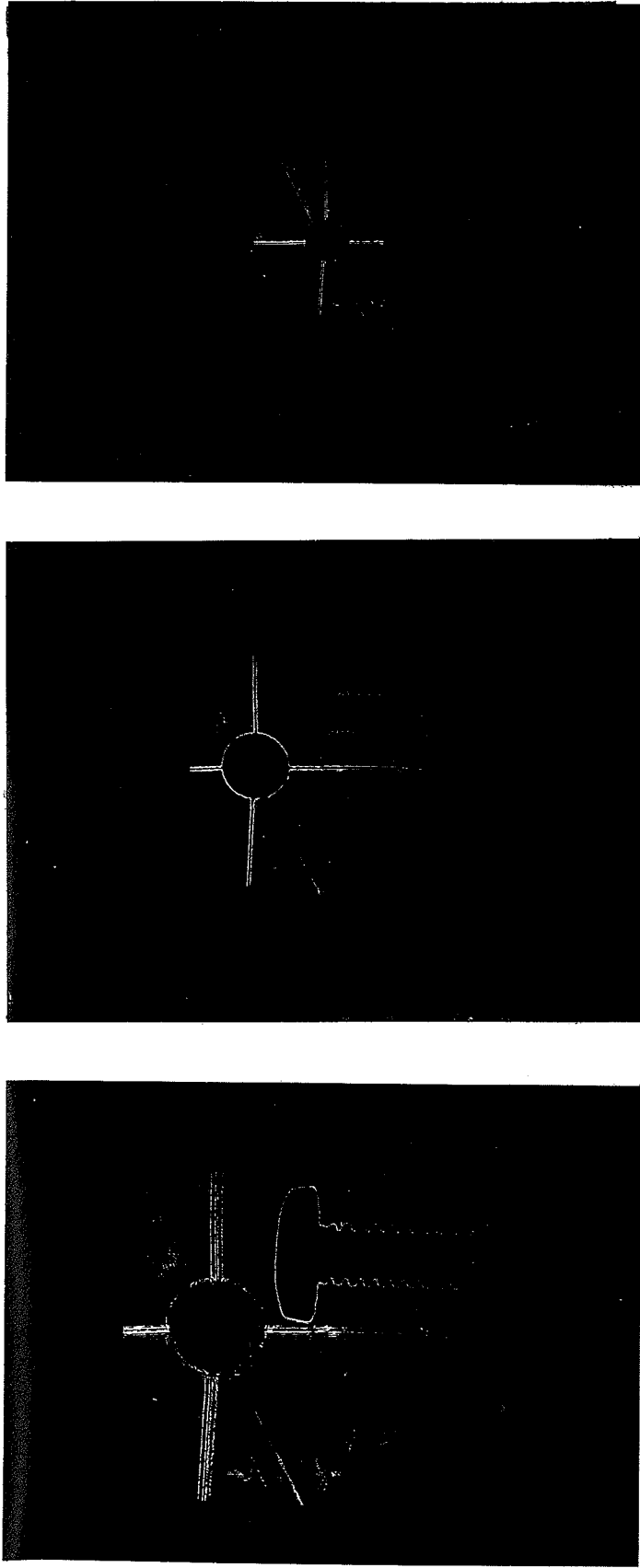


Fig. 7.23 Dark-field photographs recorded in the conjugate planes of the three objects. Exposure time: 10 sec, transverse displacement: 0. The focussed images are especially easy to recognize. Note the dark fringe on the Gaussian images. $\epsilon = 0.3\text{mm}$, $\tau = 8\text{mm}$.

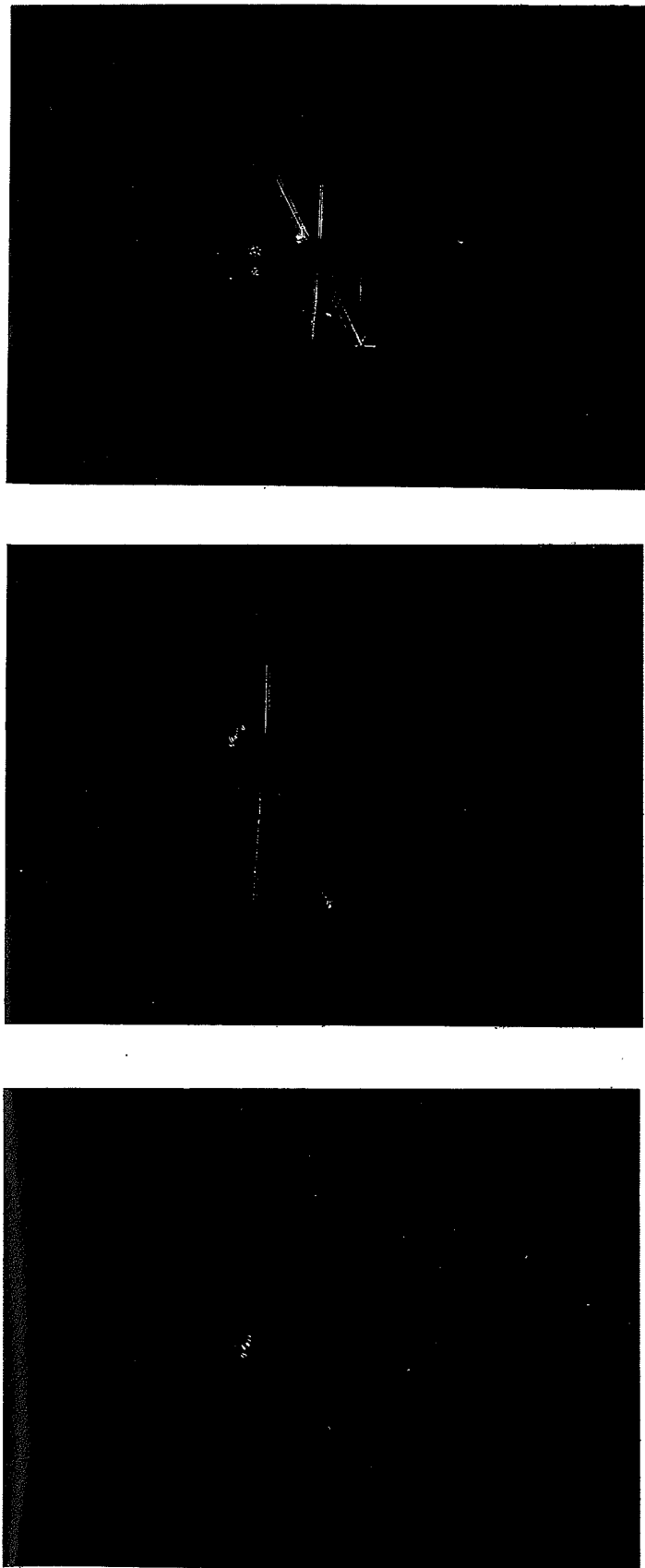


Fig. 7.24 Dark-field photographs recorded in the conjugate planes of the three objects. Exposure time: 10 sec, transverse displacement: $\sim 7\text{mm}$, the mirror rotation is not linked with the transverse scene motion. The images of the three objects have almost disappeared; the horizontal wire, however, is still visible. $\epsilon = 0.3\text{mm}$, $\tau = 8\text{mm}$.

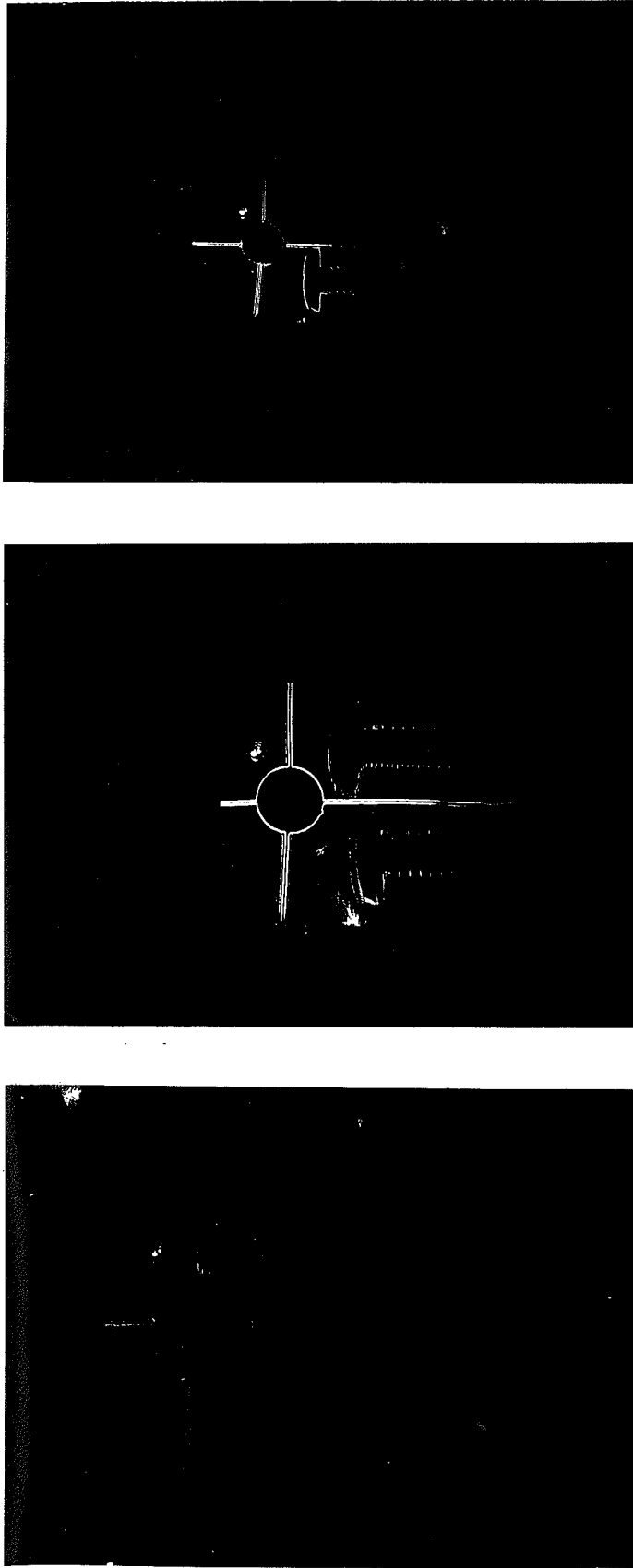


Fig. 7.25 Dark-field photographs recorded in the conjugate planes of the three objects. Exposure time: 10 sec , transverse displacement: $\sim 7\text{mm}$, the mirror rotation is linked with the transverse scene motion. The image of the central object is not affected by the displacement. However, the vertical lines of the other objects have almost disappeared.

vations can be mentioned:

i) There is no scene displacement during the 10 sec exposure time. The recorded photographs (Figs. 7.20 and 7.23) show the three focussed bright-field and dark-field images. The focussed dark-field images have the typical dark fringe on the contour of their Gaussian images.

ii) There is a 7mm transverse scene motion during the 10 sec exposure time, and the rotation of the mirror is not linked with the scene motion. The recorded photographs (Figs. 7.21 and 7.24) display blurred images, and the effect of the scene displacement on the dark-field images is such that there is almost no trace of the objects except for the horizontal wire.

iii) There is a 7mm transverse scene motion during the 10 sec exposure time, and the rotation of the mirror is linked with the scene motion. The photographs of Figs. 7.22 and 7.25 reveal sharp images of the central object (in particular, observe the vertical wire); whereas the other two objects are blurred and their vertical lines in the dark-field images have almost disappeared.

7.5.2 Experiment B8

The purpose of this experiment is to record holograms of aerial bright-field and dark-field images. Recording is done with a ~ 7 mm transverse scene motion during the 10 sec exposure time, with and without a steel string linking the rotating mirror to the transverse slide.

Results: Photographs of Figs. 7.26 to 7.28 clearly demonstrate that proper synchronization of the angular motion of the rotating mirror with the transverse displacement of the central object permits successful

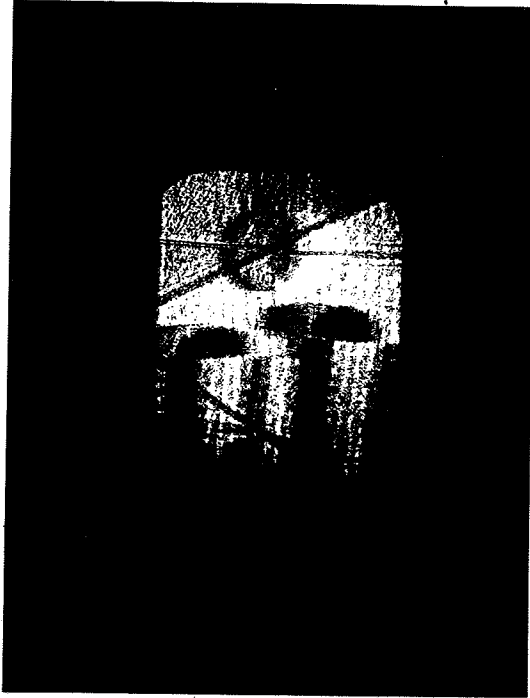


Fig. 7.26 Bright-field image reconstructed from a hologram. Exposure time: 10 sec, transverse displacement: ~ 7 mm, the mirror rotation is not linked with the transverse scene motion. This image must be compared with the central photograph of Fig. 1.21. The images in the other two planes are not recorded because they are not of interest. The reconstructed dark-field images are not shown because nothing is perceptible.

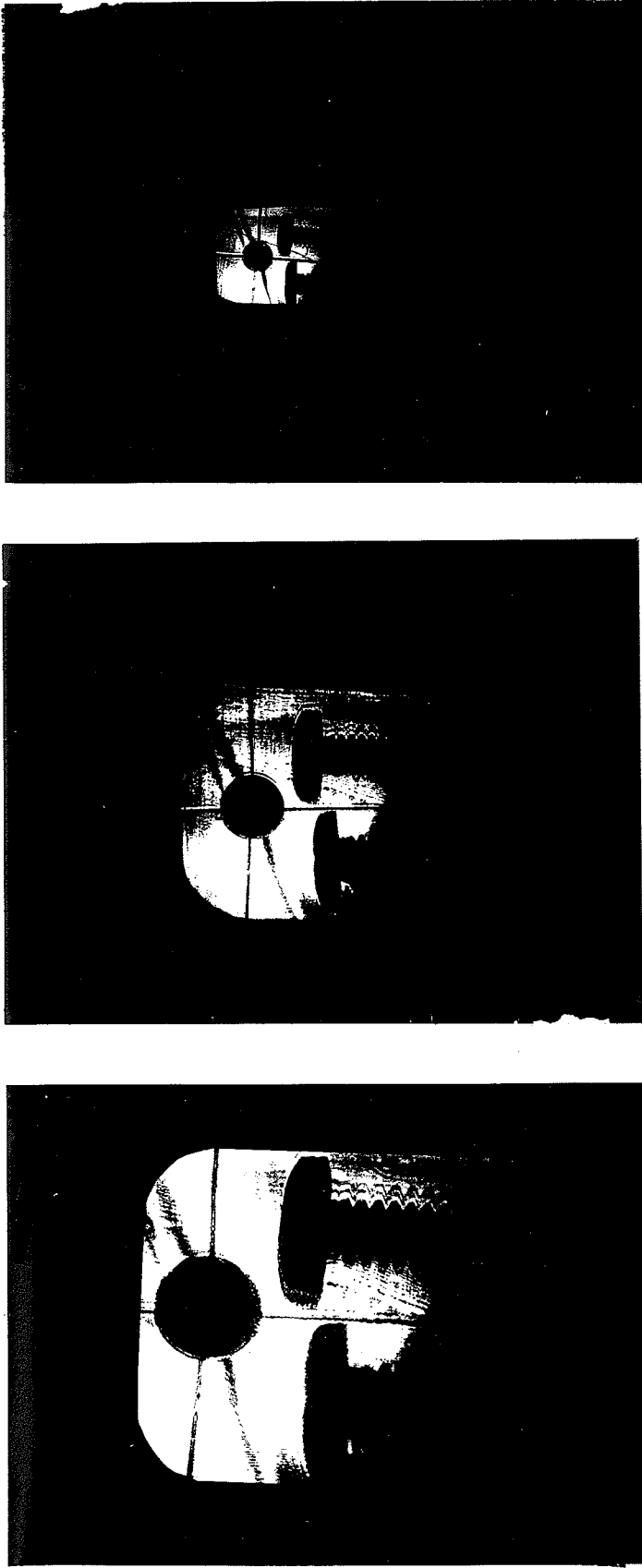


Fig. 7.27 Bright-field images reconstructed from the same hologram. Exposure time of the hologram: 10 sec, transverse displacement: $\sim 7\text{mm}$, the mirror rotation is linked with the transverse scene motion. Compare these photographs with those of Fig. 7.22.

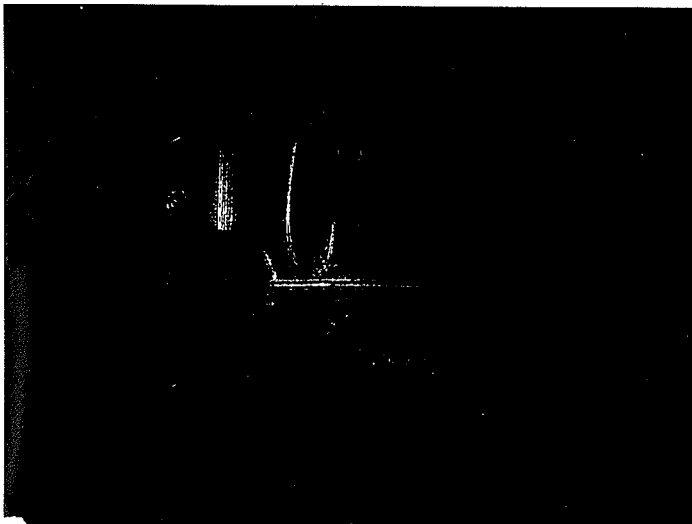
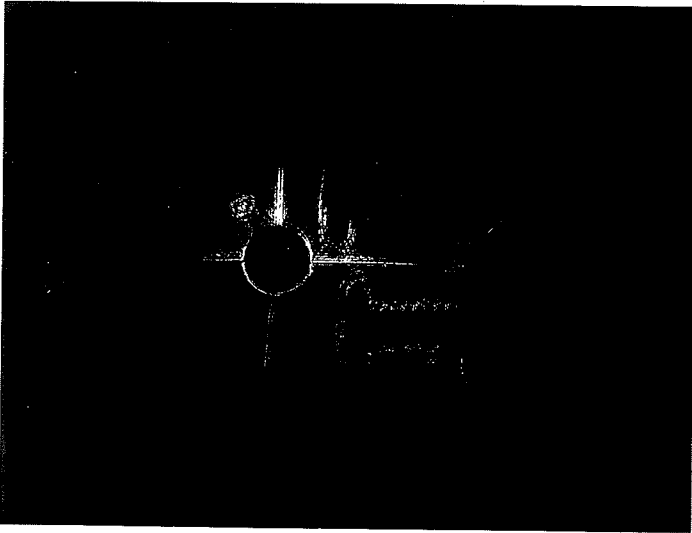


Fig. 7.28 Dark-field images reconstructed from the same hologram. Exposure time of the hologram: 10 sec , transverse displacement: $\sim 7\text{mm}$, the mirror rotation is linked with the transverse scene motion. Compare these photographs with those of Figs. 7.22 and 7.26.

holographic recording. This experimental simulation confirms the results of the theoretical study in Section 6.6. It goes without saying that each hologram allows reconstruction of the images in the conjugate planes of the three objects.

In conclusion, it can be said that dark-field imaging of dense hyper-velocity particle fields by means of the configuration using a retro-reflector and a rotating mirror would permit three-dimensional imaging of a slice of the total scene. The depth of the slice is a function of the distance between the rotating mirror axis and the slice of interest, and of the transverse displacement occurring during the exposure time.

The properties of the images reconstructed from the recorded holograms correspond precisely to those of images recorded by photographic tomography. However, the considerable advantage of holographic tomography lies in the fact that focussing is performed at the reconstruction stage only.

7.6 SUMMARY

The experimental work presented in this chapter has clearly demonstrated the practicality of holocameras with local optically processed reference beams, when they are used in the configurations studied in Chapter Six.

The effects of the scene and retroreflector motions on the images, which were holographically recorded by means of the basic beam-folded configuration, were not noticeable. Furthermore, the alignment of the holocamera

with the illuminating beam was unaffected by the retroreflector motion.

It was shown that measurement of time-varying particle fields was greatly facilitated when dark-field images were holographically recorded. In addition, dark-field recording allowed a significant increase in the power available for processing the reference wave without attenuating the image bearing wave. The quality of the bright-field and dark-field images was excellent, even though the spatial filtering of the reference wave was performed by relatively large apertures.

Finally, the experimental simulations related to the two modified beam-folded configurations (the two-retroreflector configuration and the configuration allowing imaging of hypervelocity particle fields) confirmed the validity of the theoretical arguments of Chapter Six.

PART C

USE OF HOLOGRAPHIC OPTICAL ELEMENTS IN A
HOLOCAMERA USING A LOCALLY PROCESSED REFERENCE BEAM

*Chapter Eight*GENERATION OF HOLOGRAPHIC OPTICAL ELEMENTS8.1 INTRODUCTION

Holographic optical element is the name given to an optical element which is obtained by means of holography. Conventional imaging optical elements are either refractive or reflective elements (lenses, mirrors), whereas holographic optical elements are diffractive elements. In fact, the imaging properties of holographic optical elements can be discussed with the help of a ray approach in which the image ray direction is determined by the local fringe spacing and orientation. Holographic optics has a multitude of advantages over conventional optics. These advantages can be summarized as follows: i) holographic optical elements are very economical to produce once the construction beam optical system has been built, ii) they are very light, iii) they can perform simultaneously different optical functions (this advantage is exploited in the holocamera described in a subsequent section), and iv) the imaging properties are almost independent of the substrate geometry. However, the optical efficiency of holographic optical elements is often much smaller than that of conventional elements. The diffraction efficiency of holograms greatly depends on the properties of the recording material used (silver halide emulsions, dichromated gelatin, photoresist, photopolymers, photochromic materials, electro-optical crystals or magneto-optic materials), and also on the substrate geometry. In addition, holographic optical elements cannot operate over wide spectral bandwidths since they can be regarded as being generalized diffraction

gratings with non-uniform groove spacing.

The proposed application of holographic optical elements should demonstrate the feasibility of using these elements in a holocamera with a local optically processed reference beam [58].

8.2 PRINCIPLE OF THE HOLOCAMERA [73]

The general configuration of the holocamera using holographic optical elements is represented in Fig. 8.1. Three holographic lenses are used, and the holocamera processes a local reference wave by means of the amplitude division method [27-29].

The first element H_0 performs simultaneously the functions of beam splitter and imaging element. The construction of such an element requires the use of a diverging wave filtered by a pinhole, and a collimated wave slanted with respect to the normal of the hologram plate. These two waves play the role of reference and object waves. Note that at the recording stage the intensity distribution of the former wave must be larger than that of the latter. Upon illumination of the processed hologram H_0 with a duplicate of the diverging construction wave, a virtual image of the collimated wave used at the recording stage is generated. Now, when a collimated beam illuminates a scene placed near the location of the pinhole used at the recording stage, a certain amount of light will be scattered by the scene. The scattered rays will generate an off-axis wave, propagating in the direction of the hologram optical element H_1 (as predicted by (2.13)). A fraction of the rays unscattered by the scene will suffer a uniform attenuation when passing

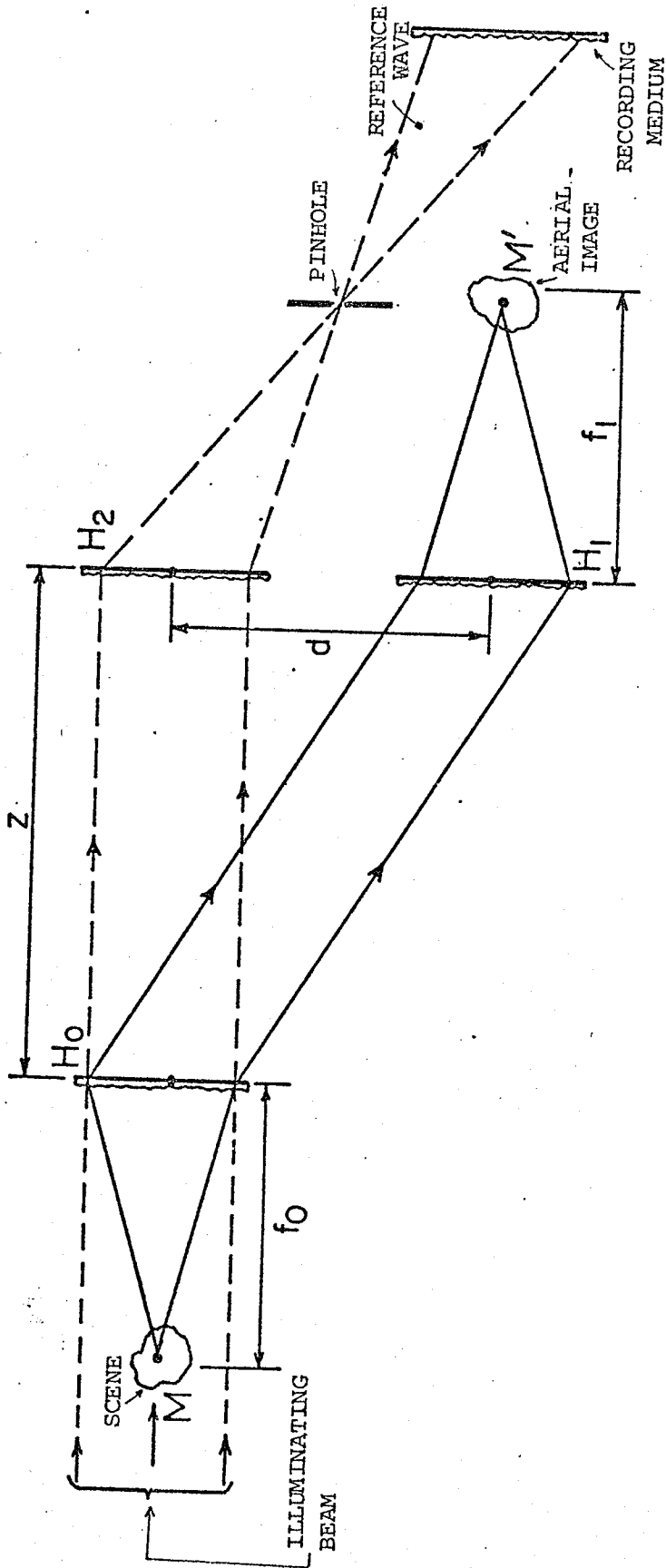


Fig. 8.1 Holocamera using three holographic optical elements: H_0 , H_1 and H_2 . H_0 performs simultaneously the functions of beam splitter and imaging element. The rays scattered by an object point M are collimated by H_0 and then focussed by H_1 onto the conjugate image point M' . The rays which are not diffracted by the scene and H_0 are focussed by H_2 onto a pinhole, which filters the reference wave.

through the hologram. They will not be deflected but will propagate in the direction of H_2 . The intensity ratio between the reconstructed wave and the undiffracted wave which passes through H_0 without any deflection is a function of the scattering properties of the scene and of the diffraction efficiency of H_0 .

The second element H_1 is recorded with an off-axis collimated wave and a converging wave, the collimated wave playing the role of reference wave. Upon illumination of the processed hologram with a duplicate of the collimated wave, a converging wave is obtained. It is easily seen that an object point placed in the vicinity of the original location of the pinhole used to record H_0 will be mapped onto an image point by the two-hologram optical element H_0-H_1 . Therefore, a scene placed in front of H_0 is mapped onto an image in the space behind H_1 .

The third element H_2 is recorded with a collimated wave (playing the role of the reference wave) propagating in a direction normal to the recording plane, and with a converging wave. The converging wave reconstructed by the processed hologram H_2 is filtered by a pinhole.

By placing a photographic plate behind the pinhole plane, a hologram can be recorded, using the aerial image of the scene produced by H_0-H_1 and the reference wave generated by H_0-H_2 . The recording plane may be placed either before or behind the focussed aerial image of the scene. For a detailed discussion of the properties of the reconstructed images, refer to Section 3.5.1.

Hologram optical elements can be recorded on curvilinear surfaces (spherical, cylindrical, conical, etc.). In essence, the holographic process permits reconstruction of unaberrated images. However, the reconstructed wave propagates through the substrate, and therefore the amplitude distribution of the reconstructed wave just behind the substrate is equal to the product of the amplitude distribution of the wave entering the substrate and the substrate transmittance. Hence, substrate irregularities deteriorate the quality of the reconstructed image which is either viewed or recorded behind the substrate. The use of emulsions on micro flat glass substrate readily eliminates the effect of the substrate on the image. Micro flat glass is somewhat more expensive than the substrate commonly used in holography. In addition, the use of flat glass does not permit recording of curvilinear holograms. The shape of a hologram is an important factor which may permit: correction of geometrical aberrations [74], enhancement of the diffraction efficiency over the surface of the hologram, and optimization of the field of view [75]. In order to alleviate the deterioration of the image quality caused by the substrate irregularities, a compensation method is proposed. This method requires sequential recording of the holograms when multiple-hologram optical elements are constructed, and is applicable to the holocamera analysed in the last section.

Consider Fig. 8.2, showing the imaging systems composed of a two-hologram optical element $H_0 - H_1$. In the compensation method presented, the hologram elements H_0 and H_1 are constructed in such a way that the amplitude

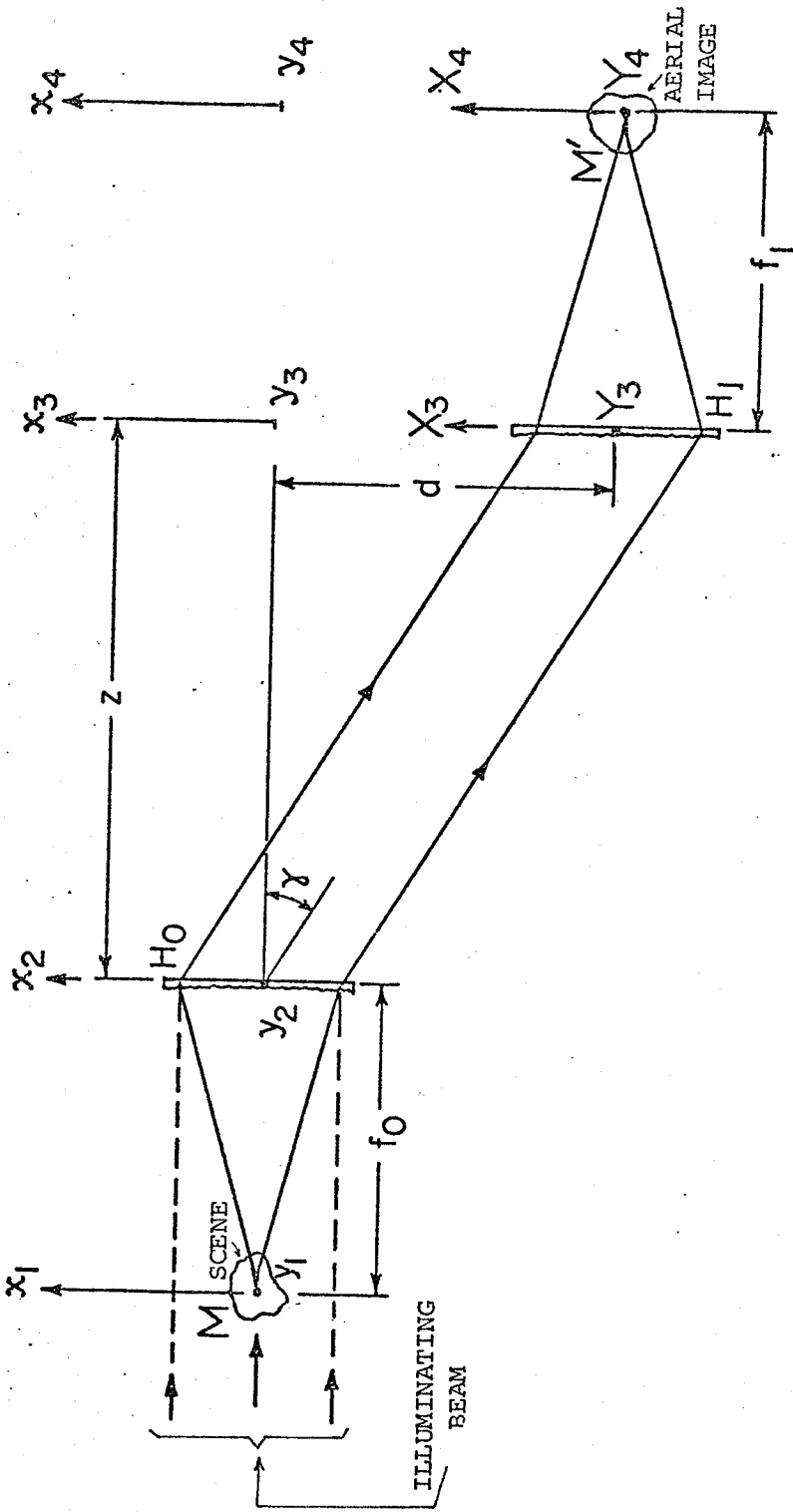


Fig. 8.2 Imaging system composed of a two-hologram optical element.

distribution of the object wave bears the conjugate of the phase errors introduced by the substrate. Upon reconstruction, the primary image which propagates through the substrate is free of any aberrations [76,77]. For the sake of simplicity, the analysis assumes that the holograms are plane holograms. This assumption permits simple mathematical analysis and does not restrain the scope of the method. The configuration allowing construction of the hologram H_0 is illustrated in Figs. 8.3 and 8.4. An auxiliary hologram H' is used and the sensitivity of its recording material should be much greater than that of H_0 in order to avoid a uniform bias exposure of the emulsion of H_0 . By immersing H' in an optically corrected glass tank (liquid gate) containing a liquid of refractive index matching that of the emulsion and the glass substrate, a perfect duplicate of the conjugate of the illuminating wave $[O_2^*(x_2, y_2)]$ can be reconstructed. If the phase errors are represented by $D_0(x_2, y_2)$ and if $R_2^*(x_2, y_2)$ is the amplitude distribution of the collimated wave in the plane (x_2, y_2) , it follows that the amplitude distribution just behind H_0 is given by

$$O_2^*(x_2, y_2) = D_0(x_2, y_2) R_2^*(x_2, y_2) \quad (8.1)$$

In a first step, H' is recorded (see Fig. 8.3), and upon reconstruction with a conjugate of the reference wave, a collimated wave $O_2(x_2, y_2)$, bearing the substrate aberration of H_0 , is obtained. In a second step, H_0 is irradiated by $O_2(x_2, y_2)$ and by a diverging wave coming from the source $P_1(x_1, y_1)$ (see Fig. 8.4). After processing of H_0 and upon its illumination by $P_1(x_1, y_1)$, the primary wave $S_2(x_2, y_2)$ is generated. Assuming that $S_2(x_2, y_2)$ is a perfect duplicate of $O_2(x_2, y_2)$, the amplitude distribution behind the substrate is

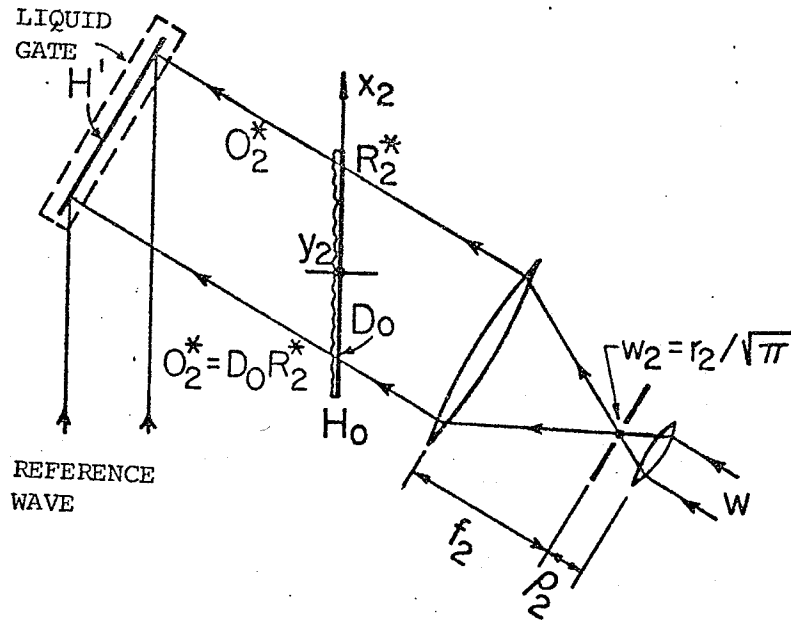


Fig. 8.3 Recording of the auxiliary hologram H' using a collimated wave for reference wave, and $O_2^*(x_2, y_2) = D_0(x_2, y_2) R_2^*(x_2, y_2)$ for object wave. The wave $O_2^*(x_2, y_2)$ bears the phase errors caused by the substrate irregularities of H_0 .

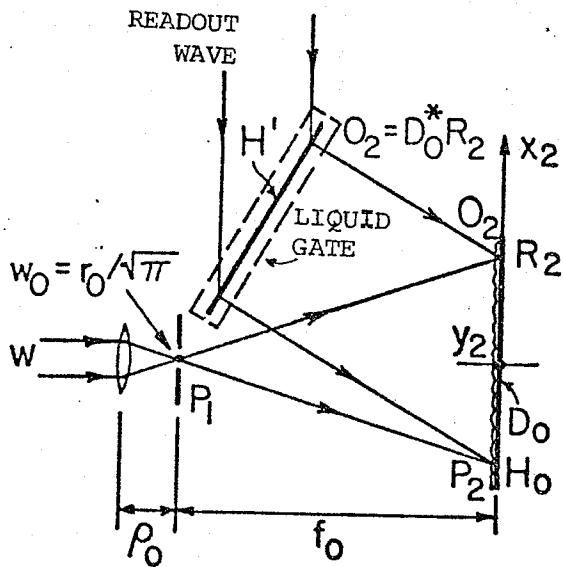


Fig. 8.4 Recording of H_0 by means of a physical point source in the plane P_1 and the reconstructed wave $O_2(x_2, y_2)$ which is generated by H' .

$$\begin{aligned}
 O_2(x_2, y_2) D_0(x_2, y_2) &= [D_0^*(x_2, y_2) R_2(x_2, y_2)] D_0(x_2, y_2) \\
 &= R_2(x_2, y_2)
 \end{aligned}
 \tag{8.2}$$

$R_2(x_2, y_2)$ is the conjugate of the collimated wave $[R_2^*(x_2, y_2)]$, thus it propagates from the plane $\{x_2, y_2\}$ to the plane $\{x_3, y_3\}$. It should be noted that the relative position of H' with respect to H_0 must not be altered during the two-step procedure.

Figs. 8.5 and 8.6 illustrate the configurations used for the construction of the auxiliary hologram H'' and the optical element H_1 . The compensation method is used once more. Yet in this case, the reference and illuminating waves irradiating H_1 consist of a collimated wave $R_3(x_3, y_3)$ and a converging wave $U_3(x_3, y_3)$ which are generated by the holograms H_0 and H'' respectively. By analogy with (8.1), it follows that

$$U_3^*(x_3, y_3) = D_1(x_3, y_3) T_3^*
 \tag{8.3}$$

Hence, upon illumination of the two-hologram optical element $H_0 - H_1$ by the reference source $P_1(x_1, y_1)$, an unaberrated converging wave $T_4(x_4, y_4)$ is created in the plane (x_4, y_4) .

The system $H_0 - H_1$ can be regarded as being an imaging system in which the object and its conjugate image are located in the planes $\{x_1, y_1\}$ and $\{x_4, y_4\}$ respectively. Note that the size of the reference and readout sources used for recording and reading the auxiliary holograms H' and H'' can be reduced to an infinitely small size by increasing the focal length and the aperture of the collimating lens. Thus, H' and H'' reconstruct the waves $O_2(x_2, y_2)$ and $U_3(x_3, y_3)$, which are perfect conjugates of the waves $O_2^*(x_2, y_2)$ and $U_3^*(x_3, y_3)$. The effect of the

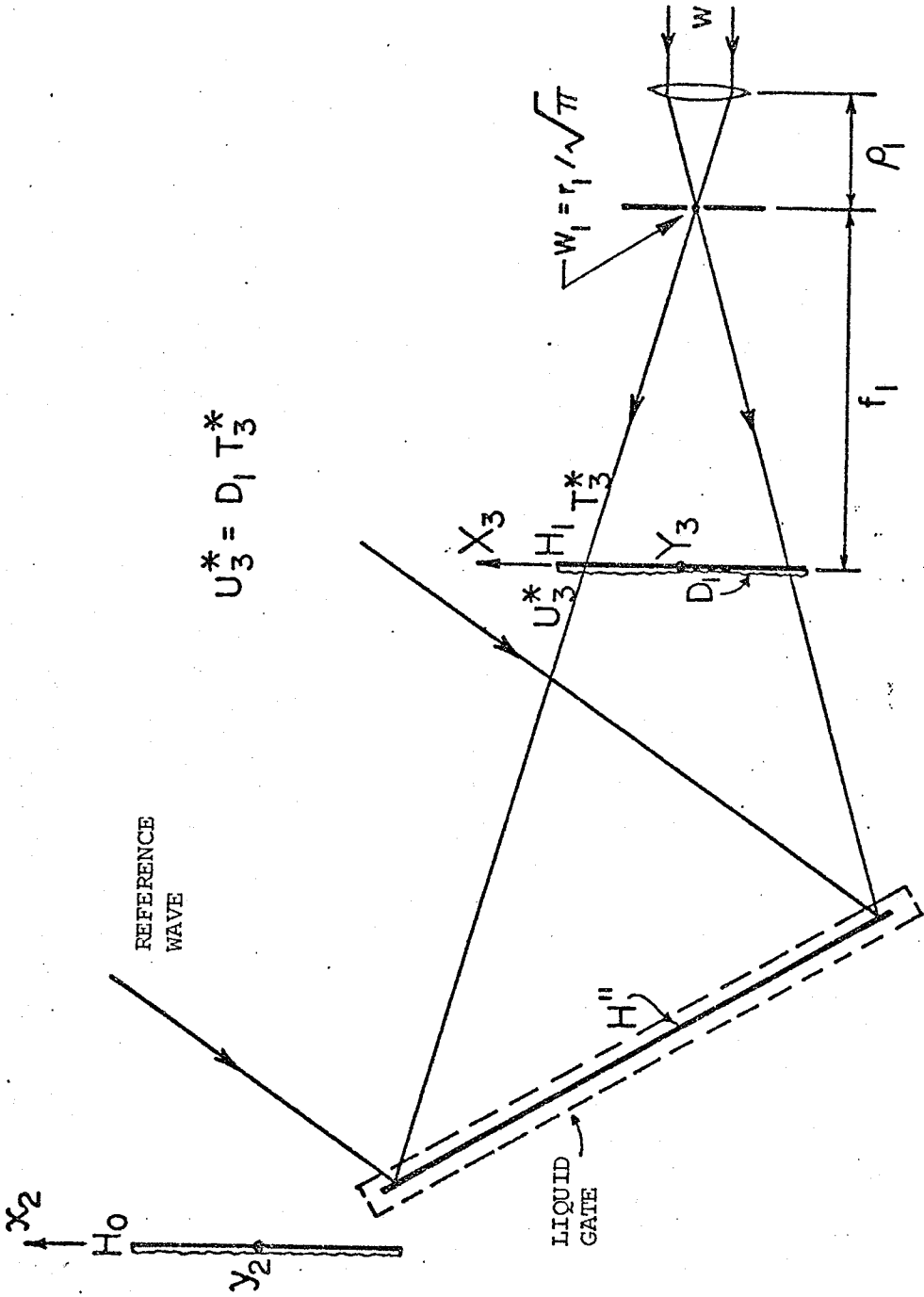


Fig. 8.5 The compensation technique is used once more. Recording of the auxiliary hologram H'' by means of a collimated wave and an object wave $U_3^*(x_3, y_3) = D_1(x_3, y_3) T_3^*(x_3, y_3)$. The wave $U_3^*(x_3, y_3)$ is a diverging wave which comes from a physical point source in the plane P_4 , and which propagates through the substrate of H_1 .

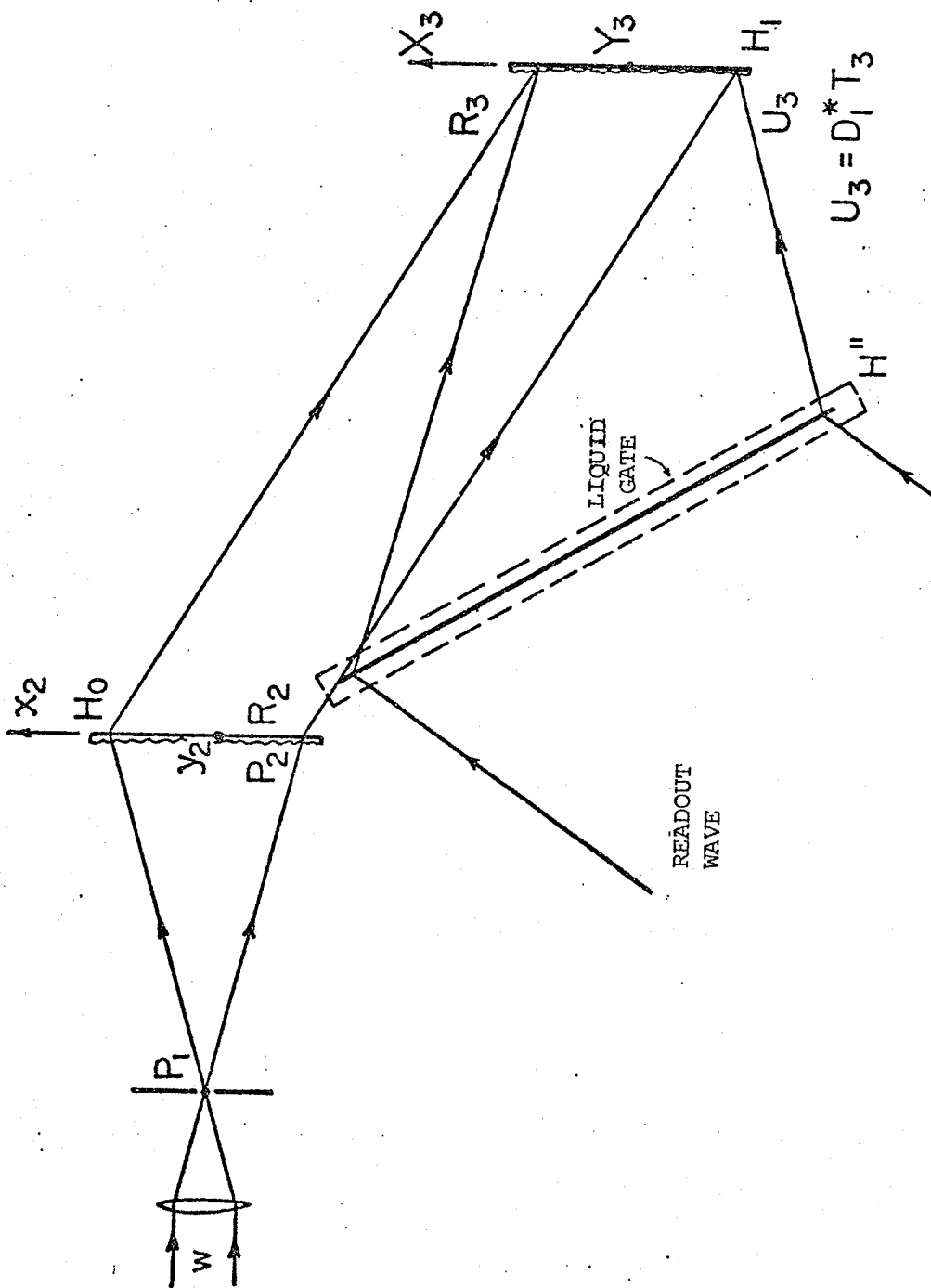


Fig. 8.6 Recording of H_1 by means of the reconstructed waves $R_3(x_3, y_3)$ and $U_3(x_3, y_3)$ which are generated by H_0 and H'' .

physical extent of the recording sources on the resolution of the system $H_0 - H_1$ will be studied in Chapter Nine.

8.4 COMMENTS

If errors in alignment of the conjugate waves used for the illumination of the auxiliary hologram occur, geometrical aberrations such as astigmatism and coma are induced in the reconstructed waves. A study of these aberrations has been given by Close [75].

For best results, it is recommended to perform in situ processing of all the holograms. A single liquid gate with optically corrected glass windows is required, since H' and H'' are neither recorded nor reconstructed simultaneously. For laboratory demonstration of the method, the use of a liquid gate equipped with a drain hose is satisfactory. The auxiliary holograms H' and H'' must only be used for recording those holograms H_0 and H_1 for which they have been specifically constructed. If the recording media of H_0 and H_1 require immersion into liquid for processing, a special apparatus allowing immersion of H_0 and H_1 during chemical processing may be easily designed. The walls of this immersion apparatus may be opaque since the apparatus is employed only during chemical processing.

In spite of the fact that the compensation method may appear to be unpractical at first sight, its applications in connection with the production of multiple hologram optical elements embodying curvilinear holograms are of fair importance. It is clear that the method enables the

production of good quality optical elements recorded on very inexpensive curvilinear substrates, since substrate irregularities are entirely compensated for.

The method is well adapted to production of a large number of high quality holographic optical elements. The use of a unique construction setup, equipped with automatic photographic processors and designed to provide rigorous alignment of the reference waves with their conjugates, would drastically decrease the production cost per element.

If, for economical reasons, it is preferable to record H_0 and H_1 on micro flat glass, the compensation method is no longer justified. Sequential recording of H_0 and H_1 is simplified since the intermediate steps, consisting of recording and reconstructing the auxiliary hologram H' , are deleted. H'' can now be used as a holographic optical element generating an exact duplicate of the physical source in the plane $\{x_4, y_4\}$. Throughout the production, the same hologram H' is used. The advantage of using the holographic optical element H'' over conventional optical elements lies in the fact that the holographic optical element will correct geometrical aberrations which occur when a converging beam propagates through a plate of constant thickness (note that the reconstructed converging beam is unaberrated only if H'' is recorded as specified in the last section).

8.5

SUMMARY

A holocamera embodying holograms as optical components has been described. It has been theoretically shown that by using an original compensation method, the phase errors caused by substrate irregularities are completely compensated for. This method of employing auxiliary holograms is expected to be most effective in the synthesis of hologram optical elements when inexpensive glass substrate is used, and/or when the holograms are recorded on curvilinear surfaces. Hence, good quality optical components can be synthesized by means of the method of wavefront reconstruction.

*Chapter Nine*RESOLUTION OBTAINABLE WITH MULTIPLE-HOLOGRAM OPTICAL ELEMENTS9.1 INTRODUCTION

Since the publication of the paper by Rogers [78] on the analogy between holograms and zone plates, imaging properties and aberrations of point holograms have been extensively studied [79-83]. However, little consideration has been given to the study of the effect of the source size on the point spread function of the point hologram. Recently, Latta was able to reduce both dispersion and aberrations in optical systems using optical elements, by designing multiple-hologram optical elements [84]. It is the aim of this chapter to analyze the effect that the finite size of the recording sources has on the resolution of the two-hologram optical element H_0-H_1 (see Fig. 8.2), which is the imaging element of the hologram camera described in the last chapter, and then to generalize the results obtained to the case of an (n)-hologram optical element. The obtainable resolution of optical elements having sequentially recorded holograms (refer to Section 8.3) is compared with the resolution obtainable when the elements have holograms recorded independently. The derivation is valid only for the pair of conjugate points, i.e., the points which coincide with the points duplicating the construction geometry of the holograms. Due to the geometrical aberrations, the resolution is impaired for the other points; nevertheless the study is of interest since in many imaging systems only the points located within a small space around the pair of conjugate points are relevant.

In holography, it is usually assumed that the construction waves originate from true mathematical point sources. This assumption is valid when the resolution criteria are not critical and when a single construction wave, namely the reference wave, is used at the recording stage. In the case of multiple-hologram optical systems, the effect of the physical size of the recording sources must not be overlooked, since the actual resolution capabilities diminish as the number of holograms increases.

In the following analysis it will be assumed firstly, that the diffraction efficiency does not depend on the spatial frequency of the recorded fringes, and secondly, that the spatial resolution of the recording medium is large enough so that the MTF has the value one over the hologram apertures. Therefore, the diffraction efficiency remains constant over the entire hologram apertures. It will also be assumed that the dimensions of the holograms are such that the diffraction phenomenon does not noticeably affect the realizable resolution.

9.2 THEORETICAL ANALYSIS [85]

The following analysis is based on the scalar theory of diffraction in which the propagation phenomenon from one plane to another is expressed in mathematical terms by the so-called Rayleigh-Sommerfeld diffraction formula. It is assumed that the Fresnel approximations remain valid for the configurations studied (refer to Appendix).

9.2.1 H₀ and H₁ are Sequentially Recorded

The holograms H₀ and H₁ are synthesized according to the method described in Section 8.3.

Transmission functions of the holograms H₀ and H₁. The transmission function of the hologram H₀ is given by (2.12)

$$T_0(x_2, y_2) = E_0(O_2, P_2; x_2, y_2) D_0(x_2, y_2) P_2^*(x_2, y_2) O_2(x_2, y_2) \quad (9.1)$$

where the subscript "0" refers to H₀. Upon illumination of H₀ with the readout wave P₂(x₂, y₂), the reconstructed wave S₂(x₂, y₂) has the following amplitude distribution

$$S_2(x_2, y_2) = E_0(O_2, P_2; x_2, y_2) D_0(x_2, y_2) |P_2(x_2, y_2)|^2 O_2(x_2, y_2) \quad (9.2)$$

Substitution of (8.1) into the above equation leads to

$$S_2(x_2, y_2) = E_0(O_2, P_2; x_2, y_2) |P_2(x_2, y_2)|^2 R_2(x_2, y_2) \quad (9.3)$$

It is seen that the substrate irregularities do not affect the quality of the reconstructed wave. Hence the effectiveness of the compensation method of Section 8.3 is proved.

Using (A.6), the propagation phenomenon of the wave S₂(x₂, y₂) from the plane {x₂, y₂} to the plane {x₃, y₃} can be expressed by

$$S_3(x_3, y_3) = H_Z(x_3, y_3) \int_{1/\lambda Z} [E_0(O_2, P_2; x_2, y_2) |P_2(x_2, y_2)|^2 R_2(x_2, y_2) H_Z(x_2, y_2)] \quad (9.4)$$

The waves $S_3(x_3, y_3)$ and $U_3(x_3, y_3)$ interfere in the plane (x_3, y_3) .

The transmission function of the hologram H_1 is given by (2.12). Hence,

$$\tau_1(x_3, y_3) = E_1(S_3, U_3; x_3, y_3) D_1(x_3, y_3) U_3(x_3, y_3) S_3^*(x_3, y_3) \quad (9.5)$$

where the subscript "1" refers to H_1 .

Point spread function. In the above section, the two-hologram optical element $H_0 - H_1$ was illuminated with the physical source $P_1(x_1, y_1)$. In order to determine the realizable resolution of the element $H_0 - H_1$, a true mathematical point source must be substituted for $P_1(x_1, y_1)$. The limit of resolution can be found from the knowledge of the point spread function in the plane $\{x_4, y_4\}$. As has already been stated, the study is limited to the derivation of the point spread function for the pair of conjugate points duplicating the construction geometry. Representing the mathematical point source by a Dirac delta function $\delta(x_1, y_1)$, and using (A.6), it follows that H_0 is illuminated by a readout wave, the expression of which is

$$Q_2(x_2, y_2) = H_{f_0}(x_2, y_2) \int_{1/\lambda f_0} [\delta(x_1, y_1) H_{f_0}(x_1, y_1)] \\ = H_{f_0}(x_2, y_2) \quad (9.6)$$

The reconstructed field just behind H_0 is

$$\psi_2(x_2, y_2) = \tau_0(x_2, y_2) H_{f_0}(x_2, y_2) \\ = E_0(O, P; x_2, y_2) D_0(x_2, y_2) P_2^*(x_2, y_2) O_2(x_2, y_2) H_{f_0}(x_2, y_2) \quad (9.7)$$

By substituting the expression of $D_0(x_2, y_2) O_2(x_2, y_2)$ given by (8.1) into the above equation, the amplitude distribution of the reconstructed

field in the plane $\{x_3, y_3\}$ is found by using (A.6). Hence,

$$\psi_3(x_3, y_3) = H_z(x_3, y_3) \mathcal{F}_{1/\lambda z} [E_0(0, P_2; x_2, y_2) H_{f_0}(x_2, y_2) P_2^*(x_2, y_2) R_2(x_2, y_2) H_z(x_2, y_2)] \quad (9.8)$$

The hologram H_1 is now illuminated by the readout wave $\psi_3(x_3, y_3)$, and therefore the expression of the reconstructed wave just behind H_1 is

$$\begin{aligned} \Omega_3(x_3, y_3) &= \tau_1(x_3, y_3) \psi_3(x_3, y_3) \\ &= E_1(S_3, U_3; x_3, y_3) D_1(x_3, y_3) U_3(x_3, y_3) S_3^*(x_3, y_3) \psi_3(x_3, y_3) \end{aligned} \quad (9.9)$$

Again, by substituting the expressions of $D_1(x_3, y_3) U_3(x_3, y_3)$, given by (8.3), into the last equation, the expression of the reconstructed field in the plane $\{x_4, y_4\}$ is found by using (A.6). Thus,

$$\begin{aligned} \Omega_4(x_4, y_4) &= H_{f_1}(x_4, y_4) \mathcal{F}_{1/\lambda f_1} [E_1(S_3, U_3; x_3, y_3) S_3^*(x_3, y_3) \\ &\quad \psi_3(x_3, y_3) T_3(x_3, y_3) H_{f_1}(x_3, y_3)] \end{aligned} \quad (9.10)$$

In the above equation, the amplitude distribution $T_3(x_3, y_3)$ in the plane $\{x_3, y_3\}$ can be expressed in terms of the amplitude distribution $T_4(x_4, y_4)$ in the plane $\{x_4, y_4\}$. $T_4(x_4, y_4)$ is known, since it represents the amplitude distribution of the field of one of the construction sources (it is used to record the auxiliary hologram H''). By using (A.6) and by taking the Fourier transform on both sides, $T_3(x_3, y_3) H_{f_1}(x_3, y_3)$ can be expressed as

$$T_3(x_4, y_4) H_{f_1}(x_4, y_4) = \mathcal{F}_{-1/\lambda f_1} [T_4(x_4, y_4) H_{-f_1}(x_4, y_4)] \quad (9.11)$$

and hence (9.10) reduces to

$$\Omega_4(x_4, y_4) = H_{f_1}(x_4, y_4) \mathcal{F}_{1/\lambda f_1} \{ E_1(S_3, U_3; x_3, y_3) S_3^*(x_3, y_3) \psi_3(x_3, y_3) \mathcal{F}_{-1/\lambda f_1} [T_4(x_4, y_4) H_{-f_1}(x_4, y_4)] \} \quad (9.12)$$

$\Omega_4(x_4, y_4)$ represents the point spread function of an ideal point source (Dirac delta function). $\Omega_4(x_4, y_4)$ permits appreciation of the limits of resolution of the two-hologram optical element $H_0 - H_1$. Two points in the object plane $\{x_1, y_1\}$ are resolved in the image plane $\{x_4, y_4\}$ only if the images of the object points are observable as two individual objects. Thus, if the spread functions of the two object points do not overlap appreciably, the image of the two points is resolvable [86].

Obtainable resolution. Assuming that (2.14) is verified for both holograms H_0 and H_1 , (9.12) can be simplified as follows

$$\Omega_4(x_4, y_4) = H_{f_1}(x_4, y_4) \mathcal{F}_{1/\lambda f_1} \{ S_3^* \psi_3(x_3, y_3) \mathcal{F}_{-1/\lambda f_1} [T_4(x_4, y_4) H_{-f_1}(x_4, y_4)] \} \quad (9.13)$$

Substituting the expressions of $S_3^*(x_3, y_3)$ and $\psi_3(x_3, y_3)$, given by (9.4) and (9.9), into (9.13), the expression of $\Omega_4(x_4, y_4)$ becomes

$$\begin{aligned} \Omega_4(x_4, y_4) = & H_{f_1}(x_4, y_4) \{ [|P_2(x_4 z/f_1, y_4 z/f_1)|^2 R_2^*(x_4 z/f_1, y_4 z/f_1) \\ & H^*(x_4 z/f_1, y_4 z/f_1)] * [P_2^*(-x_4 z/f_1, -y_4 z/f_1) H_z(-x_4 z/f_1, -y_4 z/f_1) \\ & H_{f_0}(-x_4 z/f_1, -y_4 z/f_1) R_2(-x_4 z/f_1, -y_4 z/f_1)] * \\ & [T_4(x_4, y_4) H_{f_1}^*(x_4, y_4)] \} \quad (9.14) \end{aligned}$$

In the following, the expressions of $P_2(x_2, y_2)$, $R_2(x_2, y_2)$ and $T_4(x_4, y_4)$ are going to be determined. The parameters a_j , b_j and c_j encountered will be defined by: $a_j = (r_j/\rho_j)^2 / [(\lambda \rho_j f_j)^2 + r_j^4 (f_j + \rho_j)^2]$, $b_j = 1/\lambda f_j$

and $c_j = [x_j^4 \rho_j (f_j + \rho_j)] / \{\lambda f_j [(\lambda \rho_j f_j)^2 + r_j^4 (f_j + \rho_j)^2]\}$, where $j = 0, 1, 2$.

$P_2(x_2, y_2)$ represents a diverging wave processed by a beam spatial filter, which is composed of a converging lens and a pinhole (see Fig. 8.4 for notation and geometry of the filter). If the collimated beam has a Gaussian profile, the amplitude distribution of which is $\exp[-(x^2+y^2)/\omega^2]$, it follows that by considering the phase transformation of the lens $H_{\rho_0}^*(x, y)$, [87] and by making use of (A.6), the expression of $P_2(x_2, y_2)$ is obtained.

$$\begin{aligned} P_2(x_2, y_2) &= H_{f_0} \mathcal{F}_{1/\lambda f_0} \{ H_{\rho_0}(x_1, y_1) H_{f_0}(x_1, y_1) \mathcal{F}_{1/\lambda \rho_0} [P(x, y)] \} \\ &= \exp[-\pi(x_2^2 + y_2^2)(a_0 - ib_0 + ic_0)] \end{aligned} \quad (9.15)$$

Similarly, $T_3(x_3, y_3)$ represents a diverging wave generated by a beam spatial filter. However, it propagates in a direction antiparallel to that of $P_2(x_2, y_2)$, and the beam spatial filter is located at a distance d from the y axis. Hence, with the notations of Fig. 8.2 and 8.5, it follows from (9.15) that

$$T_3(x_3 + d, y_3) = \exp\{-\pi(a_1 + ib_1 - ic_1)[(x_3 + z \tan \gamma)^2 + y^2]\} \quad (9.16)$$

$R_2^*(x_2, y_2)$ represents a collimated wave coming from the beam collimator illustrated in Fig. 8.3. The pinhole is in the front focal plane of the collimating lens. Assuming that the wavefront of the collimated beam does not change appreciably when the wave propagates from the collimating lens to H^1 , the expression of $R_2(x_2, y_2)$ can be found by using the phase transform formulae of the collimating lens and the converging lens [87]. Hence,

$$R_2(x_2, y_2) = \exp[-\pi(a_2 - ic_2)(x_2^2 \cos^2 \gamma + y_2^2)] \exp[-i(2\pi/\omega)x_2 \sin \gamma] \quad (9.17)$$

The point spread function is expected to be centered around the origin of the rectangular system of coordinates X_4 and Y_4 . It is therefore logical to describe the point spread function in terms of the coordinates $X_4 = x_4 + d$ and $Y_4 = y_4$. Using the results (9.15)-(9.17), when $z \sim f_1$, (9.14) leads to

$$\Omega_4(X_4, Y_4) = \exp[-\pi(b_1 X_4 - m_x)^2 p_x / q_x^2] \exp[-\pi(b_1 Y_4 - m_y)^2 p_y / q_y^2] \exp[i\pi b_1 (X_4^2 + Y_4^2)] \quad (9.18)$$

where $m_x = (id - iz \sin \gamma)(3a_0 + 2a_2 \cos^2 \gamma + ic_0)$, $p_x = (3a_0 + a_1 + 2a_2 \cos^2 \gamma - ic_0 + ic_1)$, $q_x = (3a_0 + a_1 + 2a_2 \cos^2 \gamma)$, $m_y = [m_x]_{\gamma=0}$, $p_y = [p_x]_{\gamma=0}$ and $q_y = [q_x]_{\gamma=0}$.

For small values of γ , $d = z \tan \gamma \sim z \sin \gamma$. Hence $m_x = m_y = 0$ and (9.18) yields:

$$\Omega_4(X_4, Y_4) = \exp[-\pi X_4^2 b_1^2 p_x / q_x^2] \exp[-\pi Y_4^2 b_1^2 p_y / q_y^2] \exp[i\pi b_1 (X_4^2 + Y_4^2)] \quad (9.19)$$

The above result is the product of three Gaussian functions: one having a complex variance, the other two having a real variance with beam half-widths $\omega_y \sim \omega_x = [q_x^2 / \pi b_1^2 p_x]^{1/2}$. By comparing this beam half-width with that of the initial physical source $T_4(X_4, Y_4)$, it is readily seen that the hologram optical element $H_0 - H_1$ has a point spread function which has a beam half-width larger than the beam half-width of the construction sources.

At this point, it is worthwhile to take a numerical example. Assuming that $\cos \gamma \sim 1$, $\lambda = 5 \cdot 10^{-7} \text{m}$, $r = r_j = 5 \cdot 10^{-6} \text{m}$, $\rho = \rho_j = 10^{-2} \text{m}$ and

$f = z = f_j = 10^{-1} \text{ m}$, it follows that $a = a_j = 10^4$, $b = b_j = 2 \cdot 10^7$ and $c = c_j = 50$. Eq. (9.19) yields

$$\begin{aligned} \Omega_4(X, Y) &= \exp[-\pi(b^2/a)(X^2+Y^2)] \exp[i\pi b(X^2+Y^2)] \\ &= \exp[-(\pi/25)(1/6)10^{12}(X^2+Y^2)] \exp[i\pi 10^7(X^2+Y^2)]. \end{aligned} \quad (9.20)$$

The beam half-width $\omega_y \sim \omega_x = [6(25/\pi)]^{1/2} 10^{-6} \text{ m}$ is $(6)^{1/2}$ times larger than that of the physical source used to synthesize H_0 and H_1 .

When the beam collimator providing $R^*(x_2, y_2)$ is equipped with a lens of very large focal length ($f_0 \ll f_2$ and $f_1 \ll f_2$), the coefficients a_2 , b_2 and c_2 take the common value $a_2 = b_2 = c_2 = 0$. Therefore, the beam half-width of the point spread function is reduced to

$\omega_y \sim \omega_x = [4(25/\pi)]^{1/2} 10^{-6} \text{ m}$ for the holographic optical element obtained by sequential recording.

9.2.2 H_0 and H_1 are Independently Recorded

Two independently recorded holograms H_0 and H_1' can be used in the imaging system of Fig. 8.2. In this case, the same configurations shown in Figs. 8.3 and 8.4 can be used to synthesize both H_0 and H_1' . The hologram H_1' is positioned in the imaging system in such a way that the collimated readout wave reconstructed by H_0 reconstructs a converging wave which is the conjugate of the diverging wave used at the construction stage. Both holograms have the same transmission function given by (9.1). Hence, it is easily shown that the point spread function of the two hologram optical element $H_0 - H_1'$ is now given by

$$\begin{aligned}
\Omega'_4(x_4, x_4) &= H_{f_1}(x_4, y_4) \int_{1/\lambda f_1}^{\infty} [P_2^*(-x_3, -y_3) R_2(-x_3, -y_3) \psi(x_3 - d, -y_3) H_{f_1}(x_3, y_3)] \cdot \\
&= \exp[-\pi x_4^2 b_1^2 p'_x / (q'_x)^2] \exp[-\pi y_4^2 b_1^2 p'_y / (q'_y)^2] \\
&\quad \exp[i\pi b_1 (x_4^2 + y_4^2)] \quad , \quad (9.21)
\end{aligned}$$

where $p'_x = p_x - 2a_0$, $q'_x = q_x - 2a_0$, $p'_y = [p'_x]_{y=0}$ and $q'_y = [q'_x]_{y=0}$.

The numerical values used previously lead to $\omega'_y \sim \omega'_x = [4(25/\pi)]^{1/2}$.

It is clear that the hologram optical element $H_0 - H_1$ has better resolution than the element $H_0 - H_1$. However, the holograms H_0 and H_1 cannot be perfectly positioned with respect to each other, and therefore geometrical aberrations are induced [75].

Again, when $f_0 \ll f_2$ and $f_1 \ll f_2$, the beam half-width of the point spread function reduces to a smaller value $\omega_y \sim \omega_x = [2(25/\pi)]^{1/2}$.

9.2.3 Generalization to an (n)-Hologram Optical Element

The results obtained with two-hologram optical elements can be generalized for a system having a larger number of holograms. In Table 9.1, the beam half-width ω_n of the point spread function of the system obtained by sequentially recording (n) holograms, is compared with the beam half-width ω'_n of the point spread function of systems obtained by independently recording (n) holograms. The elementary construction sources are assumed to have an identical beam half-width ω ; in addition the distance between holograms is assumed to be z , with $z \sim f_1 \sim f_2$.

Table 9.1 Generalization of the results to (n)-hologram optical elements

n =	Sequential recording: $(\omega_n)^2 =$	Independent recording: $(\omega'_n)^2 =$
1	$2\omega^2$	$2\omega^2$
2	$6\omega^2$	$4\omega^2$
3	$14\omega^2$	$6\omega^2$
4	$30\omega^2$	$8\omega^2$
5	$62\omega^2$	$10\omega^2$
-----	-----	-----
n-1	$(\omega_{n-1})^2$	$2(n-1)\omega^2$
n	$2[(\omega_{n-1})^2 + \omega^2]$	$2n\omega^2$

9.3 APPLICATIONS

Full potential applications of multiple-hologram optical elements have not yet been extensively explored. As already mentioned, multiple-hologram optical elements may be used for improving imaging capabilities and/or for reducing dispersion of single-lens optical elements. The feasibility of using a large number of holograms in holographic optical elements will depend on the availability of photosensitive materials offering a very high diffraction efficiency associated with a very good resolution. Combination of several lenses permits greater control over geometrical and chromatic aberrations in conventional optical elements; likewise, combination of several holograms in holographic optical elements will restrain geometrical aberrations and dispersion [84].

As an example of application, consider the holocamera described in

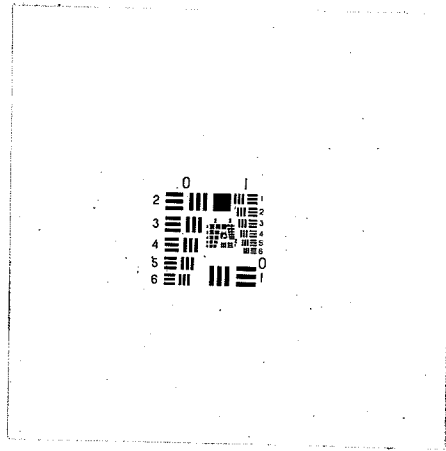
Section 8.2. This holocamera uses a two-hologram optical element for imaging the transilluminated scene. It can be seen that H_0 and H_1 may be recorded either sequentially or independently, while the scene recording hologram is necessarily sequentially recorded. Therefore, the resolution of the reconstructed images will correspond either to the resolution of a sequentially recorded three-hologram optical element, or to the resolution of an independently recorded two-hologram optical element associated with a sequentially recorded single-hologram element. This correspondence will depend on the way H_0 and H_1 are recorded.

Results of an experimental investigation conducted with independently recorded holograms are shown in Fig. 9.1. The aim of this work is merely to demonstrate the usefulness of multiple-hologram optical elements. The magnification factor is proportional to the ratio of the "focal lengths" of H_0 and H_1 . Maximum resolution is obtained for those points which coincide with the construction sources. As it can be seen in Figs. 9.1 (b) and (c), the results obtained are quite remarkable and it is thought that in the near future such diffractive imaging systems will replace conventional imaging systems which use refractive and/or reflective optical components.

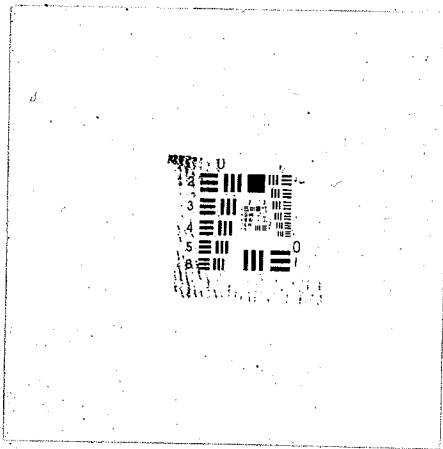
9.4 SUMMARY

The point spread function for a two-hologram optical element has been found, and the generalization to an (n)-hologram optical element has been obtained.

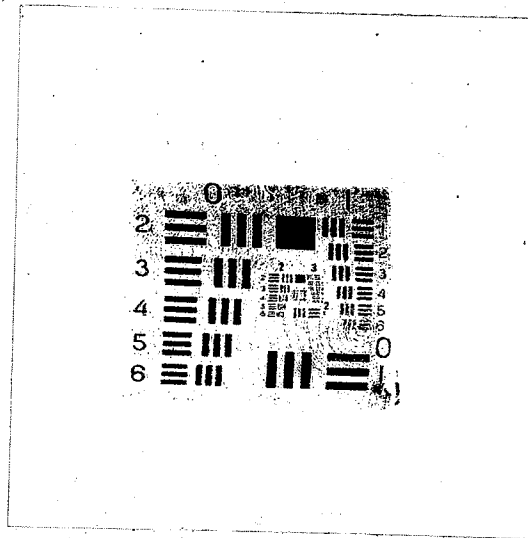
The Rayleigh-Sommerfeld diffraction model permits simple mathematical



(a)



(b)



(c)

Fig. 9.1 Holographic imaging of a resolution test target by means of the holocamera embodying three-hologram optical elements: (a) shows a contact print of the original transparency, (b) and (c) show the reconstructed images with transverse magnification factors $M \sim 1$ and $M \sim 2$ respectively.

manipulations when Fresnel's approximations are considered. In dealing with holograms of large dimensions which are often at a close distance from one another, Fresnel's approximations regarding the distance between the two planes of interest (which must be much greater than the maximum linear dimension of the holograms) are not always valid; however, the analysis leads to meaningful results, as the numerical example shows. In fact, the concepts involved in the analysis could also permit the study of the obtainable resolution with hologram optical elements containing reflection type holograms.

Even though the point spread function obtained with an optical element having (n) sequentially recorded holograms widens considerably as (n) increases, geometrical aberrations do not increase in consequence as they do when holograms are recorded independently.

*Chapter Ten*CONCLUSIONS10.1 RÉSUMÉ OF THE ACHIEVEMENTS

The scope of this thesis has been limited to the presentation of new methods and concepts in the challenging area of particle field measurement by holography with a local optically processed reference beam.

The significant contributions of the work presented can be summarized as follows:

PART A Holographic recording of filtered aerial images can be performed by means of a new holographic method allowing simultaneous image filtering and processing of a local reference beam. Very simple spatial filters, such as contrast enhancement and dark-field and phase contrast filters, permit improvement of the visibility of certain image details. Since an optical processor forms an aerial image of the scene, the position of the recording plane with respect to this aerial image can be easily controlled, and a premagnified image can be recorded. The generation of a local reference wave is performed without attenuating the object bearing wave, as the unwanted zero order spatial frequency component provides a reference wave with a well defined wavefront. Thus, energy requirements of the laser source are greatly reduced.

Three different types of optical processors have been analysed and it has been shown that their imaging properties are essentially similar, since the amplitude distributions of the electric fields of the three reconstructed images differ only by a phase factor which cannot be recorded

by a square-law detector. The three amplitude distributions have been expressed by a common equation (refer to (3.35)).

Using (3.35), a mathematical analysis of the reconstructed filtered images has shown that a dark-field image has a dark fringe located on the profile of the Gaussian image when the amplitude transmittance of the object has discontinuities, and that the recovery of the depth dimension is very accurate. Computation of the theoretical amplitude distribution for an opaque disk proves the existence of a dip which, for certain values of the disk radius and of the filter parameters, is exactly located on the contour of the Gaussian image (refer to (4.31)). The effects of the filter parameters on the width, depth and position of the dip have been discussed and the results have been compared with those obtained by Birch in the case of a one-dimensional slit.

The experimental investigations substantiate the theoretical analysis, namely, a systematic study of the effect of the parameters of dark-field filters on the images of disks has proved the validity of the theoretical results. The reconstructed images of different classes of objects have confirmed the general properties of dark-field images, and holographic imaging of particles sprayed on a flat glass has demonstrated the potential advantages of holography with a local reference beam obtained by spatial frequency component separation. Furthermore, the experimental results have clearly indicated that spatial filtering of the reference wave does not require a very fine filtering of the central ordinate.

PART B The original principles in holographic instrument design which have been presented are aimed at improving the practicality of holocameras with local reference beam generation. By treating the holocamera as a "black box", it has been shown that remote sensing measurements are feasible and that the three beam-folded configurations embodying retroreflectors permit holographic imaging of particle field under very harsh environmental conditions.

Of particular interest to the area of particle measurement is the configuration allowing imaging of hypervelocity transilluminated scenes, since pulsed laser sources generating pulses of relatively large pulse width can "freeze" a three-dimensional field of particles with the possibility of retrieving the three-dimensional relative velocity vector of one particle with respect to another one. Conventional double pulse holography using pulses with small pulse widths does not permit recovery of the relative velocity vector when the average velocity vector of the particles is much larger than the relative velocity vector.

Holographic tomography has been considered and a configuration has been proposed. The great advantage of holographic tomography over photographic tomography lies in the fact that there is no focussing requirement of the recording system on the slice of interest.

The results of the experimental investigations have clearly demonstrated the usefulness of the configurations proposed. In spite of the fact that a pulsed laser was not available in the laboratory, attempts at recording moving scenes have been made possible by selecting slowly moving particle

fields and by using short recording exposures. Meaningful simulation experiments based on the two-reflector configuration and on the configuration allowing imaging of hypervelocity transilluminated scenes have been performed using slowly moving scenes and long recording exposures.

PART C The considerable advantages of holographic optical elements over conventional imaging elements have been pointed out, and a compensation method allowing recording of high quality holographic optical elements has been suggested. This method is most effective when the holograms are recorded in photosensitive recording materials coated onto very cheap substrates or on curvilinear surfaces, and when mass production of holographic optical elements is considered.

Holographic optical elements are best suited for imaging in monochromatic illumination and an important use of such elements in a holocamera has been put forward. This holocamera, which generates a local optically processed reference beam, has important applications in holographic recording of particle fields.

The effect of the finite size of the recording sources on the resolution of a two-hologram optical element has been studied in detail. (The study has been carried out in the cases of sequential and independent recording of the holograms.) In addition, generalization of the results obtained with a two-hologram optical element has shown that in the absence of any other resolution reducing factors, the finite extent of the recording sources notably increases the point spread function as the number of holograms used in the multiple-hologram optical element increases.

Finally, the imaging properties of the holocamera using holographic elements have been experimentally investigated and the reconstructed images of a resolution test target definitely indicate the great potential of such a holocamera.

10.2 SUGGESTIONS FOR APPLICATIONS AND FURTHER RESEARCH

The most important applications of the methods and principles reported in this thesis were suggested as the theoretical and experimental studies were conducted; however, only vague examples were given. The relevance of particle measurements in cloud microphysics and pollution control were pointed out in Section 1.3. Figs. 10.1 and 10.2 illustrate a few specific applications of the beam-folded configurations in pollution control and in cloud microphysics.

It should be emphasized that the theoretical and experimental results obtained so far should provide substantial grounds for undertaking immediate field experiments that would lead to a widespread use of holocameras with local optically processed reference beams, when typical applications such as those shown in Figs. 10.1 and 10.2 are considered.

However, considerable theoretical and experimental research work is still required if applications of such holocameras to remote imaging of particle fields (refer to Section 6.2), or to long distance holography [88], are to be developed. In addition, viable applications of holographic instruments are hindered by the cumbersome processing of most photosensitive recording media available. The competitiveness of holographic

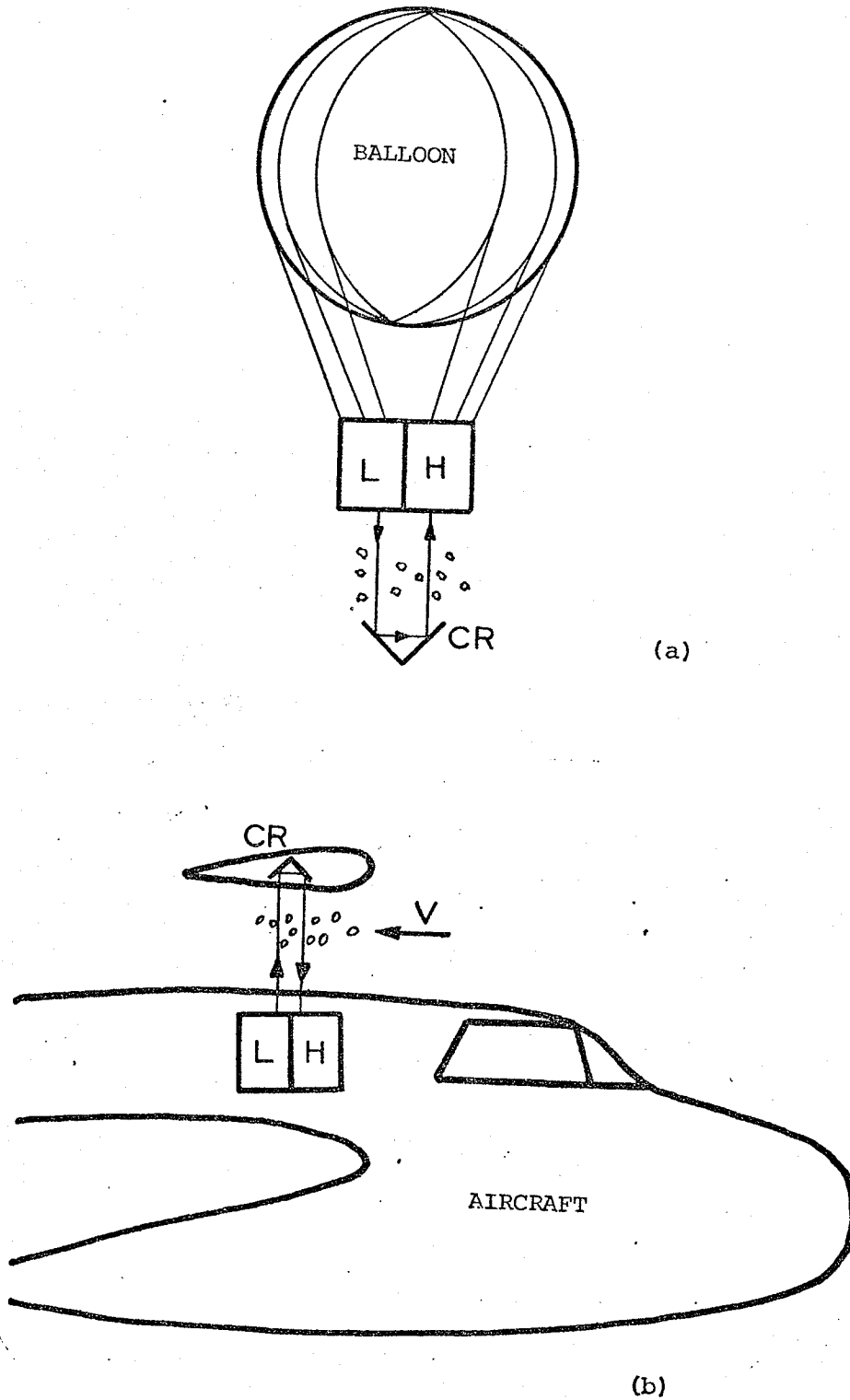


Fig. 10.1 Imaging of particle fields in cloud microphysics: (a) from a balloon, (b) from an aircraft.

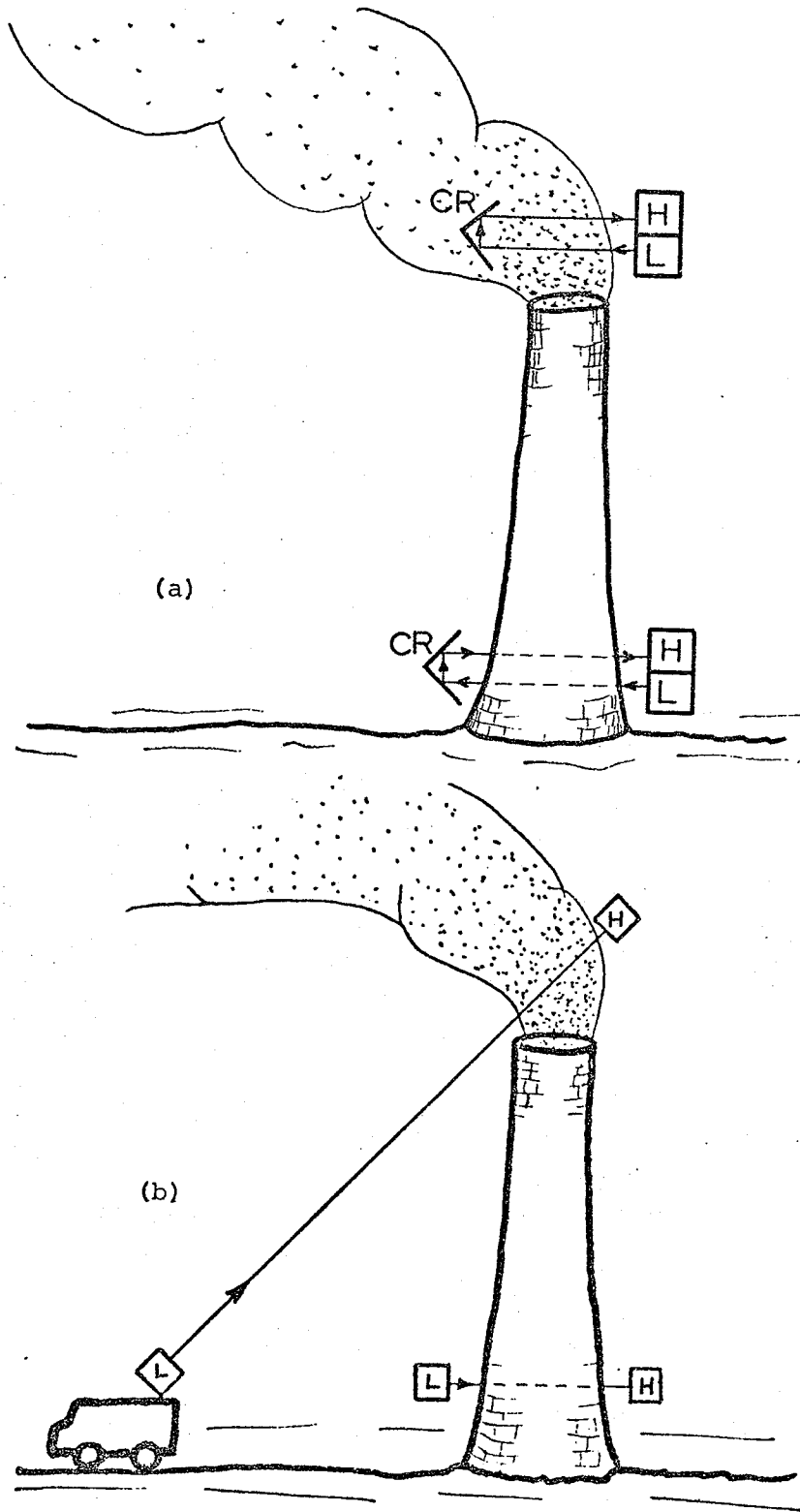


Fig. 10.2 Imaging of particle fields in pollution control: (a) using beam-folded configurations and (b) using conventional configurations.

methods with other modern methods of measurement of particle fields greatly depends on a rapid development of erasable recording media [89] which would permit real-time reconstruction. In situ real-time reconstruction would allow immediate scanning of the reconstructed images, and instantaneous processing and recording of the pertinent data.

AppendixSCALAR THEORY OF DIFFRACTION

Most of the mathematical derivations encountered in the thesis are based on the scalar theory of diffraction.

The propagation phenomenon of an electromagnetic wave from one plane to another plane can be expressed in mathematical terms by the so-called Rayleigh-Sommerfeld diffraction formula [90]

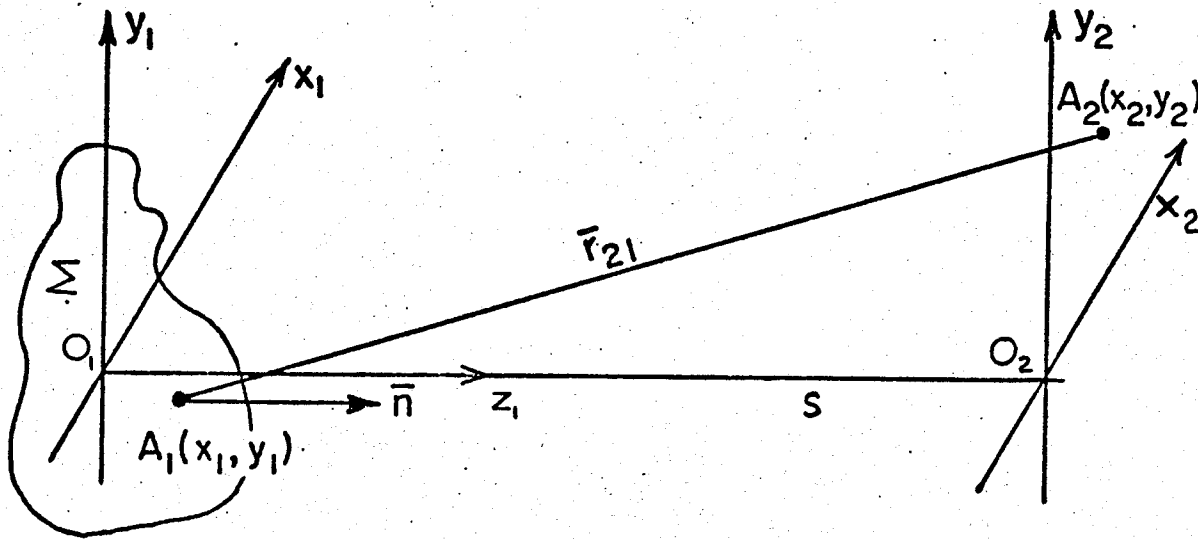
$$A_2(x_2, y_2) = (i\lambda)^{-1} \iint_{\Sigma} A_1(x_1, y_1) (r_{21})^{-1} \exp(i2\pi r_{21} / \lambda) \cos(\bar{n}, \bar{r}_{21}) d\sigma. \quad (A.1)$$

where λ is the wavelength, and the other notations used are depicted in Fig. A.1. By assuming that the distance s between the planes $\{x_2, y_2\}$ and $\{x_1, y_1\}$ is much larger than the dimensions of the aperture in the plane $\{x_1, y_1\}$, and much larger than the dimensions of the surface of interest in the plane $\{x_2, y_2\}$, the obliquity factor and the quantity r_{21} in the denominator of (A.1) can be approximated by $\cos(\bar{n}, \bar{r}_{21}) \sim \text{constant}$ and $r_{21} \sim s$. The quantity r_{21} in the exponent cannot be simply replaced by s , for the wave number k is very large.

The distance r_{21} can be expressed in terms of the coordinates of the points A_1 and A_2 . It follows that

$$r_{21} = [s^2 + (x_2 - x_1)^2 + (y_2 - y_1)^2]^{1/2}. \quad (A.2)$$

By retaining only the two first terms of the binomial expansion of the square root, r_{21} can be approximated by



$$A_2(x_2, y_2) = \frac{1}{i\lambda} \iint_{\Sigma} A_1(x_1, y_1) \frac{\exp(i2\pi r_{21}/\lambda)}{r_{21}} \cos(\vec{n}, \vec{r}_{21}) d\epsilon$$

Fig. A.1 Rayleigh-Sommerfeld diffraction model.

$$r_{21} = s[1 + (x_2 - x_1)^2 / (2s^2) + (y_2 - y_1)^2 / (2s^2)] \quad (A.3)$$

Taking into account the assumptions made on the obliquity factor, and on the quantity r_{21} in the denominator and exponent, (A.1) can be rewritten in the form known as the Fresnel diffraction equation

$$A_2(x_2, y_2) = [\exp(i2\pi s/\lambda)] (i\lambda s)^{-1} \exp[i\pi(x_2^2 + y_2^2)/(\lambda s)] \\ \iint_{\Sigma} \{A_1(x_1, y_1) \exp[i\pi(x_1^2 + y_1^2)/(\lambda s)]\} \exp[-i2\pi(x_1 x_2 + y_1 y_2)/(\lambda s)] dx_1 dy_1 \quad (A.4)$$

The Fourier transform of $\{A_1(x_1, y_1) \exp[i\pi(x_1^2 + y_1^2)/(\lambda s)]\}$ appears on the RHS of the above equation if $A_1(x_1, y_1)$ is identically zero outside the aperture Σ . Hence, (A.4) can be rewritten as follows

$$A_2(x_2, y_2) = [\exp(iks)] (i\lambda s)^{-1} H_s(x_2, y_2) \mathcal{F}_{1/\lambda s} [A_1(x_1, y_1) H_s(x_1, y_1)] \quad (A.5)$$

where $H_s(x_1, y_1) = \exp[(i\pi/\lambda s)(x_1^2 + y_1^2)]$ and $\mathcal{F}_{1/\lambda s}$ represents the two-dimensional Fourier transform operator, the Fourier transform being evaluated at spatial frequencies $x_2/(\lambda s)$ and $y_2/(\lambda s)$. The proportionality constant $[\exp(i2\pi s/\lambda)] (i\lambda s)^{-1}$ can be ignored. Thus, (A.5) yields

$$A_2(x_2, y_2) = H_s(x_2, y_2) \mathcal{F}_{1/\lambda s} [A_1(x_1, y_1) H_s(x_1, y_1)] \quad (A.6)$$

The above equation permits expression in concise terms of most of the phenomena of diffraction of light on passing through imaging systems.

REFERENCES

1. Gabor, D., A New Microscopic Principle, *Nature* 161, 777-778, 1948.
2. Gabor, D., Microscopy by Reconstructed Wave Fronts: II, *Proc. Roy. Soc., Ser. A* 197, 454-487, 1949.
3. Gabor, D., Microscopy by Reconstructed Wave Fronts, *Roy. Soc., Ser. A* 197, 454-487, 1949.
4. Leith, E.N. and Upatnieks, J., Reconstructed Wavefronts and Communication Theory, *J. Opt. Soc. Am.* 51, 1469, 1961.
5. Thompson, B.J., Holographic Particle Sizing Techniques, *J. Phys., Ser. E* 7, 781-788, 1974.
6. Trolinger, J.D., Airborne Holography Techniques for Particle Fields Analysis, *Annals of the New York Academy of Sciences* 267, 448-459, 1976.
7. Mason, B.J., The Physics of Clouds, Oxford Univ. Press, London, 427-443, 1957.
8. Jones, D.M.A. and Dean, L.A., A Raindrop Camera, Res. Rep. No.3, Contract DA-36-039 SC-42446, Illinois State Water Survey, Urbana, Ill., USA, 1953.
9. Jones, D.M., The Shape of Raindrops, *J. Meteorol.* 16, 504-510, 1959.
10. Pfeifer, H.J., The Development and Use of Laser Anemometers in Transonic and Supersonic Gaseous Flows, *J. Phys., Ser. E* 8, 245-252, 1975.
11. Dunning, J.W., Jr., Application of Laser Monodyne Spectrometer to Particle Size Measurements, Ph.D. Thesis, School of Engineering, Case Western Reserve University, Cleveland, Ohio, USA, 1967.
12. Andrews, D.G. and Seiferk, H.S., Investigation of Particle-Size Determination from the Optical Response of a Laser Doppler Velocimeter, SUDAAR No. 435, 1971.
13. Ward, J.H., Determination of Particle-Size Distributions from Composite Diffraction-Pattern Data, *J. Opt. Soc. Am.* 58, 1566, 1968.
14. Anderson, W.L., Particle Counting and Sizing by Fourier-Plane Measurements of Scattered Light, *J. Opt. Soc. Am.* 58, 1566, 1968.
15. Anderson, W.L., and Beissner, R.E., Counting and Classifying Small Objects by Far-Field Light Scattering, *Appl. Opt.* 10, 1503-1508, 1971.
16. Thompson, B.J., A New Method of Measuring Particle Size by Diffraction Techniques, *Japan. J. Appl. Phys., Suppl. I* 4, 302-307, 1965.

17. Thompson, B.J., Parrent, G.B., Justh, B. and Ward, J., A Readout Technique for the Laser Fog Disdrometer, *J. Appl. Meteorol.* 5, 343-348, 1966.
18. Thompson, B.J., Ward, J. and Zinky, W., Application of Hologram Techniques for Particle-Size Analysis, *Appl. Opt.* 6, 519-526, 1967.
19. Thompson, B.J., Diffraction by Opaque and Transparent Particles, *Optical Engineering* 2, 43-46, 1963.
20. Thompson, B.J., Fraunhofer Diffraction Patterns of Opaque Objects with Coherent Background, *J. Opt. Soc. Am.* 53, 1350, 1963.
21. Parrent, G.B. and Thompson, B.J., On the Fraunhofer (Far Field) Diffraction Patterns of Opaque and Transparent Objects with Coherent Background, *Opt. Acta* 11, 183-193, 1964.
22. Born, M. and Wolf, E., Principles of Optics, Pergamon Press, Oxford, Fourth Edition, 382-386, 1970.
23. Leith, E. and Upatnieks, J., Reconstructed Wavefronts and Communication Theory, *J. Opt. Soc. Am.* 52, 1123-1130, 1962.
24. Burckhardt, C.B., Efficiency of a Dielectric Grating, *J. Opt. Soc. Am.* 57, 601-603, 1967.
25. Kolgelnik, H., Coupled Wave Theory for Thick Hologram Gratings, *Bell Syst. Tech. J.* 48, 2909-2947, 1969.
26. Smith, H.M., Principles of Holography, Wiley-Interscience, New York, 1969.
27. Cathey, W.T., Local Reference Beam Generation for Holography, U.S. Patent No. 3, 415, 387, Dec. 10, 1968.
28. Caulfield, H.J., Harris, J.L., Hemstreet, H.W., Jr. and Cobb, J.G., Local Reference Beam Generation in Holography, *IEEE Proc.* 55, 1758, 1967.
29. Som, S.C. and Lessard, R.A., Holography with Off-Axis Reference Beam Derived from the Object Beam, *Appl. Phys. Lett.* 24, 600-602, 1974.
30. Dunlop, A.J. and Stachera, H.S., Polarization of E.M. Waves Scattered by Water Drops, *Elect. Lett.* 7, 87-88, 1971.
31. Born, M. and Wolf, E., Principles of Optics, Pergamon Press, Oxford, Fourth Edition, 41-47, 1970.
32. Corcoran, V.J., Herron, R.W., Jr. and Jaramillo, J.G., Generation of a Hologram from a Moving Target, *Appl. Opt.* 5, 668-669, 1966.

33. Waters, J.P., Object Motion Compensation by Speckle Reference Beam Holography, *Appl. Opt.* 11, 630-636, 1972.
34. Denisjuk, Y.N., Representation of Optical Properties of an Object by Means of Wave Pattern of Light Scattered by It, *Soviet Phys. Doklady* 7, 543-545, 1962.
35. Neumann, D.B., Penn, R.C., Object Motion Compensation Using Reflection Holography, *J. Opt. Soc. Am.* 62, 1373, 1972.
36. Gassend, M.L.A. and Boerner, W.M., Holocameras Using Local Reference Beams Obtained by Spatial Frequency Separation, Invention reported to the Canadian Patents and Development Limited, Ottawa, Ontario, Canada, CPDL Case No. 265-6087-1, July 1975.
37. Gassend, M.L.A., Davis, K.I. and Boerner, W.M., Holographic Recording of Magnified Dark-Field Images, *Opt. Soc. Am.* 66, 384, 1976.
38. Gassend, M.L.A. and Boerner, W.M., Holography with Local Reference Beam Obtained by Spatial Frequency Separation, Paper submitted for publication in *Applied Physics*, June 1976.
39. Lipson, S.G. and Lipson, H., Optical Physics, Cambridge Univ. Press, London, 81-82, 1969.
40. Chang, B.J., Alferness, R. and Leith, E.N., Space-Invariant Achromatic Grating Interferometers, *Appl. Opt.* 14, 1592-1600, 1975.
41. Meier, R.W., Optical Properties of Holographic Images, *J. Opt. Soc. Am.* 57, 895-900, 1967.
42. Rosen, L., Focussed-Image Holography with Extended Sources, *Appl. Phys. Lett.* 9, 337-339, 1966.
43. Bracewell, R.M., The Fourier Transform and Its Applications, McGraw-Hill, New York, 14-16, 1965.
44. Dew, G.D., The Application of Spatial Filtering Techniques to Profile Inspection, and an Associated Interference Phenomenon, *Optica Acta* 17, 237-257, 1970.
45. Spierer, C., Un Nouvel Ultra-Microscope, *Arch. Sci. Phys.* 8, 121-131, 1926.
46. Lansraux, G., Diffrimoscopy, *Metrologia* 1, 31-36, 1965.
47. Born, M. and Wolf, E., Principles of Optics, Pergamon Press, Fourth Edition, 157-166, 1970.
48. Bracewell, R., The Fourier Transform and Its Applications, McGraw-Hill, New York, 244-250, 1965.
49. Watson, G.N., A Treatise on the Theory of Bessel Functions, Cambridge University Press, Second Edition, 194-195, 1966.

50. Abramowitz, M. and Stegun, I., Handbook of Mathematical Functions, Dover Pub., Third Print. 231-233, 1965.
51. Birch, K.G., A Spatial Frequency Filter to Remove Zero Frequency, Optica Acta 15, 113-127, 1968.
52. Keller, J.B., Geometrical Theory of Diffraction, J. Opt. Soc. Am. 52, 116-130, 1962.
53. Birch, K.G., An Analysis of the Generalized Binary Filter, Optica Acta 17, 43-58, 1970.
54. Minck, R.W., Optical Frequency Electrical Discharges in Gases, J. Appl. Phys. 35, 252, 1964.
55. Arsenault, H.H., Random Biaised Holograms, Opt. Commun. 4, 267-270, 1971.
56. George, N., Speckle From a Thick Diffuser, J. Opt. Soc. Am. 65, 1196, 1975.
57. Gassend, M.L.A., Morland, D.K. and Boerner, W.M., Precipitation Measurements by Optically Processed Reference Beam Holographic Methods, USNC-URSI Meeting, Univ. of Illinois, Urbana, Ill., USA, June 1975.
58. Gassend, M.L.A. and Boerner, W.M., Particle Measurements with Holo-cameras Using Holographically Generated Optical Components, International Electrical-Electronics Conference and Exposition, Toronto, Ont., Canada, Paper No.75163, Sept. 1975.
59. Gassend, M.L.A. and Boerner, W.M., Holographic Apparatus for Imaging of Transilluminated Objects, Invention reported to the Canadian Patents and Development Limited, Ottawa, Ont., Canada, CPDL Case No. 265-6090-1, July 1975.
60. Gassend, M.L.A. and Boerner, W.M., Use of Trihedral Reflectors in Holography with a Local Reference Beam, Conference Proceedings of the International Conference on Applications of Holography and Optical Data Processing, Pergamon Press, Oxford, 1976.
61. Peck, E.R., A New Principle in Interferometer Design, J. Opt. Soc. Am. 38, 66, 1948.
62. Peck, E.R., Theory of Corner-Cube Interferometer, J. Opt. Soc. Am. 38, 1015-1024, 1948.
63. Goodman, J.W., Jackson, D.W., Lehmann, M. and Knotto, M., Experiments in Long-Distance Holographic Imagery, Appl. Opt. 8, 1581-1586, 1969.
64. Goodman, J.W., Temporal Filtering Properties of Holograms, Appl. Opt. 6, 857-859, 1967.

65. Papoulis, A., The Fourier Integral and Its Applications, McGraw-Hill, New York, 27, 1962.
66. Neumann, D.B., Holography of Moving Scenes, J. Opt. Soc. Am. 38, 447-454, 1968.
67. Gassend, M.L.A. and Boerner, W.M., Holographic Instrument for Three-Dimensional Imaging of Moving Transilluminated Scenes, Invention reported to the Canadian Patents and Development Limited, Ottawa, Ont., Canada, CPDL Case No. 265-6326-1, June 1976.
68. Neumann, D.B. and Rose, H.W., Improvement of Recorded Holographic Fringes by Feedback Control, Appl. Opt. 6, 1097-1104, 1972.
69. Gassend, M.L.A. and Boerner, W.M., Holographic Instrument for Three-Dimensional Imaging of Hypervelocity Particle Fields, Invention reported to the Canadian Patent and Development Limited, Ottawa, Ont., Canada, CPDL Case No. 265-6294-1, May 1976.
70. Gassend, M.L.A. and Boerner, W.M., Hypervelocity Particle Measurements by a Holographic Method, SPIE 97, 1976.
71. Dyes, W.A., Kellen, P.F. and Klaubert, E.C., Velocity Synchronized Fourier Transform Hologram Camera System, Appl. Opt. 9, 1105-1112, 1970.
72. Peck, E.R., Polarization Properties of Corner Reflectors in Cavities, J. Opt. Soc. Am. 52, 253-257, 1962.
73. Gassend, M.L.A. and Boerner, W.M., Holocamera Using Multiple Hologram Optical Elements, Invention reported to the Canadian Patents and Development Limited, Ottawa, Ont., Canada, CPDL No. 265-6325-1, July 1976.
74. Welford, W.T., Isoplanatism and Holography, Opt. Commun. 8, 239-243, 1973.
75. Close, D.H., Holographic Optical Elements, Optical Engineering 14, 408-419, 1975.
76. Leith, E.N. and Upatnieks, J., Holographic Imagery Through Diffusing Media, J. Opt. Soc. Am. 56, 523, 1966.
77. Kogelnik, H., Holographic Image Projection Through Inhomogeneous Media, Bell Syst. Tech. J. 44, 2451-2455, 1965.
78. Rogers, G.L., Experiments in Diffraction Microscopy, Proc. R. Soc. Edinb. 51, 193-221, 1950.
79. Meier, R.W., Magnification and Third-Order Aberrations in Holography, J. Opt. Soc. Am. 55, 987-992, 1965.
80. Champagne, E.B., Nonparaxial Imaging, Magnification and Aberrations Properties in Holography, J. Opt. Soc. Am. 57, 51-55, 1967.

81. Mintz, G.D., Morland, D.K. and Boerner, W.M., Holographic Simulation of Parabolic Mirrors, *Appl. Opt.* 14, 564-565, 1975.
82. Miles, J.F., Imaging and Magnification Properties in Holography, *Optica Acta* 19, 165-186, 1972.
83. Forshaw, M.R.B., The Imaging Properties and Aberrations of Thick Transmission Holograms, *Optica Acta* 20, 669-686, 1973.
84. Latta, J.N., Analysis of Multiple Hologram Optical Elements with Low Dispersion and Low Aberrations, *Appl. Opt.* 11, 1686-1696, 1972.
85. Gassend, M.L.A. and Boerner, W.M., Resolution Obtainable with Multiple Hologram Optical Elements: Effect of the Finite Size of the Construction Sources, Paper submitted to *Optica Acta* for publication, May 1976.
86. Thompson, B.J., Image Formation with Partially Coherent Light, *Progress in Optics*, VII, Academic Press, New York, 171-229, 1969.
87. Goodman, J.W., Introduction to Fourier Optics, McGraw-Hill, New York, Chapter 5, 1968.
88. Montgomery, W.D., Increased Optical Resolution from a Sampled Wavefront, *Appl. Optics* 7, 83-85, 1968.
89. Biedermann, K., Information Storage Materials for Holography and Optical Data Processing, *Optica Acta* 22, 103-124, 1975.
90. Wolf, E. and Marchand, E.W., Comparison of the Kirchoff and the Rayleigh-Sommerfeld Theories of Diffraction at an Aperture, *J. Opt. Soc. Am.* 54, 587-594, 1964.
91. Carter, W.H., Engeling, P.D. and Dougal, A.A., Polarization Selection for Reconstructed Wavefronts and Applications to Polarizing Microholography, *IEEE Journal of Quantum Electronics* 2, 44-46, 1966.
92. Ellis, G.W., Holomicrography: Transformation of Image During Reconstruction a posteriori, *Science*, 1195-1197, 1966.

CURRICULUM VITAE

Max L. A. Gassend was born January 17, 1948, in Nice, France, where his parents were horticulturists. On the small piece of family land, he had plenty of opportunities to explore the laws of nature and he developed an early interest in physics. In 1963 he designed and built a solar heating system able to provide enough hot water for the needs of the family.

In 1966 he received a "Baccalauréat" degree in Mathematics from the University of Nice. He then went to study at the school of engineering ESME ("Grande Ecole") of the "Académie" of Paris, where he received the "Diplôme d'Ingénieur" in 1972. In 1972, under its program of Cultural Exchanges, the Department of External Affairs of the Government of Canada, through the Canada Council, offered Mr. Gassend an award to undertake studies toward a Ph.D. at the Faculty of Graduate Studies of the University of Manitoba. Since then, he has specialized in electromagnetism, and has been involved in the area of optical holography and modern optics.

After his graduation from the University of Manitoba, Mr. Gassend will join the "Institut Européen des Hautes Etudes Internationales" in Nice, where he has been awarded a scholarship.

Mr. Gassend is a member of the Sigma Pi Sigma ($\Sigma\Pi\Sigma$) Physics Honor Society. He is a member of the "Société des Electriciens des Electroniciens et des Radioelectroniciens" (France), of the European Physical Society (SWITZ), and of the Society of Photo-Optical Instrumentation Engineers (USA). He is also a student member of the Institute of Electrical and Electronics Engineers (USA), of the Optical Society of America (USA) and of the Institute of Physics (GB).